MICROGRID ENERGY MANAGEMENT SYSTEM WITH ANCILLARY SERVICES TO THE GRID

A Dissertation
Presented to
The Academic Faculty

by

Maad Alowaifeer

In Partial Fulfillment
of the Requirements for the Degree
Doctor of Philosophy in
Electrical and Computer Engineering

Georgia Institute of Technology
August 2021

MICROGRID ENERGY MANAGEMENT SYSTEM WITH ANCILLARY SERVICES TO THE GRID

Approved by:

Dr. A. P. Meliopoulos, Advisor
School of Electrical and Computer Engineering
Georgia Institute of Technology

Dr. Santiago Grijalva
School of Electrical and Computer Engineering
Georgia Institute of Technology

Dr. Daniel Molzahn
School of Electrical and Computer Engineering
Georgia Institute of Technology

Dr. Lukas Graber
School of Electrical and Computer Engineering
Georgia Institute of Technology

Dr. Andy Sun
School of Industrial and Systems Engineering
Georgia Institute of Technology

Date Approved: June 29, 2021

To my daughter Sama

"You are a blessing"

ACKNOWLEDGEMENTS

I want to express my sincere gratitude to my advisor, Professor A. P. Meliopoulos. Throughout my five years of Ph.D. study, Prof. Meliopoulos generously flooded me from his sea of knowledge. Each meeting and discussion I had with him contained multiple lessons that have improved the way I think and work. His dedication, patience, and intellect are extraordinary, and I am extremely grateful for having this golden opportunity of interacting and be advised by such a great person.

I am also grateful to my dissertation committee members: Prof. Daniel Molzahn, Prof. Andy Sun, Prof. Santiago Grijalva, and Prof. Lukas Graber for their effort and time revising my work. Their insightful questions and suggestions throughout the phase of completing this dissertation are highly appreciated.

Thanks to King Fahd University of Petroleum and Minerals (KFUPM) for providing me with a scholarship to obtain my Ph.D. I appreciate all the people at KFUPM that enabled me to receive this scholarship.

I would also like to thank my fellow lab mates and friends at the Power Systems Control and Automation Laboratory (PSCAL): Prof. Abdullah Alamri, Oresits Vasios, Dr. Chiyang Zhong, Gad Monga Ilunga, Dr. Emeka Obikwelu. Juan Lazarte, Stella Kampezidou, Dr. Seyyedmohammadsadegh Vejdan , Dr. Hussain Albinali, Dr. Jiahao Xie, and Dr. Boqi Xie. I have learned a lot from them and with them during the time we spent together. Special thanks to my dear friend and colleague Mohannad Alkhraijah for the

lengthy and extremely insightful discussions we had. Without a doubt, his smartness and attention to detail helped me in completing this dissertation.

I am also deeply grateful for the friendship and companionship I had during my Ph.D. journey with Prof. Motaz Alfarraj. Using his extreme intellect, Motaz paved my way and eased my life experience in Atlanta, and for that, I owe him many thanks. Many thanks also go to my very dear childhood friends back home: Abdulaziz Alhamidi, Mohammed Alyemeni, Dr. Musaab Alhawas, Saeed Almubarak, Fahad Alotaibi, Moath Alhamidi, Dr. Eissa Alousi, Mohammed Alismail, Abdulrahman Alhawas, Abdulatif Alismail, and Meshari Alshammari. Their continuous support and cheering have lifted many burdens in my journey.

Words cannot express my appreciation to my beloved mother Hend, and my great father Prof. Mohammed. I sincerely appreciate their continuous love and support and I will never be able to return their uncountable favors. Thanks to my amazing siblings: Dr. Abdullah, Prof. Adi, Athbah, Qutybah, Marwan, and Wajd for always being there for me. Finally, I am ever grateful to my lovely wife Amjad. With her unconditional love, unlimited support, and surprising patience during our five years in the US, Amjad made me feel at home until she became home.

TABLE OF CONTENTS

ACKNOWLEDGEMENTS iv

LIST OF TABLES ix

LIST OF FIGURES xi

LIST OF SYMBOLS AND ABBREVIATIONS xvi

SUMMARY xviii

CHAPTER 1. INTRODUCTION 1
1.1 Background and Motivation 1
1.1.1 The Proliferation of Distributed Energy Resources 1
1.1.2 The Emergence and Adoption of Microgrids 3
1.1.3 Grid Challenges 4
1.1.4 Ancillary Services 6
1.1.5 Microgrids: Towards Servicing the Grid 7
1.1.6 Challenges Facing the Contribution of Microgrids to Grid Services 7
1.2 Proposed Research 9
1.3 Dissertation Outline 14

CHAPTER 2. LITERATURE REVIEW 16
2.1 Microgrids Layers of Control 16
2.2 Microgrid Energy Management System Formulations and Solution Methodologies 18
2.3 Ancillary Services from Microgrids to the Grid 21
2.4 Controllable Loads in Microgrid Energy Management Systems 24
2.5 Summary 24

CHAPTER 3. OVERVIEW OF THE PROPOSED μGEMS AND PROVIDED SERVICES 26
3.1 Overview 26
3.2 The Microgrid System Architecture and the Interaction with an External Grid 26
3.3 Overall Framework of the μGEMS 27
3.4 Service Products 30
3.4.1 Reserve 30
3.4.2 Regulation 31
3.4.3 Voltage Support 32
3.5 Service Designs: Procurement, Compensation, and Penalties 32
3.5.1 Design 1: Day-Ahead Commitment 32
3.5.2 Design 2: Real-Time Commitment 33

CHAPTER 4. THE MATHEMATICAL MODEL OF THE MICROGRID 36
4.1 Overview 38
4.2 Circuit Model 40
4.3 Fixed-Shunt Model 40
4.4 PQ Bus Model 41
4.5 Distributed Generator Model 42
4.6 Energy Storage System Model 43
4.7 Home Model 46
4.7.1 Thermostatically Controlled Load Model 48
4.7.2 Deferrable Uninterruptible Load Model 50
4.8 External Grid Model and Power Factor Limits 52
4.9 Bus Balance and Voltage Limits 54
4.10 Summary 55

CHAPTER 5. THE FORMULATIONS OF THE μGEMS OPTIMIZATION PROBLEMS 57
5.1 Overview 57
5.2 Day-Ahead Commitment Design 58
5.2.1 Commitments Management System: The Compute Optimal Commitments Problem 58
5.2.2 Day-Ahead Unit Commitment Problem 66
5.2.3 Hours Ahead Operations Planning Problem 69
5.2.4 Real Time Control Problem 73
5.3 Real-Time Commitment Design 76
5.3.1 Commitments Management System: The Compute Optimal Commitments Problem 78
5.3.2 Operations Planning and Control Management System: DAUC, HAOP, and RTC Problems 88
5.4 Summary 91

CHAPTER 6. THE SLP SOLUTION METHODOLOGY 92
6.1 Chapter Overview 92
6.2 The General Form of the *μ*GEMS Optimization Problems 92
6.3 The Linearized Subproblem 93
6.4 The Iterative Solution Algorithm 94
6.5 Summary 98

CHAPTER 7. BENCHMARKING THE SLP SOLUTION METHODOLOGY 99
7.1 Overview 99
7.2 The Test Systems 100
7.3 Case Studies and Benchmark Criteria 104
7.4 Benchmark Results 107
7.5 Summary 114

CHAPTER 8. CURRENT VS POWER BALANCE FORMULATION: A COMPARISON CASE STUDY 116
8.1 Overview 116

8.2 Case Studies and Results 117
8.3 Summary 120

CHAPTER 9. DEMONSTRATIVE CASE STUDIES FOR SERVICE PROVISION 121
9.1 Overview 121
9.2 Test System 121
9.3 Demonstrative Case Study: Day-Ahead Commitment Design 123
9.3.1 Case Study Setup 123
9.3.2 Results and Discussion 126
9.4 Demonstrative Case Study: Real-Time Commitment Design 144
9.4.1 Case Study Setup 144
9.4.2 Results and Discussion 146
9.5 Summary 153

CHAPTER 10. EXTERNAL GRID RELIABILITY ASSESSMENT WITH AND WITHOUT MICROGRIDS SERVICES 155
10.1 Introduction 155
10.2 System Model 155
10.2.1 Microgrid Model and Operational Modes 156
10.2.2 Main Load, Total Load, and System Supply Models 157
10.3 Simulation Procedure 159
10.4 Case Study 166
10.4.1 System and Input Data 166
10.4.2 Simulation Results 168
10.5 Summary 172

CHAPTER 11. CONCLUSIONS AND FUTURE RESEARCH DIRECTIONS 174
11.1 Conclusions 174
11.1.1 Summary and Contributions 174
11.1.2 Concluding Remarks 176
11.2 Future Research Directions 177

APPENDIX A. THE CONVEXIFIED μG MATHEMATICAL MODELS 179
A.1 The SOCP Model 179
A.2 The QC Model 183
A.3 Tightness and the Dependency on the Objective Function 189

APPENDIX B. THE μG MATHEMATICAL MODEL IN POWER BALANCE FORMULATION 191

REFERENCES 194

VITA 200

LIST OF TABLES

Table 7.1 The parameters of the DGs 102

Table 7.2 The operational, startup, and shutdown costs of the DGs 102

Table 7.3 The parameters of the ESSs 102

Table 7.4 The parameters of the TCLs 102

Table 7.5 The parameters of the DULs 102

Table 7.6 Network constraints 102

Table 7.7 Optimal objective function values 108

Table 7.8 Computational times in seconds 110

Table 7.9 Maximum circuit overloading (%) 111

Table 7.10 Maximum power factor violations (1) 112

Table 7.11 The objective function value of the original problem computed using the controls obtained from the optimization methods 113

Table 8.1 Optimal costs and computational times 118

Table 9.1 Network constraints and power factor limits 122

Table 9.2 Occurrences of PCC power factor values outside the imposed limits for the case with voltage support 133

Table 9.3 Occurrences of PCC power factor values outside the imposed limits for the case without voltage support 133

Table 9.4 Total μG profits with and without voltage support 134

Table 9.5 Occurrences of circuit overloading 137

Table 9.6 Reserve products provided in real-time 145

Table 10.1 Rate definitions of the Tiers..... 167

Table 10.2 Available power capacity as a percentage of total power capacity 168

Table 10.3 State transition rates of the power supply model..... 168

Table 10.4 Reserves available for the system supply operator..... 168

Table 10.5 EENS for base case and services case 170

Table 10.6 LOLE for base case and services case..... 170

LIST OF FIGURES

Figure 1.1. A projection of the centralized generation vs DERs annual capacity instalments from 2020 to 2030 [1] 2

Figure 1.2. An anual projection of μGs' capacity and implementation spending [3] 4

Figure 1.3. Global increase of renewable energy capacitites [6] 5

Figure 1.4. Added capacity of renewable and non-renewable recources as shares of the total added capacity [7] 5

Figure 2.1. Microgrid layers of control 16

Figure 3.1: Architecture of the studied system 27

Figure 3.2. Framework of the μGEMS 28

Figure 4.1. A depiction of a general bus within the μG 39

Figure 4.2. A schematic of a home with controllable devices 47

Figure 4.3. Feasibility region of the PCC power factor. 54

Figure 5.1. The framework of the μGEMS 57

Figure 6.1. The successive linear programming solution algorithm 95

Figure 7.1 The 33-bus test system 101

Figure 7.2 The 18-bus test system 101

Figure 7.3.Total active and reactive demand of the 18-bus system 103

Figure 7.4.Total active and reactive demand of the 33-bus system 103

Figure 7.5.Total active and reactive demand of the 69-bus system 103

Figure 7.6.Total active and reactive demand of the 85-bus system 104

Figure 7.7.Total active and reactive demand of the 141-bus system 104

Figure 7.8. Energy cost at the PCC 104
Figure 7.9. Ambient temperature 104
Figure 8.1. SLP convergence and computational time per iteration 119
Figure 9.1. The 33-bus test system 122
Figure 9.2.Total active and reactive net-demand for two consecutive days 123
Figure 9.3. Ambient temperature for two consecutive days 123
Figure 9.4. Day-ahead energy price at the PCC for two consecutive days 124
Figure 9.5. Committed power exports (DA Plan) for two consecutive days 128
Figure 9.6. Committed reserve capacities for two consecutive days 128
Figure 9.7. Committed regulation up capacities for two consecutive days 128
Figure 9.8. Committed regulation down capacities for two consecutive days 129
Figure 9.9. Expected profiles of power interchange with the external grid for two consecutive days 129
Figure 9.10. Realized μG's active power exports at the PCC 130
Figure 9.11. Response to reserve calls 130
Figure 9.12. Response to regulation calls 131
Figure 9.13. PCC voltage profile with a without μG's voltage support 131
Figure 9.14. Active and reactive power exports with voltage support 132
Figure 9.15. Active and reactive power exports without voltage support 132
Figure 9.16. (a) PQ interchange at the PCC with voltage support, (b) PQ interchange at the PCC without voltage support 133
Figure 9.17. (a) PQ interchange at the PCC with voltage support from the RTC solution, (b) PQ interchange at the PCC without voltage support from the RTC solution 134

Figure 9.18. Bus voltage magnitudes 135
Figure 9.19. Maximum and minimum bus voltage magnitudes 135
Figure 9.20. Circuits loading 136
Figure 9.21. Maximum circuit loading 136
Figure 9.22. Power output of the DGs 137
Figure 9.23. Power output of the ESSs 138
Figure 9.24. State of charge of the ESSs 138
Figure 9.25. Power consumption of the TCL at Bus 3 139
Figure 9.26. Inner temperature of the TCL at Bus 3 139
Figure 9.27. Power consumption of TCLs at busses 3 to 10 140
Figure 9.28. Power consumption of TCLs at busses 11 to 18 140
Figure 9.29. Power consumption of TCLs at busses 19 to 26 140
Figure 9.30. Power consumption of TCLs at busses 27 to 33 140
Figure 9.31. Inner temperature of TCLs at busses 3 to10 141
Figure 9.32. Inner temperature of TCLs at busses 11 to 18 141
Figure 9.33. Inner temperature of TCLs at busses 19 to 26 141
Figure 9.34. Inner temperature of TCLs at busses 27 to 33 141
Figure 9.35. Aggregate power consumption of all TCLs with DA price 142
Figure 9.36. Aggregate power consumption of all DULs with DA price 142
Figure 9.37. Computational times of: (a) the DAUC problem, (b) the HAOP problem, and (c) the RTC problem 143
Figure 9.38. Day-ahead energy price at the PCC for two consecutive days 146
Figure 9.39. Committed power exports (DA Plan) for two consecutive days 147

Figure 9.40. Hourly individual reserve products available at the PCC and the lost-of-opportunity cost 147
Figure 9.41. Hourly stacked reserve products available at the PCC and the lost-of-opportunity cost 148
Figure 9.42 Sum of individual and stacked reserve products over the day 148
Figure 9.43. Power exports for upward stacked reserve, downward stacked reserve, and no reserve cases..... 149
Figure 9.44. PQ interchange at the PCC 150
Figure 9.45. Bus voltage magnitudes when upward reserves are dispatched..... 151
Figure 9.46. Bus voltage magnitudes when downward reserves are dispatched..... 151
Figure 9.47. Bus voltage magnitudes when no reserve is dispatched..... 151
Figure 9.48. Circuits loading when upward reserves are dispatched..... 152
Figure 9.49. Circuits loading when downward reserves are dispatched..... 152
Figure 9.50. Circuits loading when no reserve is dispatched 152
Figure 9.51. Computational times of all problems solved to find RT reserve products and costs..... 153
Figure 10.1. System model 156
Figure 10.2. State transition diagram and transition rate matrix..... 158
Figure 10.3. Overall simulation procedure 160
Figure 10.4. (a) total net-demand of μG1, and (b) total net-demand of μG2 167
Figure 10.5. Ambient temperature 167
Figure 10.6. Tiers of the energy rate at the PCC 167
Figure 10.7. Hourly demand of the main load 168

Figure 10.8. (a) power exports of μG1, and (b) power exports of μG2 169
Figure 10.9. Base case EENS for the three time regions 169
Figure 10.10. Services case EENS for the three time regions 170
Figure 10.11. Base case LOLE for the three time regions 170
Figure 10.12. Services case LOLE for the three time regions 170
Figure 10.13. Power exports of μG 1 in base case and services case at an incident 172
Figure 10.14. Total μGs' operational cost increase from providing services 172

LIST OF SYMBOLS AND ABBREVIATIONS

CMS	Commitments Management System.
CTMC	Continuous Time Markov Chain.
DA	Day Ahead.
DAUC	Day Ahead Unit Commitment.
DER	Distributed Energy Resource.
DG	Distributed Generator
DTMC	Discrete Time Markov Chain.
DUL	Deferrable Uninterruptible Load.
eG	External Grid.
HAOP	Hours Ahead Operation Planning.
MCMC	Markov Chain Monte Carlo.
MIQCP	Mixed Integer Quadratically Constrained Programming.
OpPC	Operations Planning and Control Management System.
PCC	Point of Common Coupling

QC	Quadratic Convex.
RT	Real Time.
RTC	Real Time Control.
SLP	Successive Linear Programming.
SOCP	Second Order Conic Programming
TCL	Thermostatically Controlled Load.
μG	Microgrid.
μGEMS	The proposed microgrid energy management system.

SUMMARY

Climate change has increased the frequency and intensity of severe weather conditions leading to catastrophic power interruptions. To mitigate these interruptions, the adoption of microgrids (μGs) emerged. A μG is a cluster of interconnected loads and distributed energy resources (DERs) that may be managed collectively to achieve given operational objectives. Concurrently to the adoption of μGs, large amounts of renewable resources have been integrated into the grid. Renewable resources are characterized by variable and uncertain power output which creates operational challenges to grid operators. Grid operators are faced with an increasing need for flexible resources that are able to absorb the variability and uncertainty in operation. Part of the need can be met by μGs; a μG may be optimized to provide different ancillary services to the grid.

We propose a microgrid energy management system (μGEMS) that optimally *plans the operations*, and *control* the DERs while *committing*, *holding*, *dispatching*, and *maintaining* different ancillary services for the grid in a *reliable* and *economical* manner. Reserve, regulation, and voltage support services can be supplied simultaneously via the μGEMS. The proposed μGEMS may be used to commit the services a Day-Ahead (DA) in advance to dispatch, or in Real-Time (RT) (i.e., DA and RT Commitments). Commitment rules that the μGEMS can consider include minimum acceptable capacities, required time to respond, and required time to maintain. We model the μG as an AC network using the current formulation to obtain a model that is mostly linear. Bus voltage, circuit loading, and point of common coupling (PCC) power factor limits are enforced during the *commitment*, the *holding*, the *dispatching*, and the *maintaining* stages of

services. The proposed μGEMS consists of a collection of interacting optimization problems each with a certain task, planning horizon, and frequency of solve. The optimization problems are generally mixed-integer quadratically constrained programming (MIQCP) problems. A solution methodology for the optimization problems is proposed based on *successive linear programming* (SLP) which promises efficient handling of discrete variables.

CHAPTER 1. INTRODUCTION

This chapter provides a background and motivation in section 1.1, followed by a summary of the proposed research in section 1.2. The dissertation outline is given in section 1.3. In the background and motivation section, we discuss the reasons behind the proliferation of distributed energy resources (DERs) and microgrids (μGs). We then indicate the challenges facing the grid from increased variability and uncertainty calling for additional ancillary service capacities. Finally, we signify how μGs may contribute to the provision of ancillary services to the grid and we explain the challenges facing this provision of services.

1.1 Background and Motivation

1.1.1 The Proliferation of Distributed Energy Resources

Traditional power systems are centralized in structure where the power is generated from central conventional power plants and then transmitted through transmission lines. The high voltage transmission lines transmit the power to medium voltage distribution systems that distribute the power to end-users. The centrality of generation in the power system was driven by the economics-of-scale; a few large power plants are more efficient in meeting the demand than many small ones. However, this central structure has been changing with the increased integration of DERs close to the end-users.

Reliability and cost have been the two main drivers for the arising integration of DERs. From the end-users' perspective, the installation of DERs increases the reliability of the power supply. When power from the upstream grid is interrupted, end-users may

supply all or part of their load by the DERs. Another advantage seen by the end-users is the reduced operational cost of electricity especially in the case of renewable-based resources due to the absence of fuel costs. The installation of DERs is expected to grow as the demand for reliable power increases and as DERs cost decreases. Figure 1.1 shows a projection of the DERs annual capacity installments along with centralized generation installments where it is forecasted that the global capacity installment of new DERs will be roughly double the capacity installment of centralized generation by 2030.

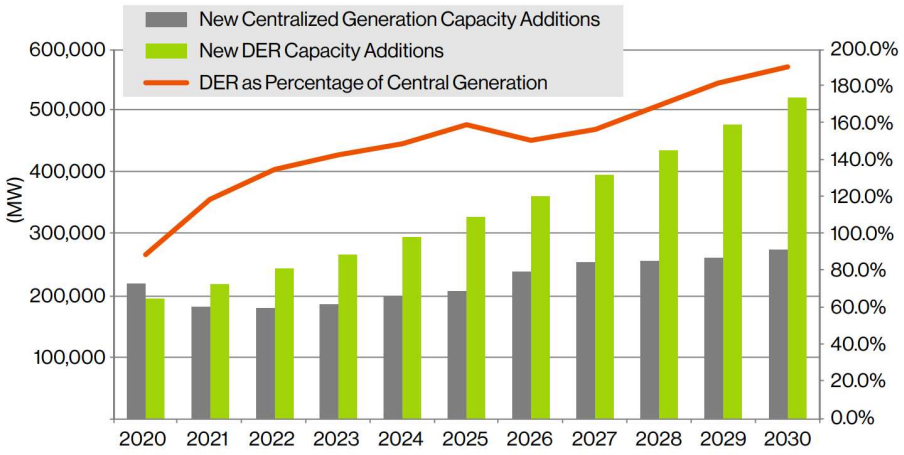

Figure 1.1. A projection of the centralized generation vs DERs annual capacity instalments from 2020 to 2030 [1]

Examples of DERs include distributed generators (DGs) and energy storage systems (ESSs) each bringing different benefits and tradeoffs to the end-users. DGs, for example, bring a reliable uninterruptible power supply as they can be dispatched when needed but with an added fuel cost. ESSs enable shifting the demand of the user from time to time to mitigate importing power from the grid during times with high grid prices. In addition, controllable loads are also seen as examples of DERs such as thermostatically controlled loads (TCLs) and deferrable uninterruptable loads (DULs).

1.1.2 The Emergence and Adoption of Microgrids

When a multiplicity of DERs is controlled within defined electrical boundaries, a new identity with sophisticated functionality emerges, a microgrid (μG). A more formal definition of a μG is as follows:

> "*a group of interconnected loads and distributed energy resources within clearly defined electrical boundaries that acts as a single controllable entity with respect to the grid. A microgrid can connect and disconnect from the grid to enable it to operate in both grid-connected or island mode*" [2].

A μG may contain different types of DERs that when combined, offer reliability and resiliency to its users, as well as economical operation. For example, a μG may contain a PV system along with an ESS to store the excess renewable energy for later use. A μG may also contain controllable loads that can be managed to relieve the system during high demand or to balance the fluctuation of renewable resources output.

With this ability to have multiple DERs, the adoption of μGs has increased substantially in the last few years driven by multiple factors including: increased major interruptions caused by severe weather, increased global demand for clean energy, and increased electrification, which makes μGs an option to offset needed electrical infrastructure investments. The global adoption of μGs is expected to increase substantially in the coming decade. Figure 1.2 shows a projection of the annual μG capacity and implementation spending from 2019 up until 2028. It is expected that the global capacity of μGs will increase from around 4GW in 2019 up to more than 20GW in 2028 associated with a quadruple in the spending to reach more than $40 billion in 2028.

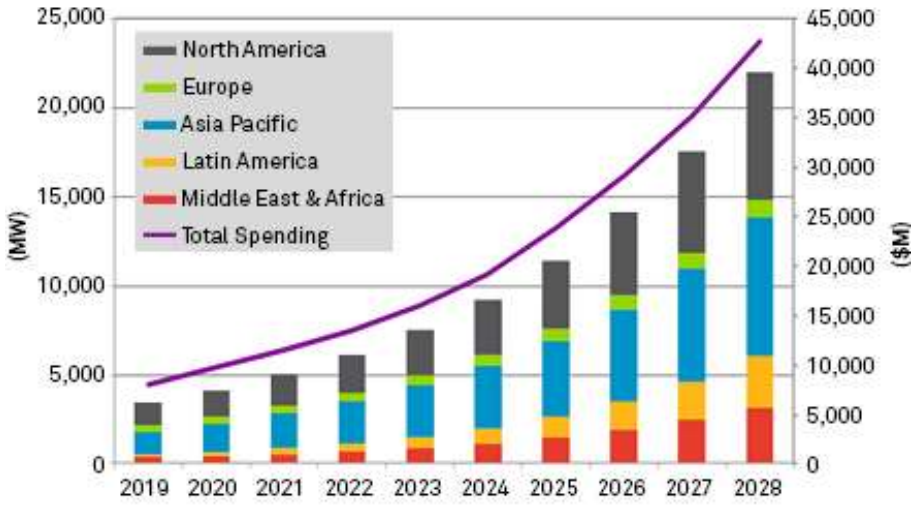

Figure 1.2. An anual projection of μGs' capacity and implementation spending [3]

1.1.3 Grid Challenges

While the adoption of μGs and the proliferation of DERs in the grid is advantageous to end-users, it is not necessarily beneficial to the main grid. In fact, DERs may cause challenges for grid operation and security such as voltage violations and current limits violations [4], [5]. In addition, as more DERs and μGs, especially renewable based ones, are connected to the grid, the variability and uncertainty of behind-the-meter power profiles increases, creating additional operational and security challenges to the grid.

The variability and uncertainty of power profiles seen by grid operators has been increasing due to both the proliferation of behind-the-meter DERs as well as the increasing deployment of large-scale grid-connected renewable resources. Figure 1.3 show the global installment of renewable energy capacity from 2001 until 2019 with an added capacity in 2019 roughly seven folds of that in 2001. Additionally, Figure 1.4 illustrates the added global renewable and non-renewable capacities as shares of the total added capacity. Observe the substantially increasing share of renewable resources relative to non-renewable resources.

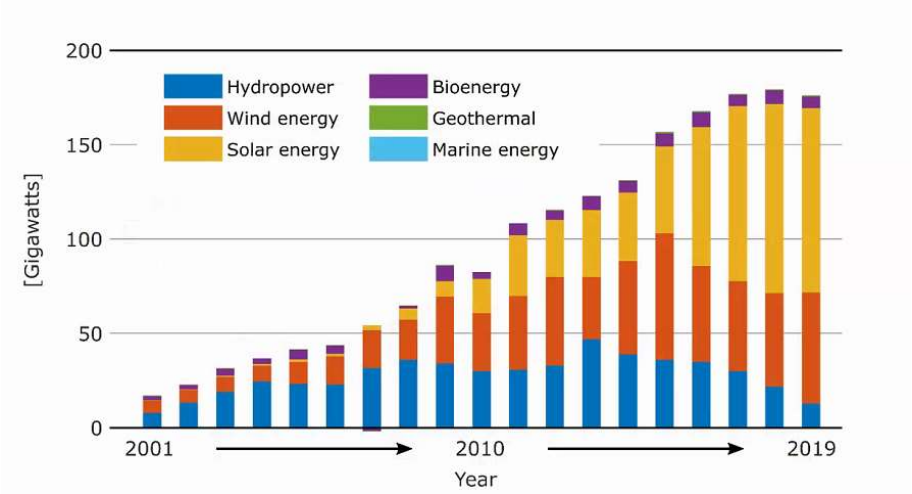

Figure 1.3. Global increase of renewable energy capacitites [6]

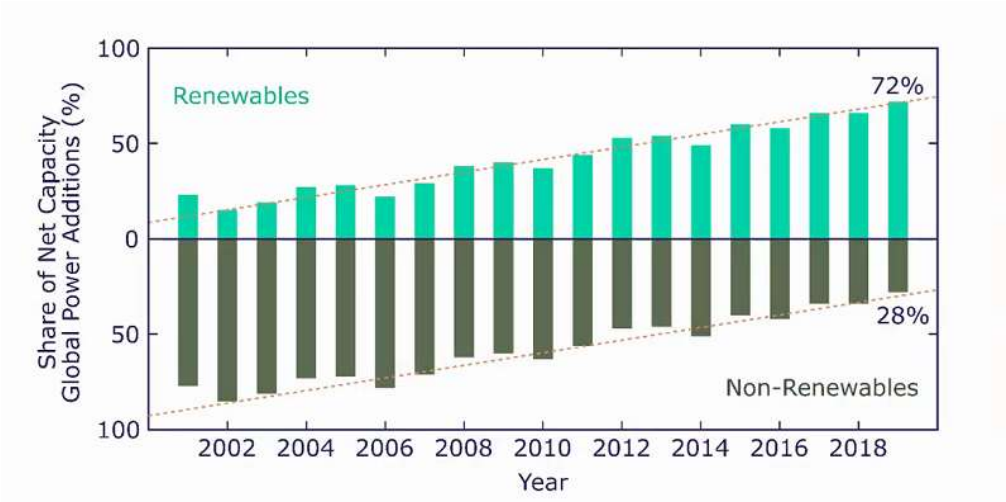

Figure 1.4. Added capacity of renewable and non-renewable recources as shares of the total added capacity [7]

A critical difference between the two sources of variability and uncertainty (i.e., behind-the-meter DERs and large-scale renewables) is that behind-the-meter DERs are generally more difficult to forecast and model than large-scale renewable resources (see [8]), which is due to the lack of detailed information seen by the grid operator for the case of behind-the meter DERs, as well as their geographically scattered nature. Another critical difference between the two sources of variability and uncertainty is the ability to be curtailed by grid operators. Large-scale renewable resources are generally curtailable

offering a degree of controllability to grid operators unlike behind-the-meter DERs. For grid operation and planning purposes, behind-the-meter DERs, and μGs in general, are usually lumped with the load and are not modeled as active resources with multiple potential functionalities [9].

1.1.4 Ancillary Services

In order to operate a power system in a reliable manner, a continuous balance between generation and demand must be met that adheres to specific levels of frequency and voltage. Reaching a continuous balance, however, is not a straightforward task due to the uncertainty and variability of the grid's conditions arising from large scale renewables, loads and DERs, grid equipment failures, and imprecise control of generators' outputs. To mitigate this uncertainty and variability and maintain a continuous power balance, grid operators procure and dispatch different ancillary services. Ancillary services are generally capacities of active and reactive power that can be injected to or absorbed from the system when needed, within specific response times, and for specific durations. Examples of ancillary services include reserve, regulation, and voltage support.

The amount of ancillary services needed to maintain a continuous balance in the system depend on the level and pace of the variability in the system. A high level of variability would require high available service capacities. Also, a rapid variability would require fast responding generation units that are able to ramp up or down in a pace that can cope with this variability. The issue of needing fast ramping generation units is magnified as more renewable resources are integrated within the power system due to their significant uncertain variability. Introducing more renewable resources into the grid requires more

ancillary service capacities to be maintained. One solution to overcome this growing need of ancillary service capacities is to install new fast-ramping generation units, an approach requiring a significant capital cost and conflicts with the move towards clean energy. Hence, it is important to find an alternative solution to meet the growing need for ancillary services and to ensure a reliable operation of the grid.

1.1.5 Microgrids: Towards Servicing the Grid

μGs can contribute to meeting the growing need of ancillary services. By having a mix of flexible fast-responding DERs, a μG may combine the capacity and flexibility of these resources to support the grid as a single flexible entity. In addition, μGs have a great potential in providing ancillary services to the grid due to their location near the loads. μGs can provide localized solutions such as reserve that can be dispatched without stressing the system lines, voltage support at the distribution level, and flexible ramping capacities to reduce the variability arising from behind-the-meter resources. These localized solutions are also important as more large-scale renewables are added to the grid which increases the possibility of transmission congestions [10]. Hence, obtaining needed services form μGs in the downstream would relief such possible congestions and pave the way towards more installation of renewable resources. It is worth noting that owners of μGs are motivated to provide ancillary services to the grid as it will bring about a new source of revenue making the cooperation between μGs and the grid beneficial for both parties.

1.1.6 Challenges Facing the Contribution of Microgrids to Grid Services

Typically, ancillary services are procured from conventional generators where the computation of service capacity is straightforward. Reserve and regulation capacities of a

generator, for example, can be simply computed given the generator's rated capacity, ramping limits, and current dispatch, which are readily available. In contrast, a μG may contain different types of DERs each having different capabilities. These capabilities must be aggregated while respecting the physical constraints of the DERs in order to present the μG total service capacity as a single product to the grid. The characteristics of storage-based DERs (e.g., ESSs and TCLs) complicates the process of computing the aggregated service capacity of the μG. Unlike a conventional generator, the capacity of an ESS or a TCL at a certain time period depends on the dispatch history. Dispatching a committed capacity of reserve at specific time periods would affect the available capacity in the consecutive time periods due to the storage behavior of these two resources.

Another challenge in providing services to the grid from a μG is the computation of the associated cost of providing the service. For a conventional generator, the operational cost is usually a given closed form function in terms of the active power output and therefore, the compensation that will be asked for in return to the services is easily computed. Even for voltage support service where reactive power is typically injected or absorbed, the compensation can be simply computed as the loss of opportunity resulting from constraining the active power output to support the voltage [11]. In contrast, the μG operational cost depends on numerous factors including each DERs cost, the cost of energy from the grid, the internal demand of the μG, the availability of renewable resources, etc. These factors make it difficult to compute the operational cost incurred by the μG when providing services to the grid.

A further issue complicating the provision of services from a μG to the grid is the internal network of the μG. When computing the aggregate service capacity, satisfying the

network constraints (e.g., circuit thermal and bus voltage limits) and considering the associated losses within the μG network are important factors. Satisfying network constraints is important because the internal network of the μG is expected to be stressed to deliver significant capacity, when needed, to the grid. The consideration of the network losses is also crucial to avoid overestimating the capacity that can be delivered to the point of common coupling (PCC) with the grid, which may lead to penalties for insufficient supply.

It is important to tackle the aforementioned challenges in order to facilitate the provision of ancillary services from μGs to the grid. A μG energy management system that ensures an optimal secure operation of the μG while considering the provision of ancillary services to the grid becomes essential.

1.2 Proposed Research

The objective of this research is to model a microgrid energy management system (*μ*GEMS) that optimally *plans the operations*, and *control* the DERs while *committing*, *holding*, *dispatching*, and *maintaining* different ancillary services for the grid in a *reliable* and *economical* manners.

To achieve this objective, we start this research by mathematically modeling the μG network, the different types of DERs, and the external grid. The μG network is modeled as an AC network using current formulation instead of the power balance formulation resulting in a model that is mostly linear. Network constraints including bus voltage limits and circuit thermal limits are enforced to ensure a reliable operation of the μG. The modeled DERs include distributed generators (DGs), energy storage systems (ESS), and

controllable house appliances such as thermostatically controlled loads (TCLs), and deferrable uninterruptible loads (DULs). House appliance are controlled while ensuring the convenience of households by including appropriate constraints. The external grid is modeled as a Thevenin equivalent circuit to incorporate the coupling between the μG injected power, and the voltage at the PCC. The mathematical model of the μG is posed as a multi-case, multi-period AC model. The multi-case, multi-period model enables planning for multiple prospective operating points crossing a horizon of multiple time periods, and ensures the feasible operation of the μG under any realized sequence of operating points. The model is similar to that appearing in a multi-period security constrained optimal power flow problem with corrective actions. The corrective actions, however, in the presented multi-case multi-period AC model are seen as responses to calls from the external grid for services.

Once the mathematical model of the μG is presented, we move to structuring the proposed μGEMS and formulating the associated optimization problems. The μGEMS is essentially a collection of interactive optimization problems that cooperate to optimally operate the μG in a continuous manner. The μGEMS is divided into two main parts. The Operations Planning and Control Management System (OpPC) and the Commitments Management System (CMS). The OpPC *plans the operations* of the μG considering a horizon of a day or two before the dispatch. The OpPC also *controls* the DERs by sending dispatch set points in real-time. Further, the CMS computes the optimal commitments of ancillary services that can be provided to the external grid, whether a day-ahead of dispatch, or in real-time.

The OpPC is structured in a hierarchical manner consisting of three modules: Level 1) the Day-Ahead Unit Commitment (DAUC) module, Level 2) the Hours Ahead Operations Planning (HAOP) module, and Level 3) the Real-Time Control (RTC) module. We propose an optimization problem for each of the three modules.

The DAUC plans the operations for an entire day with hourly steps covering the daily variation of loads, renewables, temperature and grid price. The DAUC is solved each hour or two and is responsible for finding the optimal set points for controls that require long planning horizon including the commitment of the DGs and the commitment of the DULs. Additionally, the DAUC computes the end-of-horizon limits for storage based DERs (ESSs and TCLs), which are taken as inputs along with the DERs' commitments to the next module, the HAOP.

The HAOP plans the operations for several hours with a finer time step (e.g., 10-15 minutes) and more frequent solves than the DAUC (e.g., 5-15 minutes). The HAOP finds the optimal active power controls that require a planning horizon of several minutes including DGs active power output, ESS charging/discharging, and TCL consumption. The horizon and time step of the HAOP enable the consideration of ramping constraints, the ESS capacity, and the TCL temperature limits. The active power controls computed by the HAOP are given as recommended values to the final hierarchical level, the RTC.

Taking the DERs commitment from the DAUC as fixed values, and the active power controls from the HAOP as recommended values, in addition to the real-time μG state, the RTC computes the optimal controls that will be immediately sent to the DERs. The RTC is solved each tens of seconds. Such frequency of solves enables responding to

grid calls for services in a timely manner. Notably, while performing the operations planning and control tasks, the three hierarchical modules consider the *holing*, *dispatching* and *maintaining* of committed ancillary services. The *commitments* of these ancillary services, however, are the responsibility of the commitments management system (CMS) which is the second part of the proposed μGEMS.

Services provided by the μG are governed by the procurement, compensations, and penalization procedures (i.e., *services designs*). We consider two *service designs*: 1) the Day-Ahead (DA) Commitment design, and 2) the Real-Time (RT) Commitment design. Optimization problems are formulated for the CMS considering each of the two service designs. The formulated problems enable the computation of optimal commitments considering all *service designs* rules.

In the DA Commitment design, the μG is assumed to commit reserve and regulation capacities to the external grid a day in advance to operation, which is analogous to DA markets. Given forecasted clearing prices for energy, reserve, and regulation capacities, the CMS computes the optimal energy, reserve, and regulation capacities as offers than can be committed for each hour of the following day. Reserve and regulation capacities must obey given rules including minimum acceptable capacity, a time to respond and reach the full capacity, and a time to maintain upon dispatch. Once these offers are awarded, the OpPC of the μGEMS is updated to *hold* the capacities as time passes and as forecast changes, *dispatch* the capacities in appropriate time once requested, and *maintain* the dispatch of the capacities as per the received calls.

In the RT Commitment design, the μG is assumed to commit reserve capacities in real-time and there is no hold for services as time passes, which is analogues to balancing markets. At each instant of time, the CMS computes the optimal *reserve products* that can be provided in real-time. A reserve product is categorized by a capacity, a time to provide the capacity, and a time to maintain the capacity. Because the μG, in general, contain multiple types of DERs including storage based DERs, multiple *reserve products* can be provided by the μG in real-time. The CMS computes these multiple products, as well as the associated cost for each product, and submits the product-cost pairs to the external grid. The cost is computed by calculating the lost-of-opportunity cost from providing the product. If the external grid requests the dispatch of a specific product, the OpPC is immediately updated to *dispatch* and *maintain* the requested product.

Notably, in both service designs, the μG can provide voltage support to the external grid simultaneously to the provision of reserve and regulation capacities. Voltage support can be provided by the μGEMS in two ways: 1) by minimizing the deviation of the voltage magnitude at the PCC bus from a target value given by the external grid, and/or 2) by maintaining the power factor at the PCC within pre-specified ranges given by the external grid.

After presenting the μG mathematical model, structure the μGEMS and formulating the OpPC and the CMS optimization problems, we propose a solution methodology for the resultant optimization problems. The optimization problems are generally mixed-integer quadratically constrained programming (MIQCP) problems. We propose a solution methodology for the MIQCP problems based on successive linear programming (SLP). The SLP methodology solves the optimization problems in an

iterative manner by linearizing the problem and solving a mixed-integer linear programming (MILP) problem at each iteration. We implement two updates at each iteration and before the consecutive linearization iterations: 1) a reduction to the continuous variables' trust regions depending on their oscillation, and 2) a fixing of non-changing binary variables to minimize the complexity of the upcoming MILP problems as the SLP method progress.

We perform multiple case studies in this work which can be separated into four parts: 1) we benchmark the SLP solution method with two convexification-based solutions methods, and a commercial MIQCP global solver, on multiple test systems and for multiple optimization problems. The two convexification-based methods are the second-order conic programming (SOCP) relaxation approach proposed in [12], and the quadratic convex (QC) relaxation approach proposed in [13]. The commercial MIQCP solver used in the benchmark is Gurobi [14], 2) we compare the current formulation of the μG model with a power balance formulation using multiple test systems. The SLP solution method is used to in the comparison study, 3) we simulate the operation of a μG when optimized by the μGEMS for both the DA and RT service designs. This part includes a minute-by-minute simulation of the μG considering forecast errors, and finally, 4) we assess the reliability improvements of a system when services are provided from connected μGs. This case study contains a simulation of the μGs for multiple years via the μGEMS.

1.3 Dissertation Outline

The dissertation is organized as follows: Chapter 2 presents a literature review of the different μG control layers, a review of μGs energy management systems' formulations

and solution methodologies, a review of μGs energy management systems in providing ancillary services to the grid, a review of controllable loads in μGs, and finally, a summary connecting the literature with the proposed work. Chapter 3 provides an overview of the proposed μGEMS and covers definitions and assumptions related to the μG system architecture, the interaction with the external grid, services provided, and service designs. Chapter 4 introduces the mathematical model of the μG which is posed as a multi-case, multi-period AC model. The optimization problems of the μGEMS considering both service designs (DA Commitment and RT Commitment) are formulated in Chapter 5. The SLP solution methodology is proposed in chapter 6 and is benchmarked with the other solution methodologies in Chapter 7. Chapter 8 compares the current formulation and the power balance formulation by optimizing multiple systems. Further, Chapter 9 delivers demonstrative case studies for both service designs, the DA Commitment, and the RT Commitment. Chapter 10 presents the reliability assessment case study to quantify the reliability enhancement of a system due to μGs service provision. Finally, conclusions and future research directions are drawn in Chapter 11.

CHAPTER 2. LITERATURE REVIEW

This chapter is divided into five sections. In section 2.1, we define the different control layers of µGs and identify the role of our µGEMS within these layers. Section 2.2 reviews the various formulations and solution methodologies used to tackle the µG energy management system task. Section 2.3 reviews models used to consider the provision of ancillary services form µGs, and section 2.4 reviews controllable loads in the context of µG energy management systems. Finally, a summary connecting the literature survey with the proposed work is given in section 2.5.

2.1 Microgrids Layers of Control

The µG control can be conceptually divided into three hierarchical control layers (depicted in Figure 2.1): *primary control*, *secondary control*, and *tertiary control* [15].

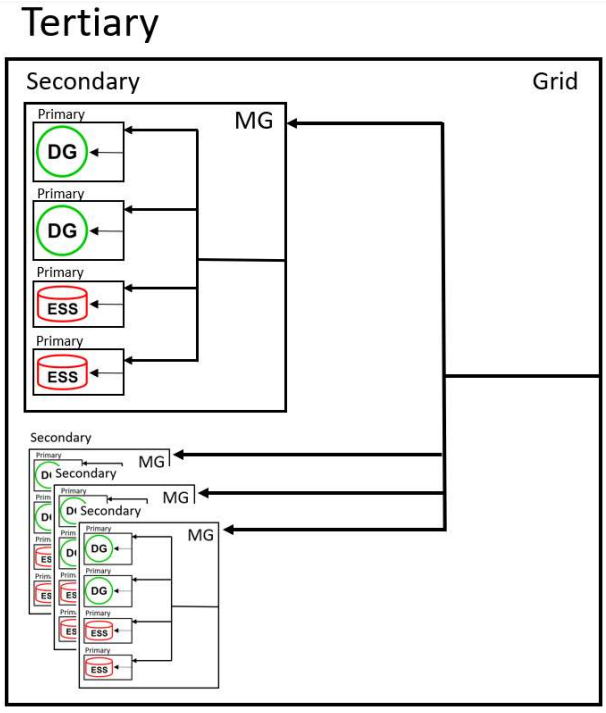

Figure 2.1. Microgrid layers of control

These control layers differ in two main aspects: (a) the scale of the systems they control, and (b) the control time response. The *primary control* layer is responsible for locally controlling the DERs based on set points received from the secondary control layer. In some cases, the primary layer also deals with regulating the disturbance in voltage and frequency where designated resources share the active and reactive power mismatches within the μG. Each DER has its own local controller that responds to events in milliseconds or tens of milliseconds [16]. The *secondary control* layer oversees the coordination between the outputs of all μG resources by setting set points to the local controllers in the *primary control layer*. Further, this layer ensures a secure, reliable and economical operation of the μG, so that certain objectives are achieved. Example of objective functions include minimizing the μG's total operational costs [17], minimizing greenhouse gas (GHG) emissions [18], and maximizing supplied loads [19]. This layer is referred to as the μG energy management system. The response time of this control layer is typically in the range of multiple seconds to minutes [20]. Finally, the *tertiary control* layer is the layer responsible for the communication between the μG and the external grid. The external grid may send dispatch commands to the μG through this layer. The response time of this layer depends on the commitments between the external grid and the μG and could range from multiple seconds to minutes.

The focus of this work is on the secondary control layer with some emphasis on the tertiary control layer. Regarding the primary control layer, we assume that the DERs are not locally controlled for the purpose of regulating the system's voltage and/or frequency.

Rather, the DERs only follow the set points given by the secondary control layer, the energy management system.

2.2 Microgrid Energy Management System Formulations and Solution Methodologies

The solution methodologies utilized to solve the μG energy management system problem depend on the used formulation. Multiple formulations in the literature neglect the μG topology and assume that all μG components are connected to a single bus [21]-[26]. Generally, with this simplification, the μG energy management system problem can be directly formulated as a linear programming (LP) problem or a as Mixed integer linear programming (MILP) problem if discrete decision variables (e.g., ON/OFF switches of controllable loads) are considered. The simplification allows the direct use of efficient LP and MILP solvers, such as CEPLEX and Gurobi, to obtain optimal solutions. Hence, a great advantage is achieved when such linear formulation is used, as global optimal solutions to the formulated problem may be found within short computational times. Nonetheless, the formulation neglects the system power losses, and is unable to impose network constraints such as voltage limits and circuit flow limits. Thus, optimal solutions may be physically infeasible.

Factoring in the μG topology in the formulation and considering AC circuit flows result in a non-convex optimization problem of the form of a non-linear programming (NLP) or mixed integer non-linear programming (MINLP) problem. Classical methods have been used to solve the optimization problem including nonlinear programming [27], linear programming [28], and Mixed integer linear programming [29], [30]. Since the

optimization problem is non-linear, different linearization techniques are used to directly solve the problem using LP and MILP solvers including first order Taylor approximation [29] and piece-wise approximation [30]. However, due to the approximations used to linearize the nonlinear equations, optimal solutions may be physically infeasible, so successive linear programming (SLP) is utilized to limit this issue [31]. SLP uses first order Taylor approximation to linearize the problem around an operating point. Then, the linearized problem is solved to find a solution. The solution is used as the new operating point for the next linearization iteration. The process of linearizing and solving the linear problem is repeated until feasibility to the original non-linear problem is achieved or minimal changes between consecutive solutions is obtained. Notably, a great advantage of using linear programming over non-linear programming is the efficient handling of binary and integer variables [32].

Due to the non-convex nature of the AC network flows, convex relaxation methods have also been applied to solve the μG energy management system problem, and power system optimization problems in general. Specifically, semidefinite programming (SDP) [33] and second order conic programming (SOCP) [34] were used to solve the optimal power flow (OPF) problem. Also, mixed integer SOCP was used to solve the μG energy management system problem [35], [36]. The attractiveness of convexification methods is that they provide a lower bound for the global optimal solution. Also, having a convex problem enables the use of many efficient convex optimization solution algorithms. In their trend setting work [37], J. Lavaei and S. H. Low derived a sufficient zero optimality gap that when met, a global optimal solution is guaranteed. In many cases, however, the optimality gap is not zero [38], and the solution of the convexified problem must be

translated to a physically realizable solution. Furthermore, Hijazi et al. showed that scalability issues arise in convex relaxations when integer variables are included [39].

Heuristic and meta heuristic methods have also been used to solve the μG energy management system problem. Heuristic methods are rule based methods and are specific to the system in hand [40], [41]. Hence, applying similar rules for different systems may not be possible. Meta heuristic methods, also known as search-based methods, are problem independent. The theory of such methods may be applied to different problems and systems. In general, these methods start with an initial population, where the population represents several prospective solutions. Then, a fitness value is assigned for each individual solution, typically based on the objective function value at that particular solution. Afterwards, the population is randomly updated depending on the specific heuristic method and the fitness values, thus, generating a new set of solutions. The process is repeated until a terminating condition is satisfied. Although the concept of Heuristic methods was introduced in the late 1950's [42], due to the lack of powerful computer processors, these types of optimization methods did not evolve until the late 1980's [43]. Examples of such methods include: the Genetic Algorithm (GA) method ([44], [45]), the Particle Swarm Optimization (PSO) method ([46], [47]), and the Ant Colony Optimization (ACO) method [48]. These methods are attractive due to their direct applicability to non-linear non-convex optimization problems. However, the performance of such methods is highly dependent on parameters fine tuning (e.g., the mutation parameter in GA, the particle speed parameter in PSO, and the pheromone decay parameter in ACO) and they suffer from scalability issues. These methods also face difficulties when equality constraints are involved in the optimization problems.

Machine learning (ML) algorithms were also used to tackle the μG energy management system problem. These algorithms use large amount of data to learn and find patterns in the problem to be solved. They are generally considered model free algorithms and are data dependent. Examples of such algorithms include: the Lagrange programming neural network [49], the Feedforward neural network [50], the recurrent neural network [51], and the reinforcement learning [52]. All previous studies consider neither the topology of the system nor reactive power and were tested on small cases. While ML algorithms have proven to be effective in many fields of study (voice and image recognition, virtual personal assistants, email spam filtering, etc.), their applicability to the μG energy management system problem needs further development.

2.3 Ancillary Services from Microgrids to the Grid

The problem of providing ancillary services from μGs is basically a problem of aggregating a multiplicity of DERs and scheduling them as one block seen by the external grid. This problem is not new. It has gained, however, a great interest in the last decade. The problem has been approached in the context of μGs' ([53]-[57]) as well as virtual power plant' (VPP) ([58]-[60]). With the ever-increasing need of service capacities, emphasis in the recent literature on incorporating ancillary services to the grid in addition to the typical power scheduling task of an aggregator have been noticed; the aggregator's goal is to represent the service capabilities of the internal resources as a single product to the external grid.

In terms of service scheduling, relevant works include [53]-[58].The authors in [53] develop a μG optimization model that schedules the operation of distributed generators

(DGs), energy storage systems (ESSs), and adjustable loads to provide service to the external grid. The service provision is modeled as limiting the ramping of the power flow at the interconnection with the external grid, while no capacities are preserved for grid services calls. On the other hand, the work in [54] considers preserving active reserve capacities from DGs and interruptible loads (ILs) within a μG in case a call for service is received. Although ESSs are modeled and scheduled in [54], they are not considered as service responders. That is, under a grid call for service, an ESS is assumed to not change its set points. Conversely, the works in [55], [56], [58] consider ESSs as service responders. Specifically, an ESS reserve at a time instant is modeled as the minimum between the rated power and the remaining state-of-charge (SOC) at that instant (this model will be referenced as the MinPS model herein). The reserve computed from the MinPS model at each time instance is then added to the reserve of DGs and ILs to compute the total system reserve. The simple addition to compute the total reserve is facilitated by the assumption in [55], [56], [58] that all resources are connected to a single node, the point of common coupling (PCC). The authors of [57] omit this assumption and do consider equations and constraints of the aggregated network. Additionally, the reserve is procured from DG units as well as ESSs using the MinPS model. Nevertheless, the effective service capability at the PCC is not precisely defined in the model. Rather, the total reserve is modeled as the summation of DERs' individual reserves. Hence, possible losses encountered when reserve is supplied to the external grid are not considered. Including the network equations and constraints is crucial for the underlying problem for two main reasons: 1) to avoid overestimating the μG's capability at the PCC due to neglecting losses, and 2) to ensure

that the network constraints are not violated under normal operation, and when services are being provided.

Another practical limitation in the work presented in [55]-[58] is the ESS model. Because the ESS commits the minimum between the rated power and the remaining SOC at each time step (i.e., the MinPS model), the aggregator encounters the risk of failure-to-activate penalties. When the committed regulation or reserve capacities are called for in multiple time periods, the ESS will be unable to provide what has been committed. The MinPS model may be practical under the assumption that service calls are rarely activated. However, as more renewables are integrated into the grid, it is expected that service calls will be more frequent. In addition, ISOs may perform unannounced testing and dispatch of committed services and apply penalties for insufficient supply [61].

Notably, the works in [53]-[60] only consider solving the resource scheduling problem without considering the computation of the actual controls of the resources in real-time and when service calls are received. When service capacities are committed, the μG does not have prior knowledge about the exact call of the external grid; the grid at any committed time may ask for the full capacity, or any value less than the committed capacity. Hence, the pre-computed schedule before receiving the call is inapplicable. An optimization problem that is solved upon receiving a call becomes necessary to compute the actual controls to be sent to the resources (i.e., a real-time control (RTC) problem). This problem should consider the future horizon to ensure the ability to maintain the services, and at the same time, should be solved very fast to respond to service calls in a timely manner.

2.4 Controllable Loads in Microgrid Energy Management Systems

The US residential load accounts for %30 among the industrial, commercial, and residential sectors [62]. Residential loads commonly have storage and shiftable capabilities. For example, air-conditioners, fridges, and water-heaters may precool or preheat for the thermal energy to be released later [63], [64]. Moreover, dishwashers, cloth washers, and clothes dryers are shiftable devices meaning that households are typically indifferent on when to operate such devices as long as they start and finish their tasks within a specified time period. It is therefore important to consider the flexibility of home controllable devices to add to the flexibility of the μG which in turn maximizes the possible services provided to the external grid. Multiple studies in the literature modeled controllable loads in the context of a μG energy management system. For example, shiftable loads [24], curtailable loads [65], and sheddable loads [35]. However, these models are generic and do not necessary apply to home controllable loads. The models do not utilize the storage potential of home thermal devices and do not consider the inconvenience of the households (e.g., limiting the water-heater temperature to a certain range, operating the clothes dryer after the clothes washer, etc).

2.5 Summary

We identify a gap in the literature for a comprehensive μG energy management system with the following characteristics:

- Models the μG network as an AC network without topological restrictions (e.g., single node, radial, etc) or physical simplifications (e.g., neglecting losses, reactive power, etc.). An accurate model of the network is necessary to compute the

effective service capability at the PCC and ensure satisfying network constraints under normal operation, and when services are provided.

- Models home controllable devices to utilize their flexibility while imposing household convenience constraints.
- Optimizes for the provision of multiple services simultaneously including reserve, regulation, and voltage support. The energy management system should enable the μG to *commit* services by computing the optimal commitments that may be provided at the PCC whether in advance to dispatch (e.g., Day-Ahead (DA) commitment), or at the moment of dispatch (e.g., Real Time (RT) commitment). Commitment rules such as minimum acceptable capacity, minimum time to respond, and minimum time to maintain providing the service should be considered.
- Optimizes the operations planning and control of the μG. To avoid penalties of insufficient service supply, the μG should: 1) *hold* the committed capacities as time passes and as forecast updates, 2) *dispatch* the capacity when requested and within committed time, and 3) *maintain* supplying the capacity for as long as requested. These three steps should be performed optimally with lowest operational cost.
- Augments a solution methodology that enables attaining feasible and optimal solutions of the underlying optimization problems within acceptable computational times.

This work aims to fill the aforementioned gap by proposing a μG energy management system (the μGEMS) that addresses all points above. The following chapter provides an overview about the μGEMS and the provided services.

CHAPTER 3. OVERVIEW OF THE PROPOSED μGEMS AND PROVIDED SERVICES

3.1 Overview

This chapter provides an overview of the proposed μGEMS as well as definitions and underlying assumptions. We start by presenting the system architecture of the μG in section 3.2, followed by the overall framework of the proposed μGEMS in section 3.3. Section 3.4 defines the service products that are provided by the μG and section 3.5 provides the design for the procurement, compensation, and penalization (i.e., service designs).

3.2 The Microgrid System Architecture and the Interaction with an External Grid

Figure 3.1 depicts a sample network of the system to be studied. The network is modeled as a single-phase AC network consisting of a μG connected to an external grid (eG) through a PCC bus. The PCC bus is where the interaction between the two entities (the eG and the μG) occur. We assume that the eG has no information about the internal resources of the μG and only sees the measured complex power $\tilde{S}_{pcc}$ and the complex voltage $\tilde{V}_{pcc}$ at the PCC bus.

Service commitments provided from the μG are procured, compensated, and penalized based on the measured values at the PCC. Therefore, the goal of the proposed μGEMS is to aggregate the μG resources while respecting the μG network constraints to behave as a single entity seen by the eG. We assume that the μGEMS communicate with

the eG operator the necessary components for energy and service commitments. The µGEMS also receives from the eG operator commitment awards and dispatch commands to operate the µG accordingly and avoid penalties. The eG operator can be seen as the control center of a utility where the µG is connected, or a DSO governing the energy and ancillary services market of the area where the µG is connected.

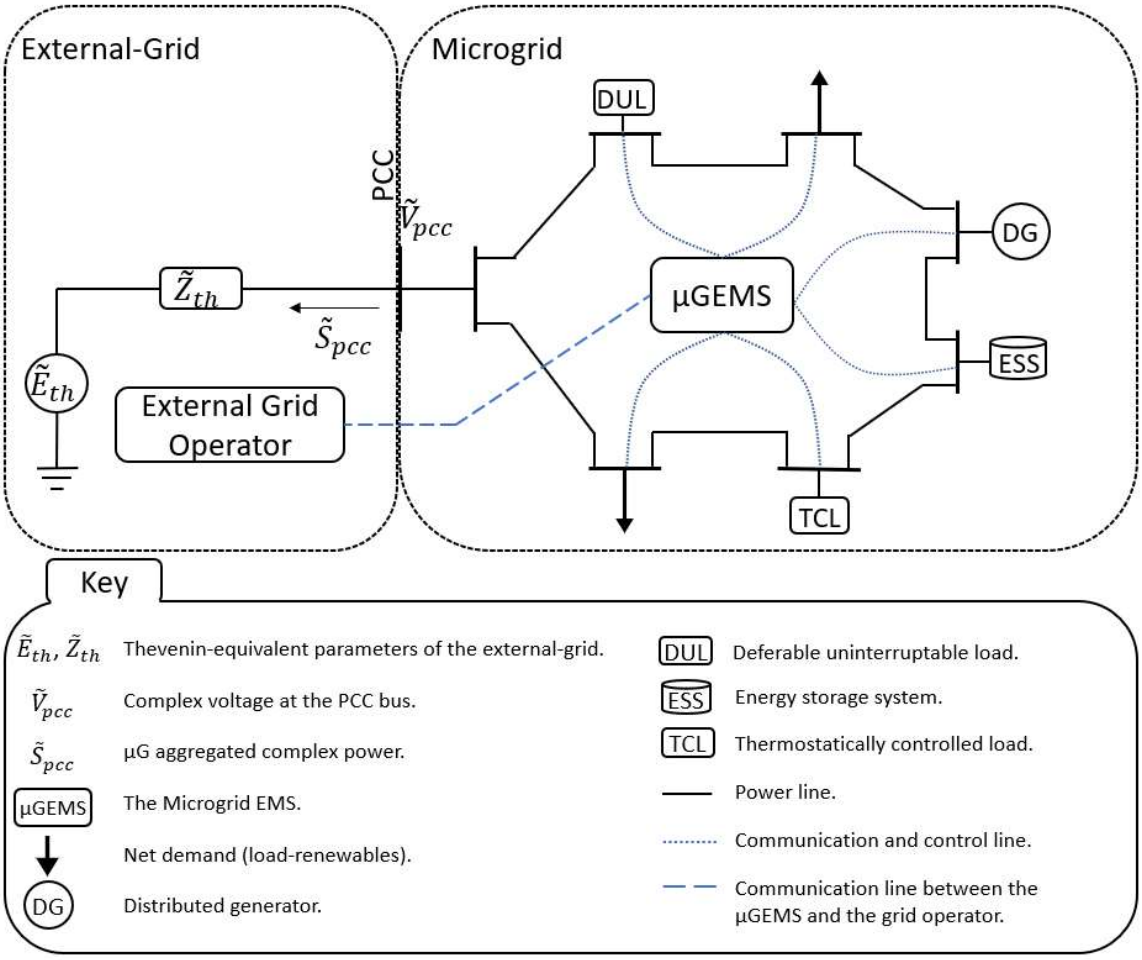

Figure 3.1: Architecture of the studied system

3.3 Overall Framework of the µGEMS

Figure 3.2 shows the overall framework of the developed µGEMS. The µGEMS is divided into two main parts: (a) the Operations Planning and Control Management System (OpPC) and (b) the Commitments Management System (CMS). The OpPC is responsible

for planning and controlling the operations of the µG in an optimal manner given net-demand, ambient temperature, and energy price forecasts, as well as the µGs' energy and service commitments. The CMS holds the responsibility of computing the optimal µG energy and service capabilities via the *compute optimal commitments* module which takes forecasts (service capacity prices in addition to the aforementioned forecasts) and commitment rules (e.g., minimum capacity, ramp rate, etc.). These commitments are assumed to be sent to the eG operator. If a commitment is awarded, the OpPC is updated to plan and control the operations of the µG accordingly.

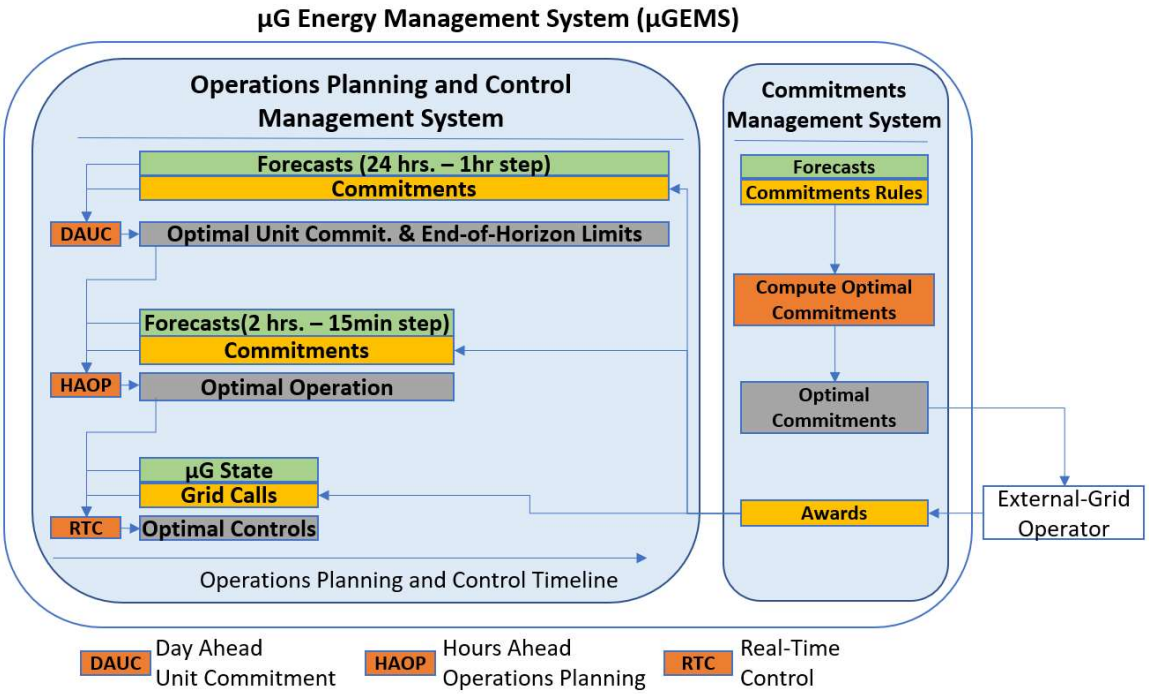

Figure 3.2. Framework of the µGEMS

Three modules colored in orange exist within the OpPC which are: the Day-Ahead Unit Commitment (DAUC), the Hours-Ahead Operations Planning (HAOP), and the Real-Time Control (RTC). The modules are set in a hierarchical manner where each upper level provides set points and recommendations to the lower level until the actual dispatch is sent to the controllable devices via the RTC. The DAUC module is formulated as look-ahead

multi-period optimization problem solved in a moving horizon manner where updated forecasts are given at each run. A wide planning horizon is considered in the DAUC problem such as a complete day to incorporate the daily cycles of loads and renewables. The DAUC sets unit commitments and end-of-horizon limits for storage-based DERs which are given as inputs to the HAOP. The HAOP is also formulated as look-ahead multi-period optimization problem with a shorter planning horizon and more frequent runs relative to the DAUC. The planning horizons and the time steps of the DAUC and HAOP problems shown in Figure 3.2 are typical values and the proposed formulation can be solved with different horizons and time steps. In contrast to the DAUC and HAOP, the RTC is formulated as a single-period optimization problem because it is solved at an instant of time given the current state of the μG, the unit commitment plan from the DAUC, and the recommended controls received from the HAOP. Specifically, the recommended controls include those that have a multi-period dependency (e.g., DGs active power output, ESSs charging/discharging, and TCLs operation), while other instantaneous controls (e.g., reactive power injection of DERs) are computed independently by the RTC. As depicted in Figure 3.2, the DAUC and HAOP receive energy and service commitments awarded from the eG operator to ensure holding the commitments in the produced look-ahead operations plans. The RTC receives instantaneous grid calls for service, which are also seen as awards in case of real-time commitments (the real-time commitments are discussed in section 3.5.2).

3.4 Service Products

Typically, the terminology of services and their actual functionality differ across regions and based on regulations. This section defines the considered services provided by the μG to the eG through the PCC:

3.4.1 Reserve

An active power capacity that can be *injected* to or *absorbed* from the eG, when requested, and is characterized by three components: 1) reserve capacity, 2) response time (i.e., ramp rate), and 3) maintainability (i.e., for how long this reserve can be sustained). Reserve is typically triggered if there is a system contingency (contingency reserve) or an unexpected increase or decrease in the net-demand (balancing reserve). Both upward and downward reserves are considered in our formulation.

Unlike a conventional generator, a μG in general contains varying net-demand. Therefore, in order for the eG to penalize or compensate the μG on its maintainability of reserve, a baseline acting as the reference for reserve maintainability should be established. The baseline is taken to be the Day-Ahead scheduled energy with the eG (i.e., the DA plan). Suppose a reserve with the capacity R is requested, the μG should shift the DA plan by an amount of R throughout the maintainability time. Note that since the DA plan is generally varying, the resultant active power injection at the PCC may vary during the maintainability time of reserve.

3.4.2 Regulation

An active power capacity that can be *injected* to or *absorbed* from the eG, when requested, within a given response time. A common classification divides regulation products that are used to regulate power system's frequency into three tiers based on their response times: 1) primary regulation which is typically provided within tens of milli-seconds by on-line generators via governor response, 2) secondary regulation provided within multiple seconds via automatic generation control (AGC) signals sent to participating generators to adjust their power output, and 3) tertiary regulation with response times within tens of seconds to few minutes and could be carried out automatically or through manual settings. We consider that the μG participates in providing secondary and tertiary regulation given its suitable control structure and response time, where the μG receives upward regulation or downward regulation calls from the eG to change the active power injection at the PCC. Essentially, the response time of the regulation from the μG would depend on the communication speed between the eG and the μG, the time needed to estimate the state of the μG, the time needed to solve the RTC optimization problem, the communication speed between the μGEMS and the responding DERs, and finally, the response time of the DERs. In this work, where the focus is on the optimization problems, the RTC problem that is used to immediately respond to grid calls is solved within fractions of seconds to few seconds for moderate sized μGs on a personal laptop, facilitating the provision of secondary and tertiary regulation.

3.4.3 Voltage Support

Minimizing the deviation of the voltage magnitude at the PCC from a pre-defined value set by the eG. Voltage support is usually activated within short period of times by injecting or absorbing reactive power to regulate the voltage. Given the computational time of the RTC problem, the μG may also provide this service.

The active and reactive capabilities of the μG at the PCC are coupled due to the DER's and network limits. Therefore, the provision of reserve or regulation may conflict with the provision of voltage support. In addition, maximizing the provided reserve or regulation capacity (active power) may degrade the quality of the power factor at the PCC when service is being dispatched; a μG may absorb substantial amounts of reactive power to improve the voltage within the μG and enable further provision of active power at the PCC. To address the coupling, we assume that the eG sets power factor limits at the PCC that must be honored at all times. In addition, the conflicting services can be weighted in the objective functions of the model to reflect the priority of service.

3.5 Service Designs: Procurement, Compensation, and Penalties

We consider two service designs which differ as a result of the service commitment time of the μG relative to the dispatch time.

3.5.1 Design 1: Day-Ahead Commitment

The μG has access to the day-ahead (DA) energy and ancillary services market through the eG operator (e.g., ISO/DSO). The CMS computes hourly DA energy, reserve, and regulation capacities. Market rules given as inputs to the *compute optimal commitments*

module include reserve and regulation minimum acceptable capacities, minimum acceptable response time, and minimum maintainability time for reserve. We assume the μG as an energy price taker and that the μGEMS is given hourly price forecast for the DA energy and ancillary service capacities. If service capacities are awarded, the μG receives a compensation for holding the reserve and regulation capacities, as well as energy compensation in case a capacity is actually called for. The energy compensation is taken to be the DA energy price. Further, the μG incurs failure-to-active penalties in case of insufficient service supply. Under normal operation, the μG should follow the DA committed energy interchange (i.e., DA plan) or otherwise mismatch penalties or intra-day prices are incurred.

Voltage support can be provided simultaneously in this design using the proposed model. As for the compensation for voltage support, we assume that the μG submits lost-of-opportunity cost to the ISO/DSO caused from minimizing the deviation of the voltage at the PCC from the requested target. The lost-of-opportunity cost can be computed by optimizing the μG operation with and without the provision of voltage support.

3.5.2 Design 2: Real-Time Commitment

The commitment of services in this design is assumed to be in real-time (RT). At each instant of time, the proposed μGEMS, and specifically the CMS, computes the instantaneous services at the PCC. Five services are considered in this design: 1) upward primary reserve (i.e., upward regulation), 2) downward primary reserve (i.e., downward regulation), 3) upward secondary reserve, 4) downward secondary reserve, and 5) tertiary reserve. Primary reserves (up or down) are supplied within 1 minute and maintained for 10

minutes, while secondary reserves are supplied in 10 minutes and maintained for 1 hour. Tertiary reserve, also known as supplementary or replacement reserve, is supplied in 1 hour. The maintainability time of tertiary reserve can be constrained to a given number of hours. Alternatively, it can be included as a variable to be maximized. Both options are considered in our formulation. Notably, the CMS in this design may output multiple reserve products that can be supplied by the μG as an individual service or as a stacked service. For example, the μG may only supply upward primary reserve (individual service), or it may supply upward primary reserve, followed by upward secondary reserve, followed by tertiary reserve (stacked service).

In addition to computing the available reserves at the PCC, the CMS computes the associated cost for each reserve product. Once a specific product is requested from the eG, the OpPC is immediately updated to dispatch and maintain the reserve accordingly. The μG is compensated the cost sent to the eG and penalties are incurred if the μG deviates from the committed reserve/s. The deviation is based on a pre-established power profile at the PCC. Similar to the DA Commitment design, the μG in the RT Commitment design may also be providing voltage support. The compensation for providing voltage support is assumed to be based on the lost-of-opportunity cost where the μG submits this cost after the services has been provided (e.g., in a daily or weekly basis).

In terms of modeling, the two service designs discussed above differ because the DA Commitment design requires *holding* reserve and regulation capacities in advance that may or may not be called for. In contrast, the RT Commitment design requires computing the instantaneous reserve capacities and there is no hold for capacities as time passes. Therefore, the μGEMS in the DA Commitment design must plan for multiple prospective

operating points (i.e., call and no call cases). For this reason, we propose a multi-case, multi-period mathematical model for the μG to ensure the feasible operation under normal conditions when no call is received, and under the cases where the full capacity of each committed service is called for. The modeling approach is analogous to modeling a multi-period security constrained optimal power flow problem with corrective actions. The contingencies in our case are service calls and the corrective actions are the DERs controls when a service is requested. Note that the multi-case, multi-period μG mathematical model is directly applicable to any of the two service designs discussed, where in the RT Commitment design, a single case is considered. Additionally, for simplicity and to avoid conflicting commitments, we do not consider the simultaneous application of the two service designs (i.e., simultaneously committing in DA and in RT).

In the next chapter, we present the proposed multi-case, multi-period μG mathematical model. After presenting the μG mathematical model, chapter 5 presents the problem formulation of all modules in the μGEMS under both service designs. These problems are formulated by setting the μG mathematical model as problem constraints along with design-dependent constraints and objective functions.

CHAPTER 4. THE MATHEMATICAL MODEL OF THE MICROGRID

Attached Notations

$x^{(.)}$	Superscript is used for symbol description.
$x_{(.)}$	Subscript is used for indexing.

Indices and Sets

$d \in \mathcal{D}_h^{dul}$	Controllable DULs in home *h*.
$d \in \mathcal{D}_h^{tcl}$	Controllable TCLs in home *h*.
$e \in \mathcal{E}$, $\mathcal{E}(k)$	ESS, and ESS connected to bus *k*.
$g \in \mathcal{G}$, $\mathcal{G}(k)$	DGs, and DGs connected to bus *k*.
$h \in \mathcal{H}$, $\mathcal{H}(k)$	Homes, and homes connected to bus *k*.
$k \in \mathcal{K}$	Busses.
$m \in \mathcal{A}(k)$	Busses adjacent to bus *k*.
$km \in \mathcal{F}$	Circuit flows. Index *km* indicates the flow from bus *k* to bus *m*.
$s \in \mathcal{S}$	Cases.
$t \in \mathcal{T}$	Time periods.

Variables

e, f	Real and imaginary bus voltage.
$i^{r,(.)}$, $i^{i,(.)}$	Real and imaginary current injection. Superscripted with *cr*, *eg*, *fx*, and *pq* for circuits, external grid, fixed-shunts, and aggregated PQ devices.
$p^{(.)}, q^{(.)}$	Active and reactive power. Superscripted with *dg*, *dul*, *eg*, *ess*, (*ess,ch*), (*ess,ds*), *home*, *pq*, and *tcl* for DGs, DULs, external grid, ESSs, ESSs charging, ESS discharging, homes, aggregated PQ devices, and TCLs, respectively.
$s^{(.)}$	Binary: 1 if the home controllable device is operating and 0 otherwise. Superscripted with *dul* and *tcl* for DULs and TCLs.

$\underline{soc}$, $\overline{soc}$	Lower and upper bound variables for ESSs' state-of-charge.
u^{dul}	Binary: 1 if DUL start its task and zero otherwise.
u	Binary: 1 if DG is ON, 0 otherwise.
v	Binary: 1 if DG is starting-on, 0 otherwise.
$v^{pcc,sq}$	Voltage magnitude squared of the PCC bus.
w	Binary: 1 if DG is shutting-off, 0 otherwise.
α^{ess}	Binary: 1 if ESS is discharging and 0 otherwise.
$\underline{\theta}^{in}$, $\overline{\theta}^{in}$	Lower and upper bound variables for TCLs' inner temperature.

Parameters

A^{tcl}	A parameter accounting for the amount of thermal energy supplied the TCL is operating.
$B^{(.)}$	Susceptance. Superscripted with *cr*, *crs*, *fx*, and *eg* for circuit series susceptance, circuit shunt susceptance, fixed-shunt susceptance, and susceptance of the external grid model, respectively.
C^{tcl}	A parameter accounting for the thermal conductivity of the TCL.
$E^{eg,(.)}$	Voltage of the external grid model. Superscripted with *r* and *i* for the real part and the imaginary part, respectively.
$G^{(.)}$	Conductance. Superscripted with *cr*, *crs*, *fx*, and *eg* for circuit series susceptance, circuit shunt susceptance, fixed-shunt susceptance, and susceptance of the external grid model, respectively.
$\underline{H}^{(.)}$, $\overline{H}^{(.)}$	Lower and upper bounds for the final step to eliminate end-of-horizon effect. Superscripted with *ess* and *tcl* for ESS's state-of-chare and TCL's inner temperature.
$\overline{I}$	Circuit's maximum current limit.

$P^{(.)}$, $Q^{(.)}$	Active and reactive power demand. Superscripted with *dul*, *tcl*, and *uc* for DUL's rated demand, TCL's rated demand, and total demand of uncontrollable home loads, respectively.
$\underline{P}^{(.)}$, $\overline{P}^{(.)}$	Lower and upper active power limits. Superscripted with *dg* and *ess* for DGs' active power limits and ESSs' active power limits.
$\underline{Q}^{(.)}$, $\overline{Q}^{(.)}$	Lower and upper reactive power limits. Superscripted with *dg* and *ess* for DGs' reactive power limits and ESSs' reactive power limits.
R^{dg}	Ramping limit of the DG.
$\underline{SOC}$, $\overline{SOC}$	Lower and upper bounds of the ESS state-of-charge.
$\underline{V}$, $\overline{V}$	Lower and upper bus voltage limits.
η	Charging and discharging efficiency of the ESS.
$\underline{\Theta}$, $\overline{\Theta}$	Household's lower and upper temperature settings for the TCL.
Θ^{out}	Outer temperature of the TCL.
ρ^{dul}	Time to finish the DUL's task.
τ	Time step as a fraction of an hour.

4.1 Overview

This chapter presents the proposed mathematical model of the μG. The model is a multi-case, multi-period AC model. The model can be used directly and for each case, it results in a multi-period AC optimization model. We use the rectangular coordinates to represent voltage, current and power quantities. Further, the current bus balance formulation is used as opposed to the power bus balance formulation. Subsequently, the model has mostly linear equations and constraints with a few quadratic ones.

A general bus (bus k) of the modeled µG is shown in Figure 4.1. Multiple devices are connected to the general bus including a circuit, a fixed shunt device, and a group of PQ devices. The PQ devices are: a controllable distributed generator (DG), a controllable energy storage system (ESS), and a home with controllable appliances including thermostatically controlled loads (TCLs) and deferrable uninterruptible loads (DULs). The arrow near the home in Figure 4.1 represents the net demand of the home. The PQ devices are grouped under a fictitious PQ bus to reduce the number of quadratic equations as will be explained in detail in section 4.4. The external grid (eG) shown in the far right of Figure 4.1 is modeled as a Thevenin equivalent circuit.

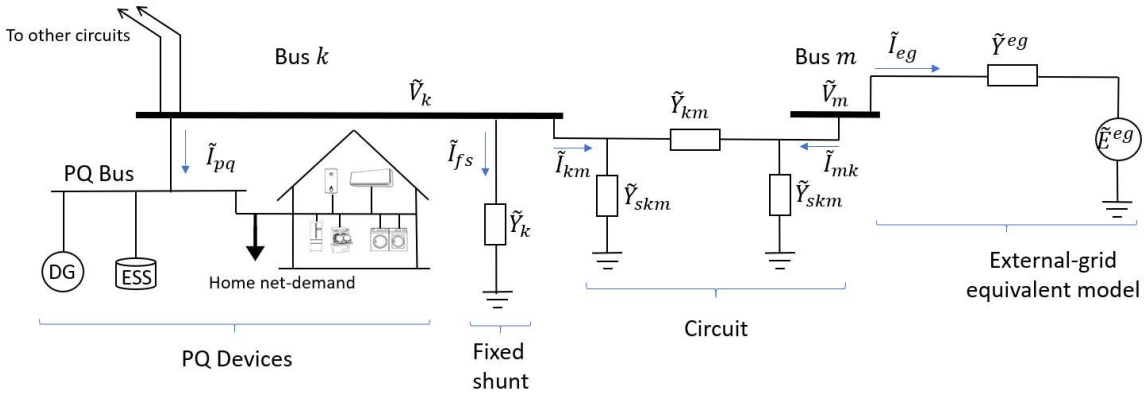

Figure 4.1. A depiction of a general bus within the µG

The model of each device connected to the general bus as well as the eG model is governed by a set of equations and constraints. These equations and constraints define the device's current injection, the internal operation of the device, and the operational constraints. In the subsequent sections of this chapter, we illustrate the mathematical model of each device. We then define the current balance equations and the bus voltage constraints which are applied to all busses in the µG network, by that, concluding the µG mathematical model.

4.2 Circuit Model

A circuit connecting bus k to bus m is represented using the positive-sequence pi-equivalent model. The equations defining the real and the imaginary injected currents into the circuit at each time period and at each case are as follows:

$$i^{r,cr}_{(km)ts} = (G^{cr}_{km} + G^{crs}_{km})e_{kts} - (B^{cr}_{km} + B^{crs}_{km})f_{kts} - G^{cr}_{km}e_{mts} + B^{cr}_{km}f_{mts} \tag{4.1}$$

$$i^{i,cr}_{(km)ts} = (B^{cr}_{km} + B^{crs}_{km})e_{kts} + (G^{cr}_{km} + G^{crs}_{km})f_{kts} - B^{cr}_{km}e_{mts} - G^{cr}_{km}f_{mts} \tag{4.2}$$

$\forall km \in \mathcal{F}, \quad \forall t \in \mathcal{T}, \quad \forall s \in \mathcal{S}$

The current magnitude following through the circuit is limited by the following constraint:

$$(i^{r,cr}_{(km)ts})^2 + (i^{i,cr}_{(km)ts})^2 \le (\overline{I}_{km})^2 \tag{4.3}$$

$\forall km \in \mathcal{F}, \quad \forall t \in \mathcal{T}, \quad \forall s \in \mathcal{S}$

4.3 Fixed-Shunt Model

The real and imaginary current injections into a fixed shunt device connected at bus k are defined as follows:

$$i^{r,fx}_{kts} = G^{fx}_{k}e_{kts} - B^{fx}_{k}f_{kts} \tag{4.4}$$

$$i^{i,fx}_{kts} = B^{fx}_{k}e_{kts} + G^{fx}_{k}f_{kts} \tag{4.5}$$

$\forall k \in \mathcal{K}, \quad \forall t \in \mathcal{T}, \quad \forall s \in \mathcal{S}$

4.4 PQ Bus Model

The DG, the ESS, and the home are modeled as PQ devices connected to a fictitious PQ bus. Let p and q represent the active and reactive power injections into a PQ device connected to bus k. Then, the real and imaginary current injections into the PQ device are governed by the following two quadratic equations:

$$p = e_k i^r + f_k i^i \tag{4.6}$$

$$q = f_k i^r - e_k i^i \tag{4.7}$$

Therefore, if the current flowing through each PQ device is modeled explicitly in the μG model, each connected PQ device would add two quadratic equations. Under the assumption that no constraints exist on the individual currents of the PQ devices, we can aggregate these currents and avoid the addition of two quadratic equations for each connected PQ device at a bus; the number of quadratic equations will be limited to two per PQ bus. The aggregated current is then included in the model with the active and reactive powers representing the sum of the PQ injections as follows:

$$p_{kts}^{pq} = e_{kts} i_{kts}^{r,pq} + f_{kts} i_{kts}^{i,pq} \tag{4.8}$$

$$q_{kts}^{pq} = f_{kts} i_{kts}^{r,pq} - e_{kts} i_{kts}^{i,pq} \tag{4.9}$$

$$p_{kts}^{pq} = \sum_{\forall h \in H(k)} p_{hts}^{home} - \sum_{\forall g \in G(k)} p_{gts}^{dg} - \sum_{\forall e \in E(k)} p_{ets}^{ess} \tag{4.10}$$

$$q_{kts}^{pq} = \sum_{\forall h \in H(k)} q_{hts}^{home} - \sum_{\forall g \in G(k)} q_{gts}^{dg} - \sum_{\forall e \in E(k)} q_{ets}^{ess} \tag{4.11}$$

$\forall k \in \mathcal{K}, \quad \forall t \in \mathcal{T}, \quad \forall s \in \mathcal{S}$

where p_{kts}^{pq} and q_{kts}^{pq} are the sum of the active and reactive power injections of all PQ devices connected to bus *k*. Similarly, $i_{kts}^{r,pq}$ and $i_{kts}^{i,pq}$ represent the aggregated real and imaginary currents flowing through the PQ devices connected to bus *k*. In the following sections, we introduce the equations and operational constraints governing the operation of the PQ devices which are the DG, the ESS, and the home.

4.5 Distributed Generator Model

The DG is modeled as a PQ controlled device with limits on the active and reactive power supply. The commitment of the DG unit is also modeled. The complete model of the DG is as follows:

$$u_{gt} - u_{g(t-1)} = v_{gt} - w_{gt} \tag{4.12}$$

$$\sum_{\delta=t-UT_g+1}^{t} v_{g\delta} \le u_{tg}, \qquad t \ge UT_g \tag{4.13}$$

$$\sum_{\delta=t-DT_g+1}^{t} w_{g\delta} \le 1-u_{tg}, \qquad t \ge DT_g \tag{4.14}$$

$$u_{gt} = 1, \qquad for \;\; t = 1,\ldots,UT_g^0 \tag{4.15}$$

$$u_{gt} = 0, \qquad for \;\; t = 1,\ldots,DT_g^0 \tag{4.16}$$

$$u_{gt}\underline{P}_g^{dg} \le p_{gts}^{dg} \le u_{gt}\overline{P}_g^{dg} \tag{4.17}$$

$$u_{gt}\underline{Q}_g^{dg} \le q_{gts}^{dg} \le u_{gt}\overline{Q}_g^{dg} \tag{4.18}$$

$$\underline{Q}_g^{dg} \le q_{gts}^{dg} \le \overline{Q}_g^{dg} \tag{4.19}$$

$$\left| p_{gts}^{dg} - p_{g(t-1)s}^{dg} \right| \leq \tau R_g^{dg} \tag{4.20}$$

$$u_{g,(|\mathcal{T}|-t+1)} = 1 \quad for \quad t = 1,...,UT_g^{|\mathcal{T}|} \tag{4.21}$$

$$u_{g,(|\mathcal{T}|-t+1)} = 0 \quad for \quad t = 1,...,DT_g^{|\mathcal{T}|} \tag{4.22}$$

$$u_{gt}, v_{gt}, w_{gt} \in \{0,1\} \tag{4.23}$$

$\forall g \in \mathcal{G}, \qquad \forall t \in \mathcal{T}, \qquad \forall s \in \mathcal{S}$

where (4.12) relates the ON/OFF variable with the startup and shutdown variables. (4.13) and (4.14) respectively enforce the minimum-up time and minimum-down time of the DGs, while (4.15) and (4.16) enforces the number of time periods the unit should be initially ON or OFF, respectively. (4.17) and (4.18) limit the active and reactive power outputs, respectively while (4.20) enforces the ramping limits between consecutive time periods. The equality constraints in (4.21) and (4.22) are added to enforce end-of-horizon commitment constraints. Specifically, (4.21) ensures the unit is ON for the last $UT_g^{|\mathcal{T}|}$ time periods, and (4.22) ensures the unit is OFF for the last $DT_g^{|\mathcal{T}|}$ time periods. These constraints are added if it is required to maintain specific initial up-time and down-time for the next optimization horizon. (4.23) enforces the binarity of the variables related to the unit's commitment. Notably, we assume that the time-to-start and the time-to-shunt down are negligible, and the DG can start-up and shut down instantly.

4.6 Energy Storage System Model

The ESS is modeled as a controlled PQ device with capabilities to inject both active power and reactive power. The power injection can be positive or negative where in our

convention, a positive ESS injection indicates power flowing into the μG (discharge) and a negative ESS injection indicates power flowing into the ESS (charge).

Unlike the DG where the active power output at time step *t* is only limited by the instantaneous bounds and the power output at *t*-1 for ramping limits, the ESS active injection capability at time step *t* depends on the initial state-of-charge in the planning horizon as well as all injections up until time step *t*. The dependency of the instantaneous active power injection on all previous injections from the beginning of the planning horizon complicates the multi-case modeling. Specifically, it cannot be determined what exact trajectory the ESS active power injection will follow up until time step *t* which depends on the requested services throughout the planning horizon. One approach to overcome this issue is to introduce a state-of-charge variable for all possible trajectories and enforce that all these variables stay within the physical state-of-charge limits. However, the number of possible trajectories grows combinatorically with the planning horizon making such an approach infeasible. Alternatively, in modeling the ESS, we adapt the model proposed in [66], [67] where we introduce two state-of-charge variables per time period: an upper bound ($\overline{soc}_t$) and a lower bound ($\underline{soc}_t$) state-of-charge. These bounds model an envelope that guarantees supplying the services from the ESS without exceeding the ESS state of charge limits. Inter-period constraints on the state-of-charge variables are imposed to maintain feasible bounds at *t*+1 under all possible injections at *t*. The complete model of the ESS is as follows:

$$p_{ets}^{ess} = p_{ets}^{ess,ds} - p_{ets}^{ess,ch} \tag{4.24}$$

$$0 \leq p_{ets}^{ess,ds} \leq (1 - \alpha_{ets}^{ess})\overline{P}_{e}^{ess} \tag{4.25}$$

$$0 \le p_{ets}^{ess,ch} \le \alpha_{ets}^{ess} \overline{P}_e^{ess} \tag{4.26}$$

$$\underline{Q}_e^{ess} \le q_{ets}^{ess} \le \overline{Q}_e^{ess} \tag{4.27}$$

$$\underline{SOC}_e \le \underline{soc}_{et} \le \overline{soc}_{et} \le \overline{SOC}_e \tag{4.28}$$

$$\underline{soc}_{e(t+1)} \le \underline{soc}_{et} - \tau\, p_{ets}^{ess,ds} / \eta + \tau\, p_{ets}^{ess,ch} \eta \tag{4.29}$$

$$\overline{soc}_{e(t+1)} \ge \overline{soc}_{et} - \tau\, p_{ets}^{ess,ds} / \eta + \tau\, p_{ets}^{ess,ch} \eta \tag{4.30}$$

$$\underline{soc}_{et_0} = \overline{soc}_{et_0} = SOC_e^0 \tag{4.31}$$

$$\underline{H}_e^{ess} \le \underline{soc}_{e(|\mathcal{T}|+1)} \le \overline{soc}_{e(|\mathcal{T}|+1)} \le \overline{H}_e^{ess} \tag{4.32}$$

$$\alpha_{ets}^{ess} \in \{0,1\} \tag{4.33}$$

$\forall e \in \mathcal{E}, \quad \forall t \in \mathcal{T}, \qquad \forall s \in \mathcal{S}$

where (4.24) defines the active power injection of the ESS to the μG. (4.25) and (4.26) limit the ESS discharging and charging power to the rated values. The binary variable α_{ets}^{ess} is added to eliminate simultaneous charging and discharging. (4.27) limits the reactive power injection of the ESS. The bounds are set to zero if the ESS is not supplying reactive power. (4.28) limits the ESS state-of-charges that are used to model the envelope. The envelope is defined by (4.29) and (4.30) which together guarantee not violating the state-of-charge lower and upper bounds at *t+1* under all cases of power injection at *t*. (4.31) set the initial state-of-charge and (4.32) limits the ESS state of charges at time step $|\mathcal{T}|+1$ to be within specified values ($\underline{H}_e^{ess}$, $\overline{H}_e^{ess}$) to avoid overcharging or over discharging the ESS for the next optimization horizon. (4.33) enforces binarity of α_{ets}^{ess}.

Compared to the model illustrated in [66], [67], we do not include an equality sign constraint representing the evolution of the ESS state-of-charge at the base case. By enforcing the inequality constraints in (4.29) and (4.30), it is guaranteed that the physical bounds are not violated under all cases and hence, it is not necessary to add the ESS dynamics equality constraint. Note that the above model can be used directly even if only one case is considered since the rated injections are enforced by (4.25)-(4.27), the state-of-charge evolution is captured in (4.29) and (4.30), and the state-of-charge physical bounds are imposed by (4.28).

4.7 Home Model

This section presents the model of the home with controllable devices. All devices inside the home are modeled as PQ loads and are assumed to be connected to the same node since the distance between the devices is typically electrically short allowing the simplification assumption of zero voltage drop. Consequently, the total active and reactive load of the home is defined as the summation of the individual active and reactive device loads, respectively.

Figure 4.2 shows a schematic of a home connected to the μG. The home consists of several devices. We classify those devices into three categories: (a) thermostatically controlled loads (TCLs) (e.g., air-conditioner, fridge, and water heater), (b) deferrable uninterruptible loads (DULs) (e.g., dish washer, clothes washer, and clothes dryer), and (c) uncontrollable loads (e.g., electronics and lights). The PQ demands of the uncontrollable loads are assumed forecasted in the optimization model. While it is generally difficult to forecast the demand of those devices due to the social interaction, the stochasticity arising

from the home load as a whole is substantially reduced when controlling major devices that contribute to the majority of a home's load such as TCLs and DULs. Therefore, even though the forecast of the uncontrollable home loads may have large errors, the propagated error to the μGEMS is minimized by controlling the TCLs and the DULs.

The controllable devices are connected to μGEMS through a communication and control line as depicted in Figure 4.2 where the μGEMS communicate the set points to these devices while respecting the household settings (e.g., temperature limits for TCLs and timing limits for DULs). In the following sub-sections, we present the mathematical models of the TCL and the DUL, which are then aggregated along with the forecast of the uncontrollable loads to represent the total PQ demand of the home.

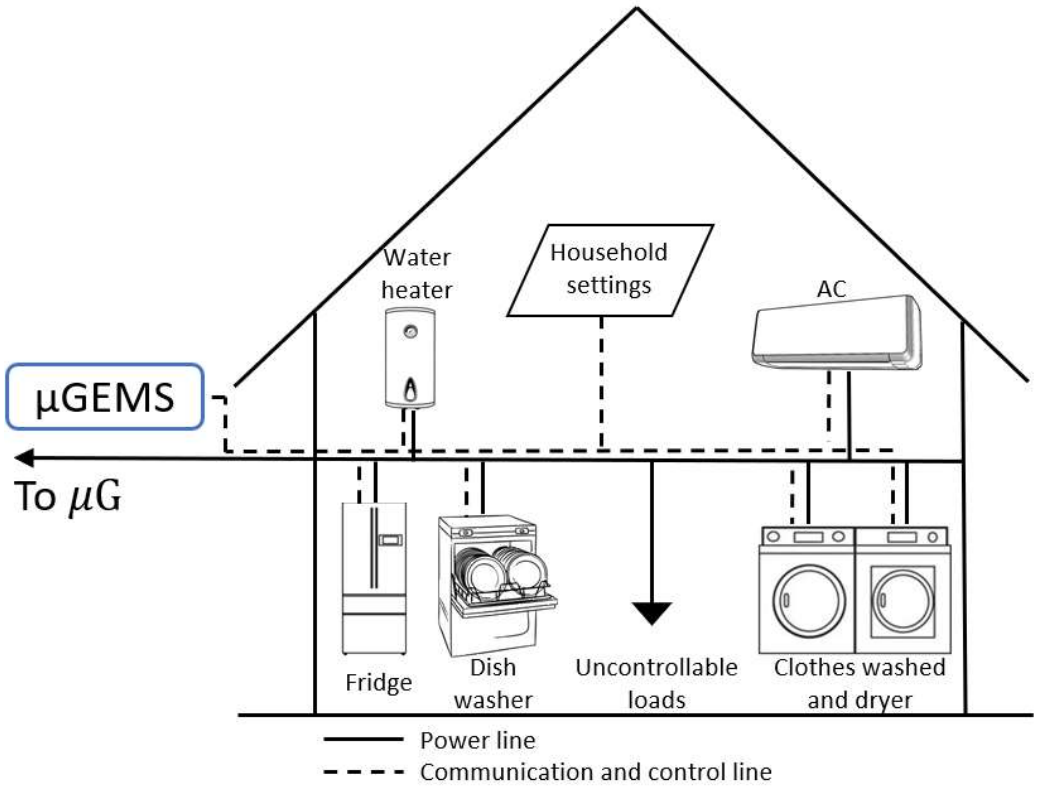

Figure 4.2. A schematic of a home with controllable devices

4.7.1 Thermostatically Controlled Load Model

TCLs are characterized with storage capability motivating the task of controlling them to utilize this capability in assisting the flexibility of the μG and increasing the service capability that can be provided to the eG. The TCL model is governed by a thermal dynamic equation defining the evolution of the inner temperature (see [68], [69]) and specified temperature limits defining the convenience settings of the TCL user. The specified temperature limits must not be exceeded to avoid causing inconvenience to the TCL user. In terms of controllability, some modern TCLs can range their consumption from zero to the rated value in a continuous manner via variable frequency drives (VFDs) ([70]). Other TCLs, however, can only be in two states: ON with rated power consumption, or OFF with zero power consumption. TCLs with VFD offer more flexibility than discrete switching TCLs. Nonetheless, both types can be utilized to enhance the flexibility of the μG and assist in the provision of services to the eG. Therefore, we propose the following TCL model which is generic for both discrete and continuous types:

$$s_{dts}^{tcl} \in [0,1] \qquad for\ continuous\ TCLs \tag{4.34}$$

$$s_{dts}^{tcl} \in \{0,1\} \qquad for\ discrete\ TCLs \tag{4.35}$$

$$p_{dts}^{tcl} = s_{dts} P_d^{tcl} \tag{4.36}$$

$$q_{dts}^{tcl} = s_{dts}^{tcl} Q_d^{tcl} \tag{4.37}$$

$$\underline{\Theta}_d \le \underline{\theta}_{dt}^{in} \le \overline{\theta}_{d,t}^{in} \le \overline{\Theta}_d \tag{4.38}$$

$$\underline{\theta}_{dt}^{in} + \tau \left(C_d^{tcl} \left(\Theta_{dt}^{out} - \underline{\theta}_{dt}^{in} \right) - s_{dts} A_d^{tcl} \right) \ge \underline{\theta}_{d(t+1)}^{in} \tag{4.39}$$

$$\overline{\theta}_{dt}^{in} + \tau\left(C_d^{tcl}\left(\Theta_{dt}^{out} - \overline{\theta}_{dt}^{in}\right) - s_{dts} A_d^{tcl} \right) \leq \overline{\theta}_{d(t+1)}^{in} \tag{4.40}$$

$$\underline{\theta}_{dt_0}^{in} = \overline{\theta}_{dt_0}^{in} = \Theta_d^0 \tag{4.41}$$

$$\underline{H}_d^{tcl} \leq \underline{\theta}_{d,|\mathcal{T}|+1}^{in} \leq \overline{\theta}_{d,|\mathcal{T}|+1}^{in} \leq \overline{H}_d^{tcl} \tag{4.42}$$

$\forall d \in \mathcal{D}_h^{tcl}, \quad \forall h \in \mathcal{H}, \quad \forall t \in \mathcal{T}, \quad \forall s \in \mathcal{S}$

where (4.34) and (4.35) define the range of the switching control depending on the TCL type. (4.36) and (4.37) define the actual active and reactive consumption of the TCL, respectively, where we assume a constant power factor for the TCL. (4.38) limits the temperature of the TCL to the user-defined limits. Similar to the concept presented in the ESS model for the state-of-charge, in the TCL model, we add two temperature states to model an envelope that guarantees supplying the services from the TCL without violating the user-defined temperature limits. The envelope is defined by (4.39) and (4.40) which together guarantee not violating the temperature bounds at *t+1* under all cases of power consumption at *t*. (4.41) sets the initial temperature of the TCL and (4.42) limits the temperature states at time step $|\mathcal{T}|+1$ to be within specified values ($\underline{H}_d^{tcl}$, $\overline{H}_d^{tcl}$) to avoid overcooling or overheating the space for the next optimization horizon. Notably, the parameter C_d^{tcl} appearing in (4.39) and (4.40) accounts for the thermal conductivity between the interior and the exterior of the thermal appliance, and the parameter A_d^{tcl} accounts for the amout of thermal energy supplied when the TCL is operating. These paramters might differ, for an identical TCL, when used by differet users. This is due to the activity of the user and its effect on the parameters. For example, a user that frequently

opens the home windows will cause an increase to the conductivity parameter for an air-conditioner. Hence, these parameters are typically estimated as in [71], [72].

Observe from (4.39) and (4.40) that the evolution of the TCL inner temeprature depends on the surrounding tempereture Θ_{dt}^{out}. For an air-conditioner, the surrounding temperature represents the ambient temperature outside the home whereas for other TCLs (e.g., fridge and water heater) the surrounding temperature is usually the inner temperature of the home. If the home air-conditioner is controlled along with another TCL located inside the home, the outer temperature of the other TCL is taken to be the inner temperature of the air-conditioner (i.e., the home temperature) and is therefore, a variable in the model. Otherwise, if the home air conditioner is not controlled, the outer temperature of the controlled TCLs is taken as an input parameter in the model representing a forecast of the home inner temperature.

4.7.2 Deferrable Uninterruptible Load Model

A DUL is deferrable in time, but uninterruptible once it starts its task. A DUL have a task to complete within given time boundaries. Unlike the TCL where the consumption profile can be controlled, the consumption profile of a DUL is uncontrollable once it is operated. Therefore, we model the DUL with a single case. This is due to the DUL's uninterruptable nature.

The given parameter for the DUL model is the consumption profile. The user's convenience settings contain the allowable time to start the task and the time when the task must be finished. The proposed mathematical model of the DUL is as follows:

$$u_{dt}^{dul},\ s_{dt}^{dul} \in \{0,1\} \qquad \forall t \in \mathcal{T} \tag{4.43}$$

$$p_{dt}^{dul} = s_{dt}^{dul} P_d^{dul} \qquad \forall t \in \mathcal{T} \tag{4.44}$$

$$q_{dt}^{dul} = s_{dt}^{dul} Q_d^{dul} \qquad \forall t \in \mathcal{T} \tag{4.45}$$

$$\sum_{\forall t \in \mathcal{T}} s_{dt}^{dul} = \rho_d^{dul} / \tau \tag{4.46}$$

$$\sum_{t=t_d^{min}}^{t_d^{max}+1-\rho_d^{dul}/\tau} u_{dt}^{dul} = 1 \tag{4.47}$$

$$\frac{u_{dt}^{dul}\,\rho_d^{dul}}{\tau} \le \sum_{k=1}^{\rho_d^{dul}/\tau} s_{d(t+k-1)}^{dul} \qquad \forall t \in [t_d^{\min}, t_d^{\max}+1-\rho_d^{dul}/\tau] \tag{4.48}$$

$$\forall d \in \mathcal{D}_h^{dul}, \quad \forall h \in \mathcal{H}$$

where (4.43) enforces the binarity of the start-task variable and the operating state variable of the DUL. (4.44) and (4.45) define the active and the reactive power consumption of the DUL, respectively. (4.46) enforces the uninterruptable device to remain ON for its specified operational period. (4.47) limits the start and the finish time of the device to the household settings (i.e., between the start of time step t_d^{min} and the end of time step t_d^{max}). (4.48) connects the starting binary variable u_{dt} with the operating state binary variable s_{dt}.

In some cases, a DUL can only start after another DUL has finished its task. For example, a clothes dryer task should start only after the completion of the clothes washer task. For such linked DULs, we introduce constraint (4.49) enforcing the second DUL (d_j) to start only after the first DUL (d_i) has finished its task. We also introduce the parameter

$gap_{d_i d_j}$ which is set by the household defining the maximum allowable gap between the end of the first DUL's task and the start of the second DUL's task:

$$u_{d_j t} \leq \sum_{k=0}^{gap_{d_i d_j}} u_{d_i (t-k-\rho_{d_i}^{dul}/\tau)} \quad \forall t \in \left[t_{d_j}^{min}, t_{d_j}^{max} + 1 - \rho_{d_j}^{dul} / \tau \right] \tag{4.49}$$

$$\forall \left(d_i, d_j \right) \in \mathcal{D}_h^{dul,linked}, \forall h \in \mathcal{H}$$

Finally, the total PQ load of the home is defined as the summation of the uncontrollable loads, the DULs, and the TCLs:

$$p_{hts}^{home} = P_{ht}^{uc} + \sum_{\forall d \in D_h^{dul}} p_{dt}^{dul} + \sum_{\forall d \in D_h^{tcl}} p_{dts}^{tcl} \tag{4.50}$$

$$q_{hts}^{home} = Q_{ht}^{uc} + \sum_{\forall d \in D_h^{dul}} q_{dt}^{dul} + \sum_{\forall d \in D_h^{tcl}} q_{dts}^{tcl} \tag{4.51}$$

$$\forall d \in \mathcal{D}_h^{tcl}, \quad \forall h \in \mathcal{H}, \quad \forall t \in \mathcal{T}, \quad \forall s \in \mathcal{S}$$

4.8 External Grid Model and Power Factor Limits

The eG is modeled as a Thevenin equivalent circuit connected to the PCC bus. The model of the eG is described as follows:

$$i_{ts}^{r,pcc} = G_{ts}^{eg} (e_{(pcc)ts} - E_{ts}^{r,eg}) - B_{ts}^{eg} (f_{(pcc)ts} - E_{ts}^{i,eg}) \tag{4.52}$$

$$i_{ts}^{i,pcc} = B_{ts}^{eg} (e_{(pcc)ts} - E_{ts}^{r,eg}) + G_{ts}^{eg} (f_{(pcc)ts} - E_{ts}^{i,eg}) \tag{4.53}$$

$$p_{ts}^{pcc} = e_{(pcc)ts} i_{ts}^{r,pcc} + f_{(pcc)ts} i_{ts}^{i,pcc} \tag{4.54}$$

$$q_{ts}^{pcc} = f_{(pcc)ts} i_{ts}^{r,pcc} - e_{(pcc)ts} i_{ts}^{i,pcc} \tag{4.55}$$

$$v_{ts}^{pcc,sq} = (e_{(pcc)ts})^2 + (f_{(pcc)ts})^2 \tag{4.56}$$

$\forall t \in \mathcal{T}, \quad \forall s \in \mathcal{S}$

where (4.52) and (4.53) respectively define the real and imaginary currents flowing to the eG. (4.54) and (4.55) define the active and reactive powers flowing to the eG, respectively, and (4.56) defines the voltage magnitude squared at the PCC bus.

The eG Thevenin equivalent parameters appearing in (4.52) and (4.53) are typically estimated using the measured voltage and current at the PCC (see [73]). Consequently, forecasted values for these parameters may be obtained from the history of estimated values. In this thesis, we assume that the parameters are given inputs to the μG model.

In some cases, the eG sets power factor limits that must be honored by the μG at the PCC. To model the power factor limits, we add the following constraints (the feasibility region of those constraints is depicted in Figure 4.3):

$$-(1 - z_{ts}^{p}) M^{pf} + \rho_4 p_{ts}^{pcc} \leq q_{ts}^{pcc} \leq \rho_1 p_{ts}^{pcc} + (1 - z_{ts}^{p}) M^{pf} \tag{4.57}$$

$$-z_{ts}^{p} M^{pf} + \rho_3 p_{ts}^{pcc} \leq q_{ts}^{pcc} \leq \rho_2 p_{ts}^{pcc} + z_{ts}^{p} M^{pf} \tag{4.58}$$

$$p_{ts}^{pcc} = p_{ts}^{pcc,export} - p_{ts}^{pcc,import} \tag{4.59}$$

$$0 \leq p_{ts}^{pcc,export} \leq z_{ts}^{p} M^{p} \tag{4.60}$$

$$0 \leq p_{ts}^{pcc,import} \leq (1 - z_{ts}^{p}) M^{p} \tag{4.61}$$

$$z_{ts}^{p} \in \{0,1\} \tag{4.62}$$

$\forall t \in \mathcal{T}, \quad \forall s \in \mathcal{S}$

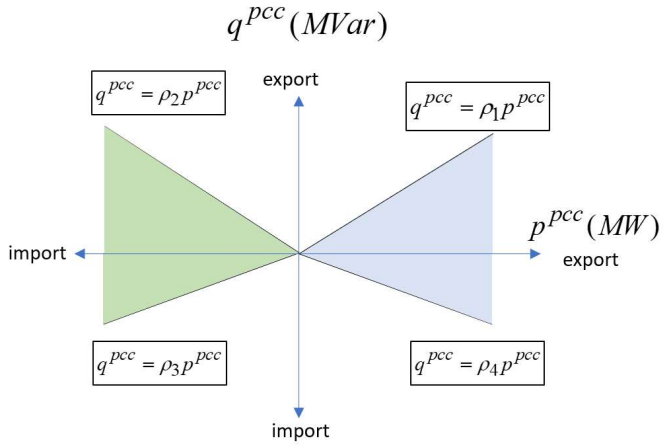

Figure 4.3. Feasibility region of the PCC power factor.

The feasibility region of constraint (4.57) is the blue one in quadrants 1 and 4 of Figure 4.3, while the feasibility region of constraint (4.58) is the green one in quadrants 2 and 3. The constants ρ_1, ρ_2, ρ_3, and ρ_4 are input parameters to the model and are based on the enforced power factor limits where $\rho_1, \rho_3 > 0$ and $\rho_2, \rho_4 < 0$. The binary variable z_{ts}^{p} is added to activate only one of the two constraints depending on whether the µG is exporting active power ($z_{ts}^{p} = 1$), or it is importing active power ($z_{ts}^{p} = 0$) at time step *t* at case *s*. Constraints (4.59), (4.60), and (4.61) define the power exports and imports and eliminate simultaneous export and import. Notably, one may eliminate the need for the binary variable if the mode of the µG (i.e., exporting or importing active power) is known before solving the problem.

4.9 Bus Balance and Voltage Limits

Kirchoff's Current Law (KCL) is applied at each bus in the µG resulting in the following set of equations:

$$i_{kts}^{r,pq} + i_{kts}^{r,fx} + \sum_{\forall m \in A(k)} i_{(km)ts}^{r,cr} = 0 \tag{4.63}$$

$$i_{kts}^{i,pq} + i_{kts}^{i,fx} + \sum_{\forall m \in A(k)} i_{(km)ts}^{i,cr} = 0 \tag{4.64}$$

$\forall k \in \mathcal{K} \setminus \{pcc\}, \quad \forall t \in \mathcal{T}, \quad \forall s \in \mathcal{S}$

$$i_{kts}^{r,pcc} + i_{kts}^{r,pq} + i_{kts}^{r,fx} + \sum_{\forall m \in \mathcal{A}(k)} i_{(km)ts}^{r,cr} = 0 \tag{4.65}$$

$$i_{kts}^{i,pcc} + i_{kts}^{i,pq} + i_{kts}^{i,fx} + \sum_{\forall m \in \mathcal{A}(k)} i_{(km)ts}^{i,cr} = 0 \tag{4.66}$$

$k = pcc, \quad \forall t \in \mathcal{T}, \quad \forall s \in \mathcal{S}$

where (4.63) and (4.64) define the KCL at all buses except for the PCC bus and (4.65) and (4.66) define the KCL at the PCC bus. Typically, DGs, ESSs, homes, and fixed-shunts are not directly connected to the PCC bus, however, we include them in the KCL equations of the PCC bus for the sake of generality.

The final set of constraints in the μG model are the bus voltage magnitude limits which are defined as follows:

$$(\underline{V}_k)^2 \leq e_{kts}{}^2 + f_{kts}{}^2 \leq (\overline{V}_k)^2 \tag{4.67}$$

$\forall k \in \mathcal{K}, \quad \forall t \in \mathcal{T}, \quad \forall s \in \mathcal{S}$

4.10 Summary

This chapter presented the μG mathematical model. We used the current formulation as opposed to the power balance formulation resulting in linear equations for the network. Additionally, the model was presented as a multi-case, multi-period model that is able to

incorporate any number of periods and cases. The model contains continuous as well as binary variables. The binary variables arise from modeling the commitment of DGs, the switching of discrete TCLs, the commitment of DULs, the elimination of simultaneous charging and discharging of ESSs, and the power factor constraints at the PCC. The presented μG mathematical model will be used in the next chapter to formulate the μGEMS problems. For abbreviation, we will refer to the μG mathematical model as follows:

$$\begin{aligned} g_{ts}(X,U) &= 0 \qquad \forall t \in \mathcal{T}, \quad \forall s \in \mathcal{S} \\ h_{ts}(X,U) &\le 0 \qquad \forall t \in \mathcal{T}, \quad \forall s \in \mathcal{S} \\ \underline{H}^{sb} \le \underline{X}^{sb}_{|\mathcal{T}|} &\le \bar{X}^{sb}_{|\mathcal{T}|} \le \bar{H}^{sb} \\ x_i, u_j &\in \{0,1\} \ \forall i \in B^x, \qquad \forall j \in B^u \end{aligned} \tag{4.68}$$

where $g_{ts}(.)$ and $h_{ts}(.)$ are the equations and the constraints of the model at time period t for case s, respectively. X and U are the states and controls of the model, respectively. Further, $\underline{X}^{sb}_{|\mathcal{T}|}$ and $\bar{X}^{sb}_{|\mathcal{T}|}$ represent the lower and upper bound variables defining the envelopes of the storage-based DERs (i.e., state-of-charge of ESSs and inner temperature of TCLs). These variables at time period $|\mathcal{T}|$ are bounded between input parameters $\underline{H}^{sb}$ and $\bar{H}^{sb}$ to eliminate the end-of-horizon effect as was previously detailed in the ESS and the TCL models. Finally, B^x and B^u are the set of binary states and controls, respectively.

CHAPTER 5. THE FORMULATIONS OF THE µGEMS OPTIMIZATION PROBLEMS

5.1 Overview

This chapter presents the formulation of the µGEMS optimization problems. The overall framework of the developed µGEMS (depicted in Figure 5.1) contains four modules that are formulated as optimization problems: 1) *compute optimal commitments*, 2) DAUC, 3) HAOP, and 4) RTC. The proposed µGEMS computes the optimal commitments that can be provided by the µG by solving the *compute optimal commitments* problem. The µGEMS is also responsible for optimally planning and controlling the operation of the µG by solving the DAUC, the HAOP, and the RTC problems in a hierarchical manner.

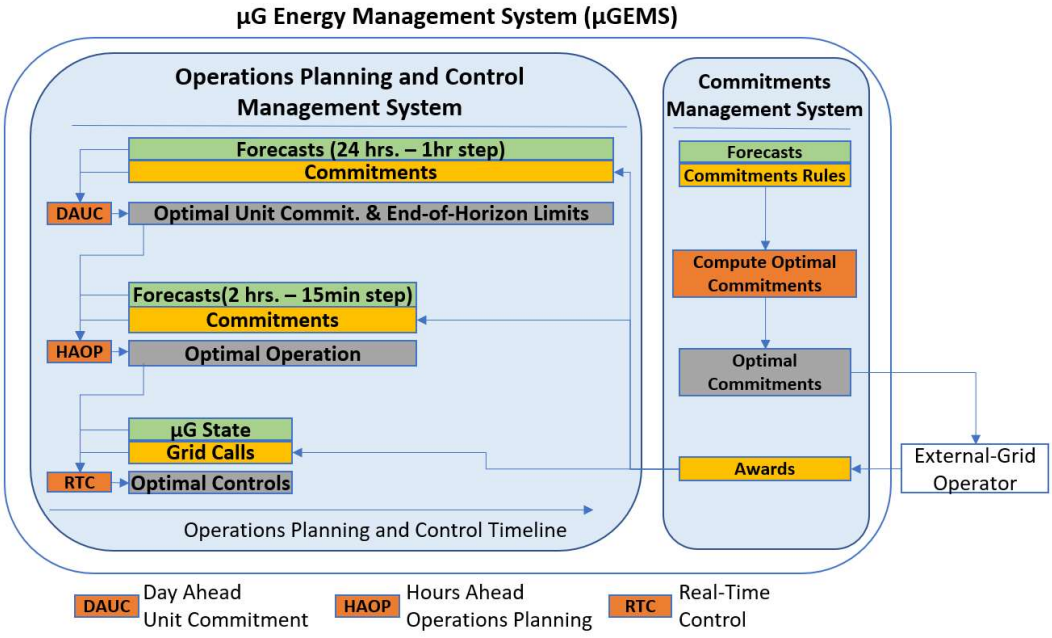

Figure 5.1. The framework of the µGEMS

As previously discussed in chapter 3, we consider two service designs, namely, the Day-Ahead (DA) Commitment design and the Real-Time (RT) Commitment design. In section 5.2 of this chapter, we present the formulation of the four μGEMS modules under the DA Commitment design. Then, in section 5.3, we introduce the problem formulation of the four modules under the RT Commitment design. Notably, the formulation of the DAUC, HAOP, and RTC problems under both service designs is similar where recommended controls are sent from the upper levels to the lower ones until actual control commands are transmitted to the DERs via the RTC. The differences, however, occur in the objective functions and few constraints that model the service design under consideration.

5.2 Day-Ahead Commitment Design

In the DA Commitment design, the *compute optimal commitments* module of the μGEMS solves an optimization problem to compute the optimal energy and ancillary service capacities to be submitted to the eG. Then, the DAUC and the HAOP modules are given the hourly committed energy and service capacities as inputs to be held throughout their planning horizons. Finally, the RTC module receives the calls from the eG for immediate response. In the following sub-sections, we present the problem formulation of the *compute optimal commitments* module, followed by the problem formulations of the DAUC, the HAOP, and the RTC modules.

5.2.1 Commitments Management System: The Compute Optimal Commitments Problem

This problem is assumed to be solved before the closure gate of the DA market given sufficient time to solve the optimization problem. It is responsible for computing the

optimal hourly DA energy and ancillary service capacities. The ancillary services include reserve capacity, upward regulation capacity, and downward regulation capacity. The formulation is posed as a multi-case, multi period optimization problem. Each case in the formulation represents a prospective state the system may be subjected to at any time instance due to a call for the full capacity of the corresponding service, in addition to the base case (energy procurement) which defines the system's state when no service is called for. Therefore, the cases set $\mathcal{S}$ consists of the following four elements: s_0 (energy procurement or base case), s_{rs} (reserve case), s_{up} (upward regulation case), and s_{dn} (downward regulation case).

In the following, we illustrate the constraints of the *compute optimal commitments* problem followed by the objective function.

5.2.1.1 Microgrid Mathematical Model

The first set of constraints in the *compute optimal commitments* problem represent the μG mathematical model introduced in chapter 4, which is expressed as follows:

$$\begin{aligned} g_{ts}(X,U) &= 0 \qquad \forall t \in \mathcal{T}_{DA}, \quad \forall s \in \mathcal{S} \\ h_{ts}(X,U) &\le 0 \qquad \forall t \in \mathcal{T}_{DA}, \quad \forall s \in \mathcal{S} \\ \underline{H}^{sb} \le \underline{X}^{sb}_{|\mathcal{T}_{DA}|} &\le \bar{X}^{sb}_{|\mathcal{T}_{DA}|} \le \bar{H}^{sb} \\ x_i, u_j &\in \{0,1\} \ \forall i \in B^x, \qquad \forall j \in B^u \end{aligned} \tag{5.1}$$

where $\mathcal{T}_{DA}$ is the set of the time periods and $\mathcal{S}$ is the set of the cases. While the *compute optimal commitments* problem is responsible for computing hourly DA energy and ancillary service capacities (i.e., capacities for 24 hours), the set $\mathcal{T}_{DA}$ should extend to

more than 24 hours for two reasons: 1) to eliminate end of horizon effect for storage-based DERs when committing the DA energy and ancillary services, and 2) to ensure the ability of the μG to supply committed services that are interdependent between time periods. This interdependence specifically occurs in reserve provision. A reserve committed at hour *t* may be conditioned to be maintained for R^{maintain} hours. Hence, $\mathcal{T}_{DA}$ should be at least 24+ R^{maintain} to ensure that the μG is able to maintain a reserve committed for hour 24 for the conditioned period.

5.2.1.2 Service Capacity Definitions

The service capacities for reserve ($r_{ts_{rs}}$), upward regulation ($r_{ts_{up}}$), and downward regulation ($r_{ts_{dn}}$) available at the PCC are defined by comparing the active power injection to the eG at the base-case and the other cases. The defining equations are shown below:

$$p^{pcc}_{ts_{rs}} - p^{pcc}_{ts_0} = r_{ts_{rs}} \tag{5.2}$$

$$p^{pcc}_{ts_{up}} - p^{pcc}_{ts_0} = r_{ts_{up}} \tag{5.3}$$

$$p^{pcc}_{ts_0} - p^{pcc}_{ts_{dn}} = r_{ts_{dn}} \tag{5.4}$$

$\forall t \in \mathcal{T}^{DA}$

For abbreviation, we will refer to these set of service defining equations as follows:

$$d(p^{pcc}_{ts_0}, p^{pcc}_{ts_i}) = r_{ts_i} \qquad \forall t \in \mathcal{T}^{DA}, \ \forall s_i \in \mathcal{S}_r = \{rs, up, dn\} \tag{5.5}$$

where $\mathcal{S}_r \subset \mathcal{S}$. These service capacities available at the PCC may or may not be eligible for bidding. They must satisfy commitment rules which are defined next.

5.2.1.3 Commitment rules

The commitment rules for an eligible capacity bid include: 1) minimum acceptable capacity, 2) minimum acceptable time to provide the capacity, and 3) minimum maintainability time for reserve (i.e., how long the reserve should be sustained from the time it is requested). Let the binary decision variables z_t^{rs}, z_t^{up}, and z_t^{dn} be indicators for acceptable bids for reserve, upward regulation, and downward regulation capacities at time step *t*, respectively; $z_t^{(.)}$ equals 1 if the capacity is acceptable and zero otherwise.

$$z_t^{rs}, z_t^{up}, z_t^{dn} \in \{0,1\} \qquad \forall t \in \mathcal{T}_{DA} \tag{5.6}$$

Further, let $r_{ts_{rs}}^{bid}$, $r_{ts_{up}}^{bid}$, and $r_{ts_{dn}}^{bid}$ represent the capacities that will be submitted as bids and must satisfy all commitment rules. In the following, we present the formulation of the commitment rules that are applied on these bid variables. We then link the bid variables to the actual capacity variables defined earlier in (5.5).

The minimum acceptable capacity rule is formulated as follows:

$$\underline{R}^{rs} z_t^{rs} \le r_{ts_{rs}}^{bid} \le z_t^{rs} M^{rs} \tag{5.7}$$

$$\underline{R}^{up} z_t^{up} \le r_{ts_{up}}^{bid} \le z_t^{up} M^{up} \tag{5.8}$$

$$\underline{R}^{dn} z_t^{dn} \le r_{ts_{dn}}^{bid} \le z_t^{dn} M^{dn} \tag{5.9}$$

$\forall t \in \mathcal{T}^{DA}$

where if $z_t^{(.)}$ equals 1, the corresponding bid capacity will be forced to be greater than the minimum acceptable capacity $\underline{R}^{(.)}$, otherwise, the bid capacity will be set to zero. $M^{(.)}$ are input parameters set to be at least greater than the maximum possible capacity $r_t^{(.)}$ provided by the μG.

The second rule is the minimum time to provide the capacity. The following ramping constraints for DGs are added to enforce this rule:

$$\left| p_{gts_{rs}}^{dg} - p_{gts_0}^{dg} \right| \leq \delta^{rs} R_g^{dg} + (1 - z_t^{rs}) \bar{P}_g^{dg} \tag{5.10}$$

$$\left| p_{gts_{up}}^{dg} - p_{gts_0}^{dg} \right| \leq \delta^{up} R_g^{dg} + (1 - z_t^{up}) \bar{P}_g^{dg} \tag{5.11}$$

$$\left| p_{gts_{dn}}^{dg} - p_{gts_0}^{dg} \right| \leq \delta^{dn} R_g^{dg} + (1 - z_t^{dn}) \bar{P}_g^{dg} \tag{5.12}$$

$\forall g \in \mathcal{G}, \qquad \forall t \in \mathcal{T}^{DA}$

where $\delta^{(.)}$ represents the minimum time to provide the service capacity in minutes and R_g^{dg} is the ramp rate of the DG in kW/min. These constraints ensure that the DGs may change their set points from the base-case to the corresponding service case within required time. Other service responding DERs (i.e., ESSs and TCLs) are assumed to have sufficiently high ramping capabilities enabling them to change their set points form the minimum rated value to the maximum rated value within a time that is less than the required minimum time for providing the service capacities.

The third rule is the minimum maintainability time, specifically for reserve capacity. It is enforced as follows:

$$
\begin{aligned}
& r^{bid}_{t_i s_{rs}} \le r_{(t_{i+k}) s_{rs}} + (1 - z^{rs}_{t_i}) M^{rs} \\
& for\ k = 1, \ldots, R^{\text{maintain}},\ \forall t_i \in \mathcal{T}^{DA},\ s.t.\ i + k \le |\mathcal{T}_{DA}|
\end{aligned}
\tag{5.13}
$$

where $R^{\text{maintain}} \geq 1$, is the time required to maintain the reserve in hours. The constraint enforces that the actual available reserve capacities during the maintainability time are no less than the submitted bid. Notably, a reserve capacity at hour t_{i+k} must be maintained due to a bid at hour t_i. However, the reserve at hour t_{i+k} may not necessary be submitted as a bid. The reserve at hour t_{i+k} may only be submitted as a bid if it satisfies all rules. Further, due to the connection between time periods (i.e., time interdependence) in the reserve maintainability rule, commitments from a previous day must be accounted for when planning for the consecutive day. Let $R^{comit}_{\tilde{t}_i s_{rs}}$ represent the pre-committed reserve at hour $\tilde{t}_i$ of the previous day. Then, the constraint added to consider the linkage between consecutive days is as follows:

$$
\begin{aligned}
& R^{comit}_{(\tilde{t}_{24-i}) s_{rs}} \le r_{(t_{1+k}) s_{rs}} \\
& for\ i = 1, \ldots, R^{\text{maintain}} - 1,\ for\ k = 1, \ldots, R^{\text{maintain}} - 1 \\
& s.t.\ i + k \le R^{\text{maintain}} - 1
\end{aligned}
\tag{5.14}
$$

Moreover, the following constraint is added to enforce the relation between the actual reserve capacity and the submitted bid capacity:

$$
-(1 - z^{rs}_t) M^{rs} \le r^{bid}_{t s_{rs}} - r_{t s_{rs}} \le (1 - z^{rs}_t) M^{rs} \qquad \forall t \in \mathcal{T}^{DA} \tag{5.15}
$$

where this constraint implies that $r_{ts_{rs}} = r^{bid}_{ts_{rs}}$ if z^{rs}_t equals to 1. Otherwise, if $z^{(.)}_t = 0$, this constraint is relaxed, and $r^{bid}_{ts_{rs}}$ will be equal to zero due to the constraint in (5.7).

The reason for not simply setting $r_{ts_{rs}} = r^{bid}_{ts_{rs}}$ is that a reserve at hour t_i may be required to be maintained due to a bid at hour t_{i-1} although the reserve at hour t_i is not submitted as a bid. Hence, $r^{bid}_{ts_{rs}}$ should equal to zero while $r_{ts_{rs}}$ should not. This time interdependence due to the maintainability rule does not appear in the regulation capacity, and hence, we link the bid capacity variables with the actual capacity variables for regulation as follows:

$$r^{bid}_{ts_{up}} = r_{ts_{up}} \tag{5.16}$$

$$r^{bid}_{ts_{dn}} = r_{ts_{dn}} \tag{5.17}$$

$\forall t \in \mathcal{T}^{DA}$

It is worth noting that in some markets, the upward and downward regulation capacities are submitted as one product with equal capacity in both directions. Such a rule may be enforced as follows:

$$r^{bid}_{ts_{up}} = r^{bid}_{ts_{dn}} \qquad \forall t \in \mathcal{T}^{DA} \tag{5.18}$$

5.2.1.4 Objective Function

The objective function is formulated as the revenues minus the operational cost. The revenues are gained from energy transaction with the eG (R^{en}) and from committing

the ancillary service capacities (R^{as}). The cost is inquired from operating the DGs, including the fuel cost (C^{fdg}) and the startup/shutdown cost (C^{cdg}). We assume given probabilities for the occurrence of each case in the model (i.e., base case and full capacity call of each committed service). The energy transaction with the eG is formulated as the expected revenue of the cases where the energy for supplying a service is assumed compensated at the DA energy price. Similarly, the fuel cost of the DGs is formulated as the expected cost of the cases. We assume that the market is sufficiently competitive, and that the μG is a price taker for energy and ancillary service capacities. The formulation of the objective function is as follows:

$$\begin{aligned} &\max R^{en} + R^{as} - C^{fdg} - C^{cdg} \\ R^{en} &= \tau \sum_{\forall s} \sum_{\forall t} \lambda_t^{en} \gamma_{ts} p_{ts}^{pcc} \\ R^{as} &= \tau \sum_{\forall t} (\lambda_t^{rs} r_{ts_{rs}}^{bid} + \lambda_t^{up} r_{ts_{up}}^{bid} + \lambda_t^{dn} r_{ts_{dn}}^{bid}) \\ C^{fdg} &= \tau \sum_{\forall s} \sum_{\forall t} \sum_{\forall g} \gamma_{ts} C_g^{dg} p_{gts}^{dg} \\ C^{cdg} &= \sum_{\forall t} \sum_{\forall g} (C_g^{su} v_{gt} + C_g^{sd} w_{gt}) \end{aligned} \tag{5.19}$$

where:

τ	Time step as a fraction of an hour.
$\lambda_t^{en}, \lambda_t^{rs}, \lambda_t^{up}, \lambda_t^{dn}$	Forecasted DA hourly prices for energy, reserve, upward regulation and downward regulation capacities, respectively.
γ_{ts}	Positive parameter representing the probability of the occurrence of case *s* at time step *t*.
p_{ts}^{pcc}	Active power injected to the eG at the PCC.
p_{gts}^{dg}	DGs active power output.

$C_g^{dg}, C_g^{su}, C_g^{sd}$ DGs fuel, startup, and shutdown costs.

v_{gt} , w_{gt} DGs start-up and shunt-down variables.

Once the DA plan (i.e., hourly DA power profile) and service capacities are awarded to the μG, they are given as input parameters to the DAUC module to plan the operation of the μG accordingly as discussed next.

5.2.2 Day-Ahead Unit Commitment Problem

The DAUC problem is formulated as a multi-case, multi-period optimization problem with hourly intervals. The DAUC have a wide planning horizon of time (e.g., 24 hours) to consider daily cycles of loads, renewables, and storage-based DERs including ESSs and TCLs. Given the DA hourly plan (P_t^{comit}) and hourly committed ancillary service capacities $(R_{ts_i}^{comit})$, the DAUC computes the optimal DER's commitment plan $(U^{uc,*})$ for its planning horizon. The DERs requiring a commitment plan (i.e., start-up and shunt-down) are DGs and DULs. The DAUC is also responsible for computing optimal "storage" plan for the storage-based DERs. A storage plan represents the state-of-charge profiles for ESSs and the inner temperature evolution for TCLs. Recall that storage profiles for ESSs and TCLs were modeled as envelopes defined by upper storage variables $(\overline{X}^{sb,*})$, and lower storage variables $(\underline{X}^{sb,*})$. The DERs commitments and storage plans computed by the DAUC are used later in the HAOP problem as it considers a shorter planning horizon such as 2 hours.

The objective function of the DAUC problem is to minimize the total expected cost throughout its planning horizon which includes the cost of deviating from the DA plan (C^{en}), the expected penalties for insufficient service supply (C^{pen}), the expected fuel cost of DGs (C^{fdg}), and the startup/shutdown cost of the DGs (C^{cdg}). For the purpose of generality, the deviation from the DA plan is modeled as having two costs, one for upward deviation (i.e., μG is exporting more than the DA plan) and one for downward deviation. The deviation costs can be taken as the real-time energy prices. Alternatively, they can be seen as penalties for deviating from committed DA plan. The complete formulation of the DAUC problem is as follows:

$$\min C^{en} + C^{pen} + C^{fdg} + C^{cdg}$$

$$C^{en} = \tau \sum_{t\in\mathcal{T}_d} (\lambda_t^{en,-}\Delta p_t^{pcc,-} - \lambda_t^{en,+}\Delta p_t^{pcc,+}), \qquad C^{pen} = \tau \sum_{s\in\mathcal{S}_r}\sum_{t\in\mathcal{T}_d} \lambda_{ts}^{pen}\gamma_{ts}\pi_{ts},$$

$$C^{fdg} = \tau \sum_{s\in\mathcal{S}}\sum_{t\in\mathcal{T}_d}\sum_{g\in\mathcal{G}} \gamma_{ts} C_g^{dg} p_{gts}^{dg}, \qquad C^{cdg} = \sum_{t\in\mathcal{T}_d}\sum_{g\in\mathcal{G}} (C_g^{su} v_{gt} + C_g^{sd} w_{gt})$$

$$s.t.$$

$$\begin{aligned}
g_{ts}(X,U) &= 0 && \forall t\in\mathcal{T}_d,\ \ \forall s\in\mathcal{S}\\
h_{ts}(X,U) &\le 0 && \forall t\in\mathcal{T}_d,\ \ \forall s\in\mathcal{S}\\
d(P_t^{comit}, p_{ts_i}^{pcc}) &= R_{ts_i}^{comit} - \pi_{ts_i} && \forall t\in\mathcal{T}_d,\ \ \forall s_i\in\mathcal{S}_r\\
p_{ts_0}^{pcc} &= P_t^{comit} + \Delta p_t^{pcc,+} - \Delta p_t^{pcc,-} && \forall t\in\mathcal{T}_d\\
0 \le \Delta p_t^{pcc,+} &\le z_t^{pcc} M^{pcc} && \forall t\in\mathcal{T}_d\\
0 \le \Delta p_t^{pcc,-} &\le (1-z_t^{pcc}) M^{pcc} && \forall t\in\mathcal{T}_d\\
\left| p_{gts_i}^{dg} - p_{gts_0}^{dg} \right| &\le \delta_{s_i} R_g^{dg} && \forall g\in\mathcal{G},\ \ \forall t\in\mathcal{T}_d,\ \ \forall s_i\in\mathcal{S}_r\\
0 \le \Delta p_t^{pcc,+}, \Delta p_t^{pcc,-}, \pi_{ts_i} && && \forall t\in\mathcal{T}_d,\ \ \forall s_i\in\mathcal{S}_r\\
\underline{H}^{sb} \le \underline{X}^{sb}_{|\mathcal{T}_d|} &\le \overline{X}^{sb}_{|\mathcal{T}_d|} \le \overline{H}^{sb}
\end{aligned} \tag{5.20}$$

$$z_t^{pcc}, x_i, u_j \in \{0,1\}\ \forall i\in B^x, \quad \forall j\in B^u, \quad \forall t\in\mathcal{T}_d$$

where:

τ	Time step as a fraction of an hour.
$\lambda_t^{en,+}, \lambda_t^{en,-}$	Upward and downward deviation cost from DA plan.
$\Delta p_t^+, \Delta p_t^-$	Upward and downward deviation from the DA plan.
λ_{ts}^{pen}	Penalty cost for insufficient service supply where $s \in \mathcal{S}_r = \{rs, up, dn\}$
γ_{ts}	Probability of the occurrence of case *s* at time step *t*.
π_{ts}	Service capacity deficiency from the DA committed capacity.
$C_g^{fdg}, C_g^{su}, C_g^{sd}$	DGs fuel, startup, and shutdown costs.
p_{gts}^{dg}	DGs active power output.
v_{gt} , w_{gt}	DGs start-up and shunt-down variables.
$g(.), h(.)$	μG mathematical model.
$d(.)$	Service defining equations.
$R_{ts_i}^{comit}$	Committed service capacities.
$p_{ts_0}^{pcc}$	Active power injected to the eG under the base case.
P_t^{comit}	Committed DA plan.
z_t^{pcc}	Binary: 1 if deviating upward from DA plan and 0 otherwise.
M^{pcc}	A constant larger than any possible value of $\Delta p_t^{pcc,+}$ and $\Delta p_t^{pcc,-}$.
δ_{s_i}	Service ramping requirement.
R_g^{dg}	DGs ramping limits.
$\underline{X}_{\lvert\mathcal{T}_d\rvert}^{sb}$	Lower bound storage state at time step $\lvert\mathcal{T}_d\rvert$ for storage-based DERs.
$\overline{X}_{\lvert\mathcal{T}_d\rvert}^{sb}$	Upper bound storage state at time step $\lvert\mathcal{T}_d\rvert$ for storage-based DERs.

Depending on the time of announcing the DA awarded bids and the horizon of the DAUC problem, it is possible that energy and ancillary service commitments for an optimized hour within the DAUC horizon are not available. This occurs, for example, if awarded bids for the following day are announced at 1:00pm of the current day, and the DAUC is being solved with a 24hrs horizon starting at 12:00pm of the current day. Hence, commitments for hours [12:00am – 12:00pm) of the following day are not available. In such cases, the *compute optimal commitments* problem is pre-solved to obtain prospective commitments of energy and ancillary services for hours with unavailable commitments.

Once the DAUC problem is solved at a given time and for a given horizon, the optimal DERs commitments $U^{uc,*}$ and storage plans $\underline{X}^{sb,*}, \overline{X}^{sb,*}$ are given as inputs to the HAOP problem.

5.2.3 Hours Ahead Operations Planning Problem

Similar to the DAUC problems, the HAOP problem is formulated as a multi-case, multi-period optimization problem. The HAOP problem considers a shorter planning horizon with a higher granularity relative to the DAUC. It is also solved more frequently than the DAUC to enhance the accuracy of the operations plan given more accurate and frequently updated forecasts. The HAOP is typically solved with a 2-hour horizon and 5min to 15min intervals. The HAOP uses the most recent optimal DERs commitment plan ($U^{uc,*}$) computed by the DAUC. Also, the HAOP uses the optimal vectors $\underline{X}^{sb,*}, \overline{X}^{sb,*}$ obtained from the DAUC to set end-of-horizon limits for storage-based DERs and eliminate the end-of-horizon effect. In some cases, the end-of-horizon limits obtained from

the DAUC become infeasible when solving the HAOP problem due to the changing forecast. Therefore, we softly enforce the end-of-horizon limits in the HAOP problem (i.e., by adding slacks minimized in the objective function). We use linear interpolation to extract higher resolution values for the vectors $\underline{X}^{sb,*}, \overline{X}^{sb,*}$ to be used in HAOP problem. This is especially necessary if the frontier of the HAOP problem does not coincide with a time step in the DAUC as the granularity of the two problems are different.

Given the DA plan (P_k^{comit}) and committed ancillary service capacities ($R_{ks_i}^{comit}$), the HAOP computes the optimal DER's active power controls plan ($U^{p,**} \subset U^{**}$) to be passed as recommendations for the lower-level problem, the RTC. Unlike the active power controls, the reactive power controls are instantaneous and are not time interdependent. Hence, only active power controls need to be passed from the HAOP problem to the RTC problem.

The objective function of the HAOP problem is to minimize the total expected cost throughout the planning horizon which includes the cost from deviating from the DA plan (C^{en}), the expected penalties for insufficient service supply (C^{pen}), the expected fuel cost of DGs (C^{fdg}), and the deviation from the DAUC end-of-horizon limits (C^{dauc}). Different from the DAUC problem, the objective function of the HAOP does not include the startup/shutdown cost of the DGs as the DGs commitment plan is predefined by the DAUC. The complete formulation of the HAOP problem is as follows:

$$\min C^{en} + C^{pen} + C^{fdg} + C^{dauc}$$

$$C^{en} = \tau \sum_{k \in \mathcal{T}_h} (\lambda_k^{en,-} \Delta p_k^{pcc,-} - \lambda_k^{en,+} \Delta p_k^{pcc,+}), \quad C^{pen} = \tau \sum_{s \in \mathcal{S}_r} \sum_{k \in \mathcal{T}_h} \lambda_{ks}^{pen} \gamma_{ks} \pi_{ks},$$

$$C^{fdg} = \tau \sum_{s \in \mathcal{S}} \sum_{k \in \mathcal{T}_h} \sum_{g \in \mathcal{G}} \gamma_{ks} C_g^{dg} p_{gks}^{dg} \qquad C^{dauc} = \Lambda^{sb,T} (\Delta^{sb,-} + \Delta^{sb,+})$$

$$s.t.$$

$$\begin{aligned}
& g_{ks}(X,U) = 0 && \forall k \in \mathcal{T}_h, \quad \forall s \in \mathcal{S} \\
& h_{ks}(X,U) \le 0 && \forall k \in \mathcal{T}_h, \quad \forall s \in \mathcal{S} \\
& d(P_k^{comit}, p_{ks_i}^{pcc}) = R_{ks_i}^{comit} - \pi_{ts_i} && \forall k \in \mathcal{T}_h, \quad \forall s_i \in \mathcal{S}_r \\
& p_{ks_0}^{pcc} = P_k^{comit} + \Delta p_k^{pcc,+} - \Delta p_k^{pcc,-} && \forall k \in \mathcal{T}_h \\
& 0 \le \Delta p_k^{pcc,+} \le z_k^{pcc} M^{pcc} && \forall k \in \mathcal{T}_h \\
& 0 \le \Delta p_k^{pcc,-} \le (1 - z_k^{pcc}) M^{pcc} && \forall k \in \mathcal{T}_h \\
& \left| p_{gks_i}^{dg} - p_{gks_0}^{dg} \right| \le \delta_{s_i} R_g^{dg} && \forall g \in \mathcal{G}, \quad \forall k \in \mathcal{T}_h, \quad \forall s_i \in \mathcal{S}_r \\
& 0 \le \Delta p_k^{pcc,+}, \Delta p_k^{pcc,-}, \pi_{ks_i} && \forall k \in \mathcal{T}_h, \quad \forall s_i \in \mathcal{S}_r \\
& U_k^{uc} = U^{uc,*}|_{t=k} && \forall k \in \mathcal{T}_h \\
& \underline{X}^{sb,*}|_{t=|\mathcal{T}_h|} - \Delta^{sb,-} \le \underline{X}_{|\mathcal{T}_h|}^{sb} \le \bar{X}_{|\mathcal{T}_h|}^{sb} \le \bar{X}^{sb,*}|_{t=|\mathcal{T}_h|} + \Delta^{sb,+} \\
& \mathbf{0} \le \Delta^{sb,-}, \Delta^{sb,+} \\
& z_k^{pcc}, x_i, u_j \in \{0,1\} \ \forall i \in B^x, \qquad \forall j \in B^u, \qquad \forall k \in \mathcal{T}_h
\end{aligned} \tag{5.21}$$

where:

τ	Time step as a fraction of an hour.
$\lambda_k^{en,+}, \lambda_k^{en,-}$	Upward and downward deviation cost from DA plan.
$\Delta p_k^{pcc,+}, \Delta p_k^{pcc,-}$	Upward and downward deviation from the DA plan.
λ_{ks}^{pen}	Penalty cost for insufficient service supply where $s \in \mathcal{S}_r = \{rs, up, dn\}$

γ_{ks}	Positive parameter representing the probability of the occurrence of case *s* at time step *t*.
π_{ks}	Service capacity deficiency from the DA committed capacity.
p_{gks}^{dg}	DGs active power output.
Λ^{sb}	Vector of penalty weights for the deviation from the DAUC end-of-horizon limits.
$\Delta^{sb,+}, \Delta^{sb,-}$	Vectors containing the upward and downward deviations from the DAUC end-of-horizon limits.
$g(.), h(.)$	μG mathematical model.
$d(.)$	Service defining equations.
$R_{ks_i}^{comit}$	Committed service capacities.
$p_{ks_0}^{pcc}$	Active power injected to the eG under the base case.
P_k^{comit}	Committed DA plan.
z_k^{pcc}	Binary: 1 if deviating positively from DA plan and 0 otherwise.
M^{pcc}	A constant larger than any possible value of $\Delta p_k^{pcc,+}$ and $\Delta p_k^{pcc,-}$
δ_{s_i}	Service ramping requirement.
R_g^{dg}	DGs ramping limits.
$\underline{X}_{\lvert\mathcal{T}_h\rvert}^{sb}$	Lower bound storage state at time step $\lvert\mathcal{T}_d\rvert$ for storage-based DERs.
$\overline{X}_{\lvert\mathcal{T}_h\rvert}^{sb}$	Upper bound storage state at time step $\lvert\mathcal{T}_d\rvert$ for storage-based DERs.

Other than setting the commitments of the DERs and utilizing the storage plans obtained from the DAUC problem, the constraint set of the HAOP problem is identical to the set in the DAUC problem. Once the HAOP problem is solved at a given time and for a

given horizon, the optimal DERs active power controls are given as inputs to the RTC problem.

5.2.4 Real Time Control Problem

The RTC problem is responsible for computing the optimal controls U_m^{***} that will be transmitted to the controllable DERs at time m. It is formulated as a single-case single-period optimization problem and uses the realized state of μG at time m. In addition, the RTC uses the most recent active power controls of the DERs computed by the HAOP problem for time m. Recall that the HAOP is formulated as a multi-case problem where it outputs the optimal active power controls when no service is being requested ($U_{ks_0}^{p,**}$) resembling the base-case, and the optimal controls when the full capacity of each service s_i is requested ($U_{ks_i}^{p,**}$). These multi-case controls were optimally computed by the HAOP considering its planning horizon and the associated intertemporal constraints of the DERs. Therefore, we use the multi-case active power controls to set soft bounds on the RTC active power controls (U_m^p) depending on the service being requested in real-time as shown in the RTC problem formulation in (5.22).

The objective function of the RTC problem includes a penalty term on deviating from the DA plan (P_m^{comit}) if no service is being called for, while the penalty is on deviating from the eG call ($P_{ms_i}^{call}$) if service s_i is being called for. Additionally, the objective function includes a penalty term on deviating from the active power controls set by the HAOP problem (C^{haop}), the fuel cost of the DGs (C^{fdg}), and a penalty term on

the deviation of the voltage at the PCC from a target value (C^{vs}). The complete formulation of the RTC problem is as follows:

$$\min \; C^{pcc} + C^{haop} + C^{fdg} + C^{vs}$$

$$C^{pcc} = \lambda^{pcc}(\delta^{pcc,+} + \delta^{pcc,-}) \quad C^{haop} = \Lambda^{p,T}(\Delta^{p,+} + \Delta^{p,-})$$

$$C^{fdg} = \sum_{g \in \mathcal{G}} C_g^{dg} p_{gm}^{dg} \qquad C^{vs} = \lambda^{vs} \left| \left(v_m{}^{pcc,sq} \right) - \left(\mathrm{V}_m^{\text{target}} \right)^2 \right|$$

$$s.t.$$

$$g_m(X,U) = 0$$

$$h_m(X,U) \le 0$$

$$U_m^{uc} = U^{uc,*}|_{t=m}$$

$$\mathbf{0} \le \Delta^{p,-}, \Delta^{p,+}$$

$$0 \le \delta^{pcc,+}, \delta^{pcc,-}$$

$$x_i, u_j \in \{0,1\} \; \forall i \in B^x, \qquad \forall j \in B^u \tag{5.22}$$

If no service is being called for:

$$p_m^{pcc} = P_m^{comit} + \delta^{pcc,+} - \delta^{pcc,-}$$

$$U_m^p = U_{s0}^{p,**}|_{k=m} + \Delta^{p,+} - \Delta^{p,-}$$

If service s_i is being called for:

$$p_m^{pcc} = P_{ms_i}^{call} + \delta^{pcc,+} - \delta^{pcc,-}$$

$$U_m^p \le \max(U_{s0}^{p,**}|_{k=m}, U_{s_i}^{p,**}|_{k=m}) + \Delta^{p,+}$$

$$U_m^p \ge \min(U_{s0}^{p,**}|_{k=m}, U_{s_i}^{p,**}|_{k=m}) - \Delta^{p,-}$$

where:

λ^{pcc} — Penalty weight for the deviation from the scheduled power at the PCC. The scheduled power when there is no call is equal to the DA committed plan, while if there is a call for service, it is equal to the requested power from the eG.

$\delta^{pcc,+}, \delta^{pcc,-}$	Upward and downward deviations from the scheduled power at the PCC.
Λ^{p}	Vector of penalty weights for the deviation from the HAOP active power controls.
$\Delta^{p,+}, \Delta^{p,-}$	Vectors containing the upward and downward deviations from the HAOP active power controls.
C_g^{dg}	DGs fuel cost.
p_{gm}^{dg}	DGs active power output.
λ^{vs}	Penalty on the deviation from the target PCC voltage.
${v_m}^{pcc}, \mathrm{V}_m^{\mathrm{target}}$	Voltage and target voltage at the PCC.
$g(.), h(.)$	μG mathematical model.
p_m^{pcc}	Active power injected to the eG.
$P_{ms_i}^{call}$	Requested active power set point from the eG at the PCC.

Note that the term for the DGs' fuel cost in the objective function of the RTC is not necessary to be added if there is no call for services or if the call is for a full committed capacity. This is because these two cases (i.e., no call or full capacity call) are considered in the HAOP problem where DGs cost is minimized. Hence, minimizing the deviation from the HAOP controls should be sufficient. However, it might be the case that only part of a committed capacity is called for. By including the DGs fuel cost, the RTC would therefore dispatch the cheapest resources to meet the call.

5.3 Real-Time Commitment Design

In the real-time (RT) commitment design, the *commitments management system* of the μGEMS computes the instantaneous available reserve at the PCC along with the associated cost of dispatching this reserve. Five distinct reserve types are considered to be provided by the μG in this design: 1) upward primary reserve (i.e., upward regulation), 2) downward primary reserve (i.e., downward regulation), 3) upward secondary reserve, 4) downward secondary reserve, and 5) tertiary reserve. Primary reserves (i.e., types 1 and 2) are provided in 1 minute and maintained for 10 minutes, while secondary reserve (types 3 and 4) are provided in 10 minutes and maintained for 1 hour. Finally, tertiary reserve is provided in 1 hour. In our formulation, the maintainability of the tertiary reserve could be a given parameter (i.e., must be maintained for 2 hours) or could be a variable (i.e., the μGEMS maximizes the maintainability time). This would depend on the rules set with the eG. Notably, primary reserve is commonly referred to as regulating reserve, secondary reserve is commonly referred to as contingency or balancing reserve, and tertiary reserve is commonly referred to as supplementary or replacement reserve.

The five reserve types can be supplied individually or as stacked services. For example, the μG may only provide upward secondary reserve (individual service), or it may provide upward primary reserve, followed by upward secondary reserve, followed by tertiary reserve (stacked service). Essentially, the *commitments management system* of the μGEMS will produce multiple *reserve products* the μG can provide in real-time, each containing a specific capacity for each reserve type, and a labeled cost (i.e., the lost-of-opportunity cost). The reserve products available at the PCC are updated at each instant of

time. The frequency of updating the available products depends on the agreements with the eG, or the existing market rules. Typical updates could be each 5 or 15 minutes.

If the eG requests dispatching a specific reserve product, the RTC module in the μGEMS is immediately updated to transmit the optimal controls to the DERs. The DAUC and the HAOP modules are also updated to plan the operation of the μG in a manner that follows the dispatch command. The goals and formulations of the DAUC, HAOP, and RTC problems are similar to those presented in the DA Commitment design, where control directives are passed from the upper levels to the lower ones until the controls are transmitted to the DERs via the RTC module. The change, however, occurs in the objective functions as well as few constraints.

In this design, we assume that the μG has a committed DA power exchange profile with the eG (i.e., DA plan). This committed profile could be set through participating in the DA "energy" markets or through bilateral contracts. The problem formulated in section 5.2.1 can be used directly to compute the optimal DA plan without considering the provision of DA ancillary services. Once a DA plan is in place, we assume that the eG uses this plan as a baseline to compensate and penalize the μG for the provided reserves.

The following sections introduce the formulation of the problems within the *commitments management system* and the *operations planning and control management system* for the RT Commitment design.

5.3.1 Commitments Management System: The Compute Optimal Commitments Problem

The compute optimal commitments problem is responsible for outputting the available reserve products at the PCC and the cost of dispatching each reserve. Two look-ahead problems are formulated to compute the reserve and the associated cost. Problem 1 maximizes the reserve that can be supplied with minimal cost (priority for reserve), while Problem 2 minimizes the operational cost assuming no reserve is being supplied. The μG operational cost from Problem 2 is subtracted from that of Problem 1 to compute the lost-of-opportunity cost from dispatching the real-time reserve.

The initial condition of the μG, and end-of-horizon limits for storage-based DERs and DGs commitments are set equal in both problems. The initial condition is taken from the real-time state of the μG, while the end-of-horizon limits are taken from the latest DAUC solution. By constraining that these two problems return to the "end-of-horizon optimal point" taken from the DAUC solution, we ensure that the lost-of-opportunity cost is fully computed.

The horizon considered for the two problems ($|\mathcal{T}_c|$) should be at least greater than or equal to the time of maintaining primary, secondary and tertiary reserves combined (i.e., $|\mathcal{T}_c| \geq |T_P| + |T_S| + |T_T|$ where T_P, T_S, T_T are sets that include the time periods where primary, secondary, and tertiary reserve should be maintained, respectively). Further, the time step of the two problems should be less than or equal to the maintanability time of primary reserve. Without loss of generality, the horizon of the two problems is taken to be 6 hours with 10-minute steps.

In the following subsections, we first present the formulation of the problem that maximizes the reserve (Problem 1), followed by the problem that minimizes the operational cost (Problem 2).

5.3.1.1 Problem 1: Maximize Reserve

We formulate the problem of maximizing the available reserve as a weighted multi-objective optimization problem. The weights control the preference to the five distinct reserve types. In the following, we list the constraints of the problem followed by the objective function.

The first set of constraints for the maximize reserve problem is the μG mathematical model:

$$
\begin{aligned}
& g_t(X,U) = 0 \qquad \forall t \in \mathcal{T}_c \\
& h_t(X,U) \le 0 \qquad \forall t \in \mathcal{T}_c \\
& \underline{X}^{sb,*}\big|_{t=|\mathcal{T}_c|} - \Delta^{sb,-} \le \underline{X}^{sb}_{|\mathcal{T}_c|} \le \bar{X}^{sb}_{|\mathcal{T}_c|} \le \bar{X}^{sb,*}\big|_{t=|\mathcal{T}_c|} + \Delta^{sb,+} \\
& x_i, u_j \in \{0,1\} \ \forall i \in B^x, \qquad \forall j \in B^u
\end{aligned}
\tag{5.23}
$$

The third line in (5.23) sets end-of-horizon limits for storage-based devices. The values $\underline{X}^{sb,*}$, and $\bar{X}^{sb,*}$ are taken from the latest DAUC solution. Also, the constraints are relaxed to avoid infeasibilities using the variables ($\Delta^{sb,-}$, $\Delta^{sb,+}$), which are minimized in the objective function with a penalty cost.

The Maximize Reserve problem may or may not solve for the unit commitment schedule of the DULs and the DGs. If unit commitment is not solved for, the ON/OFF

schedule of the DULs and the DGs is set equal to the schedule obtained from the latest DAUC solution. Otherwise, if unit commitment is solved for in the Maximize Reserve problem, we perform the following: 1) DULs with permissible operational range completely within the horizon of the Maximize Reserve problem are scheduled in the problem, while the schedule of other DULs' is taken from the latest DAUC solution, and 2) end-of-horizon commitment constraints are enforced for the DGs using the latest DAUC DGs' schedule. Specifically, we set:

$$UT_g^{|\mathcal{T}_C|} = UT_g - UT_g^{0,*} \qquad \forall g \in \mathcal{G} \tag{5.24}$$

$$DT_g^{|\mathcal{T}_C|} = DT_g - DT_g^{0,*} \qquad \forall g \in \mathcal{G} \tag{5.25}$$

where $UT_g^{|\mathcal{T}_C|} / DT_g^{|\mathcal{T}_C|}$ is the number of final time periods the unit should be ON/OFF (see section 4.5). UT_g / DT_g is the minimum up/down time of the unit (unit specification), and $UT_g^{0,*} / DT_g^{0,*}$ is the number of time periods the unit should be ON/OFF as observed from the latest DAUC solution at time period $|\mathcal{T}_C| + 1$ (i.e., the initial time period of the horizon immediately following the horizon of the Maximize Reserve problem). With this setting of $UT_g^{|\mathcal{T}_C|} / DT_g^{|\mathcal{T}_C|}$ we ensure that the ON/OFF schedule of the DGs return to the optimal schedule obtained from the DAUC, and hence, the lost-of-opportunity cost can be fully computed within the horizon of the Maximize Reserve problem.

Taking the DULs and DGs schedule from the latest DAUC solution would reduce the complexity of the Maximize Reserve problem allowing faster computational times. However, solving for the units' commitment would result in a more optimal solution (e.g.,

a DG may be switched ON to increase the reserve capacity). Therefore, we recommend solving for the unit commitment schedule especially if the problem can be solved in a timely manner.

The deviation from the DA plan (P_t^{comit}) is formulated as follows:

$$p_t^{pcc} = P_t^{comit} + \Delta p_t^{pcc,+} - \Delta p_t^{pcc,-} \tag{5.26}$$

$$0 \le \Delta p_t^{pcc,+} \le z_t^{pcc} M^{pcc} \tag{5.27}$$

$$0 \le \Delta p_t^{pcc,-} \le (1 - z_t^{pcc}) M^{pcc} \tag{5.28}$$

$$z_t^{pcc} \in \{0,1\} \tag{5.29}$$

$\forall t \in \mathcal{T}_c$

A binary z_t^{pcc} is added to eliminate simultaneous upward and downward deviations where M^{pcc} is a large constant.

The upward primary reserve r^{upr} and downward primary reserve r^{dpr} capacities are related to the deviations as follows:

$$0 \le r^{upr} \le \Delta p_{t_1}^{pcc,+} \tag{5.30}$$

$$0 \le r^{dpr} \le \Delta p_{t_1}^{pcc,-} \tag{5.31}$$

where t_1 represents the first time period in the horizon which is where the primary reserve capacity is provided. Further, to ensure that the primary reserve is provided within

acceptable time δ, the DGs ramping from the initial operating point to the first time period are constrained as follows:

$$\left| p_{gt_1}^{dg} - P_{gt_0}^{dg} \right| \leq \delta R_g^{dg} \qquad \forall g \in \mathcal{G} \tag{5.32}$$

Similar to the primary reserve, the upward secondary reserve r^{usr} and downward secondary reserve r^{dsr} capacities are related to the deviations as follows:

$$0 \leq r^{usr} \leq \Delta p_{t_i}^{pcc,+} \qquad \forall i \in T_S \tag{5.33}$$

$$0 \leq r^{dsr} \leq \Delta p_{t_i}^{pcc,-} \qquad \forall i \in T_S \tag{5.34}$$

where the time set T_S includes the time periods where the secondary reserve should be maintained. Considering 10 minute steps and maintainability time of 1 hour for secondary reserve, the set will be $T_S = \{t_2, t_3, t_4, t_5, t_6\}$. Note that the first time period t_1 is not included as secondary reserve must be reached only after 10 minutes.

In regards to the tertiary reserve r^{tr}, there are two options to define their maintainability time which depends on the eG rules. If the maintainability time is pre-defined, the formulation of the tertiary reserve becomes similar to the upward primary and secondary reserves and the following constraint is added:

$$0 \leq r^{tr} \leq \Delta p_{t_i}^{pcc,+} \qquad \forall i \in T_T \tag{5.35}$$

where T_T includes the time periods where the tertiary reserve should be maintained. Alternatively, the maintainability time can be a variable (i.e., not restricted by a given time). In such a case, we add the following constraints:

$$0 \le r^{tr} \le \Delta p_{t_i}^{pcc,+} + (1 - z_{t_i}^{tr}) M^{tr} \qquad \forall i \in T_T \tag{5.36}$$

$$z_{t_{i_1}}^{tr} \ge z_{t_{i_2}}^{tr} \ge \ldots \ge z_{t_{i_{|T_T|}}}^{tr} \tag{5.37}$$

$$\mu^{tr} = \sum_{\forall i \in T_T} z_{t_i}^{tr} \tag{5.38}$$

$$z_{t_i}^{tr} \in \{0,1\} \quad \forall i \in T_T \tag{5.39}$$

where T_T here includes the time periods where tertiary reserve "may" be supplied. $z_{t_i}^{tr}$ is a binary taking the value 1 if the tertiary reserve is maintained in time step t_i and 0 otherwise. The constraint in (5.37) ensures continuity of supplying the reserve while the constraint in (5.38) defines the maintainability time of tertiary reserve μ^{tr}.

If specific minimum capacity requirements are set by the eG for an acceptable reserve product, the following constraints can be added:

$$\underline{R}^i \le r^i + (1 - z^i) M^i \tag{5.40}$$

$$0 \le r^i \le z^i M^i \tag{5.41}$$

$i \in \{upr, dpr, usr, dsr, tr\}$

where $\underline{R}^i$ is the minimum capacity for reserve product i. z^i equals to 1 if the reserve product satisfies the minimum capacity and 0 otherwise. The constraint in (5.41) ensures that the reserve capacity variable r^i is zeroed if minimum capacity limit cannot be satisfied.

Additionally, for secondary reserve and tertiary reserve products, it might be required from the μG to respond in a monotonic manner before reaching the capacity. For example, the μG may only deviate positively form the DA plan before reaching the capacity of the tertiary reserve. We, therefore, include the following constraints:

$$\Delta p_{t_1}^{pcc,-} \leq (1 - z^{usr}) M^{pcc} \tag{5.42}$$

$$\Delta p_{t_1}^{pcc,+} \leq (1 - z^{dsr}) M^{pcc} \tag{5.43}$$

$$\Delta p_{t_i}^{pcc,-} \leq (1 - z^{tr}) M^{pcc} \qquad \forall i \in \{1 \cup T_S\} \tag{5.44}$$

When the constraints above are not added, we noticed that the μG oppose the direction of the reserve in the time before reaching the capacity. Recall, for example, that upward secondary reserve capacity must be reached within 10 minutes. Therefore, since ESS do not have limiting ramping capabilities, the μG may charge the ESS during the first 10 minutes in order to increase the resultant upward secondary reserve capacity that can be provided following the first 10 minutes. Such practice is undesirable from the eG operator which is why we add these constraints above.

With all constraints defined, we may formulate the objective function of the Maximize Reserve problem as follows:

$$
\begin{aligned}
&\max R - C^{P1} - C^{eh} \\
R &= w^{upr} r^{upr} + w^{dpr} r^{dpr} + w^{usr} r^{ups} + w^{dsr} r^{dsr} + w^{tr} r^{tr} \\
C^{P1} &= \tau \sum_{\forall t} \sum_{\forall g} (C_g^{dg} p_{gt}^{dg} + C_g^{su} v_{gt} + C_g^{sd} w_{gt}) \\
&\quad + \tau \sum_{\forall t} (\lambda_t^{en,-} \Delta p_t^{pcc,-} - \lambda_t^{en,+} \Delta p_t^{pcc,+}) \\
C^{eh} &= \Lambda^{sb,T} (\Delta^{sb,-} + \Delta^{sb,+})
\end{aligned}
\tag{5.45}
$$

where R is a weighted sum of the capacity for the five reserve products, C^{P1} is the μG operational cost, and C^{eh} is a penalty term on deviating from the setted end-of-horizon limits. The μG's operational cost includes the DGs' fuel cost and startup/shutdown cost (first summation), and cost from deviating from the DA plan (second summation). Solving the Maximize Reserve problem multiple times while varying the weights of the five reserve types produces multiple reserve products that can be separately provided. The products can be submitted to the external grid and one product may be dispatched in real-time. A reserve product may contain a single reserve type, or multiple reserve types supplied one following the other (e.g., upward primary + upward secondary + upward tertiary). Producing the reserve products may be performed in parallel since each problem (with distinct weights for the reserve types) is independent from the other problems.

Recall that if tertiary reserve is not restricted by a given maintainability time, we include the variable μ^{tr} in the formulation (see (5.38)) defining the maintainability time. The objective function may include the tertiary reserve maintainability time to be maximized with the tertiary reserve capacity resulting the following objective function:

$$
\begin{aligned}
&\max R - C^{P1} - C^{eh} \\
R &= w^{upr} r^{upr} + w^{dpr} r^{dpr} + w^{usr} r^{ups} + w^{dsr} r^{dsr} + w^{tr} (r^{tr} + \mu^{tr}) \\
C^{P1} &= \sum_{\forall t} \sum_{\forall g} (\tau C_g^{dg} p_{gt}^{dg} + C_g^{su} v_{gt} + C_g^{sd} w_{gt}) \\
&\quad + \tau \sum_{\forall t} (\lambda_t^{en,-} \Delta p_t^{pcc,-} - \lambda_t^{en,+} \Delta p_t^{pcc,+}) \\
C^{eh} &= \Lambda^{sb,T} (\Delta^{sb,-} + \Delta^{sb,+})
\end{aligned}
\tag{5.46}
$$

Notably, in addition to computing the reserve products, this problem also computes the optimal active power set points of the DERs that can be reached within the primary reserve response time δ considering the ramping constraints. We will refer to these set points as $U_{t_1}^{p,*ramp}$. These set points will be used when formulating the RTC problem because they ensure reaching the committed primary capacity within required time.

5.3.1.2 Problem 2: Minimize Operational Cost

The complete formulation of the minimize operational cost problem is shown in (5.47). The objective function includes the operational cost (C^{P2}) which includes DGs fuel, DGs startup/shutdown, and deviation from the DA plan costs. The objective function also includes a penalty term on deviating from the setted end-of-horizon limits (C^{eh}). The constraint set includes the μG mathematical model, the constraints modeling the deviation from the DA plan, the end-of-horizon limits for storage-based DERs, and the end-of-horizon commitment constraints for DGs.

$$
\begin{aligned}
&\min C^{P2} + C^{eh} \\
&C^{P2} = \sum_{\forall t}\sum_{\forall g}(\tau C_g^{dg} p_{gt}^{dg} + C_g^{su} v_{gt} + C_g^{sd} w_{gt}) \\
&\quad + \tau \sum_{\forall t}(\lambda_t^{en,-}\Delta p_t^{pcc,-} - \lambda_t^{en,+}\Delta p_t^{pcc,+}) \\
&C^{eh} = \Lambda^{sb,T}(\Delta^{sb,-} + \Delta^{sb,+}) \\
&s.t. \\
&g_t(X,U) = 0 \qquad \forall t \in \mathcal{T}_c \\
&h_t(X,U) \le 0 \qquad \forall t \in \mathcal{T}_c \\
&p_t^{pcc} = P_t^{comit} + \Delta p_t^{pcc,+} - \Delta p_t^{pcc,-} \qquad \forall t \in \mathcal{T}_c \\
&0 \le \Delta p_t^{pcc,+} \le z_t^{pcc} M^{pcc} \qquad \forall t \in \mathcal{T}_c \\
&0 \le \Delta p_t^{pcc,-} \le (1 - z_t^{pcc}) M^{pcc} \qquad \forall t \in \mathcal{T}_c \\
&\underline{X}^{sb,*}\big|_{t=|\mathcal{T}_c|} - \Delta^{sb,-} \le \underline{X}^{sb}_{|\mathcal{T}_c|} \le \bar{X}^{sb}_{|\mathcal{T}_c|} \le \bar{X}^{sb,*}\big|_{t=|\mathcal{T}_c|} + \Delta^{sb,+} \\
&UT_g^{|\mathcal{T}_c|} = UT_g - UT_g^{0,*} \qquad \forall g \in \mathcal{G} \\
&DT_g^{|\mathcal{T}_c|} = DT_g - DT_g^{0,*} \qquad \forall g \in \mathcal{G} \\
&z_t^{pcc}, x_i, u_j \in \{0,1\} \ \forall i \in B^x, \quad \forall j \in B^u, \quad \forall t \in \mathcal{T}_c
\end{aligned}
\tag{5.47}
$$

Solving the problem above results in the optimal operational cost $C^{P2,*}$ of the μG when no reserves are provided. Subtracting this cost from the operational cost of the μG when reserve is provided (i.e., $C^{P1,*}$ in (5.45)) results in the lost-of-opportunity cost from providing the reserve (lost-of-opportunity cost = $C^{P1,*} - C^{P2,*}$).

If the reserve is requested to be dispatched, the modules in the operations planning and control management system (i.e., DAUC, HAOP, and RTC) are updated to dispatch and maintain the reserve. The formulations of these three problems are given in the following subsection.

5.3.2 Operations Planning and Control Management System: DAUC, HAOP, and RTC Problems

The DAUC problem is formulated as follows:

$$
\begin{aligned}
&\min C^{en} + C^{fdg} + C^{cdg} \\
C^{en} &= \tau \sum_{t \in \mathcal{T}_d} (\lambda_t^{en,-} \Delta p_t^{pcc,-} - \lambda_t^{en,+} \Delta p_t^{pcc,+}) \\
C^{fdg} &= \tau \sum_{t \in \mathcal{T}_d} \sum_{g \in \mathcal{G}} C_g^{dg} p_{gt}^{dg} \\
C^{cdg} &= \sum_{t \in \mathcal{T}_d} \sum_{g \in \mathcal{G}} (C_g^{su} v_{gt} + C_g^{sd} w_{gt}) \\
&s.t. \\
g_t(X,U) &= 0 && \forall t \in \mathcal{T}_d \\
h_t(X,U) &\le 0 && \forall t \in \mathcal{T}_d \\
p_t^{pcc} &= P_t^{comit} + \Delta p_t^{pcc,+} - \Delta p_t^{pcc,-} && \forall t \in \mathcal{T}_d \\
0 \le \Delta p_t^{pcc,+} &\le z_t^{pcc} M^{pcc} && \forall t \in \mathcal{T}_d \\
0 \le \Delta p_t^{pcc,-} &\le (1 - z_t^{pcc}) M^{pcc} && \forall t \in \mathcal{T}_d \\
\underline{H}^{sb} \le \underline{X}^{sb}_{|\mathcal{T}_d|} &\le \bar{X}^{sb}_{|\mathcal{T}_d|} \le \bar{H}^{sb} \\
x_i, u_j, z_t^{pcc} &\in \{0,1\} \ \forall i \in B^x, \quad \forall j \in B^u, && \forall t \in \mathcal{T}_d
\end{aligned}
\tag{5.48}
$$

where the objective function minimizes the cost of deviation from the committed power interchange with the eG (C^{en}), the DGs fuel cost (C^{fdg}), and the DGs startup and shutdown cost (C^{cdg}). Whenever a real-time reserve product is requested from the eG, two updates occur to the DAUC problem: 1) the committed power interchange P_t^{comit} is updated to reflect the reserve being requested, and 2) the deviation costs $\lambda_t^{en,-}$ and $\lambda_t^{en,+}$ during the maintainability time of reserve are modified to represent the penalties for

insufficient reserve supply. It is worth noting that the DAUC problem is typically solved with a time step of 1 hour. Therefore, the DAUC may only be affected by the dispatch of tertiary reserve. The HAOP, on the other hand is affected by the dispatch of tertiary as well as secondary reserves since it has a typical step of 10-15 minutes.

The HAOP problem is formulated as follows:

$$
\begin{aligned}
&\min C^{en} + C^{fdg} + C^{eh} \\
&C^{en} = \tau \sum_{k \in \mathcal{T}_h} (\lambda_k^{en,-} \Delta p_k^{pcc,-} - \lambda_k^{en,+} \Delta p_k^{pcc,+}) \\
&C^{fdg} = \tau \sum_{k \in \mathcal{T}_h} \sum_{g \in \mathcal{G}} C_g^{dg} p_{gk}^{dg} \\
&C^{eh} = \Lambda^{sb,T} (\Delta^{sb,-} + \Delta^{sb,+}) \\
&\qquad\qquad s.t. \\
&g_k(X,U) = 0 \qquad\qquad \forall k \in \mathcal{T}_h \\
&h_k(X,U) \le 0 \qquad\qquad \forall k \in \mathcal{T}_h \\
&p_k^{pcc} = P_k^{comit} + \Delta p_k^{pcc,+} - \Delta p_k^{pcc,-} \qquad \forall k \in \mathcal{T}_h \\
&0 \le \Delta p_k^{pcc,+} \le z_k^{pcc} M^{pcc} \qquad \forall k \in \mathcal{T}_h \\
&0 \le \Delta p_k^{pcc,-} \le (1 - z_k^{pcc}) M^{pcc} \qquad \forall k \in \mathcal{T}_h \\
&U_k^{uc} = U^{uc,*}|_{t=k} \qquad \forall k \in \mathcal{T}_h \\
&\underline{X}^{sb,*}|_{t=|\mathcal{T}_h|} - \Delta^{sb,-} \le \underline{X}_{|\mathcal{T}_h|}^{sb} \le \overline{X}_{|\mathcal{T}_h|}^{sb} \le \overline{X}^{sb,*}|_{t=|\mathcal{T}_h|} + \Delta^{sb,+} \\
&\mathbf{0} \le \Delta^{sb,-}, \Delta^{sb,+} \\
&x_i, u_j, z_t^{pcc} \in \{0,1\} \ \forall i \in B^x, \qquad \forall j \in B^u, \qquad \forall k \in \mathcal{T}_h
\end{aligned}
\tag{5.49}
$$

Similar to the DAUC, the HAOP minimizes the deviation from the committed power interchange with the eG (C^{en}), the DGs fuel cost (C^{fdg}) cost and the deviation from the end-of-horizon limits (C^{eh}). Unlike the DAUC, the HAOP does not optimize the startup

and shutdown of the DERs, and the DGs commitment plan ($U^{uc,*}$) is taken as input form the latest DAUC solution, or the solution of the Maximize Reserve if the latest DAUC solution did not consider the reserve being dispatched. This is because the Maximize Reserve problem performs unit commitment, and it may produce a commitment plan that differs from the latest DAUC problem. Similarly, the HAOP obtains the end-of-horizon limits from the solution of the Maximize Reserve problem if the latest DAUC problem did not consider the reserve being dispatched.

Finally, the RTC problem is formulated as follows:

$$
\begin{aligned}
&\min\ C^{pcc} + C^{haop} + C^{fdg} + C^{vs} \\
&C^{pcc} = \lambda^{pcc}(\delta^{pcc,+} + \delta^{pcc,-}), \qquad C^{haop} = \Lambda^{p,T}(\Delta^{p,+} + \Delta^{p,-}) \\
&C^{fdg} = \sum_{g\in\mathcal{G}} C_g^{dg} p_{gm}^{dg}, \qquad C^{vs} = \lambda^{vs}\left|\left(v_m{}^{pcc,sq}\right) - \left(\mathrm{V}_m^{\text{target}}\right)^2\right| \\
&s.t. \\
&g_m(X,U) = 0 \\
&h_m(X,U) \le 0 \\
&U_m^{uc} = U^{uc,*}|_{t=m} \\
&\Delta^{p,-}, \Delta^{p,+} \ge \mathbf{0} \\
&\delta^{pcc,+} - \delta^{pcc,-} \ge 0 \\
&p_m^{pcc} = P_m^{comit} + \delta^{pcc,+} - \delta^{pcc,-} \\
&x_i, u_j \in \{0,1\}\ \forall i \in B^x, \qquad \forall j \in B^u
\end{aligned}
\tag{5.50}
$$

If no reserve is being called for:

$$U_m^p = U^{p,**}|_{k=m} + \Delta^{p,+} - \Delta^{p,-}$$

If reserve is being ramped to:

$$U_m^p = U_{t_1}^{p,*ramp} + \Delta^{p,+} - \Delta^{p,-}$$

where the objective function includes a penalty term C^{pcc} on deviating from the committed power interchange with the eG. The objective function also includes a penalty term C^{haop} on deviating from a pre-set active power controls. This pre-set active power controls is equal to those set by the HAOP problem $U_k^{p,**}$ except when the reserve is being ramped to. If reserve is being ramped to, the pre-set active power controls are equal to $U_{t_1}^{p,*ramp}$ which were computed when solving the Maximize Reserve problem. This pre-set controls ensure the ability to reach the committed reserve capacity within the committed time. The objective function also includes the fuel cost of the DGs (C^{fdg}), and a penalty term on the deviation of the voltage at the PCC from a target value (C^{vs}). Notably, similar to the HAOP problem, the DGs commitment plan in the RTC problem is taken from the most recent DAUC solution, unless reserve is begin dispatched in which the DGs commitment plan is taken from the solution of the Maximize Reserve problem.

5.4 Summary

This chapter presented the formulation of the μGEMS optimization problems for two service design, the DA Commitment and RT Commitment designs. In each design, we formulated four set of optimization problems that are solved within the proposed μGEMS which are: the *compute optimal commitments* problem, the DAUC problem, the HAOP problem and the RTC problem.

CHAPTER 6. THE SLP SOLUTION METHODOLOGY

6.1 Chapter Overview

The optimization problems formulated in the previous chapter have the form of a mixed-integer quadratically-constrained programming (MIQCP) problem with linear objective functions. We propose solving the problems via penalty successive linear programming (SLP) to achieve computational speed and efficient handling of the binary variables. The SLP methodology is presented in this chapter. Section 6.2 introduces the general form of all problems solved within the μGEMS. Section 6.3 shows the linearized subproblem and section 6.4 illustrates the iterative solution algorithm. Finally, a summary is drawn in section 6.5.

6.2 The General Form of the *μ*GEMS Optimization Problems

The MIQCP problems of the *μ*GEMS can be written as follows:

$$\min J^L(\mathbf{x},\mathbf{z})$$

s.t.

$$\begin{aligned} g^Q(\mathbf{x}) &= 0 \\ h^Q(\mathbf{x}) &\le 0 \\ g^L(\mathbf{x},\mathbf{z}) &= 0 \\ h^L(\mathbf{x},\mathbf{z}) &\le 0 \\ \mathbf{z} &\in \{0,1\}^{|z|} \end{aligned} \tag{6.1}$$

where $J^L(\mathbf{x},\mathbf{z})$ is the linear objective function. $g^Q(.)$ indicates the quadratic equations, and $h^Q(.)$ indicates the quadratic constraints. $g^L(.)$ and $h^L(.)$ indicate the linear equations and linear constraints in the model, respectively. Notably, most of the model equations are linear due to the use of current formulation resulting in linear equations for the network flows. In addition, note that binary variables only appear in the linear equations and constraints where no linearization is needed.

6.3 The Linearized Subproblem

We use first order Taylor expansion to linearize the quadratic equations and constraints. Given an initial operating point $\tilde{\mathbf{x}}^{(u)}$, the linearized mixed-integer linear programming (MILP) problem with penalties at iteration u is formed as follows:

$$\min J^L(\mathbf{x},\mathbf{z}) + (\mathbf{w}^{slp})^T(\mathbf{s}^{g+} + \mathbf{s}^{g-} + \mathbf{s}^h)$$

s.t.

$$\begin{aligned} g^Q(\tilde{\mathbf{x}}^{(u)}) + \nabla g^Q(\tilde{\mathbf{x}}^{(u)})(\mathbf{x} - \tilde{\mathbf{x}}^{(u)}) &= \mathbf{s}^{g+} - \mathbf{s}^{g-} \\ h^Q(\tilde{\mathbf{x}}^{(u)}) + \nabla h^Q(\tilde{\mathbf{x}}^{(u)})(\mathbf{x} - \tilde{\mathbf{x}}^{(u)}) &\le \mathbf{s}^h \\ g^L(\mathbf{x},\mathbf{z}) &= 0 \\ h^L(\mathbf{x},\mathbf{z}) &\le 0 \\ \left|x_i - \tilde{x}_i^{(u)}\right| &\le \Delta_i^{(u)} \quad \forall i \in TR \\ \mathbf{z} &\in \{0,1\}^{|z|} \\ \mathbf{0} &\le \mathbf{s}^{g+}, \mathbf{s}^{g-}, \mathbf{s}^h \end{aligned} \tag{6.2}$$

where $\mathbf{w}^{slp}$ is a penalty vector with non-negative elements and $\mathbf{s}^{(.)}$ are vectors of non-negative slacks used to relax the linearized equations and constraints to avoid infeasibilities when solving the MILP problem. We also include trust region limits in the linearized subproblem to only a subset of variables to avoid over restricting the MILP problem. Specifically, the subset *TR* includes real and imaginary bus voltages ($\{e_{kts}, f_{kts}\ \forall\, k \in \mathcal{K},\ \forall\, t \in \mathcal{T}\ ,\ \forall s \in \mathcal{S}\}$).

6.4 The Iterative Solution Algorithm

Figure 6.1 shows the flow chart of the algorithm of SLP solution methodology. The algorithm starts by initializing the operating point and trust region limits. Since the linearization is only performed on the continuous variables $\mathbf{x}$, only these variables need to be initialized. Upon initializing the operating point, the MIQCP problem in (6.1) is linearized to be in the MILP form shown in (6.2). The resultant MILP problem is then solved and the optimal solution $(\mathbf{x}^{*,(u)}, \mathbf{z}^{*,(u)})$ is retrieved. Next, the error is computed by substituting the continuous variables $\mathbf{x}^{*,(u)}$ in the quadratic equations and constraints of the original MIQCP. The error is computed as follows:

$$err^{(u)} = \max[\left\|g^{Q}(\mathbf{x}^{*,(\boldsymbol{u})}\right\|_{\infty},\ \max_{i}\left(0, h_i^{Q}\left(\boldsymbol{x}^{*,(u)}\right)\right)] \tag{6.3}$$

Notably, there is no need to check for the feasibility of the linear equations and constraints of the MIQCP problem, $g^{L}(.)$ and $h^{L}(.)$, as they are satisfied by default in the MILP problem.

If the error computed in (6.3) is found to be less than a pre-specified tolerance ϵ, the algorithm terminates, and convergence is reported. Otherwise, the iteration number u

is checked and nonconvergence is reported if the iteration number exceeds a pre-defined limit (*Max.Itr*).

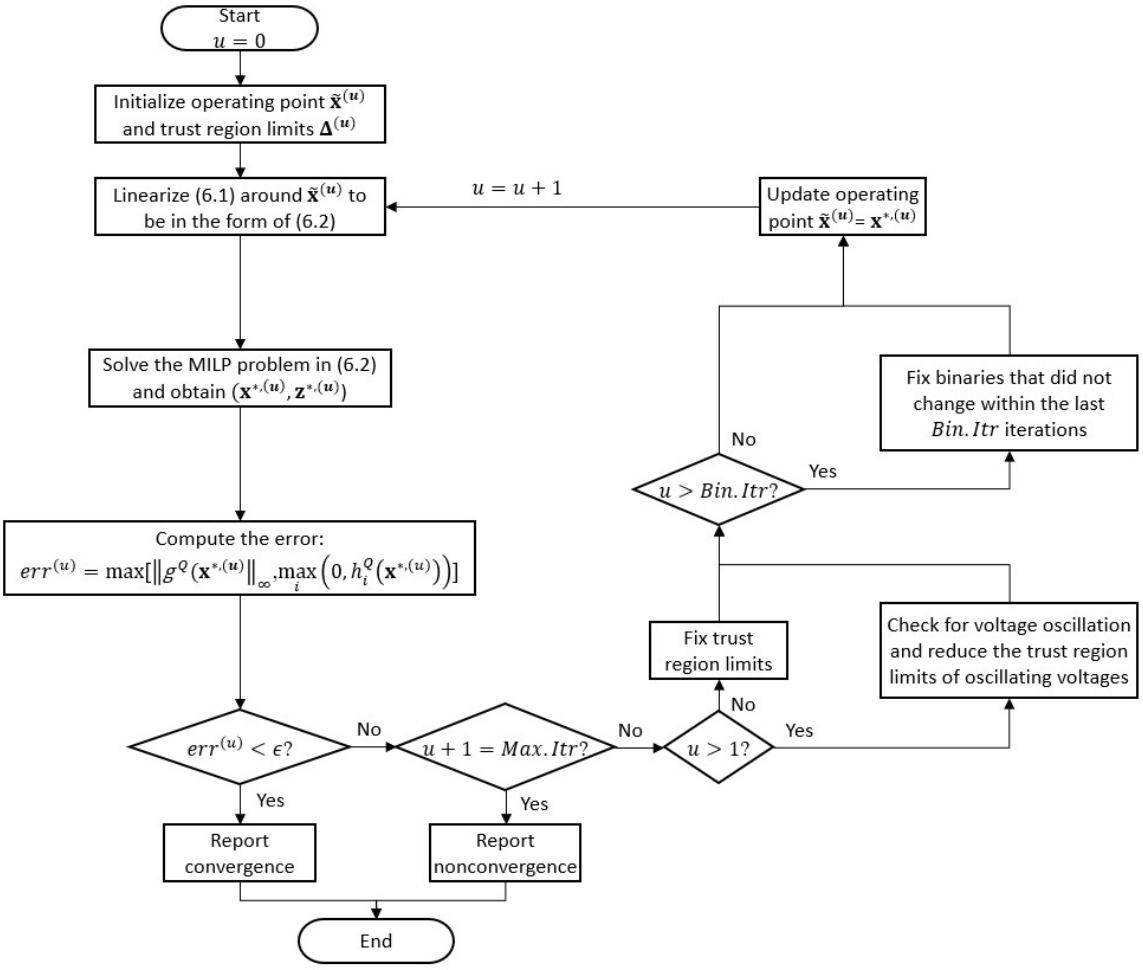

Figure 6.1. The successive linear programming solution algorithm

Under the case where the algorithm does not converge and the maximum iteration number is not reached, we perform two steps before linearizing the problem for the next iteration. The first step checks for oscillating voltages (i.e., a voltage variable bouncing between two close points within consecutive iterations). If a voltage variable was found to oscillate, the trust region limit for that variable is reduced to eliminate oscillation in the

following iterations. Otherwise, the trust region limit is not changed. The following pseudo code illustrates this procedure:

---

for all $i \in TR$:

$\delta_i^1 = x_i^{(u),*} - x_i^{(u-1),*}, \quad \delta_i^2 = x_i^{(u-1),*} - x_i^{(u-2),*}$

if $\delta_i^2 \neq 0$ **and** $\frac{\delta_i^1}{\delta_i^2} < \kappa$: **set** $\Delta_i^{(u+1)} = \xi \Delta_i^{(u)}$

else: set $\Delta_i^{(u+1)} = \Delta_i^{(u)}$

---

where $\kappa < 0$ is a parameter used to detect the oscillation and is set close to -1. A value less than -1 is less restrictive in flagging a variable as oscillating while the revers occurs when $-1 < \kappa < 0$. $\xi \in (0,1)$ is used to reduce the trust region limits of oscillating variables.

Next, and before linearizing for the next iterations, we implement an algorithm of fixing binary variables that did not change within the last pre-defined number of iterations, *Bin.Itr*. This fixing algorithm is performed to reduce the binarity of the MILP problem as the solution method progresses.

After updating the trust region limits and fixing the unchanging binary variables, we update the operating point by setting $\tilde{\mathbf{x}}^{(u)} = \mathbf{x}^{*,(u)}$. The linearization is performed again around the new operating point and the process is repeated until convergence is achieved, or the maximum number of iterations in reached.

Notably, the step of updating the trust region limits is crucial for convergence. Due to the non-linearities in the original MIQCP problem, the optimal value of a variable obtained from the successive MILP problems may oscillate indefinitely around a curvature.

We reduce the trust regions, therefore, when oscillation is detected. Furthermore, we observed that fixing unchanging binary variables result in substantial computational improvements with minimal change in the objective value relative to when binaries are not fixed. Typically, significant changes in the objective function occur only in the first few iterations of the SLP method due to the relatively wide trust region limits which is accompanied with frequent variations in the binaries. As the SLP method progresses and as trust region limits are reduced, we noticed that the objective function and binary variables encounter minimal changes. This may be due to the resultant small feasible space of the problem due to reducing the trust region limits which in turn makes performing discrete changes infeasible. The remaining iterations become merely a process of reducing the error via the continuous variables with minimal changes in the binary variables, which motivated implementing the fix-binary algorithm.

Furthermore, note that we directly use the obtained solution from the linearized subproblem to linearize for the next iteration. Another common method to update the operating point, specifically when solving the optimal power flow problem, is by obtaining the control values from the linearized subproblem and running a power flow. The power flow results are then used as the new point for the next linearization. Running a power flow essentially means satisfying the quadratic equality constraints $g^{Q}(.)$, if the power flow converges. However, solving a power flow may drift the point obtained from the MILP problem and cause violations to the linear inequality constraints $h^{L}(.)$, which were originally satisfied by the MILP problem. Solving a power flow may also alter the optimality direction followed by the SLP method. Therefore, in our implementation of the SLP method, we omit running a power flow in updating the operating point. The power

flow equations are satisfied inherently via the SLP method since the power flow equations are also linearized and included in the MILP problem. Notably, this process of directly using the solution from the linearized problem for the next iteration is the typical process used when solving a nonlinear programming problem via SLP as firstly proposed by Griffith and Stewart in 1961 [74].

6.5 Summary

This chapter presented the proposed solution method for the MIQCP problems of the μGEMS. The solution method is based on penalty SLP. We first showed the general form of the μGEMS optimization problems followed by the form of the linearized subproblem. Then, we illustrated the iterative solution algorithm which linearizes the MIQCP problem in a successive manner. Two update algorithms were introduced, which are performed before linearizing the MIQCP problem for the next iteration: 1) reducing the trust regions of oscillating voltages, and 2) fixing unchanging binary variables.

CHAPTER 7. BENCHMARKING THE SLP SOLUTION METHODOLOGY

7.1 Overview

In this chapter, we benchmark the SLP solution methodology proposed in the previous chapter against three solution methods: 1) the second-order conic programming (SOCP) relaxation approach proposed in [12] (will be referred to as the SOCP method), 2) the quadratic convex (QC) relaxation approach proposed in [13] (will be referred to as the QC method), and 3) Gurobi's global non-convex solver [14]. Both the SOCP and the QC methods are convexification-based solution methods where the non-convexities in the network flow equations are relaxed resulting in a convex quadratically constrained model for the power system (the μG in our case). Upon setting a convex objective function to the model, the optimization problems can be solved directly via efficient convex solvers. If these methods converge, the obtained objective values resemble lower bounds for the global optimal solution in the case of minimization problems. An upper bound is achieved for maximization problems. Therefore, benchmarking the SLP method with such convexification-based methods provides insights on the optimality of the solutions obtained via the SLP. Moreover, when solving the problems via Gurobi's global solver, we input the problems directly to the solver without linearization or convexification. Gurobi uses branch and bound techniques to provide the global optimal solution within a given tolerance. In principle, comparing the SLP method with only Gurobi's global solver would be sufficient to measure the optimality of the SLP method. However, we utilize the SOCP and the QC methods because Gurobi's global solver fails to provide solutions for relatively

large problems (it either outputs infeasibility flags even though the problem is feasible, or consumes significant amount of time without convergence). In addition, by comparing the computational times of the SLP method with those of the SOCP and the QC methods, we may obtain a comparative measure for the speed of the SLP method.

The μG model we presented in chapter 4 was based on the current formulation. In contrast, the SCOP and the QC methods model the network flow equations using the power balance formulation. The SOCP method uses the rectangular coordinates while the QC method uses the polar coordinates. Then, each method relaxes the non-convex equations via different techniques. The complete relaxed models of the μG for the SOCP and the QC methods are illustrated in Appendix A.

The remaining parts of the chapter are organized as follows: section 7.2 introduces the μG test systems used in the benchmark, section 7.3 illustrates the case studies and the benchmark criteria, section 7.4 presents the benchmark results, and finally, section 7.5 provides a summary of analysis and findings.

7.2 The Test Systems

The systems used to perform the benchmark analysis are adapted from MATPOWER's distributions test cases with modifications [75]. These include a 33-bus, a 69-bus, an 85-bus, and a 141-bus systems. For each test system, we connect multiple controllable DERs including four DGs, four ESS, and 31 homes each with a controllable DUL and a controllable TCL. The 33-bus system after modification is depicted in Figure 7.1.

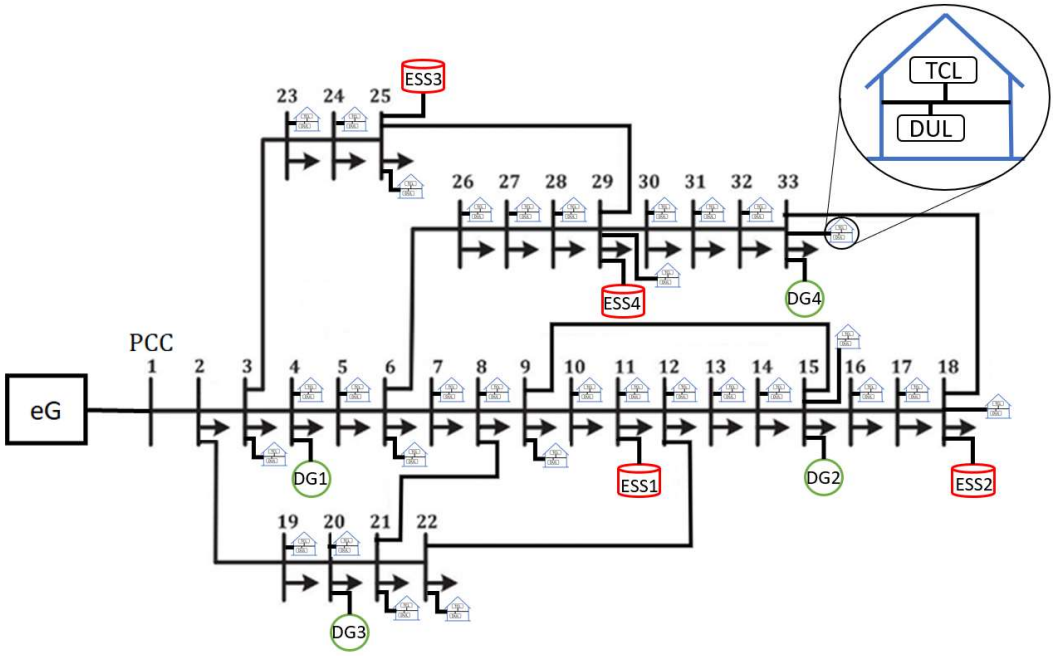

Figure 7.1 The 33-bus test system

Notably, the 33-bus system is the only meshed system. All other test systems are radial. We also utilize a fifth small-case test system consisting of busses 1 to18 of the 33-bus system (see Figure 7.2)

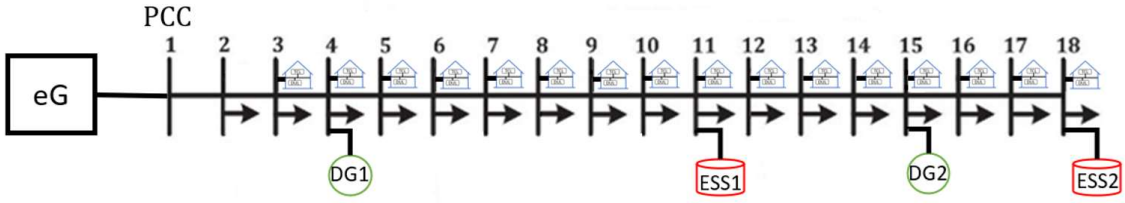

Figure 7.2 The 18-bus test system

The parameters of the DERs and their connection location are listed in Table 7.1 through Table 7.5Table 7.6. Identical DERs' parameters and connection locations are used for all test systems. Regarding network constraints, the original MATPOWER test systems only included bus voltage limits with no circuit current limits or power factor limits at the PCC with the eG. Therefore, we use assumed circuit limits and power factor limits; the network constraints are shown in Table 7.6.

Table 7.1 The parameters of the DGs

DG No.	Location	$\bar{P}_g^{dg}$ (kW)	$\underline{P}_g^{dg}$ (kW)	$\bar{Q}_g^{dg}$ (kVar)	$\underline{Q}_g^{dg}$ (kVar)	R_g^{dg} (kW/min)	DT_g (hrs)	UT_g (hrs)
1	B4	1,000	50	500	-500	200	2	2
2	B15	750	37.5	375	-375	150	2	2
3	B20	500	25	250	-250	100	2	2
4	B33	250	12.5	125	-125	50	2	2

Table 7.2 The operational, startup, and shutdown costs of the DGs

DG No.	C_g^{dg} (\$/kWh)	C_g^{su} (\$)	C_g^{sd} (\$)
1	0.15	15	10
2	0.25	12	8
3	0.35	10	6
4	0.45	8	4

Table 7.3 The parameters of the ESSs

ESS No.	Location	SOC_e^0 (kWh)	$\underline{SOC}_e$ (kWh)	$\overline{SOC}_e$ (kWh)	$\bar{P}_e^{ess}$ (kW)	$\bar{Q}_e^{ess}$ (kVar)	$\underline{Q}_e^{ess}$ (kVar)	η_e	$\underline{H}_e^{ess}$ (kWh)	$\overline{H}_e^{ess}$ (kWh)
1	B11	1,500	0	3,000	1,000	500	-500	0.95	1,500	3,000
2	B18	1,125	0	2,250	750	375	-375	0.95	1,125	2,250
3	B25	750	0	1,500	500	250	-250	0.95	750	1,500
4	B29	375	0	750	250	125	-125	0.95	375	750

Table 7.4 The parameters of the TCLs

TCL* class	Locations	P_d^{tcl} (kW)	Q_d^{tcl} (kW)	C_d^{tcl} (1/h)	A_d^{tcl} (℃/h)	Θ_e^0 (℃)	$\underline{\Theta}_d$ (℃)	$\overline{\Theta}_d$ (℃)	$\underline{H}_d^{tcl}$ (℃)	$\overline{H}_d^{tcl}$ (℃)
1	B3-B10	6	3	0.06	1.75	23	21	25	22	24
2	B11-B18	5.5	2.75	0.04	2.25	24	22	26	23	25
3	B19-B26	5	2.5	0.03	2.5	24	22	26	23	25
4	B27-B33	4.5	2.25	0.05	2	23	21	25	22	24

*All TCLs are assumed to have a continuous switching ranging from 0 to the rated value.

Table 7.5 The parameters of the DULs

DUL class	Locations	P_d^{dul} (kW)	Q_d^{dul} (kW)	t_d^{min} (hr. of the day)	t_d^{max} (hr. of the day)	ρ_d^{dul} (hrs.)
1	B3-B10	6	3	6	12	2
2	B11-B18	5.5	2.75	6	12	3
3	B19-B26	5	2.5	13	19	2
4	B27-B33	4.5	2.25	13	19	3

Table 7.6 Network constraints

PCC Power Factor	$\underline{V}_k$	$\bar{V}_k$	$\bar{I}_{km}{}^*$
0.95 lag – 0.95 lead	0.9p.u.	1.1p.u.	$15 \times \max(I_{km}, I_{mk})$

*I_{km} and I_{mk} are the magnitudes of the circuit currents obtained from the power flow solution of the original MATPOWER system.

We multiply the nominal load values of the systems' by the normalized hourly net-demand profiles in [76] to extract hourly profiles for each load point. The total uncontrollable PQ net-demand of all test systems at a particular day (August 5th, 2017) are shown in Figure 7.3 through Figure 7.7. Further, the hourly energy cost at the PCC is adapted from [77] and shown in Figure 7.8. We assume in the case studies equal prices for energy imports and exports. Reserve and regulation capacity compensations are taken to be half of the energy cost. The ambient temperature is collected from the System Advisory Model (SAM) of the National Renewable Energy Laboratory (NREL) [78] and is shown in Figure 7.9. Finally, the eG Thevenin-equivalent parameters are taken from [76] with an assumed voltage of 1p.u. unless otherwise indicated in the case studies.

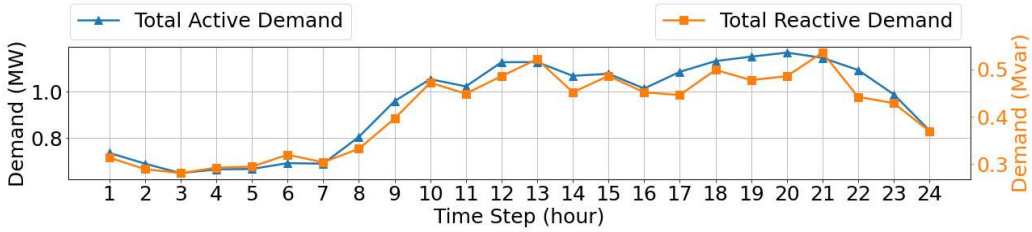

Figure 7.3.Total active and reactive demand of the 18-bus system

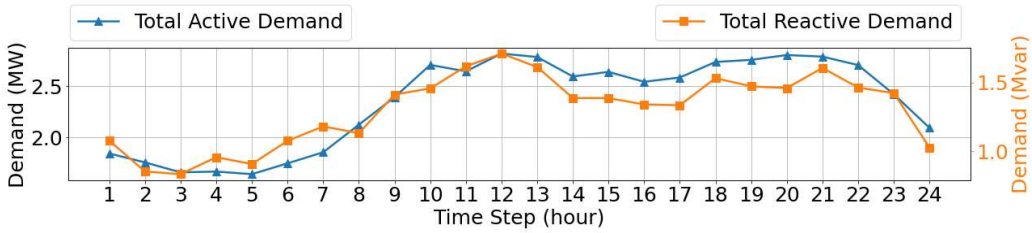

Figure 7.4.Total active and reactive demand of the 33-bus system

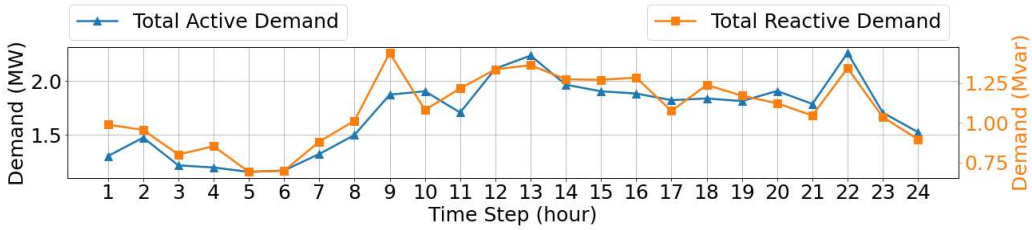

Figure 7.5.Total active and reactive demand of the 69-bus system

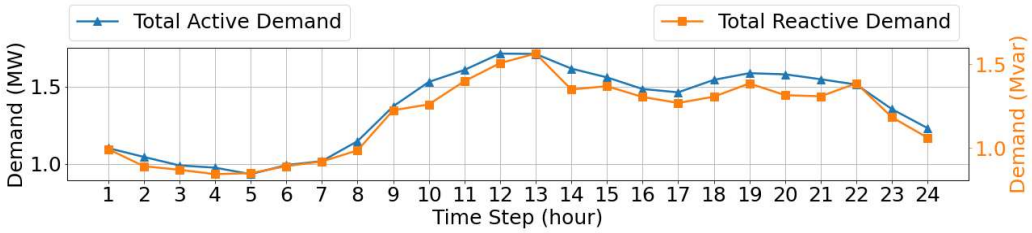

Figure 7.6.Total active and reactive demand of the 85-bus system

Figure 7.7.Total active and reactive demand of the 141-bus system

Figure 7.8. Energy cost at the PCC

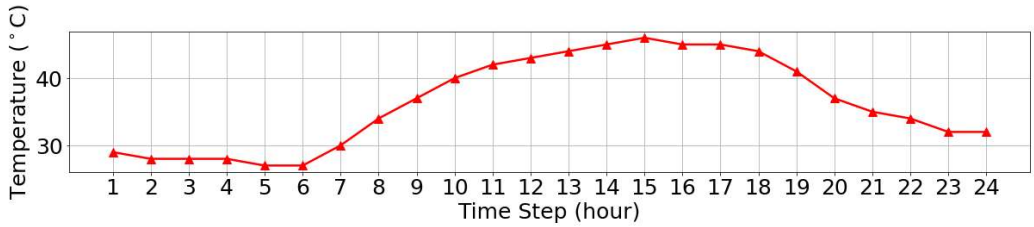

Figure 7.9. Ambient temperature

7.3 Case Studies and Benchmark Criteria

We perform three main case studies that differ in terms of the operational objective of the μG:

Case 1-Cost Minimization: The operational objective is to minimize the total operational cost of the system across a multi-period horizon. This problem is essentially a classical multi-period optimal power flow problem with unit commitment. The formulation of the

problem is shown in section 5.2.1. No services are considered in this case. Therefore, the problem is a single-case, multi-period optimization problem.

Case 2-Voltage Support: The operational objective of the μG in this case is to provide voltage support to the eG by minimizing the voltage deviation at the PCC from a target value. The problem in this case is a single-case, single-period optimization problem and is formulated in (5.50). Notably, the objective function formulated in (5.50) contains multiple weighted priority objectives. In this case study, we assume that the sole objective function is to minimize the voltage deviation with a scaling factor $\lambda^{vs} = 10$. Moreover, we run two sub-cases: case 2(a) with the eG equivalent voltage less than the target, and case 2(b) with the eG equivalent voltage greater than the target. This is to simulate the process of needing to inject reactive power (capacitive mode in case 2(a)) and absorbing reactive power (inductive mode in case 2(b)). The target voltage is set to 1p.u. and the eG equivalent voltage for case 2(a) is assumed to be 0.98 p.u. and for case 2(b) it is assumed to be 1.02 p.u..

Case 3-Energy, Reserve, and Regulation Scheduling: The operational objective in this case is to maximize the expected profits (or equivalently minimize cost) from scheduling energy, reserve, and regulation capacities. The problem is formulated in section 5.2.1. This problem is the most extensive problem in the μGEMS as it is formulated as a multi-case, multi-period optimization problem with added binaries to model the reserve and regulation commitment rules.

For each solution method, we report the objective function value from the optimization problem and the computational time. In addition, we report the maximum bus

voltage violation in p.u., the maximum circuit overloading in % (i.e., 100×violation/limit), and the maximum power factor violation. As indicated in Table 7.6, the power factor limits are taken to be 0.95 lag to 0.95 lead. For a given case at a given time period, the violation is calculated as $\max\left(0, 0.95 - \left|\frac{p}{\sqrt{p^2+q^2}}\right|\right)$ where p and q are the active and reactive power injected to the eG at the PCC. Notably, the convexification-based solution methods may result in physically unrealizable solutions where the obtained controls and states from the optimization problem are inconsistent. The same may occur in the SLP method under no convergence. To retrieve physically realizable solutions and to have a unified violations comparison for all methods, we use the controls obtained from the optimization methods to run a power flow. Then, the resultant states from the power flow are used to compute the bus voltage violations, circuit overloading, and power factor violations. In the power flow, we consider the eG equivalent voltage bus as the slack bus and all other busses as PQ buses. Notably, multiple methods exist on how to retrieve physically realizable solutions (see [79]) and this area is under active research. We use the power flow method for its simplicity. Further, in our analysis, we report the objective function value of the original problem using the controls obtained from the optimization methods. This objective function value represents the realized cost if the controls obtained from the optimization method were directly implemented to the μG. Intuitively, the discrepancy between the objective value of the optimization problem and the objective value computed directly from the controls gives an indication about the bus mismatches in the optimization results that were absorbed by the slack bus in the power flow solution.

7.4 Benchmark Results

The parameters of the SLP method are set as ($\mathbf{w}^{slp}$ =1000, κ =-0.8, ξ =1/3, $Bin.Iter$ =3, ϵ =1e-6, $Max.Iter = 100$). Notably, it is imposable to fine-tune these parameters for each individual case without affecting the results of the other cases. Therefore, we use these default parameters for all cases. The SLP method is also dependent on the initialization of the operating point and the trust region limits. Evidently, a high-quality initial operating point would result in a better performance for the SLP. Nonetheless, in the benchmark analysis, we assume the absence of a good initial point and use a flat start voltage profile ($e = 1, f = 0$) for all cases with the initial trust region limits set to 0.1.

Gurobi solver 9.1.0 [14] is used to solve the MILP subproblems in the SLP method, as well as the convex MIQCP problems in the SOCP and the QC methods. Default Gurobi's optimization settings are used across all methods including a MIP gap of 1e-4 and constraint feasibility tolerance of 1e-6. For the interface with Gurobi, we use the Python API on a personal laptop with Intel Core i7 processor and a clock speed of 2.60GHz.

The optimal objective function values for all cases are shown in Table 7.7. The considered hourly time periods starting from hour 1 of the simulated day for each case are also shown in the table. For consistency, all cases are solved as minimization problems. Further, Table 7.7 reports two percentage optimality gaps: Gap1 is defined as $100 \times \frac{SLP^* - \max(SOCP^*, QC^*)}{|SLP^*|}$ where SLP^*, $SOCP^*$, and QC^* are the optimal objective values

from the SLP, the SOCP, and the QC methods, respectively, and Gap2 is defined as $100 \times \frac{SLP^* - GRB^*}{|SLP^*|}$ where GRB^* is the optimal objective value from Gurobi's global solver.

Table 7.7 Optimal objective function values

Case	Test System	Time periods	SOCP	QC	Gurobi's Global Solver	SLP	Gap1	Gap2
1 (k$)	18-bus	1	0.0911	0.0914	0.0918	0.0919	0.54	0.11
	33-bus	24	10.1650	10.1834	NA	10.2083	0.24	NA
	69-bus	12	2.6524	2.7187	NA	2.7258	0.26	NA
	85-bus	12	1.9903	2.0132	NA	2.0188	0.28	NA
	141-bus	6	4.8031	4.9415	NA	4.9455	0.08	NA
2(a) (p.u.)	18-bus	1	0.3625	0.3625	0.3625	0.3625	0.00	0.00
	33-bus	1	0.3742	0.3743	NA	0.3744	0.03	NA
	69-bus	1	0.2293	0.3571	NA	0.3573	0.06	NA
	85-bus	1	0.3499	0.3500	NA	0.3501	0.03	NA
	141-bus	1	0.4042	0.4262	NA	0.4265	0.07	NA
2(b) (p.u.)	18-bus	1	0	0	0.3704	0.3718	100.00	0.38
	33-bus	1	0	0	NA	0.2487	100.00	NA
	69-bus	1	0	0	NA	0.2659	100.00	NA
	85-bus	1	0	0	NA	0.2701	100.00	NA
	141-bus	1	0	0	NA	0.1589	100.00	NA
3 (k$)	18-bus	1	-0.5013	-0.4366	-0.1026*	-0.1022	327.20	0.39
	33-bus	12	-2.3874	-2.3759	NA	0.9489	350.38	NA
	69-bus	6	-2.4793	-2.4392	NA	-0.5051	382.91	NA
	85-bus	6	-2.3911	-2.3785	NA	-0.8279	187.29	NA
	141-bus	3	-5.5928	0.3171	NA	1.5682	79.78	NA

*The constraint feasibility tolerance of Gurobi's global solver under this case was set to 1e-4 because the global solver did not converge when the tolerance is set to less than 1e-4.
NA: Gurobi's global solver either reports infeasibility or fails to converge within 6 hours.

Among all cases with available global solution from Gurobi, the SLP method provided optimal solutions with a maximum optimality gap of 0.39%. Moreover, in cases 1 and 2(a) when no global solution is available from Gurobi, the SLP method provided optimal solutions with a maximum gap of 0.28% relative to the best lower bound from the SOCP and the QC methods. As for cases 2(b) and 3, the computed gaps of the SLP relative to the best lower bound from the SOCP and the QC methods were significantly large. Nevertheless, observe that the objective values of both the SOCP and the QC methods

specifically in cases 2(b) and 3 were far away from Gurobi's global optimal solution; the relaxation models of the SOCP and the QC were weak in these cases. Hence, it is difficult to interpret a meaningful SLP gap relative to the SOCP and the QC method for cases 2(b) and 3.

What differentiate cases 2(b) and 3 from the other cases is that their operational objective functions do not align with minimizing the losses of the system. In case 2(b), the overvoltage occurrence in the eG relative to the target voltage at the PCC incentivizes increasing the losses of the system to reduce the voltage. Similarly, in case 3, the provision of regulation-down incentivizes increasing the losses of the system to increase the resultant regulation-down capacity. Both the SOCP and the QC relaxed models are specifically effective and "tight" only when system losses are directly or indirectly minimized. This can be seen from cases 1 and 2(a) where the lower bounds from the SOCP and the QC methods were close to the global optimal objective value from Gurobi's global solver. Case 1 solely minimizes the operational cost of the system which aligns with minimizing the losses to reduce the total needed generation. Further, in case 2(a), the undervoltage of the eG also incentives minimizing the losses of the system to be able to deliver more reactive power to the PCC and elevate the voltage to the target value. We provide a detailed discussion in section 3 of Appendix A as to why this dependency on loss minimization occur in the SOCP and the QC methods.

Table 7.8 shows the computational times in seconds for all solution methods. For the largest test-system (the 141-bus system), the computational time of the SLP significantly outperformed the SOCP and the QC methods indicating that the SLP scales better than the SOCP and the QC methods. Further, the average computational time across

all cases was 74.09, 283.52, and 55,45 seconds for the SOCP, the QC, and the SLP methods, respectively. Note that Gurobi's global solver reported the slowest computational times among all methods.

Table 7.8 Computational times in seconds

Case	Test System	Time periods	SOCP	QC	Gurobi's Global Solver	SLP
1	18-bus	1	0.17	0.11	0.54	0.08
	33-bus	24	41.00	21.86	NA	81.49
	69-bus	12	30.05	48.07	NA	24.22
	85-bus	12	17.20	84.92	NA	35.11
	141-bus	6	30.13	45.37	NA	9.96
2(a)	18-bus	1	0.12	0.22	0.59	0.08
	33-bus	1	0.28	1.27	NA	0.10
	69-bus	1	1.90	1.77	NA	0.19
	85-bus	1	0.99	2.37	NA	0.25
	141-bus	1	1.47	2.11	NA	0.33
2(b)	18-bus	1	0.02	0.07	0.546	0.15
	33-bus	1	0.05	0.24	NA	0.12
	69-bus	1	0.20	1.33	NA	0.44
	85-bus	1	0.13	0.41	NA	0.27
	141-bus	1	3.43	3.95	NA	0.36
3	18-bus	1	0.38	2.03	2.88	0.32
	33-bus	12	502.87	134.66	NA	628.62
	69-bus	6	266.70	977.96	NA	141.86
	85-bus	6	70.78	3505.03	NA	170.10
	141-bus	3	513.89	836.60	NA	14.94
Average			74.09	283.52	NA	55.45

NA: Gurobi's global solver either reports infeasibility or fails to converge within 6 hours.

No bus voltage violations were recorded in any of the cases for all methods. However, circuit limits and power factor limits violations were observed specifically in the SOCP and the QC methods. The maximum circuit limit violations and maximum power factor violations are shown in Table 7.9 and Table 7.10, respectively. As expected, the SLP and Gurobi's solver reported no violations since no approximations are involved in the model. In contrast, multiple violations were recorded under the SOCP and QC methods.

The violations are more significant in cases 2 and 3a. These are the same cases where the relaxation models of the SOCP and the QC were weak.

Table 7.9 Maximum circuit overloading (%)

Case	Test System	Time periods	SOCP	QC	Gurobi's Global Solver	SLP
1	18-bus	1	0	0.0	0.0	0.0
	33-bus	24	12.2	13.2	NA	0.0
	69-bus	12	0.0	0.0	NA	0.0
	85-bus	12	0.0	0.0	NA	0.0
	141-bus	6	0.0	0.0	NA	0.0
2(a)	18-bus	1	0.0	0.0	0.0	0.0
	33-bus	1	0.0	0.0	NA	0.0
	69-bus	1	0.0	0.0	NA	0.0
	85-bus	1	0.0	0.0	NA	0.0
	141-bus	1	0.0	0.0	NA	0.0
2(b)	18-bus	1	0.0	8.5	0.0	0.0
	33-bus	1	0.0	0.0	NA	0.0
	69-bus	1	0.0	0.0	NA	0.0
	85-bus	1	0.0	0.0	NA	0.0
	141-bus	1	0.0	0.0	NA	0.0
3	18-bus	1	0.0	0.0	0.0	0.0
	33-bus	12	21.1	14.7	NA	0.0
	69-bus	6	0.0	0.0	NA	0.0
	85-bus	6	0.0	0.0	NA	0.0
	141-bus	3	0.0	0.0	NA	0.0

NA: Gurobi's global solver either reports infeasibility or fails to converge within 6 hours.

Table 7.10 Maximum power factor violations (1)

Case	Test System	Time periods	SOCP	QC	Gurobi's Global Solver	SLP
1	18-bus	1	0.00	0.00	0.00	0.00
	33-bus	24	0.00	0.00	NA	0.00
	69-bus	12	0.21	0.00	NA	0.00
	85-bus	12	0.37	0.00	NA	0.00
	141-bus	6	0.05	0.00	NA	0.00
2(a)	18-bus	1	0.00	0.00	0.00	0.00
	33-bus	1	0.00	0.00	NA	0.00
	69-bus	1	0.69	0.00	NA	0.00
	85-bus	1	0.00	0.00	NA	0.00
	141-bus	1	0.02	0.00	NA	0.00
2(b)	18-bus	1	0.84	0.87	0.00	0.00
	33-bus	1	0.00	0.57	NA	0.00
	69-bus	1	0.15	0.09	NA	0.00
	85-bus	1	0.61	0.05	NA	0.00
	141-bus	1	0.00	0.00	NA	0.00
3	18-bus	1	0.81	0.27	0.00	0.00
	33-bus	12	0.93	0.93	NA	0.00
	69-bus	6	0.71	0.85	NA	0.00
	85-bus	6	0.88	0.948	NA	0.00
	141-bus	3	0.11	0.00	NA	0.00

NA: Gurobi's global solver either reports infeasibility or fails to converge within 6 hours.

Finally, Table 7.11 reports the objective function value obtained from the controls of the optimization methods (i.e., by solving a power flow problem using the controls). The values between parentheses in the cells of Table 7.11 represent the percentage relative difference between the computed objective function value (z^{PF}) and the objective function value reported by the optimization methods (z^*) defined as $100 \times \frac{z^{PF}-z^*}{|z^{PF}|}$. Gurobi's global solver and the SLP method had negligible differences under all cases as no approximations were involved in the μG model. The SOCP and the QC methods had low differences in the majority of cases 1 and 2(a) (i.e., cases where system losses are indirectly minimized in the objective function). In contrast, substantially large differences were reported for cases 2(b) and 3. The large differences indicate significant bus mismatches in the optimization

problems that were absorbed by the slack bus causing the increase in the realized objective function value. The large differences and bus mismatches in cases 2(b) and 3 echo our reasoning about the weakness of the SOCP and QC relaxation models when the objective function does not align with minimizing the system losses.

Table 7.11 The objective function value of the original problem computed using the controls obtained from the optimization methods

Case	Test System	Time periods	SOCP	QC	Gurobi's Global Solver	SLP
1	18-bus	1	0.0915 (0.44%)	0.0914 (0.00%)	0.0918 (0.00%)	0.0919 (0.00%)
	33-bus	24	10.1874 (0.22%)	10.1852 (0.02%)	NA	10.2083 (0.00%)
	69-bus	12	2.7206 (2.51%)	2.7187 (0.00%)	NA	2.7258 (0.00%)
	85-bus	12	2.0143 (1.19%)	2.0132 (0.00%)	NA	2.0188 (0.00%)
	141-bus	6	4.9437 (2.84%)	4.9415 (0.00%)	NA	4.9455 (0.00%)
2(a)	18-bus	1	0.3625 (0.00%)	0.3625 (0.00%)	0.3625 (0.00%)	0.3625 (0.00%)
	33-bus	1	0.3744 (0.05%)	0.3743 (0.00%)	NA	0.3744 (0.00%)
	69-bus	1	0.5286 (56.62%)	0.3571 (0.00%)	NA	0.3573 (0.00%)
	85-bus	1	0.3501 (0.06%)	0.3500 (0.00%)	NA	0.3501 (0.00%)
	141-bus	1	0.4692 (13.85%)	0.4265 (0.07%)	NA	0.4265 (0.00%)
2(b)	18-bus	1	0.4380 (100.0%)	0.4265 (100.0%)	0.3704 (0.00%)	0.3718 (0.00%)
	33-bus	1	0.3741 (100.0%)	0.4469 (100.00%)	NA	0.2487 (0.00%)
	69-bus	1	0.4229 (100.0%)	0.4104 (100.0%)	NA	0.2659 (0.00%)
	85-bus	1	0.4523 (100.0%)	0.4469 (100.0%)	NA	0.2701 (0.00%)
	141-bus	1	0.3095 (100.0%)	0.1976 (100.0%)	NA	0.1589 (0.00%)
3	18-bus	1	-0.0600 (735.5%)	-0.0843 (417.9%)	-0.1024 (0.20%)	-0.1022 (0.00%)
	33-bus	12	1.3239 (289.33%)	1.2494 (290.2%)	NA	0.9482 (-0.07%)
	69-bus	6	-0.1179 (2002.9%)	-0.1369 (1681.7%)	NA	-0.5051 (0.00%)
	85-bus	6	-0.4600 (419.8%)	-0.4762 (399.5%)	NA	-0.8279 (0.00%)
	141-bus	3	2.8965 (293.1%)	1.5692 (79.8%)	NA	1.5682 (0.00%)

NA: Gurobi's global solver either reports infeasibility or fails to converge within 6 hours.

7.5 Summary

In this chapter, we presented a benchmark analysis for the SLP method against two convexification-based methods: the SOCP method proposed in [12], and the QC method proposed in [13]. In addition, the small cases were also solved using Gurobi's global non-convex solver [14]. For the cases with available global optimal solution, the SLP solution method provided optimal solutions with a maximum optimality gap of 0.39%. In cases 1 and 2(a), the maximum optimality gap between the SLP solution and the best lower bound from the convexification methods were 0.54% and 0.07%, respectively. As for cases 2(b) and 3, it is difficult to obtain meaningful optimality gaps of the SLP relative to the convexification methods. This is because it was shown that both the SOCP and the QC methods provided low quality bounds for these cases.

It is important to note that the SLP method has no optimality guarantees. However, from the tested cases, it seems that the SLP is able to achieve near global solutions. We noticed that this ability of achieving near global solutions highly depends on the initial trust region limits. While small trust regions result in less errors from linearization and faster convergence, it typically renders the obtained solution far away from the global one. For that reason, we selected the initial trust region limits in all cases of this chapter to be 0.1, which is relatively high.

The computational times of the SLP method were generally faster than those of the SOCP and the QC methods. This is especially evident under the largest test system (i.e. the 141-bus system). On average, the SLP method was 25.16% and 80.44% faster than the SOCP and the QC methods, respectively. One should note that these timing results and

comparisons are only indicative and not definitive due to the following reasons: 1) the SOCP and the QC methods may require further computational time to retrieve feasible solutions as those reported in many cases were physically unrealizable, 2) the SLP method may require less computational time if good initial points are provided. In our analysis, we used a flat start initial point which is typically considered a low-quality start, and 3) increasing the tolerance of the MIP gap may significantly reduce the computational time for all solution methods as a low tolerance of 0.0001 was selected in all cases of this chapter.

CHAPTER 8. CURRENT VS POWER BALANCE FORMULATION: A COMPARISON CASE STUDY

8.1 Overview

The mathematical model of the μG can be expressed using the polar or the rectangular coordinates of bus voltages. The polar coordinates result in a model containing trigonometric functions while the rectangular coordinates result in a model consisting of only linear and quadratic equations; using the rectangular coordinates gives a less complex model since trigonometric functions are absent. Moreover, under the rectangular coordinates, one may enforce the bus balance equations by summing up the power injections or the current injections of connected devices at each bus (i.e., power balance or current formulations). The widely used formulation in the literature is the power balance formulation. In this thesis, however, we used the current formulation to model the μG arguing that this formulation is more efficient. The goal of this chapter is to compare the power balance formulation and the current formulation to support our argument. The μG mathematical model under the power balance formulation is shown in Appendix B. We perform the comparison analysis by optimizing the operation of multiple μG systems once using the power balance formulation and once using the current formulation. We report the computational times, the objective function values, and the gaps of these values relative to a global lower bound obtained by solving the problems using the QC method given in Appendix A.2. The case studies and results are presented in section 8.2 and a summary of the findings is drawn in section 8.3.

8.2 Case Studies and Results

Four test systems are used in the analysis. These systems are identical to those presented in section 7.2 and are the 33-bus, the 69-bus, the 85-bus, and the 141-bus systems. The problem that is solved under the two formulations is the multi-period optimal power flow problem with unit commitment. The problem formulation is given in section 5.2.1 with no services provision.

The SLP solution method presented in chapter 6 is used to solve all cases with identical SLP parameters set to ($\mathbf{w}^{slp}$ =1000, κ =-0.8, ξ =1/3, $Bin.Iter$ =3, ϵ =1e-6, $Max.Iter = 100$). A flat start voltage profile ($e = 1, f = 0$) is used with the initial trust region limits set to 0.1. Gurobi solver 9.1.0 [14] is used to solve the MILP subproblems in the SLP method. Default Gurobi's optimization settings were used across all cases including a MIP gap of 1e-4 and constraint feasibility tolerance of 1e-6. For the interface with Gurobi, we use the Python API on a personal laptop with Intel Core i7 processor and a clock speed of 2.60GHz.

Table 8.1 shows the objective function values, optimality gaps, and computational times under the power balance formulation and the current formulation. The optimality gap is computed as $100 \times \frac{SLP_i^* - QC^*}{|SLP_i^*|}$ where SLP_i^* is the optimal cost of the SLP using the corresponding formulation i (power balance or current formulation). QC^* is the optimal lower bound obtained from solving the cases via the QC method. The obtained optimal costs under the two formulations are close and are all near the global optimum with a maximum gap of 0.76% in the power balance formulation and 0.86% in the current formulation. One average, the optimality gaps of the power and current formulations are

0.25% and 0.26%, respectively. The current formulation outperformed the power balance formulation in most of the cases in terms of the computational time with an average of 49.16 seconds compared to 86.01 seconds in the power balance formulation. Additionally, note that the computational time differences between the two methods generally increases for large cases. Compared to the power balance formulation, the current formulation was 30%, 17%, 29% and 58% faster on average for the 33-bus, 69-bus, 85-bus, and 141-bus systems, respectively, indicating a better gained efficiency as the system size increases. Recall that the 33-bus system is the only meshed system and that may caused the relatively high gained speed in this system (i.e., 30%). Moreover, note that under the power balance formulation, the SLP method failed to converge within 100 iteration in case 69-bus (T=18), while the current formulation did converge.

Table 8.1 Optimal costs and computational times

Test System	Time periods	Power Balance Formulation			Current Formulation		
		Cost (k$)	Gap (%)	Time (sec)	Cost (k$)	Gap (%)	Time (sec)
33-bus	6	1.8975	0.30	3.67	1.8972	0.28	3.50
	12	4.1054	0.25	16.85	4.1029	0.19	17.32
	18	7.1925	0.23	55.61	7.1868	0.15	38.03
	24	10.2178	0.34	122.99	10.2083	0.24	81.49
69-bus	6	1.2666	0.17	8.99	1.2658	0.11	7.69
	12	2.7231	0.16	32.67	2.7258	0.26	24.22
	18	NA	NA	NA	4.8722	0.31	49.16
	24	6.4946	0.12	68.03	6.4921	0.08	59.63
85-bus	6	0.9514	0.34	12.21	0.9512	0.32	6.80
	12	2.0203	0.35	44.25	2.0188	0.28	35.11
	18	3.6611	0.42	83.08	3.6704	0.67	66.47
	24	4.5748	0.76	180.44	4.5792	0.86	117.26
141-bus	6	4.9422	0.01	16.57	4.9455	0.08	9.96
	12	10.6405	0.15	71.55	10.6420	0.17	50.97
	18	18.4148	0.10	181.30	18.4075	0.06	94.02
	24	28.3315	0.10	391.99	28.3295	0.09	124.89
Average*		7.1623	0.25	86.01	7.1615	0.26	49.16

NA: The power balance formulation did not converge within 100 iterations in this case.
*Average values exclude case 69-bus-T=18 for both formulations as the power balance formulation did not converge in this case.

To provide a more in-depth comparison about the convergence and time of the SLP method under the two formulations, Figure 8.1 shows the convergence of the SLP method for the current and the power balance formulations. The left axis of each figure indicates the error convergence and the right axis indicate the computational time per SLP iteration. The x-axis is the SLP iteration number.

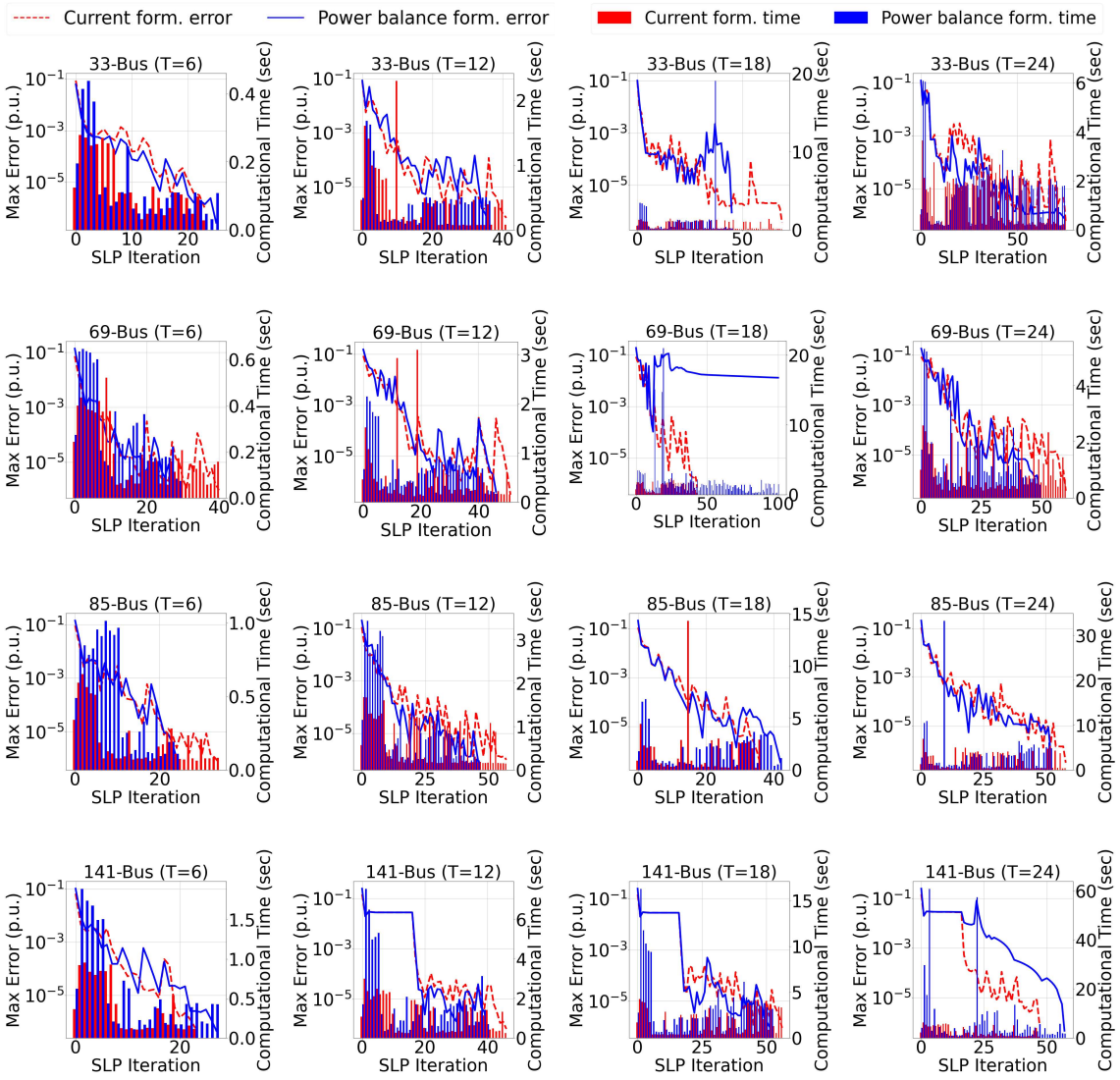

Figure 8.1. SLP convergence and computational time per iteration

From the plots in Figure 8.1, we can observe the following: 1) no formulation dominates the other in terms of the needed SLP iterations to converge though the power balance formulation generally requires less iterations, 2) the current formulation significantly outperforms the power balance formulation in terms of the computational time per iteration especially in the first couple of iterations. Recall that the proposed SLP method fixes the binary variables that do not change within a pre-defined consecutive number of iterations (i.e., 3 iterations in our setting). This is what caused the general decrease in the computational time per iteration as the SLP progress. It can be observed in the first couple of iterations of most cases that the blue bars are significantly longer than the red ones; the current formulation seems to perform even better compared to the power balance formulation when binary variables are involved.

8.3 Summary

In this chapter, we compared the use of the power balance formulation and the current formulation to model the physics and constraints of the μG. The solved problem is the multi-period optimal power flow with unit commitment. Four test-systems were used and four horizon lengths resulting in a total of 16 cases. Global optimal lower bounds for the cases were obtained from the QC method and used to report the optimality gaps of the power balance formulation and the current formulation. On average, the power balance formulation performed slightly better in terms of the optimality gap with an average of 0.25% compared to 0.26% for the current formulation. However, the power balance formulation was 75% slower on average across the cases relative to the current formulation.

CHAPTER 9. DEMONSTRATIVE CASE STUDIES FOR SERVICE PROVISION

9.1 Overview

In this chapter, we present case studies that demonstrate the provision of services via a μG using the proposed μGEMS. Both service designs are separately simulated which are: 1) Day-Ahead (DA) Commitment design and, 2) Real-Time (RT) Commitment design. Section 9.2 shows the μG used as a test system. Section 9.3 and section 9.4 present the case studies for the DA Commitment design and the RT Commitment design, respectively. Finally, a summary is drawn in section 9.5.

The parameters of the Successive Linear Programming (SLP) solution method used across all optimization problems in this section are: $\mathbf{w}^{slp}$ =1000, κ =-0.8, ξ =1/3, $Bin.Iter$ =3, ϵ =1e-4, $Max.Iter = 100$. All MILP problems are solved by Gurobi solver [14] with the MIP gap set to 0.1 and the constraints tolerance set to 1e-6.

9.2 Test System

The test system used for the case studies is a meshed 33-bus system with 37 circuits, adapted from [75]. The system is shown in Figure 9.1. Four DGs, four ESS, and 31 homes each with a controllable DUL and a controllable TCL are connected to the system. The parameters of the DERs are identical to those previously listed in Table 7.1 through Table 7.5 in section 7.2. The assumed network constraints and PCC power factor limits are listed in Table 9.1 and the external grid equivalent voltage is taken to be fixed at 1p.u.. Moreover,

we multiply the nominal load values of the systems' load points by the normalized hourly net-demand profiles in [76] to extract hourly profiles for each load point. Linear interpolation is used to have the loads as a continuously changing profiles. The total uncontrollable PQ net-demand of the system for two consecutive days is shown in Figure 9.2. Further, the ambient temperature is collected from the System Advisory Model (SAM) of the National Renewable Energy Laboratory (NREL) [78] with linear interpolation used to have the temperature as a continuous changing profile. The temperature profile for two consecutive days is shown in Figure 9.3.

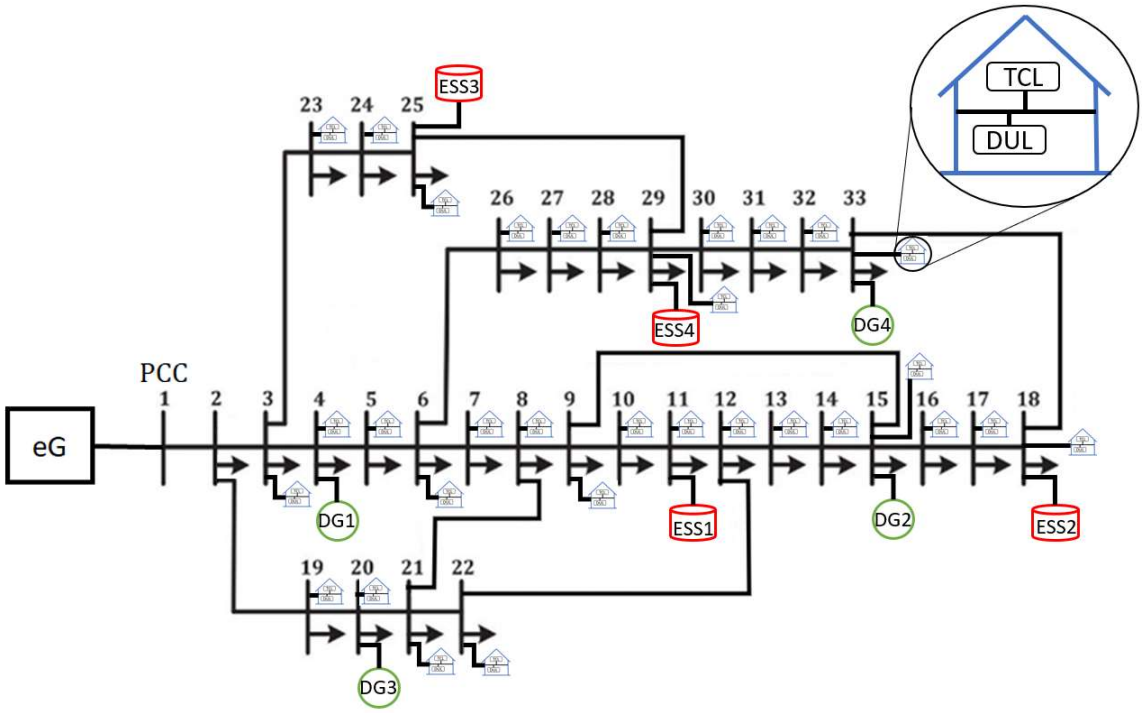

Figure 9.1. The 33-bus test system

Table 9.1 Network constraints and power factor limits

$\underline{V}_k$	$\bar{V}_k$	$\bar{I}_{km}{}^*$	Power Factor Limits at the PCC
0.95p.u.	1.05p.u.	$15 \times \max(I_{km}, I_{mk})$	0.95 lag – 0.95 lead

*I_{km} and I_{mk} are the magnitudes of the circuit currents obtained from the power flow solution of the original MATPOWER system.

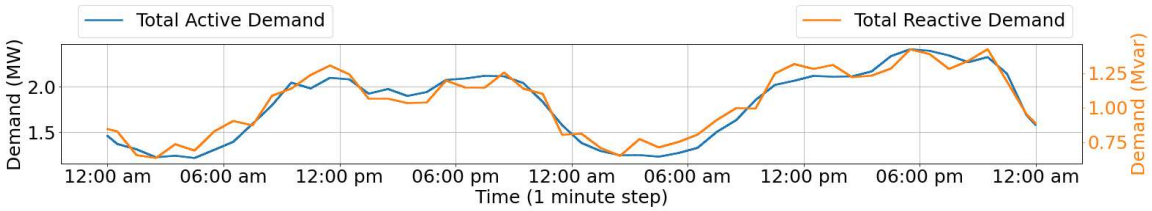

Figure 9.2.Total active and reactive net-demand for two consecutive days

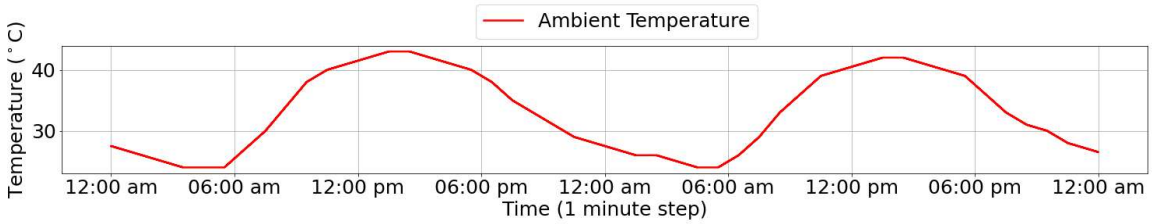

Figure 9.3. Ambient temperature for two consecutive days

9.3 Demonstrative Case Study: Day-Ahead Commitment Design

9.3.1 Case Study Setup

In this case study, we simulate the participation of the µG in a (DA) hourly energy, reserve, and regulation markets. We then simulate the operation of the µG throughout the operating day with a frequency of 1 minute. First, the proposed µGEMS computes the optimal DA energy, reserve, and regulation capacity commitments. Then, during the operating day, the µGEMS optimizes the operation of the µG via the three hierarchical modules: 1) the day-ahead unit commitment (DAUC), 2) the hours ahead operations planning (HAOP), and 3) the real time control (RTC) to follow the DA committed power, and hold, dispatch and maintain the reserve and regulation capacities. The µG is assumed to provide voltage support simultaneously by minimizing the deviation of the PCC voltage from 1 p.u. throughout the operating day.

9.3.1.1 Market Rules

We assume that the μG does not participate in the intra-day markets and must honour its DA committed power interchange (i.e., DA plan) and reserve and regulation commitments throughout the operating day, or otherwise, penalties are incurred. The DA energy price at the PCC is adapted from [77] and is shown in Figure 9.4 for two consecutive days. DA reserve and regulation capacity prices are taken to be half of the energy price and the μG is assumed to be compensated the DA energy price if a capacity is called for during the operating day. The market rules include minimum acceptable capacities of 100kW for reserve, 50kW for upward regulation, and 50kW for downward regulation. Reserve must be maintained for 1 hour and dispatched within 10 minutes, while regulation must be dispatched within 1 minute. Moreover, we assume that the μG incurs a penalty of two times the DA energy price if it exports less than the DA plan; no penalty or compensation is incurred if the μG exports more than the DA plan. Also, the μG incurs a penalty of four times the DA energy price for insufficient supply of reserve and regulation calls.

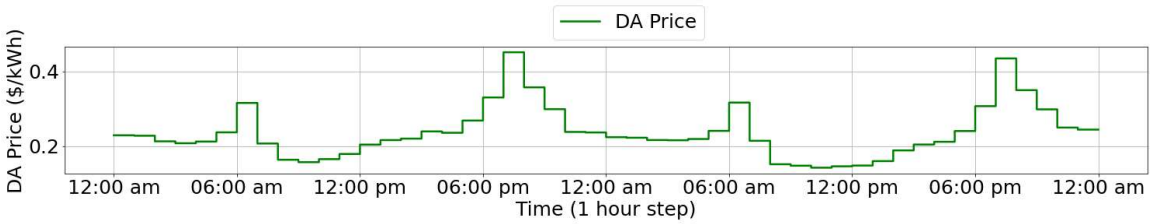

Figure 9.4. Day-ahead energy price at the PCC for two consecutive days

9.3.1.2 Timing of the Optimization Problems

The gate closure of the DA commitments is assumed to be 11 hours before the start of the operating day and the problem computing the optimal DA commitments is ran 12

hours before the start of the operating day to give sufficient time for computation. The DAUC module is ran each two hours with a 24-hour horizon and hourly intervals. The specific time to start running the DAUC is 30 minutes before the beginning of each even operating hour to give enough time for obtaining the solution (e.g., for the 24-hour schedule from 2pm to 2pm the following day, the DAUC is ran at 1:30pm of the current day). At each run, the DAUC uses the current μG state (i.e., the one at the 30th minute of the hour) as the initial conditions for the optimized horizon. Further, the HAOP is ran each 15 minutes with a 2-hour horizon and 15 minutes intervals. The HAOP starts running 2 minutes before the start of any 15-minute interval to give sufficient time for obtaining the solution. At each run, the HAOP uses the current state of the μG as the initial conditions for its optimized horizon. Finally, the RTC module is ran at the beginning of each minute and it uses the current μG state at the instant of starting the run.

9.3.1.3 Forecast Assumptions

We assume that the forecast error for net-demand, ambient temperature and grid prices is normally distributed with a standard deviation that increases linearly as we move further in time from the forecasted data. To illustrate, let the true value of a specific data point be x^T and the forecasted value be x^F. Further, let h represent how far ahead the forecast is made in hours. Then, the forecasted data given to a certain optimization problem is generated as follows:

$$x^F = norm(x^T, h \times \rho \times x^T) \tag{9.1}$$

where $norm(\mu, \sigma)$ is a normal random generator with mean μ and standard deviation σ. ρ is an assumed parameter representing the rate of increase in the standard deviation of the forecast error. σ is taken to be 0.005 in the case study. Hence, for a problem performed 24

hours in advance, the standard deviation of the forecast error will be 12% of the true value. The assumed true value of net-demand, temperature, and grid prices are those shown in Figure 9.2, Figure 9.3, and Figure 9.4, respectively. Whenever an optimization problem requires a forecast for a specific data point, a perturbed version of the data in these figures is fed to the optimization problem based on the equation in (9.1).

9.3.1.4 Computing the State of the μG

The μG state is calculated at the beginning of each minute right before solving the RTC problem. The state is calculated by running a power flow using the "current" net-demand and temperature, and the "current" DERs outputs. Note that the DERs outputs are obtained from the "latest" RTC solution (1 minute ago) and their response time. All DERs are assumed to have instantaneous response time except for the DGs, where their active power response time is limited by their ramping capabilities. Therefore, if a DG having a ramping capability of 1MW/5min is commanded to increase its output by 1 MW by the RTC, its output will only increase 0.2kW at the beginning of the next minute. Recall that the RTC is an instantaneous optimization problem, and no ramping constraints are involved.

This computed state of the μG at the beginning of each minute (and before solving the RTC for that minute) is used to report all results in the following section.

9.3.2 Results and Discussion

The results are divided into 6 sections: 1) section 9.3.2.1 gives the DA energy, reserve, and regulation commitments, 2) section 9.3.2.2 illustrates the realized active power

interchange at the PCC during the operating day and shows the μG's response to reserve and regulation calls, 3) section 9.3.2.3 is focused on the provision of voltage support and discussed the voltage profile, PQ interchange, and power factor at the PCC, 4) section 9.3.2.4 provides insights on the network conditions including bus voltages and circuit flows, 5) section 9.3.2.5 shows the operations the DERs in the μG, and finally, 6) section 9.3.2.6 reports the computational times of the optimization problems.

9.3.2.1 DA Energy and Ancillary Services Commitments

Figure 9.5 shows the profile of the μG's DA committed power interchange. We computed the DA commitments of the μG for two consecutive days. The next-day commitments shown in Figure 9.5 are used as inputs for the DAUC and HAOP modules when planning for horizons that exceeds the current operating day. Observe how the μG commits to export higher during high gird prices (i.e., around [6:00am – 7:00am) and [7:00pm – 8:00pm)), while a lower value of exports is committed during low grid prices. Moreover, the committed reserve capacity is shown in Figure 9.6. The μG commits around 2MW of reserve across all hours. Notice that the committed capacity at a given hour is always greater than or equal to the previous hour. This is due to the maintainability rule where a committed capacity of reserve must be maintained for at least an hour. Furthermore, Figure 9.7 and Figure 9.8 show the committed upward regulation and downward regulation capacitates, respectively. A noticeable increase in the committed capacity can be seen at hours [7:00pm - 9:00pm) (for both days and both directions of regulation capacity) which are the hours having the highest price for capacity compensation (see Figure 9.4). Finally, Figure 9.9 illustrates the expected profiles of the active power interchange with the external grid depending on the service calls. This figure is simply the

combination of Figure 9.5, Figure 9.6, Figure 9.7, and Figure 9.8 showing the expected active power interchange when no call is received from the external grid, and when a full capacity of reserve or regulation is called for. When solving for the optimal commitments, the μGEMS guarantees the ability to be on any of the curves of Figure 9.9, at any time, while also ensuring the ability to transition from the DA plan to the specific service curve.

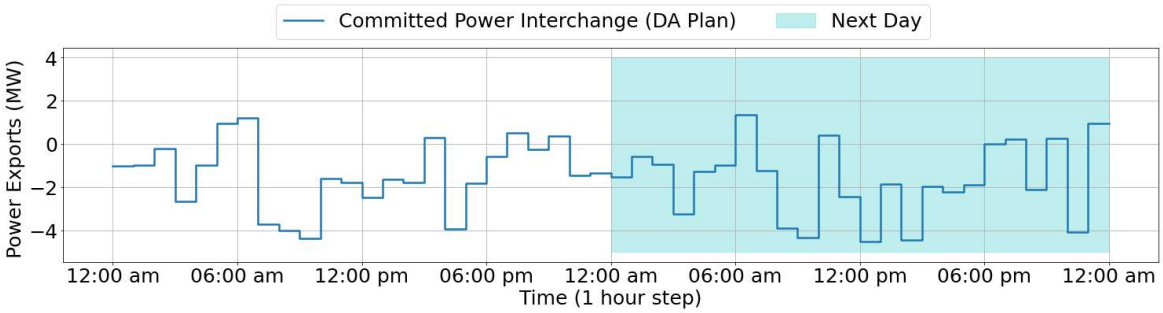

Figure 9.5. Committed power exports (DA Plan) for two consecutive days

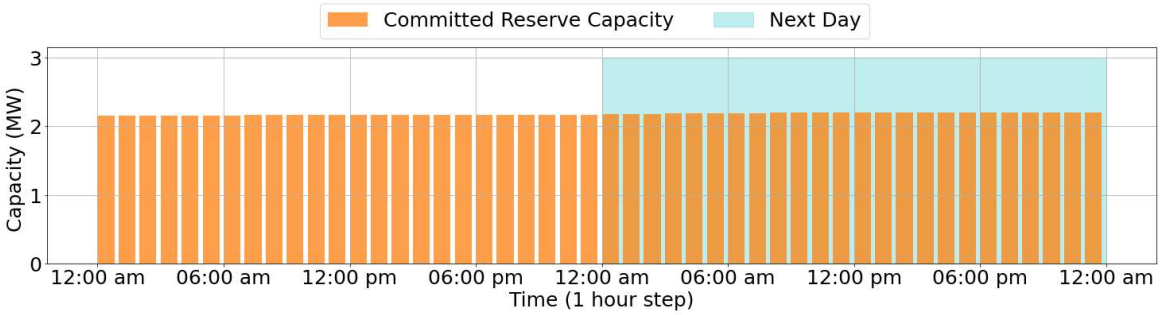

Figure 9.6. Committed reserve capacities for two consecutive days

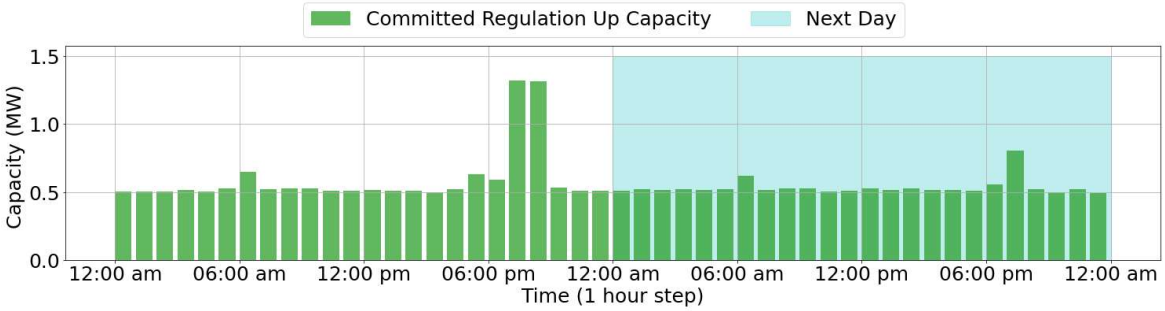

Figure 9.7. Committed regulation up capacities for two consecutive days

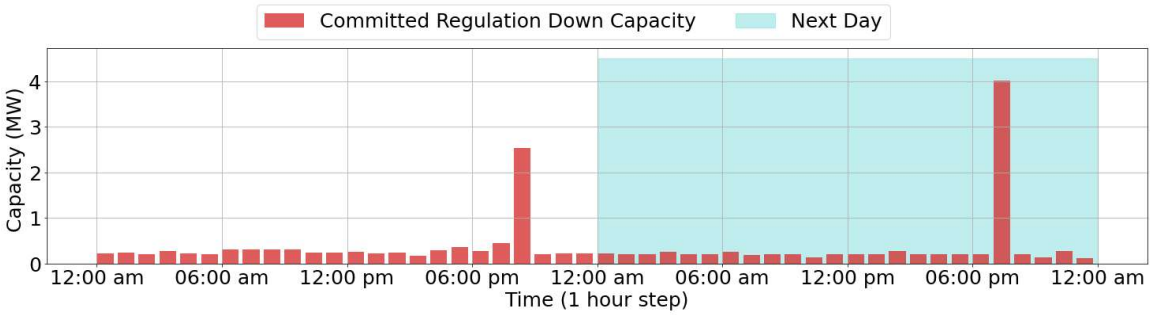

Figure 9.8. Committed regulation down capacities for two consecutive days

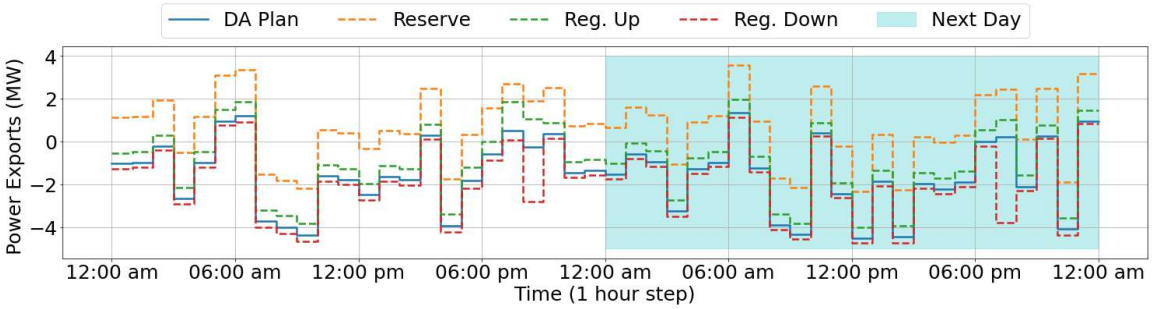

Figure 9.9. Expected profiles of power interchange with the external grid for two consecutive days

9.3.2.2 Realized Active Power Interchange at the PCC

Figure 9.10 shows the realized active power interchange between the µG and the external grid during the operating day, with a frequency of one minute. The DA plan is also shown on the figure where it can be seen how the µGEMS enabled an almost perfect follow for the committed DA plan despite the forecast error. We also simulate two reserve calls at hours [1:00am-2:00am) and [7:00pm-8:00pm). The reserve calls are assumed to be for the full committed capacity and requested to be maintained for 1 hour. In addition, multiple upward and downward regulation calls are simulated occurring within hours [11:00am-12:00pm), [1:00pm-2:00pm), and [3:00pm-4:00pm). The regulation calls are for the full committed capacity each sustaining 5 minutes. The µG was able to deliver the called for capacities within the required times (i.e., 10min for reserve and 1 minute of regulation). Close ups for the µG's response during the reserve and regulation calls are

shown in Figure 9.11 and Figure 9.12, respectively. Both reserve calls were delivered in 5 minutes. Notably, the capacity of the first reserve call was delivered in somewhat uniform ramping (i.e., the rate of increase in µG exports until reaching the requested capacity is constant). In contrast, the ramping of the second call is not uniform where almost 50% of the capacity was delivered in the first minute, and the reaming capacity within 4 minutes. This is due to the specific DERs contributing to the provision of reserve and the difference in their ramping capabilities; a large portion of the second reserve was supplied by ESSs and TCLs (the DERs operation is shown in section 9.3.2.5). As for the regulation capacities, the full capacity of each call was reached within 1 minute. Note that the regulation capacities may have been delivered in less than 1 minute. However, because the frequency of our simulation is 1 minute, the µG's state is only updated once per minute. Hence, changes occurring within a minute are not observed.

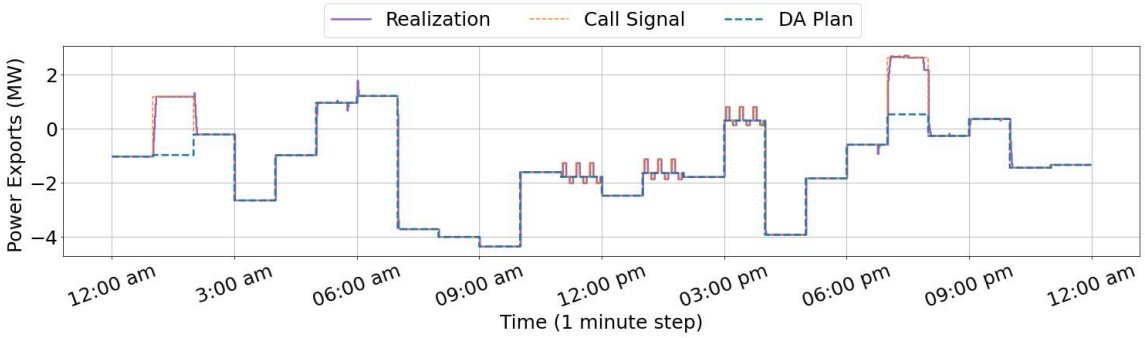

Figure 9.10. Realized µG's active power exports at the PCC

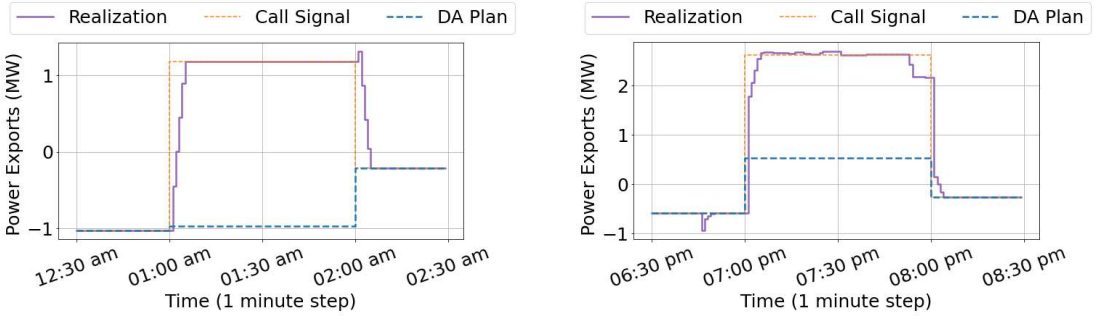

Figure 9.11. Response to reserve calls

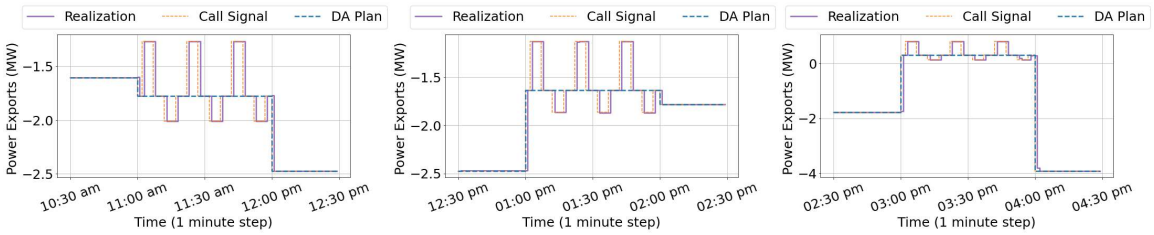

Figure 9.12. Response to regulation calls

9.3.2.3 Voltage Support

Simultaneously to supplying reserve and regulation services, the µG supplied voltage support service. Figure 9.13 demonstrates the variation of the voltage magnitude at the PCC bus with and without the µG's voltage support. While the voltage variation scale for both cases is small, it can be clearly seen how the voltage profile was of a better quality for the voltage support case, being closer to 1p.u..

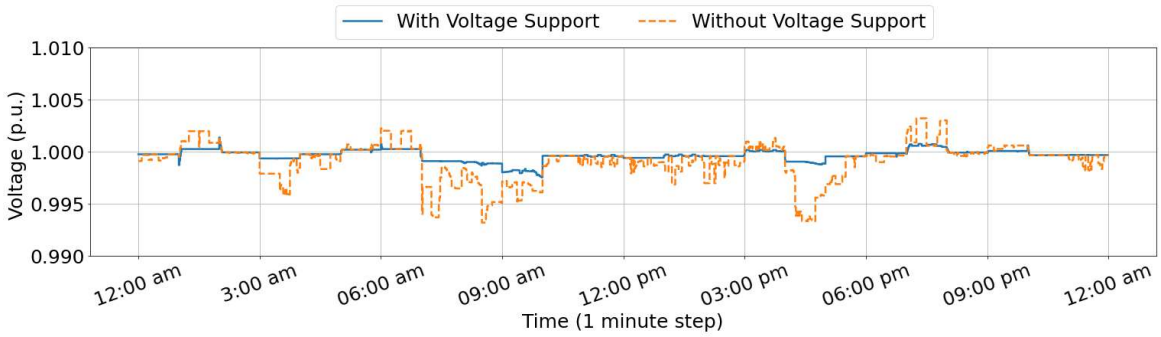

Figure 9.13. PCC voltage profile with a without µG's voltage support

Figure 9.14 and Figure 9.15 show the active and reactive power interchange profiles at the PCC for the two cases: with and without voltage support, respectively. The active power interchange is similar in both cases driven by the cost of active power and the calls of reserve and regulation capacities. However, the reactive power interchange is more uniform and "regulated" when the µG provides voltage support, in contrast to the abruption of reactive power in the other case. Further, note how the reactive power is acting in an inverse proportion manner relative to the active power when voltage support is provided.

This can be explained as follows: the decrease of μG exports (or equivalently, the increase of its imports) causes the PCC voltage to drop. To eliminate this drop and "regulate" the voltage, the μG increases its exports of reactive power, and vice versa.

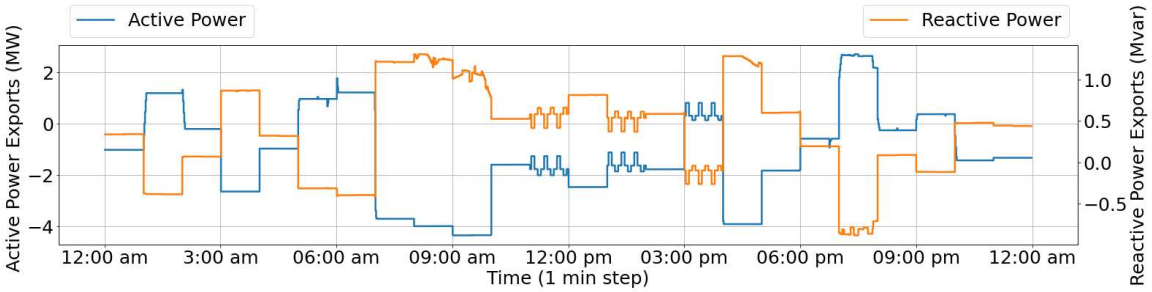

Figure 9.14. Active and reactive power exports with voltage support

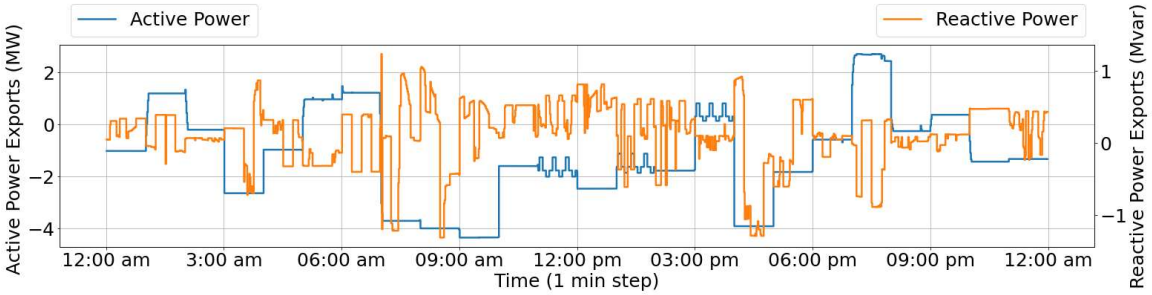

Figure 9.15. Active and reactive power exports without voltage support

Figure 9.16 plots points representing all incidents of PQ interchange at the PCC for the voltage support case and for the case with no voltage support. Observe the clear inverse proportion in the case with voltage support. Figure 9.16 also plot the power factor limits. Most of the points lie within the imposed limits. Some points, however, are outside the limits. The occurrence of those points for both cases is listed in Table 9.2 and Table 9.3.

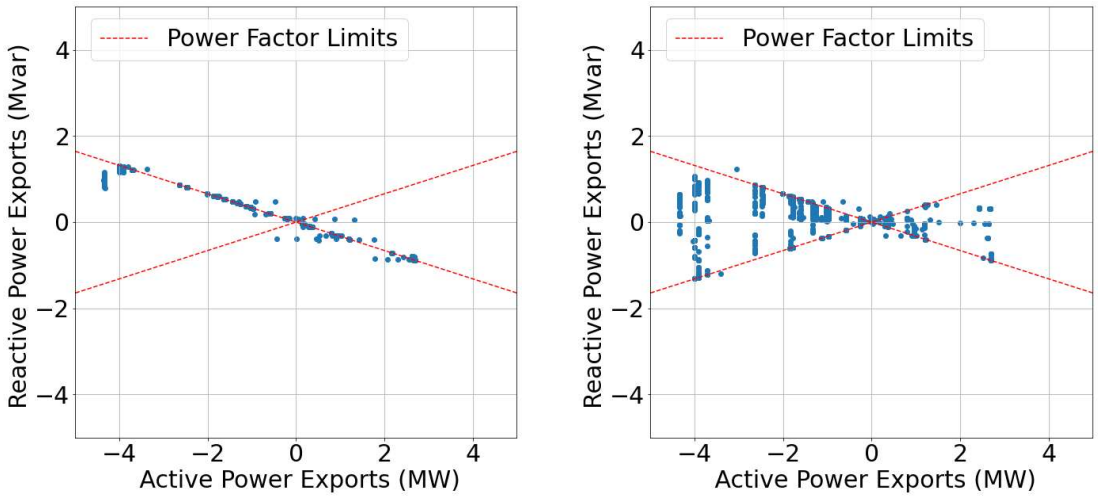

(a) (b)

Figure 9.16. (a) PQ interchange at the PCC with voltage support, (b) PQ interchange at the PCC without voltage support

Table 9.2 Occurrences of PCC power factor values outside the imposed limits for the case with voltage support

Power Factor Range	Total minutes of occurrence	Percentage of total time
[0.949 – 0.95)	562	39.0%
[0.940 – 0.949)	114	7.9%
[0.900 – 0.940)	11	0.76%
[0 – 0.900)	12	0.83%

Table 9.3 Occurrences of PCC power factor values outside the imposed limits for the case without voltage support

Power Factor Range	Total minutes of occurrence	Percentage of total time
[0.949 – 0.95)	327	22.7%
[0.940 – 0.949)	70	4.9%
[0.900 – 0.940)	4	0.28%
[0 – 0.900)	9	0.63%

It is important to note that the occurrence of points outside the limits is not caused by the RTC optimization problems; all optimization problems converged with no constraint violations (Figure 9.17 show the results from the RTC "solutions"). The occurrence of points outside the limits is caused by our simulation procedure. Recall that we evaluate the μG state at the beginning of each minute and immediately before running the RTC. Therefore: 1) some DERs may be still transitioning to the commands received from the

latest RTC solution (1 minute ago), and 2) the net-demand changed from the net-demand used by the latest RTC problem (1 minute ago). Updating the μG state in the simulation more frequently and running the RTC problem more frequently would reduce the percentage of the points outside the limits. Notably, the points outside the limits are more frequent in the case with voltage support. This is because when voltage support is provided, the PQ points are shifted to the power factor limits to supply/consume the optimal reactive power. Hence, small perturbation would result in those points being outside the limits.

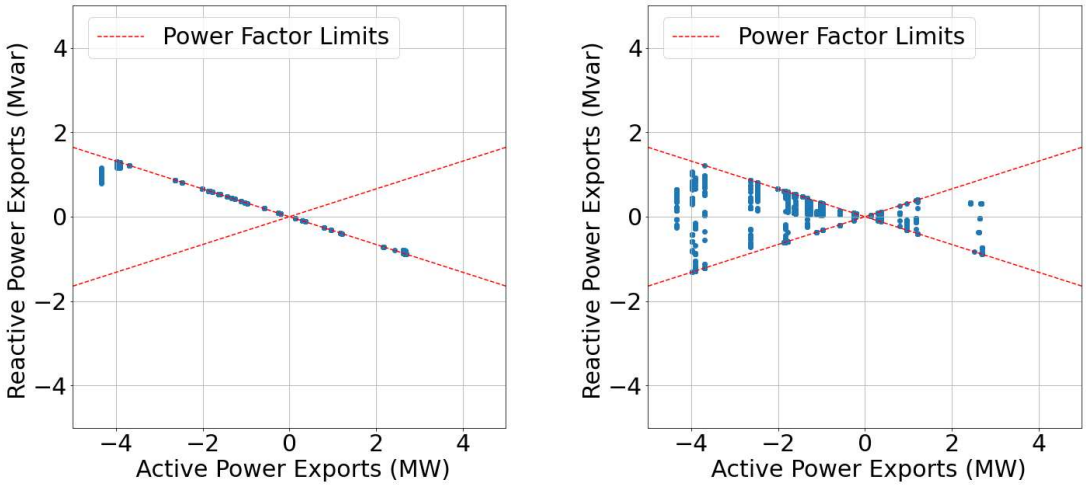

(a) (b)

Figure 9.17. (a) PQ interchange at the PCC with voltage support from the RTC solution, (b) PQ interchange at the PCC without voltage support from the RTC solution

The provision of voltage support comes with a cost, the lost-of-opportunity cost. Table 9.4 shows the total profit of the μG with and without the provision of voltage support. The slight decrease in profits due to providing voltage support resembles the lost-of-opportunity cost for the μG. This cost can be submitted to the external grid (or the market operator) for compensation.

Table 9.4 Total μG profits with and without voltage support

Profits with Voltage Support	Profits without Voltage Support	Lost-of-opportunity cost
$830.77	$875.45	$44.68

9.3.2.4 Network Conditions

Figure 9.18 shows a histogram plotting all values of bus voltages (i.e., across all minutes in the operating day across all busses). The majority of occurrences are around 1p.u. and all values are within the enforced bus voltage limits (i.e., 0.95-1.05 p.u.). Further, Figure 9.19 show the values of the maximum and the minimum bus voltages at each minute throughout the operating day. The maximum bus voltage peaks when the µG is exporting power (i.e., around 2am, 6am, 4pm, and 7pm). Similarly, the minimum bus voltage drops when the µG is importing power (i.e., the remaining time periods).

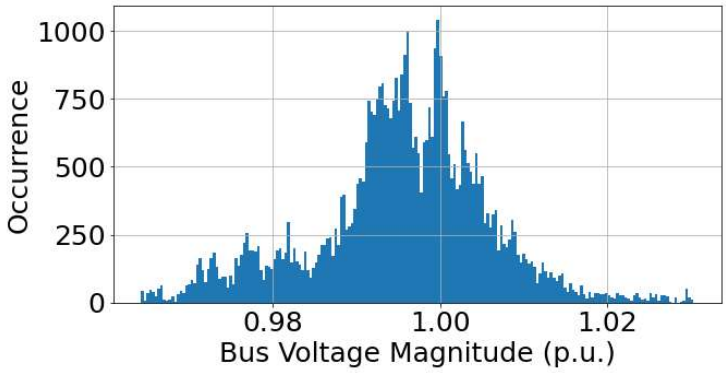

Figure 9.18. Bus voltage magnitudes

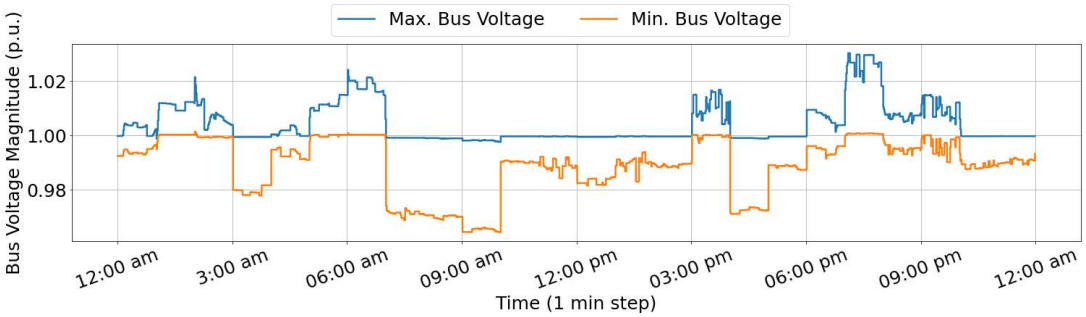

Figure 9.19. Maximum and minimum bus voltage magnitudes

Figure 9.20 show a histogram plotting all values of circuit loading in (%), and Figure 9.21 plots the maximum circuit loading value at each minute throughout the operating day. From these two figures, the following can be observed: 1) the majority of

circuit loading is around 10% with a noticeable spike at 100% seen in the histogram, 2) network congestion occurs around times with extreme imports or exports occurring [5am – 10am) and [3pm – 8pm).

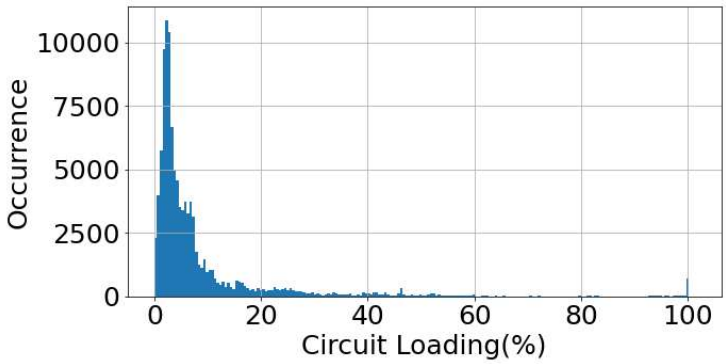

Figure 9.20. Circuits loading

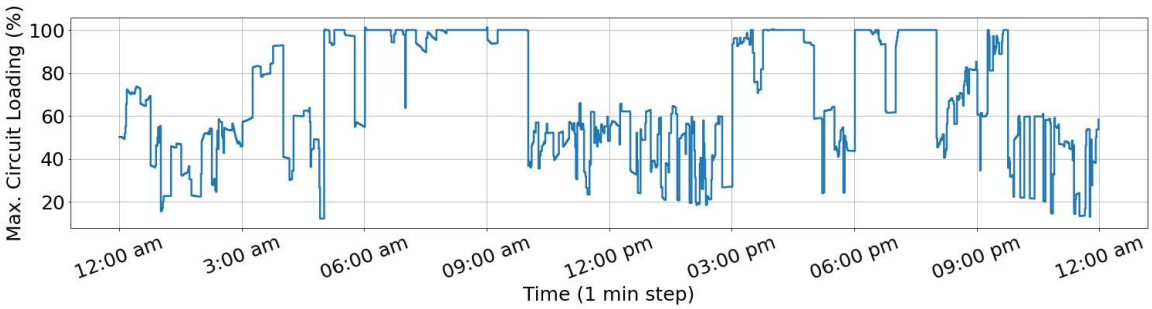

Figure 9.21. Maximum circuit loading

Regarding circuit overloading, few occurrences were detected. Table 9.5 lists the circuit overloading occurrences across multiple ranges. The overloading values are practically negligible with a maximum overloading of 101.2%. As we discussed in the case with the power factor and the PQ points occurring outside the limits, the occurrence of overloading is not caused from the RTC problem not converging. All optimization problems converged. The overloading is rather a consequence of the simulation procedure where the μG state is computed at the beginning of each minute immediately before running the RTC.

Table 9.5 Occurrences of circuit overloading

Circuit Loading Range (%)	Total minutes of occurrence*	Percentage of total time
(100.0 – 100.01]	137	9.51%
(100.01– 100.1]	166	11.53%
(100.1 –101.0]	5	0.35%
(101.0 – 101.2]	2	0.14%
(101.2 – ∞)	0	0.0%

* All circuit loading violations occur in the circuit connecting busses 10 and 11.

9.3.2.5 DERs Operation

Figure 9.22 shows the power output of all four DGs, where the contribution of the DGs to the reserve calls can be noticed occurring in [1am-2am) and [7pm-8pm). Additionally, the DGs participated in providing upward regulation when calls were received around [11am-4pm). The operating cost of the DGs follow the following relation: DG1<DG2<DG3<DG4 (refer to Table 7.2), which is observable form the profiles in Figure 9.22. DGs with lower cost are dispatched more frequently than DGs with higher cost. Notably, the DGs were committed to operate ON across the entire operating day.

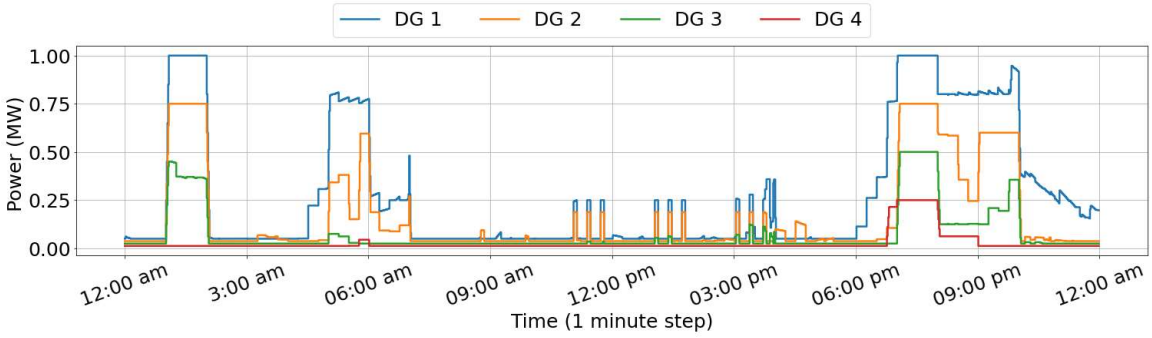

Figure 9.22. Power output of the DGs

Figure 9.23 show the power output of all ESSs (positive for discharge and negative for charge). Observe the ESSs' contribution to downward regulation calls around 1:00pm, especially ESS 1. The state-of-charge profile of all ESSs is shown in Figure 9.24. The figure shows the realized state-of-charge during the operating day, as well as the scheduled

operation for the next day which is obtained from the DAUC module (hourly schedule). For each ESS, two trajectories for the next day schedule are shown resembling an envelope for the state-of-charge. The envelope ensures the ability of the ESSs to contribute to the next day service calls without violating the state-of-charge limits. Further, it can be seen how the ESSs are fully discharged around hour 10pm and they are scheduled to start charging again around 3am of the next day. This is because the μG was exporting during high grid prices (7pm) leading to the discharge of the ESSs, and that the next valley of grid prices occur around 3am the next day, where the ESSs are scheduled to start charging.

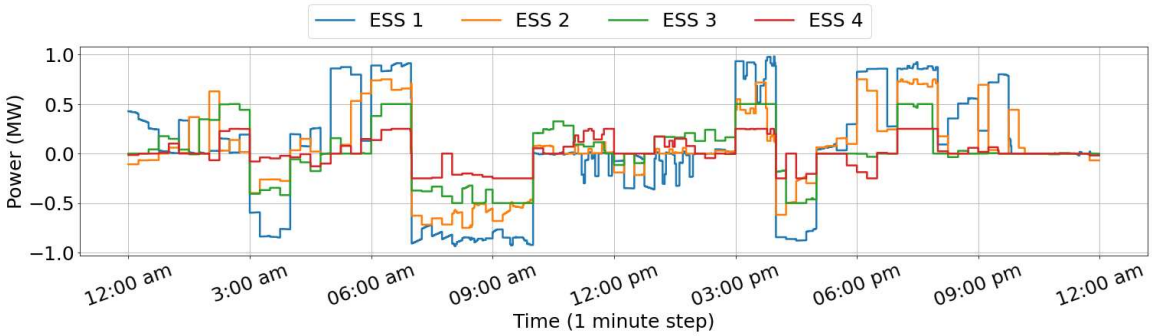

Figure 9.23. Power output of the ESSs

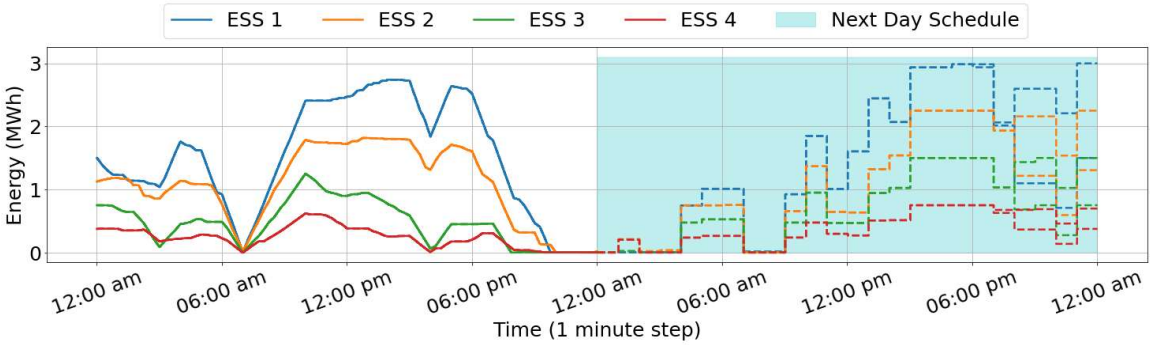

Figure 9.24. State of charge of the ESSs

The power consumption of the TCL at Bus 3 and its inner temperature are shown in Figure 9.25 and Figure 9.26, respectively. As can be seen from Figure 9.26, the temperature was kept within bounds and by that, maintaining the user's convenience. Similar to the ESS, the scheduled temperature of the TCL for the next day is also shown in

Figure 9.26 via the two trajectories (i.e., the envelope). The actual temperature for the next day depends on the realized operation and service calls. The TCL temperature follows a similar behaviour relative to the ESSs state-of-charge; the temperature reaches its highest point (the TCL is fully "discharged") at the end of the operating day, and is scheduled to "charge" or cool again at the next grid price valley around 3am of the following day. For more insights about the operation of the TCLs in the µG, Figure 9.27 though Figure 9.30 plot all TCLs' consumptions and Figure 9.31 through Figure 9.34 plot all TCLs' temperature evolutions. The behaviour of all TCLs is similar with some changes mainly caused by the different parameters of the TCLs (see Table 7.4 for the TCLs parameters).

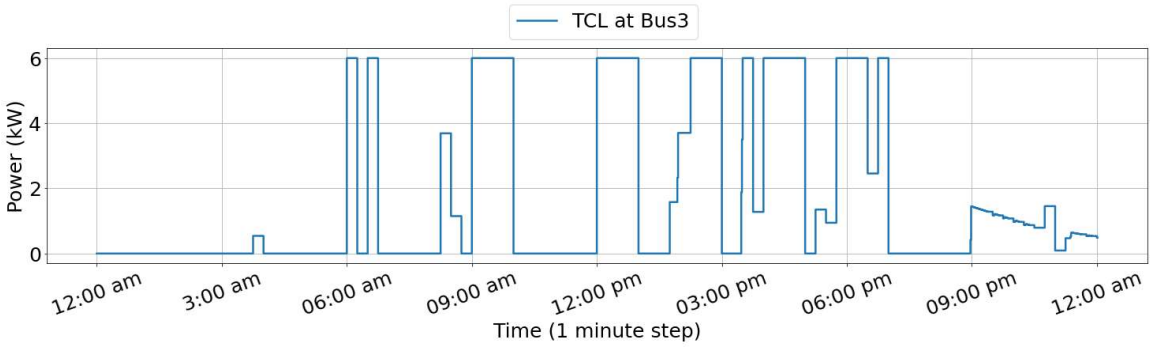

Figure 9.25. Power consumption of the TCL at Bus 3

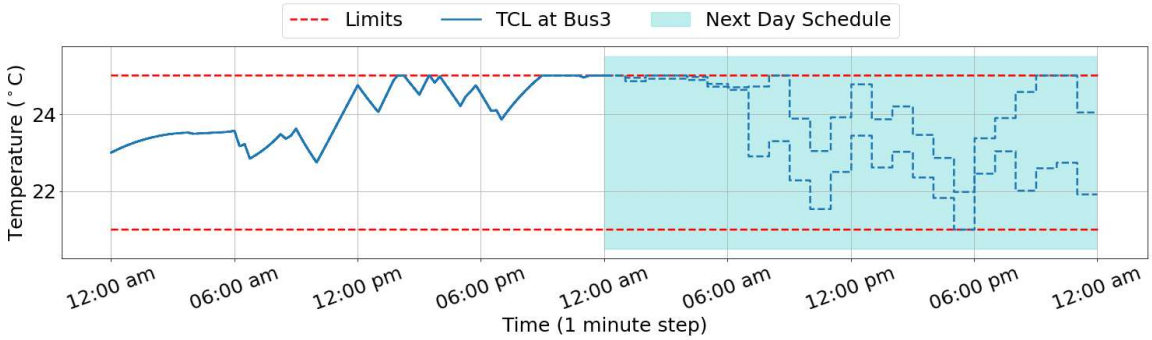

Figure 9.26. Inner temperature of the TCL at Bus 3

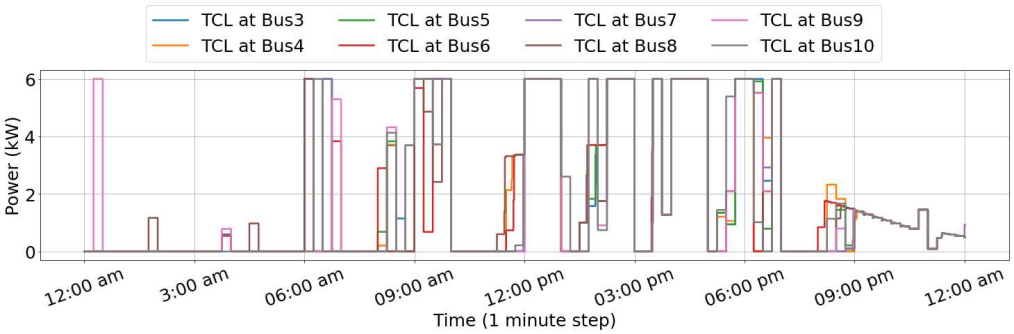

Figure 9.27. Power consumption of TCLs at busses 3 to 10

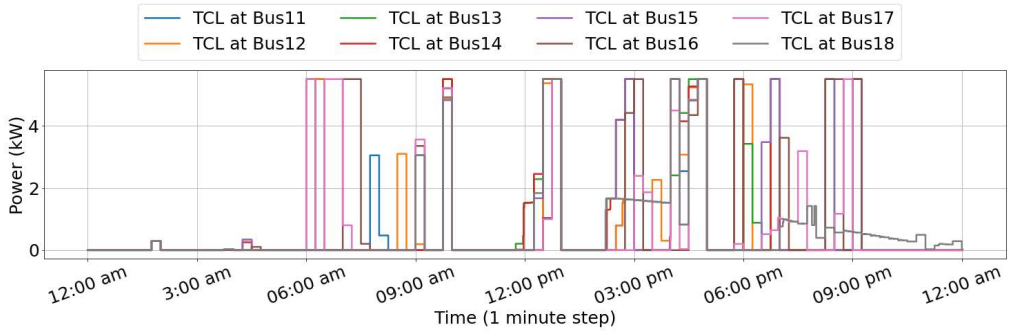

Figure 9.28. Power consumption of TCLs at busses 11 to 18

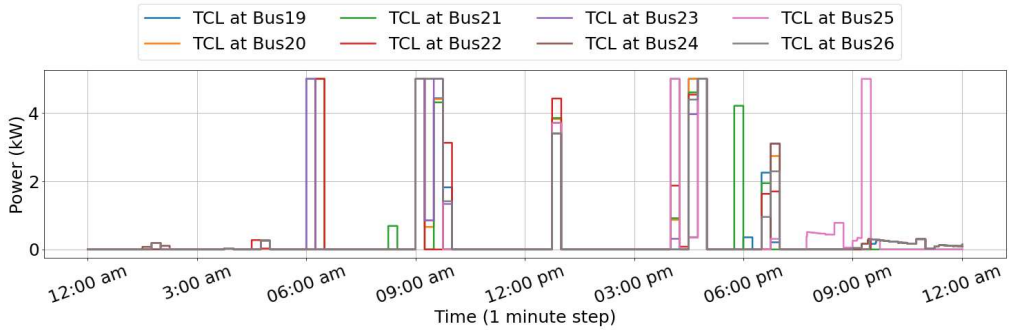

Figure 9.29. Power consumption of TCLs at busses 19 to 26

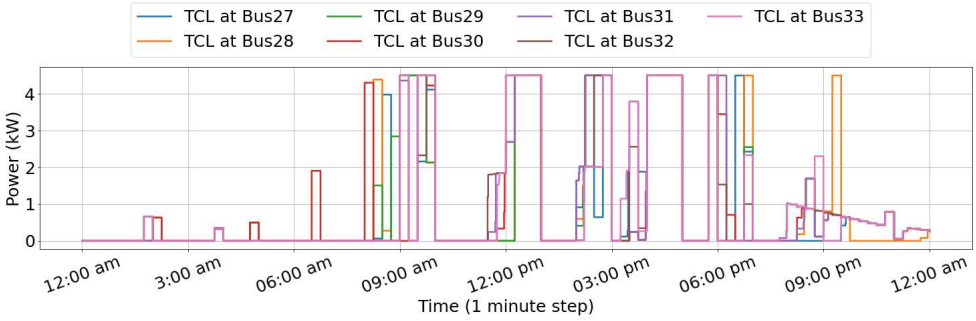

Figure 9.30. Power consumption of TCLs at busses 27 to 33

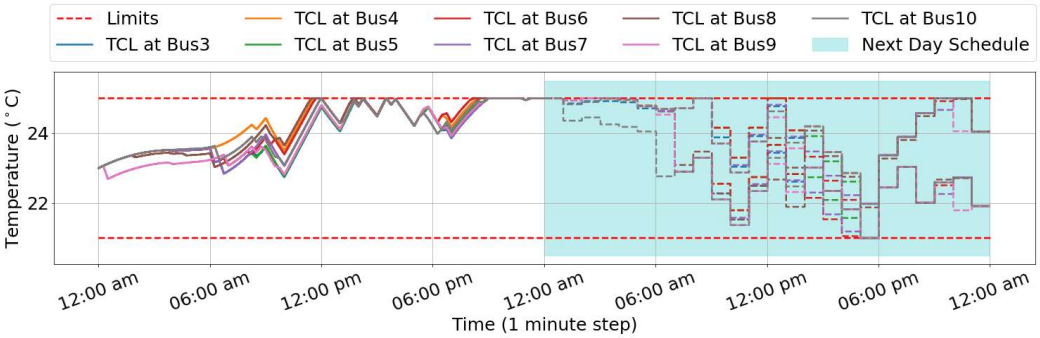

Figure 9.31. Inner temperature of TCLs at busses 3 to10

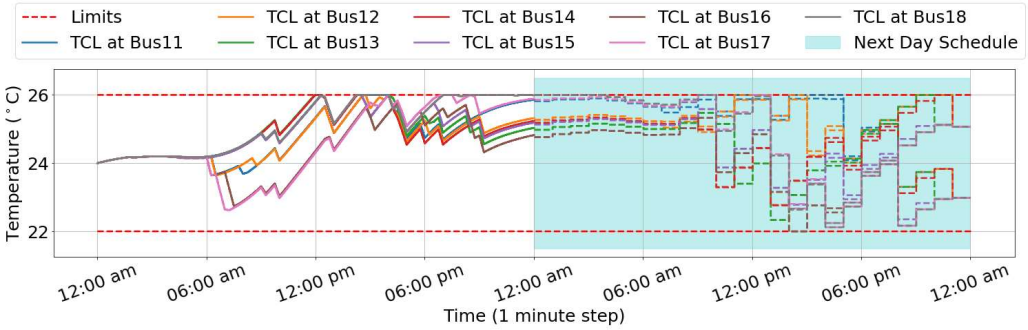

Figure 9.32. Inner temperature of TCLs at busses 11 to 18

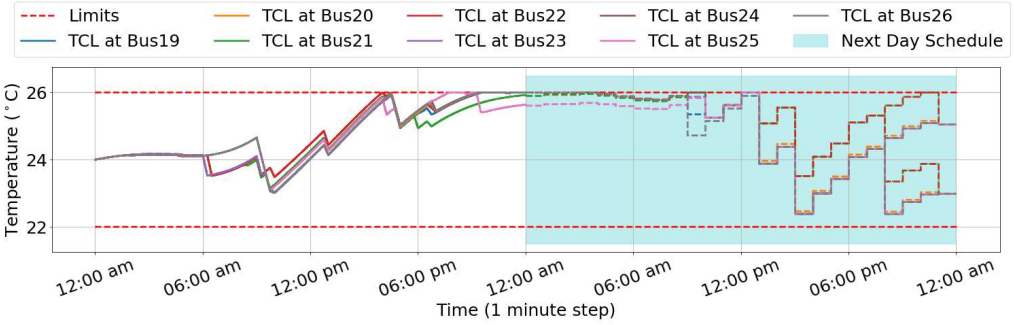

Figure 9.33. Inner temperature of TCLs at busses 19 to 26

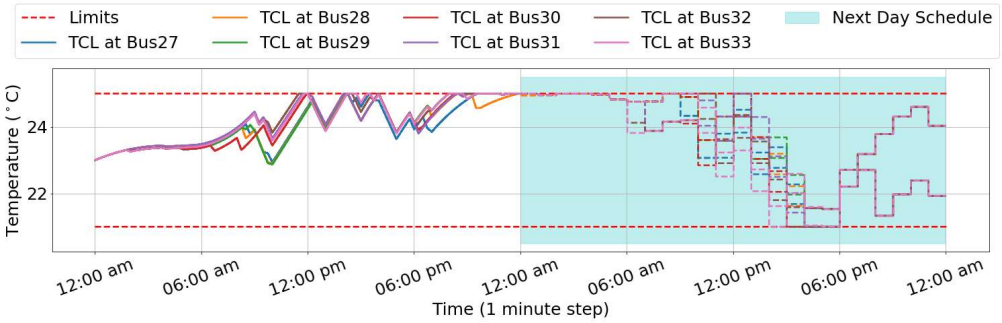

Figure 9.34. Inner temperature of TCLs at busses 27 to 33

Figure 9.35 illustrates the aggregate consumption of all TCLs along with the DA price. One can observe that the µGEMS minimizes the consumption of the TCLs during times with high prices. A similar behaviour can be seen in the aggregate consumption of the DULs shown in Figure 9.36. All DULs were scheduled within the allowable time assumed given by the households (see Table 7.5 for the parameters of the DULs).

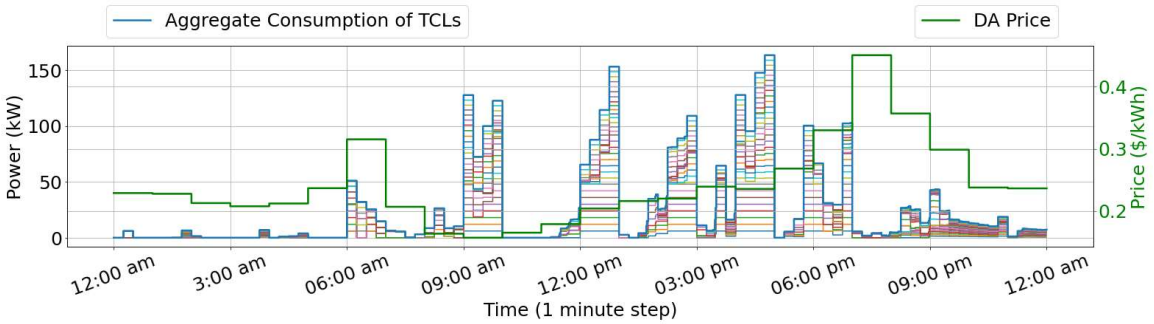

Figure 9.35. Aggregate power consumption of all TCLs with DA price

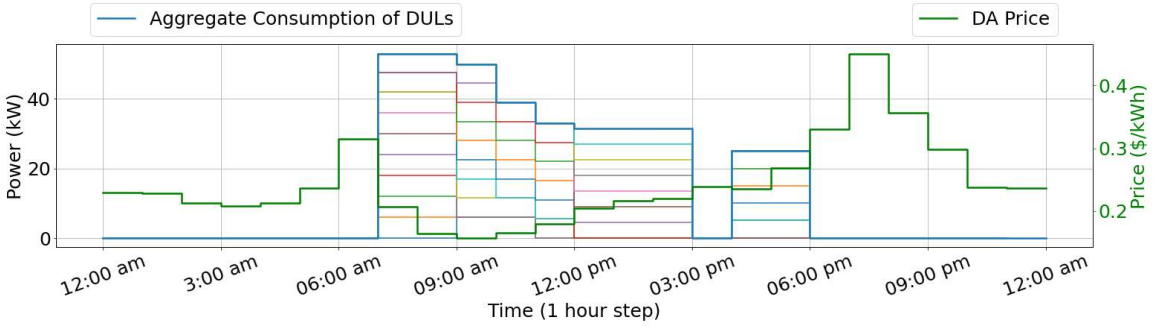

Figure 9.36. Aggregate power consumption of all DULs with DA price

9.3.2.6 Computational Times

The problem computing the optimal DA energy and ancillary service commitments was solved twice to compute the commitments for two day. Each problem considered a 26 hour horizon (24+2) to reduce the end-of-horizon effect. The solution of the two problems took 23.5 and 36.7 minutes, respectively. Recall that these problems were ran 1 hour before the closure gate giving sufficient time to produce the solutions. During the simulation of

the day, the DAUC problem was solved 13 times (each 2 hours), the HAOP problem was solved 97 times (each 15 minutes), and the RTC problem was solved 1440 times (each minute). Histograms for the computational times for each of the three problems are shown in Figure 9.37. As expected, the DAUC problem required relatively significant computational time ranging from 10 minutes to 25 minutes. This is because this problem included a considerable number of binary variables related to scheduling the ON/OFF operation of DGs and DULs, and it spanned 24 time periods. Nevertheless, we run the DAUC 30 minutes before the start of its scheduled horizon giving sufficient time for finding the optimal solution. In contrast to the DAUC, the HAOP did not perform unit commitment and only spanned 8 time period resulting in the computational times being substantially less than the DAUC. The maximum HAOP computational time is less than two minutes. Recall that we run the HAOP 2 minutes before the start of its scheduling horizon giving sufficient time to solve the problem. The RTC problem required small computational times with a mean around 0.5 seconds and a maximum value around 4.6 seconds. Hence, the RTC may even be solved more frequently than once per minute.

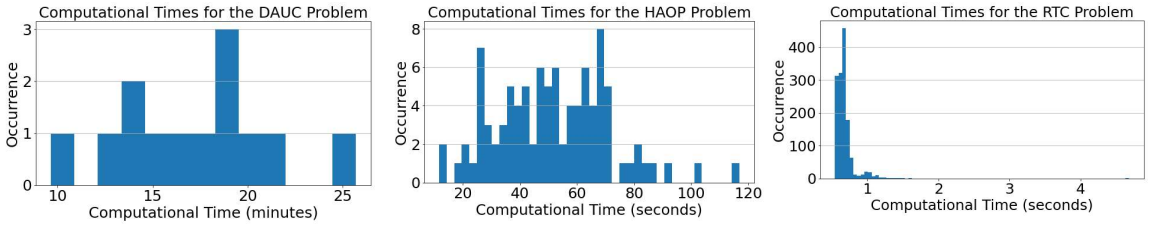

(a) (b) (c)

Figure 9.37. Computational times of: (a) the DAUC problem, (b) the HAOP problem, and (c) the RTC problem

The decrease in computational time as we move from the DAUC to the HAOP, and then to the RTC is the essence of the proposed μGEMS hierarchical structure. By separating the controls recommendations and set points across the three layers, we achieve

a compromise between optimality from considering long planning horizons, and acceptable computational times. Additionally, the small computational time required to solve the RTC problem enable rapid updates to DERs' set points. This rapid update of DERs' setpoints allows the μG to optimally respond to grid calls for services within appropriate times and maintain the committed power interchange at the PCC despite the continuous change of net-demand and temperature, and despite the forecast errors.

9.4 Demonstrative Case Study: Real-Time Commitment Design

9.4.1 Case Study Setup

In this case study, we assume that the μG participates in the DA energy markets and schedules a DA plan without any DA ancillary service commitments. The μG does not participate in the intra-day energy markets and must honour its DA committed power interchange. Once a DA plan is established, we simulate the operation of the μG hourly across the operating day. At the beginning of each hour, the *reserve products* available at the PCC are computed along with the cost of dispatching each *reserve product* (i.e., the lost-of-opportunity cost). The reserve and cost are computed by running two look-ahead optimization problems (refer to section 5.3.1). The horizon of these problems is taken to be 6 hours with 10 minutes steps resulting in 36 time periods. While reserve is usually maintained for less than 6 hours, a 6 hours horizon is used to compute the lost-of-opportunity cost considering the μG operation after the provision of a *reserve product*. Such practice is especially necessary as more storage devices exist in the μG.

We consider five reserve types in this case study: 1) upward primary reserve, 2) downward primary reserve, 3) upward secondary reserve, 4) downward secondary reserve,

and 5) tertiary reserve. Recall that the proposed formulation allows computing different *reserve products* by tuning the weights of the objective function. A reserve product may include a single reserve type from the five types (i.e., *individual reserve products*), or may include multiple reserve types that are committed to be provided one following the other (i.e., *stacked reserve products*). An example of a stacked reserve product is providing upward primary reserve, followed by upward secondary reserve followed by tertiary reserve. Seven *reserve products* are computed for each hour in the simulation. The reserve products are listed in Table 9.6. For each reserve product, a weight of 10 is set for all reserve types appearing in the product when solving the optimization problem. For example, for the last product in Table 9.6, the reserve capacities of downward primary and downward secondary are multiplied by 10 in the objective function while other capacities are multiplied by zero.

Table 9.6 Reserve products provided in real-time

Individual Reserve Products	Upward Primary Reserve
	Downward Primary Reserve
	Upward Secondary Reserve
	Downward Secondary Reserve
	Tertiary Reserve
Stacked Reserve Products	Upward Primary reserve +Upward Secondary Reserve +Tertiary Reserve
	Downward Primary Reserve + Downward Secondary Reserve

Assumed commitment rules include: primary reserves (up or down) must be supplied within 1 minute and maintained for 10 minutes, secondary reserves (up or down) must be supplied within 10 minutes and maintained for 1 hour, and Tertiary reserve must be supplied within 1 hour and maintained for 2 hours. We also assume that the μG incurs

a penalty of two times the DA energy price if it consumes more than the DA plan during the day; no penalty or compensation is incurred if the μG consumes less than the DA plan. The assumed DA energy price at the PCC is adapted from [77] and is shown in Figure 9.38 for two consecutive days, which is identical to the price used in the previous case study. Notably, perfect forecast is assumed in this case study.

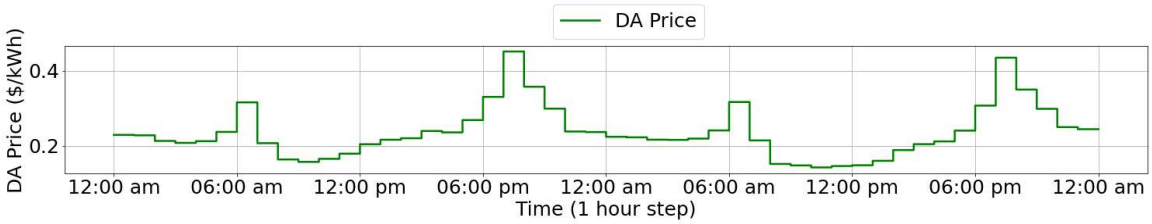

Figure 9.38. Day-ahead energy price at the PCC for two consecutive days

9.4.2 Results and Discussion

Figure 9.39 shows the committed DA plan for two consecutive days. Observe how the μG power exports are driven by the DA price where the μG schedules to export during high grid prices and schedules to import during low grid prices. The DA plan in Figure 9.39 also resembles the μG hourly operation since perfect forecast is assumed. The μG state at each hour of the operating day is used as initial conditions to compute the available service capacities at the beginning of each hour. Also, the μG state 6 hours ahead of each simulated hour is used to set end-of-horizon limits for the optimization problems computing the reserve and cost.

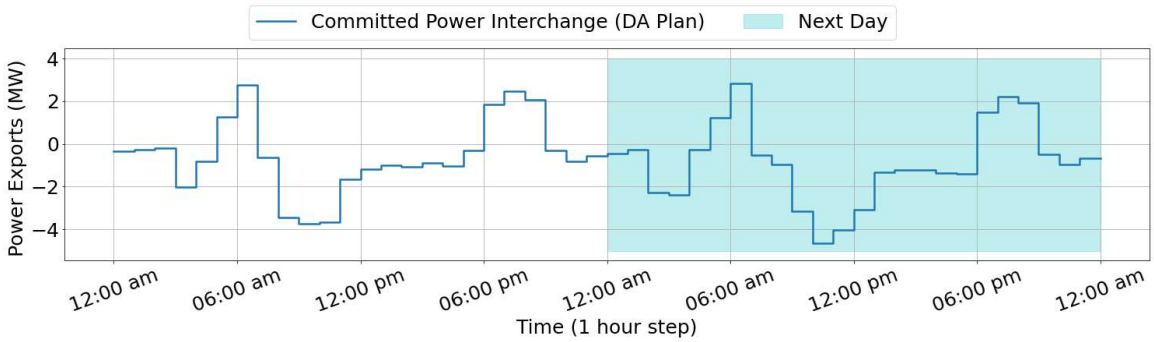

Figure 9.39. Committed power exports (DA Plan) for two consecutive days

Figure 9.40 and Figure 9.41 show the computed capacities of *individual reserve products* and *stacked reserve products*, respectively. The products are computed at the beginning of each hour of the operating day. For each product, an associated lost-of-opportunity cost is computed which is also shown in Figure 9.40 and Figure 9.41. The pair of capacity and cost for each product can be submitted as a bid in real-time to the external grid. Observe how the capacities of downward reserve products reach their peaks during periods with high grid prices (i.e., around 6am and 7 pm). This is because the µG is exporting the most during these periods resulting in an available downward capacity. The same can be observed for upward reserve capacities reaching their peaks during periods with low grid prices (around 9 am), since the µG is importing power during these times.

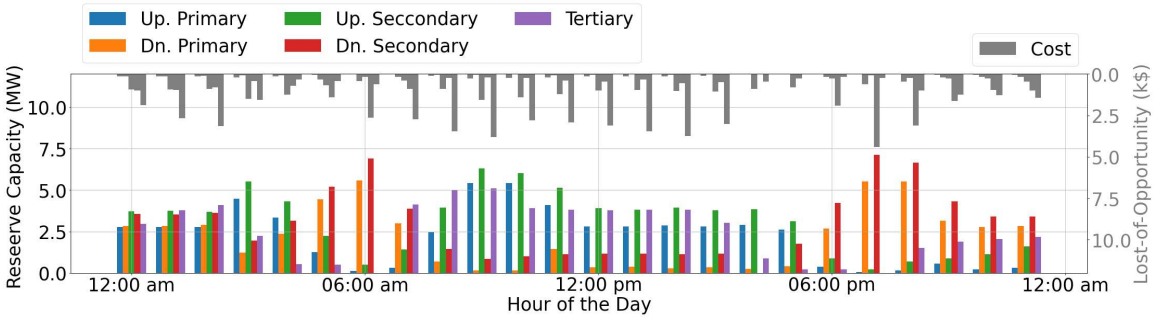

Figure 9.40. Hourly individual reserve products available at the PCC and the lost-of-opportunity cost

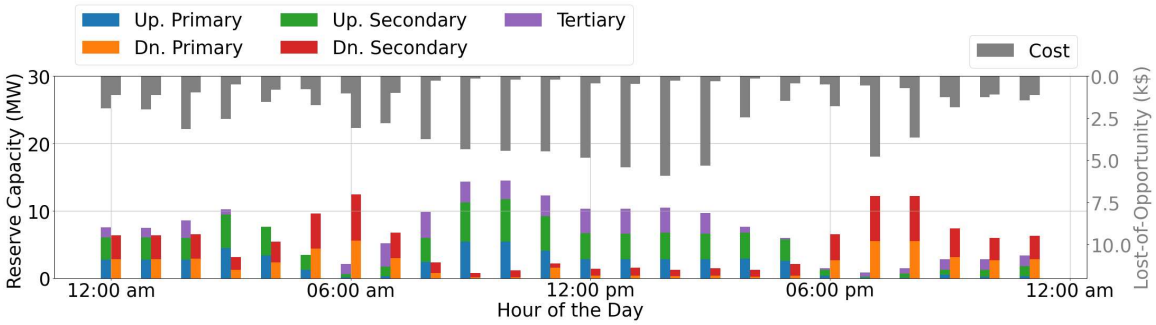

Figure 9.41. Hourly stacked reserve products available at the PCC and the lost-of-opportunity cost

Figure 9.42 shows the sum of individual reserve products (framed with grey) along with the sum of stacked reserve products (framed with black). As expected, the sum of stacked reserve products is less than the sum of individuals reserve products, especially for the upward reserves containing the tertiary reserve type. This is mainly due to the storage-based DERs; after the provision of primary and secondary reserves within a stacked product, the available stored energy for tertiary reserve reduces in comparison to when tertiary reserve is supplied as an individual product without primary and secondary.

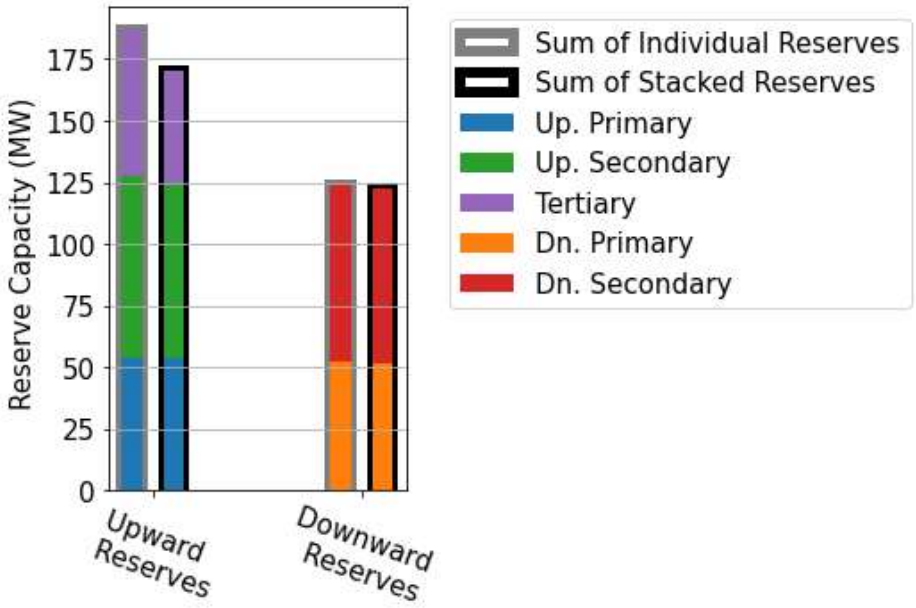

Figure 9.42 Sum of individual and stacked reserve products over the day

Figure 9.43 plots the active power export at the PCC starting from 2am for three cases: case 1) when the upward stacked reserve product is dispatched, case 2) when the downward stacked reserve product is dispatched, and case 3) when no reserve is dispatched (base case). Notice how the μG in case 1 provides upward primary reserve, followed by upward secondary reserve, followed by tertiary reserve. Then, the exports of the μG drop to a value that is less than the value of the base case profile. This is to return to the optimal trajectory before the end of the 6 hour horizon. Recall that the end of horizon limits for the base and reserves cases are set using the μG optimal trajectory that considers the next 24 hours, and by that, ensuring that the lost-of-opportunity cost is fully computed within the 6 hours horizon.

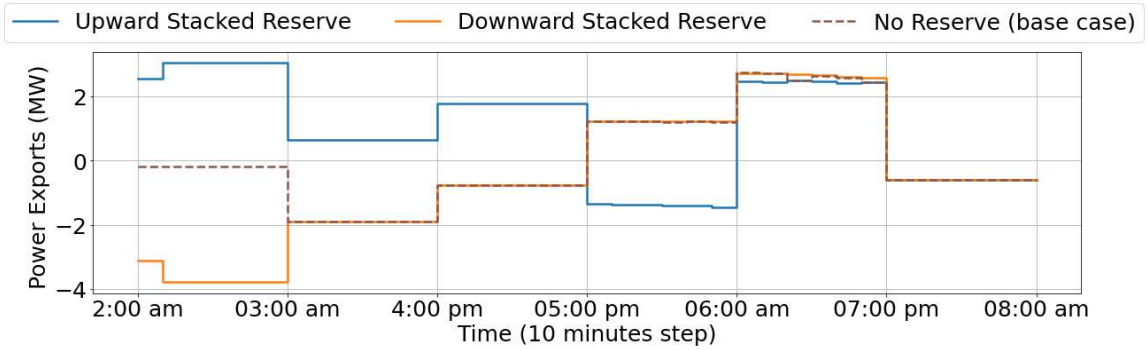

Figure 9.43. Power exports for upward stacked reserve, downward stacked reserve, and no reserve cases

Figure 9.44 shows points resembling the PQ interchange at the PCC of all possible scenarios of dispatched products. The term “Upward Reserves” in Figure 9.44 includes all upward reserve products, whether individual or stacked. Similarly, for the term “Downward Reserves”. Notice how providing upward reserve products extends the range of the active power exports to the right of the figure with respect to the case when no reserve is provided. Similarly, the provision of downward reserve products extends the active power exports to the left of the figure. All PQ point lie within the power factor limits.

The inverse proportion relation between the active power and reactive power noticed in the previous case study is not appearing here because voltage support is not considered in this case.

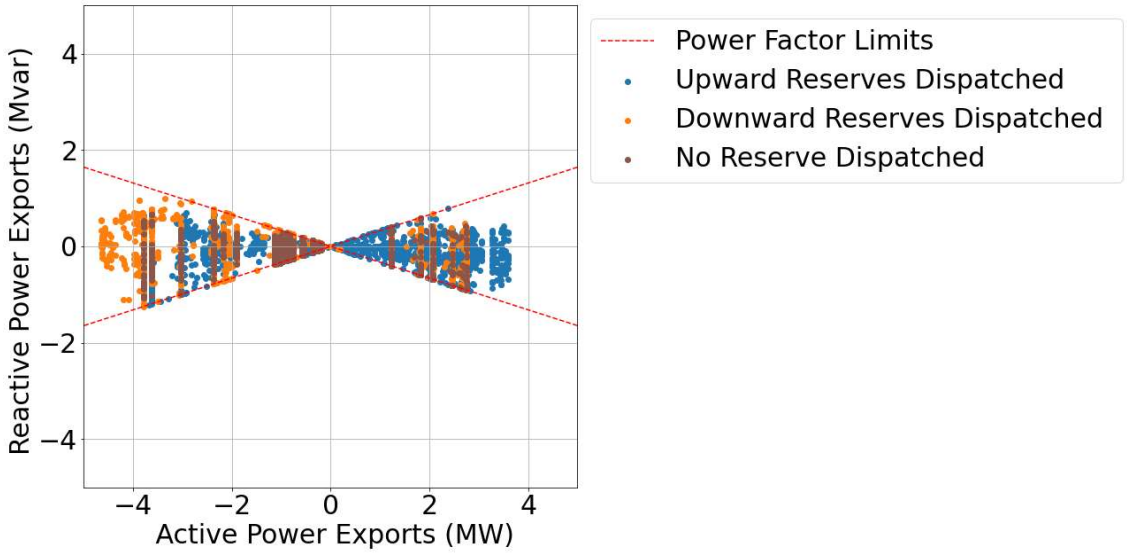

Figure 9.44. PQ interchange at the PCC

Figure 9.45, Figure 9.46, and Figure 9.47 show histograms of the µG bus voltages when upward reserves, downward reserves, and no reserves are dispatched, respectively. All bus voltages were within the limits. One can observe how the provision of reserve, whether upward or downward, extends the range of the bus voltages relative to when no reserve is dispatched. Further, Figure 9.48, Figure 9.49, and Figure 9.50 show histograms of the µG's circuit loading when upward reserves, downward reserves, and no reserves are dispatched, respectively. All circuit flows were within their limits in all cases.

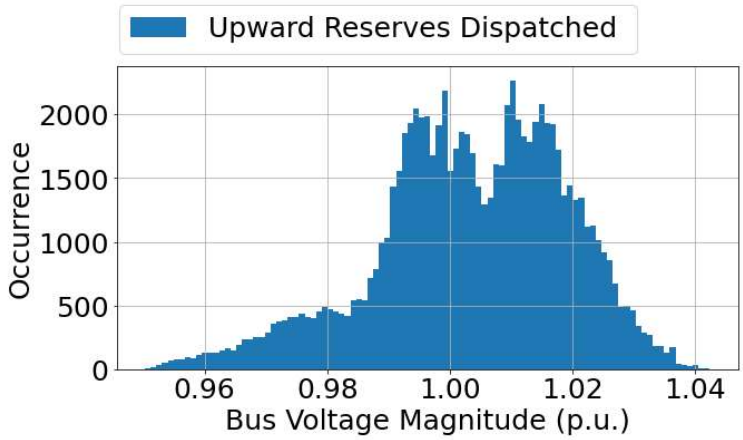

Figure 9.45. Bus voltage magnitudes when upward reserves are dispatched

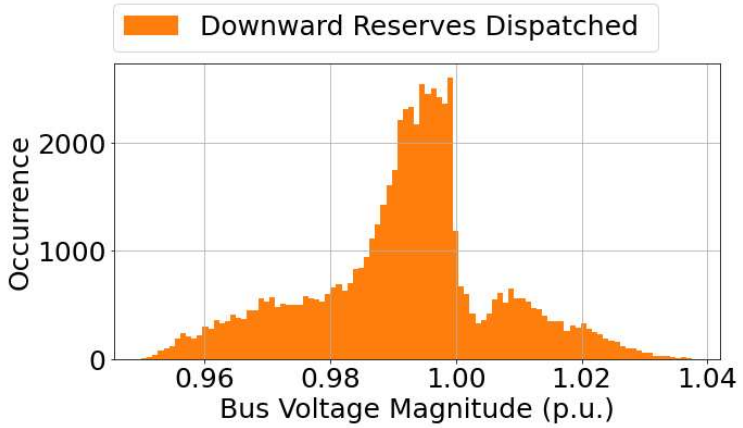

Figure 9.46. Bus voltage magnitudes when downward reserves are dispatched

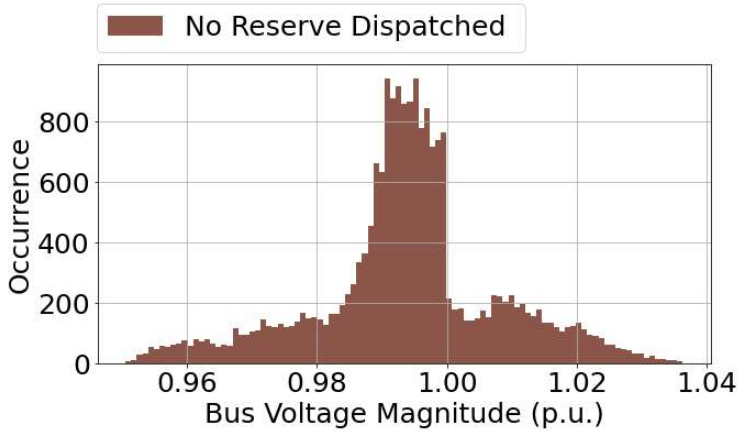

Figure 9.47. Bus voltage magnitudes when no reserve is dispatched

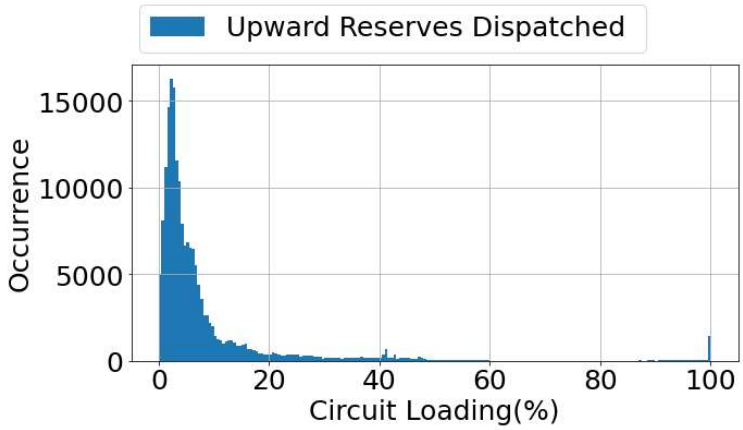

Figure 9.48. Circuits loading when upward reserves are dispatched

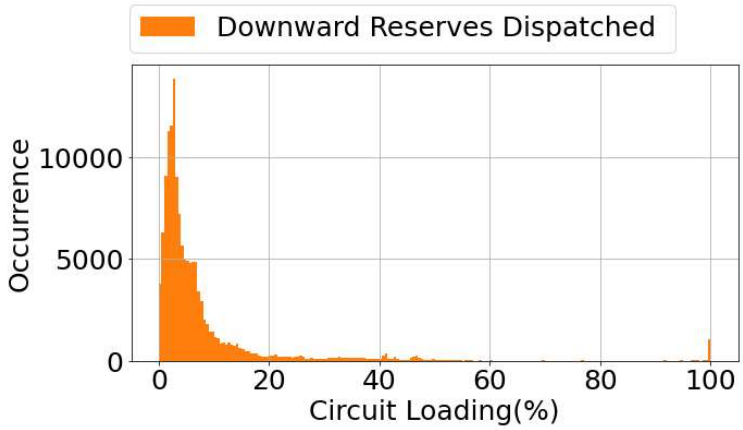

Figure 9.49. Circuits loading when downward reserves are dispatched

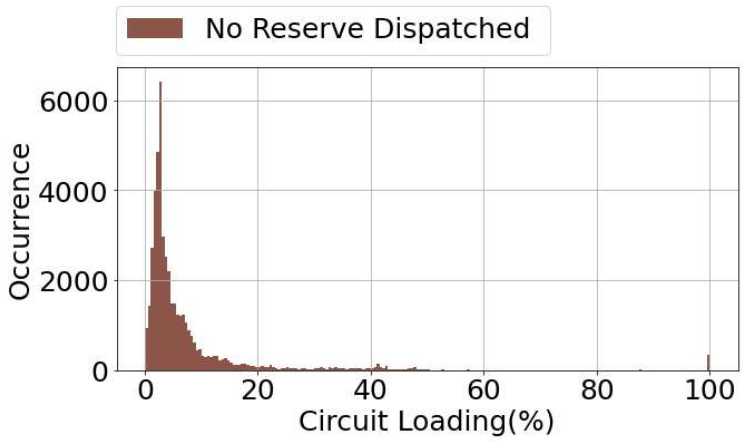

Figure 9.50. Circuits loading when no reserve is dispatched

Finally, Figure 9.51 shows a histogram of the computational time of all problems solved to compute the real-time reserve products and their costs. Most of the problems were solved in roughly 50 seconds with a maximum computational time of 90 seconds.

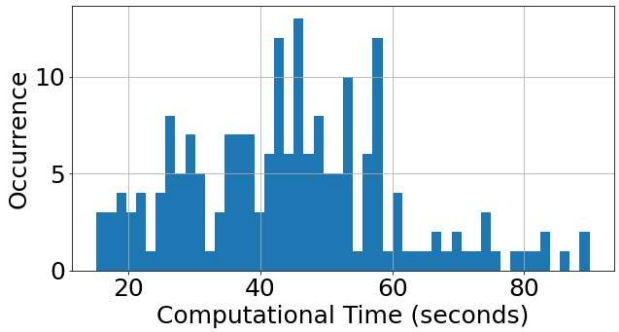

Figure 9.51. Computational times of all problems solved to find RT reserve products and costs

9.5 Summary

This chapter provided case studies that demonstrated service provision form a test μG using the proposed μGEMS. Two case studies were performed simulating the DA Commitment design and the RT Commitment design.

In the DA Commitment design, the μGEMS computed the optimal DA power, reserve and regulation commitments. Then, the μGEMS optimized the operations planning and control of the μG during the operating day where the operation of the μG was simulated for an entire day with 1 minute frequency. We demonstrated in the case study how the μG was able to follow the DA power commitment, and respond to reserve and regulation calls within the committed time, for the committed capacity, and for the requested maintainability time. In addition, voltage support was provided simultaneously by minimizing the deviation of the PCC voltage from 1 p.u.. The provision of voltage support resulted in a more stable reactive power interchange at the PCC relative to when voltage support is not provided. We also computed the lost-of-opportunity cost for the provision of voltage support which can be submitted to the external grid for compensation.

In the RT Commitment design, the μGEMS first computed the DA power commitments. Then, throughout the operating day, the μGEMS computed multiple reserve products along with the lost-of-opportunity cost of each product. Both individual and stacked reserve products were computed. The reserve products were computed at the beginning of each hour of the operating day. The provided reserve types included upward and downward primary reserves, upward and downward secondary reserves, and tertiary reserve.

In both cases, bus voltage limits, circuit flow limits, and power factor limits were enforced and were maintained within acceptable ranges via the μGEMS. We showed how the network limits and power factor limits are stressed when services are provided indicating the importance of considering these constraints in the model of the μGEMS. Moreover, the computational times for all optimization problems solved were reported and were within adequate ranges signifying the effectiveness of the proposed hierarchical structure of the μGEMS augmented with the proposed SLP solution methodology.

CHAPTER 10. EXTERNAL GRID RELIABILITY ASSESSMENT WITH AND WITHOUT MICROGRIDS SERVICES

10.1 Introduction

One of the main goals of procuring ancillary services from μGs is to improve the reliability of the system or the local area where the μGs are connected. In this chapter, we assess the reliability of a system when services are procured from connected μGs. We benchmark the assessment with a base case study where the connected μGs do not provide services to the system. The studies are based on Markov Chain Monte Carlo (MCMC) simulation [80] where we simulate the operation of the system through multiple sampled years.

The model of the system is described in section 10.2 and the simulation procedure is detailed in section 10.3. In section 10.4, we present the input data of the study along with the results and discussion. Finally, a summary of the chapter is presented in section 10.5.

10.2 System Model

The system model is depicted in Figure 10.1. The system includes multiple connected μGs, a main load, and a system supply. The μGs are modeled as described in chapter 4 which in general contain multiple busses and are AC networks. The main load is modeled as an active power consumption device, and the system supply is modeled as an active power generation device. All three distinct components of the system are connected at the PCC bus. The voltage of the PCC bus is assumed fixed. Reactive power is considered within the μGs to ensure the feasibility of the μGs' networks in normal operation, and in

service operation when services are provided to the system. However, the reactive power is neglected for the system supply and main load.

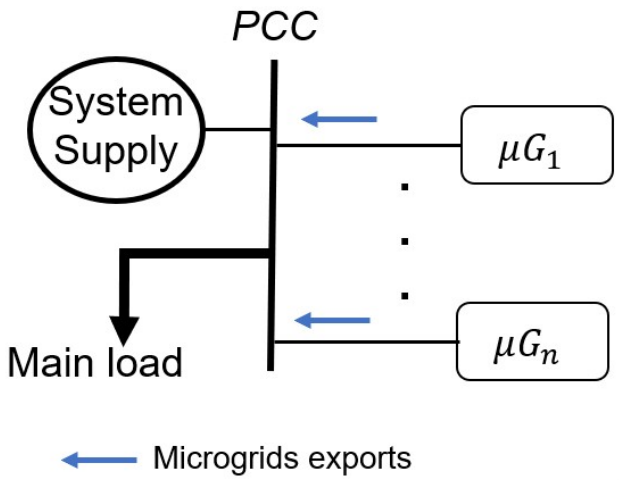

Figure 10.1. System model

10.2.1 Microgrid Model and Operational Modes

Let the optimal power exports of µG i at time step t be represented by $p_{i,t}^{\mu G,mode*}$ where $mode$ represents the operational mode of the µG, and $mode \in \{base, services\}$. In $base$ mode, the µG operation is optimized via the problem presented in section 5.2.1 (without considering the services) which minimizes the operational cost given an energy rate ($/kWh) at the PCC. In $services$ mode, the µG operation is optimized using the RT commitment problem in section 5.3 which maximizes the available real-time services at the PCC. We consider three services in the reliability assessment: 1) upward primary reserve supplied within 1 minute and maintained for 10 minutes, 2) upward secondary reserve supplied within 10 minutes and maintained for 1 hours, and 3) upward tertiary reserve supplied within 1 hour. The maintainability of tertiary reserve is not restricted by a time. Rather, we use the objective function in (5.46) which maximizes the maintainability time of tertiary reserve. Note that only upward reserve capacitates are considered. We focus

in the reliability assessment on system supply shortage and assume the system supply operator has enough downward reserve capacity.

10.2.2 Main Load, Total Load, and System Supply Models

The main load in the study is taken as given hourly data. Let the main load be expressed by P_t^{main} . Then, the total system load seen by the system supply can be expressed as follows:

$$p_t^{mode} = P_t^{main} - \sum_{\forall i} p_{i,t}^{\mu G,mode*} \tag{10.1}$$

where $mode \in \{base, services\}$ represent the total load when the μGs are operating in the base and services modes, respectively.

The system supply is molded as having an active power capacity p_t^{ss} , in addition to separate upward reserve capacities r_t . The separation between the power capacity and reserve capacities is analogues to a utility supplying its own demand, but not participating in self-provision of ancillary services; the required ancillary services for the utility's area are procured from another entity.

Starting with p_t^{ss} , it is modeled as a multi-state probabilistic model. Each state represents a percentage of available power capacity with respect to a given value of the total power capacity (G^{ss}). To illustrate, let i_t represent the system's state at time t. The available power capacity at time *t* is then defined as follows:

$$p_t^{ss} = G^{ss} \times s_{i_t} \quad \text{where } s_{i_t} \in [0,1] \tag{10.2}$$

Assuming the state durations of the systems' available power capacity follow an exponential distribution function, the system power capacity can be modeled as a Continuous Time Markov Chain (CTMC) [81]. Figure 10.2 depicts the state transition diagram of the CTMC considering three states as an example. The CTMC is fully described by the transition rate matrix Q in Figure 10.2. The entry q_{ij} for $i \neq j$ is the transition rate from state i to state j, while $q_{ii} = -\sum_{\forall j \neq i} q_{ij}$.

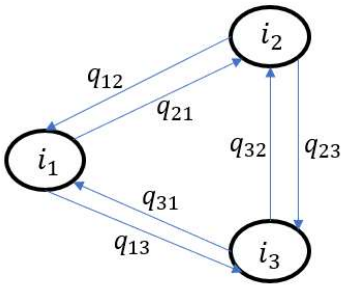

$$Q = \begin{bmatrix} -(q_{12}+q_{13}) & q_{12} & q_{13} \\ q_{21} & -(q_{21}+q_{23}) & q_{23} \\ q_{31} & q_{32} & -(q_{31}+q_{32}) \end{bmatrix}$$

Figure 10.2. State transition diagram and transition rate matrix

From the matrix Q, we may deduce the embedded Discrete Time Markov Chain (DTMC) which defines the transition probabilities $P_{i,j}$ as given in (10.3). Both the transition rates $q_{i,j}$ and the transition probabilities $P_{i,j}$ are used in the simulation procedure explained later in section 10.3.

$$P_{i,j} = \begin{cases} \dfrac{q_{i,j}}{\sum_{\forall j \neq i} q_{i,j}} & i \neq j \\ 0 & i = j \end{cases} \tag{10.3}$$

Further, the system supply operator is assumed to have three types of reserves available for dispatch. The reserve types are: 1) primary reserve supplied within 1 minute and maintained for 10 minutes, 2) secondary reserve supplied within 10 minutes and maintained for 1 hour, and 3) tertiary reserve supplied within 1 hour and maintained indefinitely. The reserve capacity available of each type is defined as a percentage of the day peak of the total system load in the base case, p_t^{base}. To illustrate, suppose an incident n occurred at t^n, and let $p_{t^n}^{base,day.peak}$ represents the peak of p_t^{base} at the day of t^n. Then, the reserve capacity available for the system supply operator can be expressed as follows:

$$r_t = \begin{cases} R_P p_{t^n}^{base,day.peak} & t^n \le t < t^n + 10\,\text{min} \\ R_S p_{t^n}^{base,day.peak} & t^n + 10\,\text{min} \le t < t^n + 1hr \\ R_T p_{t^n}^{base,day.peak} & t^n + 1hr \le t \end{cases} \tag{10.4}$$

where R_P, R_S, and R_T are given parameters for primary, secondary, and tertiary reserves, respectively. Note that while primary reserve takes seconds to 1 minute in practice to reach full capacity from the time of dispatch, we assume here that it is available at the instant of an incident. That is, we neglect the power imbalance in the system from $[t^n, t^n + 1\text{min})$.

10.3 Simulation Procedure

The overall simulation procedure is shown in the flow chart in Figure 10.3. The reliability of the system is assessed in two cases: the base case (left side of the flow chart), and the services case (right side of the flow chart). The base case is when no services are provided from the μGs while the services case is when services are provided from the μGs.

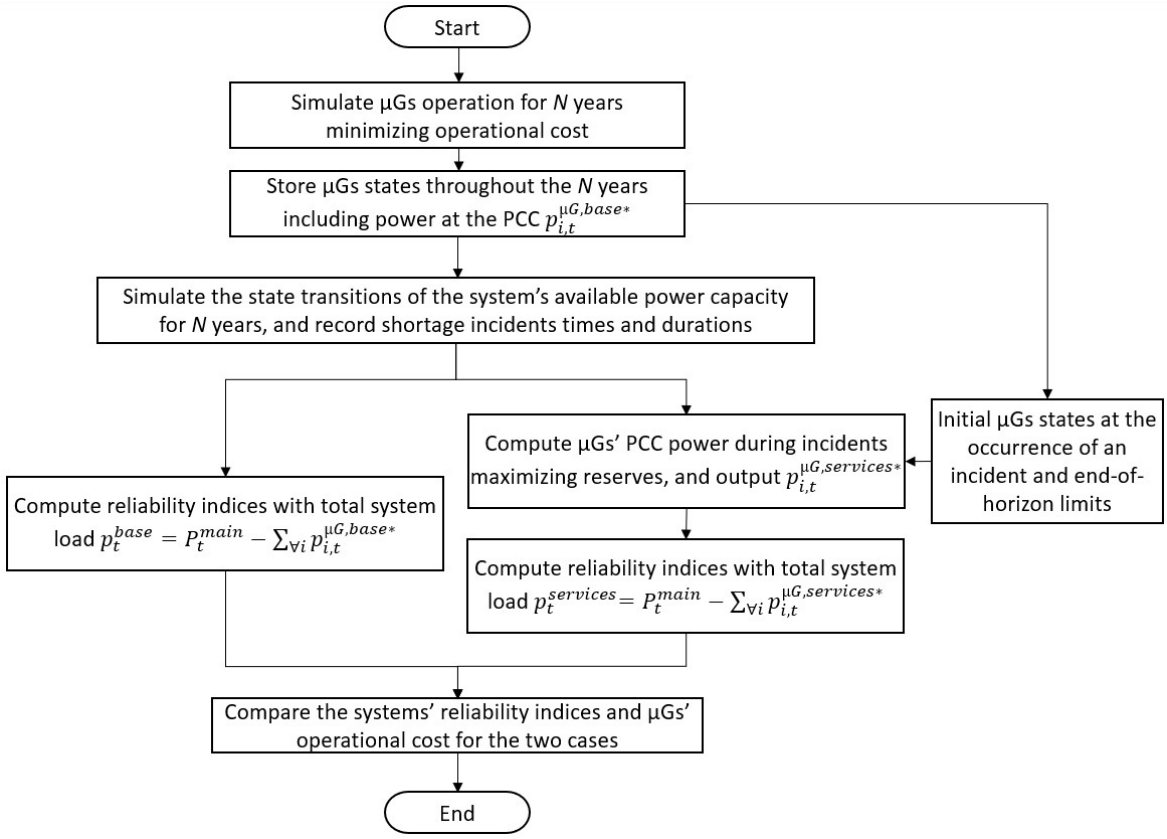

Figure 10.3. Overall simulation procedure

The simulation is performed for N years. Given hourly data for the main load, µGs net-demand, ambient temperature, and energy cost at the PCC for the N years, the simulation procedure in Figure 10.3 starts by simulating the operation of the µGs minimizing the operational cost. We duplicate available data of 1 year to represent the N years of the simulation. We then optimize the operation of the µGs through the 1 year minimizing the operational cost. The problem minimizing the operational cost of the µG is solved 365 times each with 1-day horizon and hourly steps. The end-of-horizon limits for storage-based devices at each optimized day are assumed to be in the middle of the device limits. The optimized days are solved in a consecutive manner to consider the minimum up and minimum down times of the DG units; the commitment of a DG unit at a given day may be restricted due to the DGs commitment in the previous day. Once the µGs are

simulated, we may compute the base case total system load seen by the system supply throughout the year (p_t^{base}) as shown in (10.1). Without loss of generality, the total power capacity of the system is taken to be equal to the peak of the total system load ($G^{ss} = \max\{p_t^{base} : t = 1, 2, ..., 8760\}$).

After simulating the operation of the μGs and storing their states throughout the year, the system's available power capacity state transitions are simulated considering hourly steps. The simulation up until hour $T_N = 8760 \times N$ is outlined in the algorithm below:

Algorithm: Sampling System Supply State Transitions

1: **Set** $n = 0$, $t = t^n = 0$ and chose an initial state, $X^n = i^0$.
2: **Sample** residence time at state X^n (also called hold time) via the inverse transform method:

$$T^n = -\frac{\ln(U)}{\sum_{\forall j \neq i} q_{i.j}} \qquad s.t. \quad i = X^n, \;\; U \sim unif[0,1]$$

3: **Record** transition time $t^n = t + T^n$
4: **Sample** and **record** destination state:

$$X^{n+1} = j \qquad s.t. \quad \sum_{k=1}^{j-1} P_{kj} < U \leq \sum_{k=1}^{j} P_{kj}, \;\; U \sim unif[0,1]$$

5: **Set** $n = n + 1$, $t = t + T^n$
6: **If** $t > T_N$, stop, **else**, go to step 2

The algorithm above outputs a sequence of states for the system's available power capacity $X^0, X^1, \ldots, X^n$ along with the associated transition times $t^0, t^1, \ldots, t^n$. We use these values to assess the reliability of the system in both: the base case and the services case.

To assess the reliability of the system, we locate the transitions leading to states with shortage of supply (i.e., $p_t^{base} > (p_t^{ss} + r_t)$ and compute the energy not served (ENS) and Unavailability (U) of the incidents. Suppose an incident occurs at time t^n leading to a state with shortage of supply. Then, ENS and U of the incident at the base case are computed as follows:

$$ENS_n^{base} = \sum_{t=t^n}^{t^n+T^n} \max\{0, p_t^{base} - (p_t^{ss} + r_t)\}$$
$$U_n^{base} = \sum_{t=t^n}^{t^n+T^n} \mathrm{I}_+(p_t^{base} - (p_t^{ss} + r_t)) \quad (10.5)$$

where $\mathrm{I}_+(x)$ is an indicator function that equals 1 if $x > 0$, and zero otherwise. Recall that p_t^{base} is the total system load seen by the supply in the base case as defined in (10.1), p_t^{ss} is the available power capacity defined in (10.2), and r_t is the reserve capacity available for the system operator as defined in (10.4). Note that the length of the time step when calculating the ENS and U as is taken to be 10 minutes. This is to consider the changing reserve available for the system supply operator which changes in 10 minutes steps. Linear interpolation is used to extract 10min steps for the total load p_t^{base}. Also, recall that the frequency considered for the residence time of a state before transitioning to another state is taken to be 1 hour in the simulation. Therefore, whenever a new state is entered, the primary and secondary reserves are fully restored, while the tertiary reserve may still be operating from the previous state.

The reserve available for the system supply operator was defined within three time regions: primary reserve region ($t^n \leq t < t^n + 10\text{min}$), secondary reserve region ($t^n + 10\text{min} \leq t < t^n + 1\text{hr}$), and tertiary reserve region ($t^n + 1\text{hr} \leq t$). Due to this change in reserve within these three regions, and for the purpose of computing finer reliability metrics, we compute separate ENS and U values for each of the three regions. Let T_{R_P}, T_{R_S}, and T_{R_T} represent the time regions of primary, secondary, and tertiary reserves,

respectively. Then, the ENS and U for each of the three regions at the base case are computed as follows:

$$\begin{aligned} ENS_n^{base,R_i} &= \sum_{\forall t \in T_{R_i}} \max\{0, p_t^{base} - (p_t^{ss} + r_t)\} \\ U_n^{base,R_i} &= \sum_{\forall t \in T_{R_i}} \mathrm{I}_+(p_t^{base} - (p_t^{ss} + r_t)) \\ i &\in \{P, S, T\} \end{aligned} \tag{10.6}$$

The ENS and U in the services case are computed in a similar manner. However, before computing them, the μGs profiles during the services mode ($p_{i,t}^{\mu G,services*}$) are computed by solving the RT commitment problem. Recall that this problem optimizes the real-time available reserve at the PCC of the μGs given wights for each reserve type (see the objective function in (5.46)). In the reliability assessment study, we set the weights of the optimization problem for the primary, secondary, and tertiary reserves as follows:

$$w_{R_i} = 100 \times \frac{ENS_n^{base,R_i}}{\sum_i ENS_n^{base,R_i}} \qquad i \in \{P, S, T\} \tag{10.7}$$

Therefore, the weight for each reserve type will depend on the scarcity of this type of reserve relative to the other types as seen by the system supply operator. The weights can be viewed as real-time price signals. Moreover, the RT commitment problem is solved with a horizon of 6 hours and 10-minute steps resulting in 36 time periods. As indicated in the far right of the flow chart in Figure 10.3, the initial state of a μG is fed to this problem from the μG's states stored when solving for the base case PCC profile. The end-of-horizon

limits are also taken from the stored states of the μG. By comparing the operational cost of the μG in the $base$ mode and in the $services$ mode within the optimized 6 hours, we may obtain the μGs' incurred cost from providing the services. Notably, the duration of the incident is assumed known by the μG. By this, the μG may avoid maximizing reserves during regions where the incident will be revealed. Also, we assume that the μGs provide reserves for a maximum of 6 hours from the occurrence of an incident. This is to limit the number of time periods in the optimization problem to 36 and to expedite the solution process in the reliability assessment case study.

Once the μGs profiles with the provision of services are computed (i.e., $p_{i,t}^{\mu G,services*}$), we may calculate the ENS and U for the services case as follows:

$$\begin{aligned} ENS_n^{services} &= \sum_{t=t^n}^{t^n+T^n} \max\{0, p_t^{services} - (p_t^{ss} + r_t)\} \\ U_n^{services} &= \sum_{t=t^n}^{t^n+T^n} \mathrm{I}_+(p_t^{services} - (p_t^{ss} + r_t)) \end{aligned} \tag{10.8}$$

where

$$p_t^{services} = \begin{cases} P_t^{main} - \sum_{\forall i} p_{i,t}^{\mu G,services*} & for \quad t \le t^n + 6\text{hrs.} \\ P_t^{main} - \sum_{\forall i} p_{i,t}^{\mu G,base*} & otherwise \end{cases} \tag{10.9}$$

Similar to the base case, in the services case, we also compute separate ENS and U for each of the three reserve regions:

$$
\begin{aligned}
ENS_n^{services,R_i} &= \sum_{\forall t \in T_{R_i}} \max\{0, p_t^{services} - (p_t^{ss} + r_t)\} \\
U_n^{services,R_i} &= \sum_{\forall t \in T_{R_i}} \mathrm{I}_+(p_t^{services} - (p_t^{ss} + r_t)) \\
i &\in \{P, S, T\}
\end{aligned}
\tag{10.10}
$$

Once the ENS and U for all simulated incidents across all sampled years are computed, we calculate the expected energy not served (EENS) and the loss of load expectation (LOLE) as follows:

$$
\begin{aligned}
EENS^{case} &= \frac{1}{N} \sum_{\forall n} ENS_n^{case} \,/\, 6 \\
LOLE^{case} &= \frac{1}{N} \sum_{\forall n} U_n^{case} \,/\, 6 \\
case &\in \{base, services\}
\end{aligned}
\tag{10.11}
$$

Similarly, the EENS and the LOLE for each reserve region are computed as follows:

$$
\begin{aligned}
EENS^{case,R_i} &= \frac{1}{N} \sum_{\forall n} ENS_n^{case,R_i} \,/\, 6 \\
LOLE^{case,R_i} &= \frac{1}{N} \sum_{\forall n} U_n^{case,R_i} \,/\, 6 \\
case &\in \{base, services\} \\
i &\in \{P, S, T\}
\end{aligned}
\tag{10.12}
$$

The division by 6 is included in (10.11) and (10.12) because the time step of computing ENS and U was in 10 minutes (1/6 hours). Hence, with this division, the resultant EENS will be in MWh/year and the LOLE will be in hours/year.

10.4 Case Study

10.4.1 System and Input Data

A system with two μGs, a main load, and a system supply is considered. The two μGs have identical networks and DERs but have different internal net-demand profiles. The 33-bus test system illustrated in section 7.2 is used in this case study to represent each of the two μGs. Each μG contains four DGs, four ESSs, 31 TCLs, and 31 DULs (see section 7.2). We assume that the TCLs are operated throughout the year and are required to maintain the temperature within the household specified temperature limits. The DULs are assumed to operate once every day as per the household settings. The household settings for the TCLs and DULs are shown in Table 7.4 and Table 7.5 in section 7.2. The data in [76] contains one-year hourly net-demand profiles for multiple buses at the distribution level. These profiles are used as the net-demand profiles of the busses in μG1. The net-demand profiles in μG2 are generated randomly using the net-demand profiles of μG1. Figure 10.4 show histograms of the total net-demand of μG1 and μG2. Moreover, the one-year hourly ambient temperature is taken from [78] and its histogram is shown in Figure 10.5. The one-year energy rate seen by the μGs at the PCC is also taken from [78] and is defined with four tiers as illustrated in Figure 10.6 and Table 10.1. Additionally, the main load one-year hourly demand is taken from [82] and its histogram is shown in Figure 10.7.

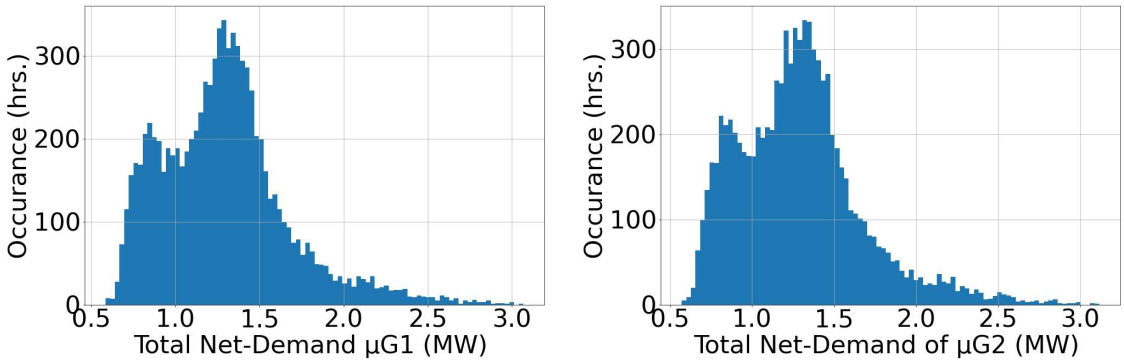

(a) (b)

Figure 10.4. (a) total net-demand of µG1, and (b) total net-demand of µG2

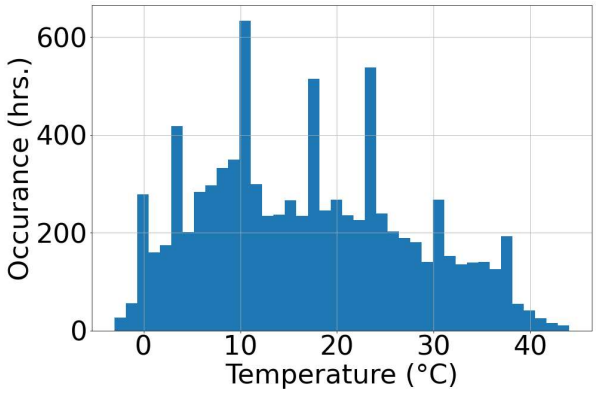

Figure 10.5. Ambient temperature

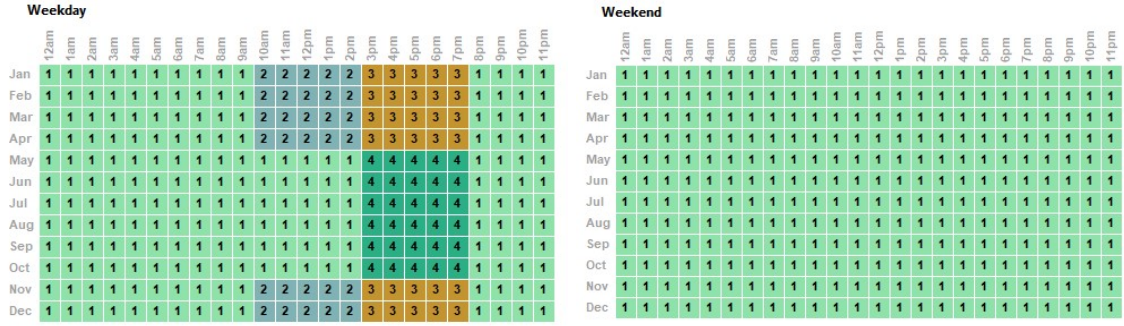

Figure 10.6. Tiers of the energy rate at the PCC

Table 10.1 Rate definitions of the Tiers

Tier No.	1	2	3	4
Rate ($/kWh)	0.1	0.05	0.2	0.25

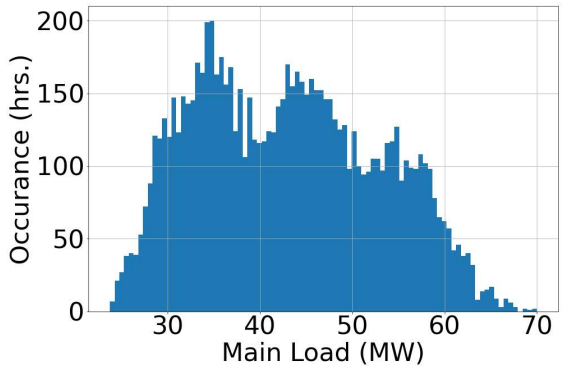

Figure 10.7. Hourly demand of the main load

The system's available power capacity is modeled with 3 states defined in Table 10.2. The transition rates from distinct sates are listed in Table 10.3 and are aligned with the work in [83]. The total system power capacity is taken to be equal to the one-year peak of the total system load which is 74.42 MW. Lastly, the assumed available reserve capacities to the system supply operator are given in Table 10.4.

Table 10.2 Available power capacity as a percentage of total power capacity

State	1	2	3
Available Power Capacity (%)	100	66.6	33.3

Table 10.3 State transition rates of the power supply model

From State	1	1	2	2	3	3
To State	2	3	1	3	1	2
Transition Rate (1/hr)	4/8760	2/8760	1	1/8760	1/2	1

Table 10.4 Reserves available for the system supply operator

Reserve Type	Primary	Secondary	Tertiary
Quantity as % of the daily total system load peak	5	15	30

10.4.2 Simulation Results

The simulation is performed for 500 years by duplicating the 1-year data of main load, μGs net-demand, ambient temperature, and energy rate at the PCC. Figure 10.8 show histograms of the μGs' 1-year power exports at the PCC, respectively, after optimizing their operations by minimizing their operational cost.

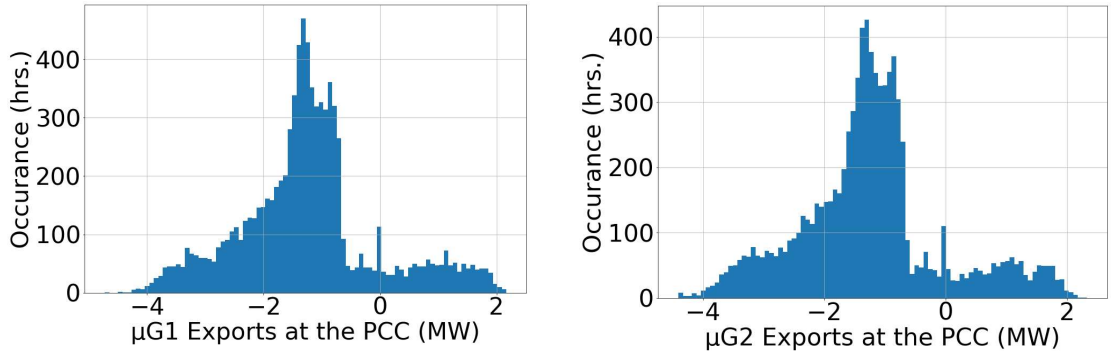

(a) (b)

Figure 10.8. (a) power exports of μG1, and (b) power exports of μG2

The reliability of the system is assessed considering two cases: 1) base case when services are not provided from the μGs, and 2) services case when services are provided form the μGs. The EENS for the three time regions (i.e., primary reserve, secondary reserve and tertiary reserve regions) are computed for both cases and the convergence of their values after running the MCMC simulation are shown in Figure 10.9 and Figure 10.10, respectively. Similarly, Figure 10.11 and Figure 10.12 show the convergence of the LOLE for the base case and the services case, respectively, for all three time regions. Table 10.5 and Table 10.6 summarizes the EENS and LOLE values for both cases at all regions.

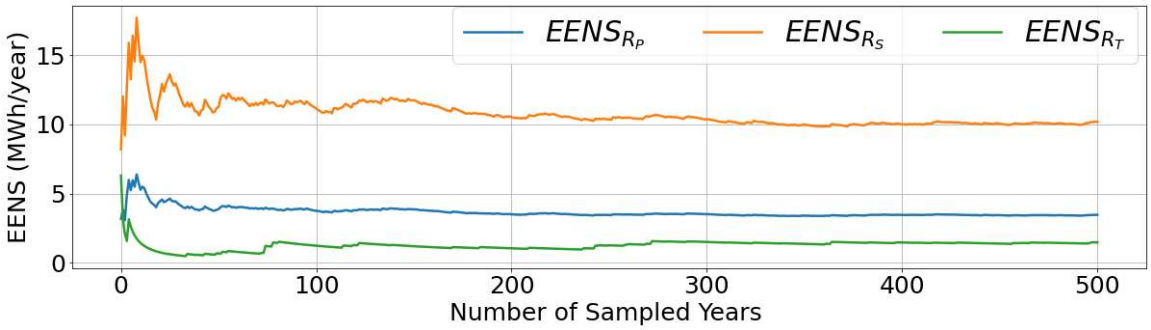

Figure 10.9. Base case EENS for the three time regions

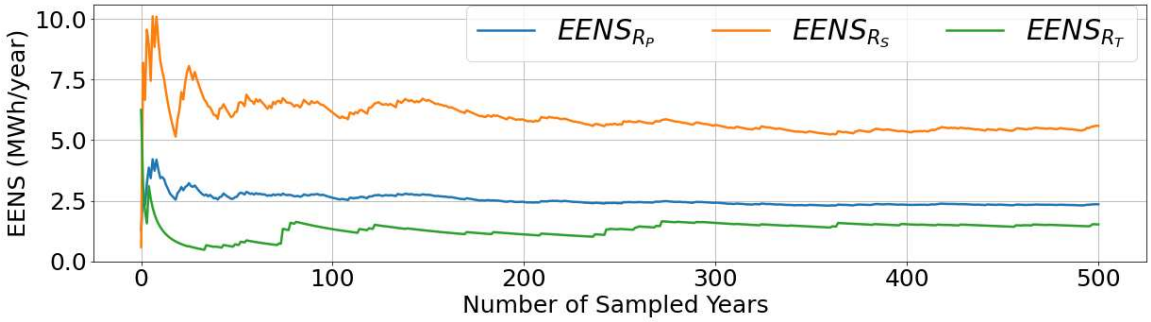

Figure 10.10. Services case EENS for the three time regions

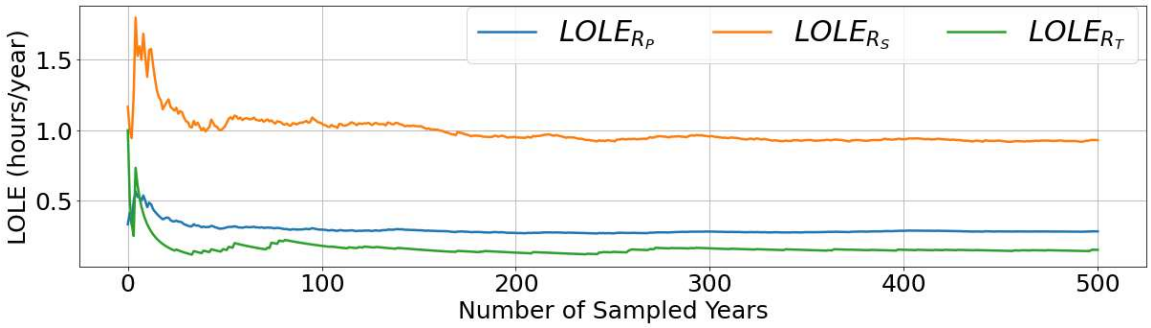

Figure 10.11. Base case LOLE for the three time regions

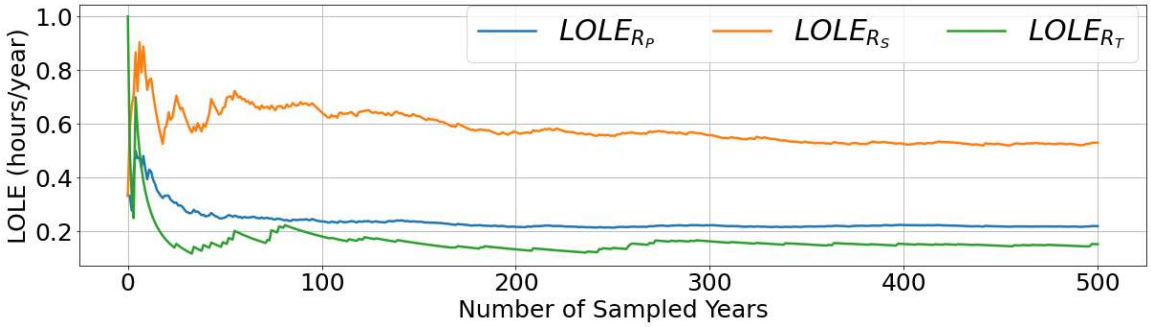

Figure 10.12. Services case LOLE for the three time regions

Table 10.5 EENS for base case and services case

	$EENS_{R_P}$ (MWh/yr.)	$EENS_{R_P}$ (MWh/yr.)	$EENS_{R_P}$ (MWh/yr.)	Total *EENS* (MWh/yr.)
Base Case	3.46	10.17	1.47	15.10
Services Case	2.35	5.59	1.52	9.46
Improvement	32.08%	45.03%	-3.40%	37.35%

Table 10.6 LOLE for base case and services case

	$LOLE_{R_P}$ (hrs./yr.)	$LOLE_{R_P}$ (hrs./yr.)	$LOLE_{R_P}$ (hrs./yr.)	Total *LOLE* (hrs./yr.)
Base Case	0.283	0.929	0.151	1.363
Services Case	0.220	0.530	0.153	0.903
Improvement	22.26%	42.95%	-1.32%	33.75%

Substantial improvements in the EENS and LOLE are recorded for the primary reserve and secondary reserve regions when services are provided from the μGs. This is due the ability of the μGs to supply fast reserve (primary and secondary). Interestingly, the EENS and LOLE for the tertiary reserve region slightly worsened when services were provided from the μGs. The reason is as follows: in some incidents, the μGs can only provide primary and secondary reserve without providing any tertiary reserve. After providing these reserves, the μGs optimize their operation as to return to their optimal economical operation trajectory. This behaviour of returning to the optimal trajectory after providing the primary and secondary reserves is what causes the decline in the EENS and LOLE of the tertiary reserve region. To illustrate the behaviour of returning to the optimal trajectory, Figure 10.13 shows the active power exports at the PCC of μG1 during a sample incident with a duration of 4 hours. The figure shows the power exports for the base case and the services case. Observe how the μG in the services case provides primary and secondary reserve during the first hour. Then, during the remaining hours of the incident duration, the μG exports drop to a value that is less than that of the base case in order to return to the optimal trajectory. Storage based devices such as ESSs and TCLs are the reason behind this behaviour. Consider an ESS that has been fully charged and is scheduled to export during high grid prices. If reserve is procured from the ESS during an incident and before the high grid prices, the μGEMS will try to recharge the ESS before the high grid prices.

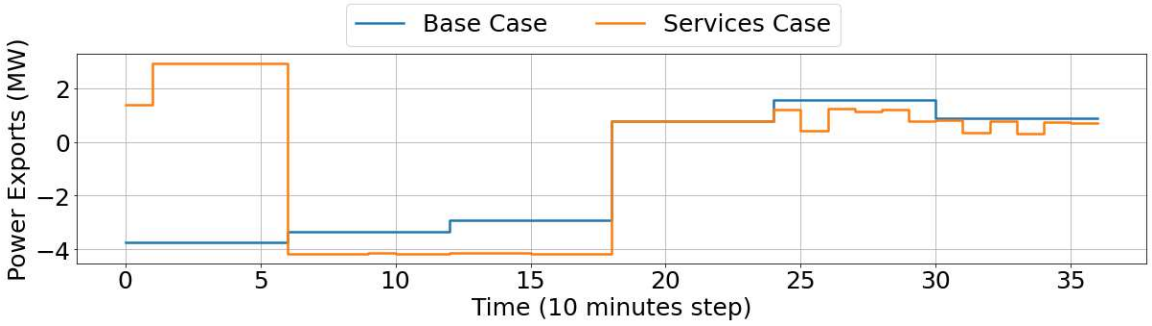

Figure 10.13. Power exports of µG 1 in base case and services case at an incident

Finally, Figure 10.14 plots the convergence of the total µGs operational cost increase from providing services (i.e., cost of services case minus cost of base case). The expected yearly cost after simulating the 500 years was $1,474.03. This cost represents the cost for improving the reliability of the system.

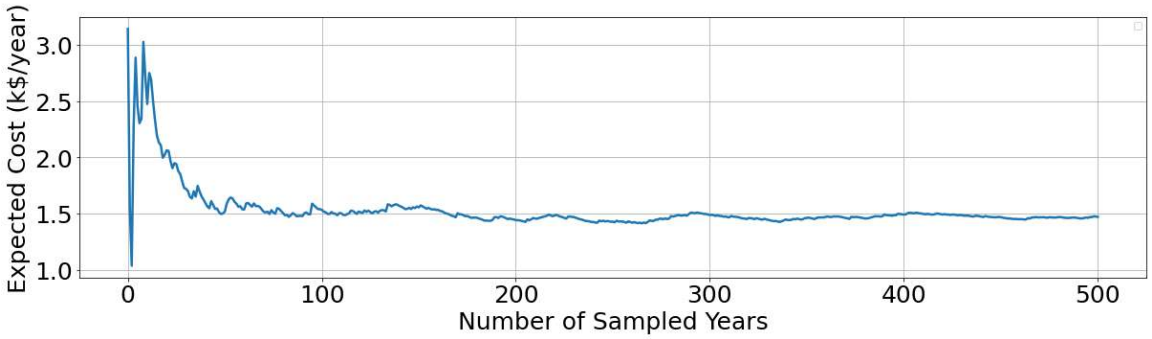

Figure 10.14. Total µGs' operational cost increase from providing services

10.5 Summary

In this chapter, we presented a reliability assessment case study to quantify the reliability improvements of a system when services are provided from connected µGs. The case study was based on MCMC simulation. The studied system consisted of a system supply, a main load, and two connected µGs. The system's available power supply was modeled as CTMC with multiple states each representing the shortage in available power supply. We used the inverse transform method to sample shortage incidents and assess the reliability of the system. The system was simulated multiple years and the reliability was

assessed under two cases: 1) when no services are provided form the connected μGs (base case), and 2) when services are provided from the connected μGs (services case). The EENS and LOLE for each case were computed and it was shown that the provision of services from the μGs improved the EENS by 37.35% and the LOLE by 33.75%. Additionally, we computed the expected cost incurred by the μGs from the provision of services which was $1,474.03 This cost represents the cost for improving the reliability of the system.

CHAPTER 11. CONCLUSIONS AND FUTURE RESEARCH DIRECTIONS

11.1 Conclusions

11.1.1 Summary and Contributions

This Thesis has made the following contributions:

1) We proposed the multi-case multi-period μG mathematical model. The network was modeled as generally being an AC meshed network and current formulation was used. We also modeled several DERs each having its own operational characteristics: distributed generators (DGs), energy storage systems (EESs), and household appliances including thermostatically controlled loads (TCLs), and deferrable uninterruptible loads (DULs). The model of the μG allows controlling these DERs while ensuring the network feasibility for multiple prospective operating points (cases) across a future time horizon (periods). We compared the current formulation with a power balance formulation by optimizing the operation of multiple μG test systems using each approach. Both gave similar optimal values. The current formulation, however, was computationally faster than the power balance formulation.
2) We proposed the μGEMS that optimally *plans the operations*, and *control* the DERs while *committing*, *holding*, *dispatching*, and *maintaining* different ancillary services including reserve, regulation, and voltage support, simultaneously. The proposed μGEMS may be used to commit the services a Day-Ahead in advance to

dispatch, or in real-time. Commitment rules of the μGEMS include minimum capacities, time to respond, and time to maintain. The μGEMS also ensures a feasible operation of the network without violating bus voltage, circuit loading, and PCC power factor limits. The operation of a 33-bus μG was optimized using the μGEMS with a frequency of 1 minute while considering forecast errors. The μGEMS showed good performance keeping feasible operation during the *commitment*, the *holding*, the *dispatching*, and the *maintaining* stages of services.

3) We also proposed a solution method based on successive linear programming (SLP). The solution method controls the trust regions of continuous variables depending on their oscillation as the SLP iterations progress. Also, as the SLP iterations progress, the solution method detects unchanging discrete variables, and fixes them to their value, and by that, substantially reducing the number of discrete variables in upcoming iterations. The SLP method was benchmarked against three methods, the second order conic programming (SOCP) method [12], the quadratic convex (QC) method [13], and Gurobi's global solver [14]. The SLP method computed near global optimal solutions in the majority of the cases. For the remaining cases, there were no "trustworthy" lower optimality bound. We showed that unlike the SLP method, the feasibility of solutions and the optimality gaps of the SOCP and the QC methods depended on the objective function of the problem. The SLP method also outperformed all methods in terms of scalability.
4) We performed a reliability assessment case study to measure the improvement in reliability of a system when services are provided from multiple μGs, each operated via the proposed μGEMS. We simulated the system across multiple sampled years

using Markov Chain Monte Carlo (MCMC) simulation. It was shown that the provision of services from connected μGs improved two reliability indices: the expected energy not served (EENS), and loss of load expectation (LOLE) of the system.

11.1.2 Concluding Remarks

1) The provision of ancillary services can stress the network of the μG including bus voltage limits and circuit flow limits. In addition, the provision of services may drive the μG to operate in undesired power factor regions. This can be seen from our results in chapter 9. Hence, considering these limits when *committing*, *holding*, *dispatching* and *maintaining* the services is necessary to avoid operational violations.
2) To respond to grid calls for capacities, new optimal controls need to be computed for the DERs in short periods of time (less than a minute). The speed in finding new optimal controls is also crucial to "regulate" and support the PCC voltage, which generally varies very frequently. One may pre-assign a single or multiple DERs to respond to fast calls and voltage variations. Pre-assigning, however, might under-estimate the capability of the collective DERs (suboptimality), or may result in infeasible controls due to the unpredictability of net-demand and ambient temperature (infeasibility). Having a real time controller becomes necessary to achieve an economical (optimal) and reliable (feasible) provision of services, as we demonstrated in section 9.3.2.
3) The provision of services from μGs alters their optimal trajectory of operation. This is during external grid calls, and more importantly, after the call has been lifted.

After the call has been lifted, the power exports at the PCC tend to deviate from the pre-scheduled optimal exports as we showed in section 9.4.2 and section 10.4.2. This is mainly due to storage based DERs where they charge/discharge or cool/heat after the call to return to their optimal pre-scheduled states. Therefore, a) when computing the lost-of-opportunity cost from providing the services, a future horizon should be considered to measure the economic effects of returning to the optimal operational trajectory, and b) when multiple μGs are providing services, the external grid should account for the anticipated behaviour of μGs' returning to their optimal trajectory. The μGs may be collectively optimized to reduce the impact of this behaviour as seen by the external grid.

11.2 Future Research Directions

1) The presented μG mathematical model is applicable to single-phase or balanced 3-phase systems. A possible extension for the model is to consider 3-phase unbalanced systems. This extension would increase the size of the model resulting a total of three dimensions of the μG model: 1) case dimension, 2) time dimension, and 3) phase dimension. The coupling between steps within a dimension may be weak paving the way towards the use of decoupled models and solution algorithms.
2) Distributed optimization methods can be utilized to potentially reduce the solution time and/or reduce the dependency on a central controller. The optimization problems of the μGEMS may be divided into weakly coupled subproblems. The sub-problems may represent steps in a particular dimension (case, time, or phase), or may represent a single DER. Additionally, distributed optimization may be applied across multiple independently controlled μGs; the external grid may

optimality and distributedly coordinate the procurement and dispatch of services from the μGs.

3) We used a simplified model for the reliability assessment case study where the external grid was modeled as single node with an active power supply and an active load. Modeling the external grid as an AC network would allow studying the impacts of, for example, the voltage support provided from the connected μGs. Distributed optimization can be used to optimize the interaction between the external grid and the μGs while limiting the shared information to those at the PCC.
4) The proposed μGEMS have shown good performance in operational feasibility against forecast errors in the case study presented in section 9.3. The simulated μG was able to respond to all service calls within required time, and with minimal deficiency, while following the DA committed plan. The good performance against forecast errors may be due to the service capacities being held for the external grid where the μG uses these capacities to absorb the forecast errors. Further studies quantifying the μGEMS capability against forecast errors can be performed.

APPENDIX A.THE CONVEXIFIED μG MATHEMATICAL MODELS

In this appendix, we present two convexified μG mathematical models that are used in the SOCP and the QC solution methods, respectively. These models are referred to as the SOCP model and the QC model. The SOCP model is presented in section A.1 and the QC model is presented in section A.2. Further, in section A.3, we illustrate why the tightness of these two models depend on the objective function of the problem.

A.1 The SOCP Model

The SOCP model is adapted from the work in [12]. The model uses the power balance formulation instead of the current formulation. Let the active and reactive bus power balance equations in the μG system be written as follows:

$$p_{kts}^{pq} + p_{kts}^{pcc} + p_{kts}^{fx} + \sum_{\forall m \in A(k)} p_{(km)ts}^{cr} = 0 \tag{A.1}$$

$$q_{kts}^{pq} + q_{kts}^{pcc} + q_{kts}^{fx} + \sum_{\forall m \in A(k)} q_{(km)ts}^{cr} = 0 \tag{A.2}$$

$\forall k \in \mathcal{K}$, $\forall t \in \mathcal{T}$, $\forall s \in \mathcal{S}$

where p_{kts}^{pq} and q_{kts}^{pq} represent the total active and reactive power injections into the PQ devices, p_{kts}^{pcc} and q_{kts}^{pcc} define the active and reactive power injections to the external grid Thevenin equivalent model, p_{kts}^{fx} and q_{kts}^{fx} are the active and reactive power injections into the fixed shunt device, and $p_{(km)ts}^{cr}, q_{(km)ts}^{cr}$ are the active and reactive power flow through a circuit from bus *k* to bus *m*. In the SOCP model, the definitions of the active and reactive power injections into the PQ devices are identical to those presented in (4.10) and (4.11)

in chapter 4, respectively, which sum up the power injections into the net-demand, the DGs, the ESSs, and the TCLs and the DULs of connected homes. Further, the operational equations and constraints of these DERs in the SOCP model are also identical to those presented in chapter 4, as they are all linear and do not require any convexification. The differences between the presented μG model in chapter 4 and the SOCP model occur in the external-grid Thevenin-equivalent injections, the fixed shunt injections, and the circuit injections which are defined next.

The active and reactive power injections into the Thevenin-equivalent model using the rectangular coordinates are as follows:

$$p_{kts}^{pcc} = G_{ts}^{eg}(e_{kts}^2 + f_{kts}^2) - G_{ts}^{eg}(e_{kts}E_{ts}^{r,eg} + f_{kts}E_{ts}^{i,eg}) + B_{ts}^{eg}(e_{kts}E_{ts}^{i,eg} - f_{kts}E_{ts}^{r,eg}) \qquad (A.3)$$

$$q_{kts}^{pcc} = -B_{ts}^{eg}(e_{kts}^2 + f_{kts}^2) + B_{ts}^{eg}(e_{kts}E_{ts}^{r,eg} + f_{kts}E_{ts}^{i,eg}) + G_{ts}^{eg}(e_{kts}E_{ts}^{i,eg} - f_{kts}E_{ts}^{r,eg}) \qquad (A.4)$$

$$k \in \{pcc\}, \qquad \forall t \in \mathcal{T}, \qquad \forall s \in \mathcal{S}$$

Note that in our analysis, the external grid voltage imaginary part, $E_{ts}^{i,eg}$, is taken to be zero to set a reference for the system's angles.

The active and reactive power injections into the circuit are as follows:

$$p_{(km)ts}^{cr} = (G_{km}^{cr} + G_{km}^{crs})(e_{kts}^2 + f_{kts}^2) - G_{km}^{cr}(e_{kts}e_{mts} + f_{kts}f_{mts}) + B_{km}^{cr}(e_{kts}f_{mts} - f_{kts}e_{mts}) \qquad (A.5)$$

$$q_{(km)ts}^{cr} = -(B_{km}^{cr} + B_{km}^{crs})(e_{kts}^2 + f_{kts}^2) + B_{km}^{cr}(e_{kts}e_{mts} + f_{kts}f_{mts}) + G_{km}^{cr}(e_{kts}f_{mts} - f_{kts}e_{mts}) \qquad (A.6)$$

$$\forall km \in \mathcal{F}, \qquad \forall t \in \mathcal{T}, \qquad \forall s \in \mathcal{S}$$

Finally, the active and reactive power injections into the fixed shunt device are as follows:

$$p_{kts}^{fx} = G_k^{fx}(e_{kts}^2 + f_{kts}^2) \tag{A.7}$$

$$q_{kts}^{fx} = -B_k^{fx}\ (e_{kts}^2 + f_{kts}^2) \tag{A.8}$$

$\forall k \in \mathcal{K}$, $\forall t \in \mathcal{T}$, $\forall s \in \mathcal{S}$

Equations (A.3)-(A.8) are non-convex since they are equality quadratic equations. To convexify these equations, we introduce three sets of variables. First, define the set $\mathcal{K}' := \{\mathcal{K} \cup 0\}$, and the set $\mathcal{F}' := \{\mathcal{F} \cup (pcc, 0) \cup (0, pcc)\}$ where 0 represents the node at which the voltage source of the Thevenin model is connected, and *pcc* is the PCC bus. Then, we can write the introduced variables are as follows:

(a) $w_{kts} = e_{kts}^2 + f_{kts}^2 \quad \forall k \in \mathcal{K}', \quad \forall t \in \mathcal{T}, \quad \forall s \in \mathcal{S}$.

(b) $c_{(km)ts} = e_{kts}e_{mts} + f_{kts}f_{mts} \quad \forall km \in \mathcal{F}', \quad \forall t \in \mathcal{T}, \quad \forall s \in \mathcal{S}$

(c) $s_{(km)ts} = e_{kts}f_{mts} - f_{kts}e_{mts} \quad \forall km \in \mathcal{F}', \quad \forall t \in \mathcal{T}, \quad \forall s \in \mathcal{S}$

Upon introducing these variables, the non-convex equations in (A.3)-(A.8) are respectively replaced by the following linear equations:

$$p_{kts}^{pcc} = G_{ts}^{eg} w_{kts} - G_{ts}^{eg} c_{(k,0)ts} + B_{ts}^{eg} s_{(k,0)ts} \qquad k \in \{pcc\} \tag{A.9}$$

$$q_{kts}^{pcc} = -B_{ts}^{eg}\ w_{kts} + B_{ts}^{eg} c_{(k,0)ts} + G_{ts}^{eg} s_{(k,0)ts} \qquad k \in \{pcc\} \tag{A.10}$$

$$p_{(km)ts}^{cr} = (G_{km}^{cr} + G_{km}^{crs}) w_{kts} - G_{km}^{cr} c_{(km)ts} + B_{km}^{cr} s_{(km)ts} \qquad \forall km \in \mathcal{F} \tag{A.11}$$

$$q_{(km)ts}^{cr} = -(B_{km}^{cr} + B_{km}^{crs}) w_{kts} + B_{km}^{cr} c_{(km)ts} + G_{km}^{cr} s_{(km)ts} \qquad \forall km \in \mathcal{F} \tag{A.12}$$

$$p_{kts}^{fx} = G_k^{fx} w_{kts} \qquad \forall k \in \mathcal{K} \tag{A.13}$$

$$q_{kts}^{fx} = -B_k^{fx} w_{kts} \qquad \forall k \in \mathcal{K} \tag{A.14}$$

$\forall t \in \mathcal{T}, \qquad \forall s \in \mathcal{S}$

Further, note that the introduced variables are connected by the following relations:

$$c_{(km)ts} = c_{(mk)ts} \tag{A.15}$$

$$s_{(km)ts} = -s_{(mk)ts} \tag{A.16}$$

$$c_{(km)ts}^2 + s_{(km)ts}^2 = w_{kts} w_{mts} \tag{A.17}$$

$\forall km \in \mathcal{F}', \qquad \forall t \in \mathcal{T}, \qquad \forall s \in \mathcal{S}$

Note that the (A.17) is non-convex. It is convexified by replacing the equality sign with an inequality sign resulting the following second-order cone constraint:

$$c_{(km)ts}^2 + s_{(km)ts}^2 \leq w_{kts} w_{mts} \tag{A.18}$$

$\forall km \in \mathcal{F}', \qquad \forall t \in \mathcal{T}, \qquad \forall s \in \mathcal{S}$

Due to the replacement of the non-convex equations in (A.3)-(A.8) by (A.9)-(A.14), the bus voltage angle information is lost (see [84]). Therefore, we add the following constraint as derived in [85] and used in [13]:

$$c_{(km)ts} \tan(-\overline{\theta}_{(km)ts}) \leq s_{(km)ts} \leq c_{(km)ts} \tan(\overline{\theta}_{(km)ts}) \tag{A.19}$$

$\forall km \in \mathcal{F}', \qquad \forall t \in \mathcal{T}, \qquad \forall s \in \mathcal{S}$

where $\overline{\theta}_{(km)ts}$ is an assumed maximum absolute permissible angle difference between node k and node m. Note that this constraint is only valid when $0 \leq \overline{\theta}_{(km)ts} \leq \frac{\pi}{2}$ (i.e., assuming all angle differences are within $[-\frac{\pi}{2}, \frac{\pi}{2}]$). Further, the tighter the bounds the tighter the resultant convex SOCP model. In all our analysis in this thesis, we set $\overline{\theta}_{(km)ts} = 1\,rad.$

Additionally, the value of the Thevenin voltage source is included in the model as follows:

$$w_{0ts} = (E_{ts}^{r,eg})^2 + (E_{ts}^{i,eg})^2 \tag{A.20}$$

$\forall\, t \in \mathcal{T}, \qquad \forall\, s \in \mathcal{S}$

Further, we model the bus voltage limits and circuit current limits as shown below:

$$(\underline{V}_k)^2 \leq w_{kts} \leq (\overline{V}_k)^2 \tag{A.21}$$

$\forall\, k \in \mathcal{K}, \quad \forall\, t \in \mathcal{T}, \quad \forall\, s \in \mathcal{S}$

$$(p_{(km)ts}^{cr})^2 + (q_{(km)ts}^{cr})^2 \leq (\bar{I}_{km})^2 w_{kts} \tag{A.22}$$

$\forall\, km \in \mathcal{F}, \qquad \forall\, t \in \mathcal{T}, \qquad \forall\, s \in \mathcal{S}$

Finally, the full SOCP mathematical model of the μG is given by:

$$\mu G\ SOCP\ Model \equiv \begin{cases} \text{(4.10)-(4.51), (4.57)-(4.62)} \\ \text{(A.1), (A.2), (A.9)-(A.16), (A.18)-(A.22)} \end{cases}$$

A.2 The QC Model

The μG QC model is adapted from the work in [13]. The QC model uses the power balance formulation. Let the active and reactive power balance equations in the μG system be written as follows:

$$p_{kts}^{pq} + p_{kts}^{pcc} + p_{kts}^{fx} + \sum_{\forall m \in A(k)} p_{(km)ts}^{cr} = 0 \tag{A.23}$$

$$q_{kts}^{pq} + q_{kts}^{pcc} + q_{kts}^{fx} + \sum_{\forall m \in A(k)} q_{(km)ts}^{cr} = 0 \tag{A.24}$$

$\forall k \in \mathcal{K}$, $\forall t \in \mathcal{T}$, $\forall s \in \mathcal{S}$

Similar to the SOCP model, the definitions of the active and reactive injections into the PQ devices (p_{kts}^{pq} and q_{kts}^{pq}) are identical to those presented in (4.10) and (4.11) in chapter 4, respectively, where the differences between the presented μG model in chapter 4 and the QC model occur in the Thevenin-equivalent injections (p_{kts}^{pcc} and q_{kts}^{pcc}), the fixed shunt injections (p_{kts}^{fx} and q_{kts}^{fx}), and the circuit injections ($p_{(km)ts}^{cr}$ and $q_{(km)ts}^{cr}$). Moreover, the QC model uses the polar coordinates to represents the bus voltages. The active and reactive power injections into the Thevenin-equivalent model using the polar coordinates are defined as follows:

$$p_{kts}^{pcc} = G_{ts}^{eg} v_{kts}^2 - G_{ts}^{eg} v_{kts} E_{ts}^{eg} \cos(\theta_{kts} - \theta_{ts}^{eg}) - B_{ts}^{eg} v_{kts} E_{ts}^{eg} \sin(\theta_{kts} - \theta_{ts}^{eg}) \tag{A.25}$$

$$q_{kts}^{pcc} = -B_{ts}^{eg} v_{kts}^2 + B_{ts}^{eg} v_{kts} E_{ts}^{eg} \cos(\theta_{kts} - \theta_{ts}^{eg}) - G_{ts}^{eg} v_{kts} E_{ts}^{eg} \sin(\theta_{kts} - \theta_{ts}^{eg}) \tag{A.26}$$

$k \in \{pcc\}$, $\forall t \in \mathcal{T}$, $\forall s \in \mathcal{S}$

Note that in our analysis, we set the angle of the external grid voltage as the reference ($\theta_{ts}^{eg} = 0$).

The active and reactive power injections into the circuit are as follows:

$$p^{cr}_{(km)ts} = (G^{cr}_{km} + G^{crs}_{km})v^2_{kts} - G^{cr}_{km} v_{kts} v_{mts} \cos(\theta_{(km)ts}) - B^{cr}_{km} v_{kts} v_{mts} \sin(\theta_{(km)ts}) \quad \text{(A.27)}$$

$$q^{cr}_{(km)ts} = -(B^{cr}_{km} + B^{crs}_{km})v^2_{kts} + B^{cr}_{km} v_{kts} v_{mts} \cos(\theta_{(km)ts}) - G^{cr}_{km} v_{kts} v_{mts} \sin(\theta_{(km)ts}) \quad \text{(A.28)}$$

$\forall\, km \in \mathcal{F}, \qquad \forall\, t \in \mathcal{T}, \qquad \forall\, s \in \mathcal{S}$

Finally, the active and reactive power injections into the fixed shunt device are as follows:

$$p^{fx}_{kts} = G^{fx}_{k} v^2_{kts} \quad \text{(A.29)}$$

$$q^{fx}_{kts} = -B^{fx}_{k} v^2_{kts} \quad \text{(A.30)}$$

$\forall\, k \in \mathcal{K} \quad , \qquad \forall\, t \in \mathcal{T}, \qquad \forall\, s \in \mathcal{S}$

The QC model is achieved by introducing multiple convex envelopes for the non-linear terms arising in equations (A.25)-(A.30). The introduced envelopes to convexify the non-linear terms in are square term envelopes, McCormick envelopes for bilinear products [86], sine envelopes, and cosine envelopes. The sine and cosine envelopes assume a permissible angle difference for circuit km $\theta_{km} \in [-\overline{\theta}_{km}, \overline{\theta}_{km}]$ such that $0 \leq \overline{\theta}_{km} \leq \frac{\pi}{2}$. As illustrated in [87], we first present the envelopes for generic variables x, y, and θ. We then use the envelopes to convexify equations (A.25)-(A.30). Let $x \in [\underline{x}, \overline{x}]$ and $y \in [\underline{y}, \overline{y}]$. Further, let $\theta \in [-\overline{\theta}, \overline{\theta}]$ such that $0 \leq \overline{\theta} \leq \frac{\pi}{2}$. Then, the square term, McCormick, sine, and cosine envelopes are respectively defined as follows:

$$\langle x^2 \rangle^{Q} = \left\{ z : \begin{cases} z \leq (\underline{x} + \overline{x})x - \underline{x}\overline{x} \\ z \geq x^2 \end{cases} \right\} \quad \text{(A.31)}$$

$$\langle x.y\rangle^{M} = \left\{ z : \begin{Bmatrix} z \le \underline{y}x + \overline{x}y - \underline{y}\overline{x} \\ z \le \overline{y}x + \underline{x}y - \overline{y}\underline{x} \\ z \ge \underline{y}x + \underline{x}y - \underline{y}\underline{x} \\ z \ge \overline{y}x + \overline{x}y - \overline{y}\overline{x} \end{Bmatrix} \right\} \tag{A.32}$$

$$\langle \sin(\theta)\rangle^{S} = \left\{ z : \begin{Bmatrix} z \le \cos(\overline{\theta}/2)(\theta - \overline{\theta}/2) + \sin(\overline{\theta}/2) \\ z \ge \cos(\overline{\theta}/2)(\theta + \overline{\theta}/2) - \sin(\overline{\theta}/2) \end{Bmatrix} \right\} \tag{A.33}$$

$$\langle \cos(\theta)\rangle^{C} = \left\{ z : \begin{Bmatrix} z \le 1 - \dfrac{1-\cos(\overline{\theta})}{\overline{\theta}^2}\theta^2 \\ z \ge \cos(\overline{\theta}) \end{Bmatrix} \right\} \tag{A.34}$$

Visualizations for these envelopes can be found in [13] and [87]. Using these envelopes, five variables are defined:

$$w_{kts} \in \left\langle v_{kts}^2 \right\rangle^{Q} \qquad \forall k \in \mathcal{K} \tag{A.35}$$

$$c_{ts}^{eg} \in \left\langle v_{kts} E_{ts}^{eg} . \left\langle \cos(\theta_{kts} - \theta_{ts}^{eg}) \right\rangle^{C} \right\rangle^{M} \tag{A.36}$$

$$s_{ts}^{eg} \in \left\langle v_{kts} E_{ts}^{eg} . \left\langle \sin(\theta_{kts} - \theta_{ts}^{eg}) \right\rangle^{C} \right\rangle^{M} \tag{A.37}$$

$$c_{(km)ts} \in \left\langle \left\langle v_{kts} v_{mts} \right\rangle^{M} . \left\langle \cos(\theta_{(km)ts}) \right\rangle^{C} \right\rangle^{M} \qquad \forall km \in \mathcal{F} \tag{A.38}$$

$$s_{(km)ts} \in \left\langle \left\langle v_{kts} v_{mts} \right\rangle^{M} . \left\langle \sin(\theta_{(km)ts}) \right\rangle^{S} \right\rangle^{M} \qquad \forall km \in \mathcal{F} \tag{A.39}$$

$\forall\, t \in \mathcal{T}, \qquad \forall\, s \in \mathcal{S}$

where

$$c_{(km)ts} = c_{(mk)ts} \tag{A.40}$$

$$s_{(km)ts} = -s_{(mk)ts} \tag{A.41}$$

$\forall\, km \in \mathcal{F}, \qquad \forall\, t \in \mathcal{T}, \qquad \forall\, s \in \mathcal{S}$

Note that the technical bounds of the bus voltage magnitudes ($\underline{V}_k, \overline{V}_k$) are used as the voltage bounds needed to formulate the convex envelopes. Additionally, similar to the case for the SOCP mode, we set $\overline{\theta}_{(km)ts} = 1\ rad$. Consequently, upper and lower bounds for the sine and cosine terms can be deduced.

To illustrate the notation used in defining the five variables in (A.35)-(A.39), we use (A.35) as an example. (A.35) results in the following explicit constraints added to the μG model:

$$w_{kts} \le (\underline{V}_k + \overline{V}_k) v_{kts} - \underline{V}_k \overline{V}_k \tag{A.42}$$

$$w_{kts} \ge v_{kts}^2 \tag{A.43}$$

With these five variables defined, the Thevenin-equivalent, the circuit, and the fixed shunt injections can respectively be written in the following linear form:

$$p_{kts}^{pcc} = G_{ts}^{eg} w_{kts} - G_{ts}^{eg} c_{ts}^{eg} + B_{ts}^{eg} s_{ts}^{eg} \qquad k \in \{pcc\} \tag{A.44}$$

$$q_{kts}^{pcc} = -B_{ts}^{eg} w_{kts} + B_{ts}^{eg} c_{ts}^{eg} + G_{ts}^{eg} s_{ts}^{eg} \qquad k \in \{pcc\} \tag{A.45}$$

$$p_{(km)ts}^{cr} = (G_{km}^{cr} + G_{km}^{crs}) w_{kts} - G_{km}^{cr} c_{(km)ts} + B_{km}^{cr} s_{(km)ts} \qquad \forall km \in \mathcal{F} \tag{A.46}$$

$$q_{(km)ts}^{cr} = -(B_{km}^{cr} + B_{km}^{crs}) w_{kts} + B_{km}^{cr} c_{(km)ts} + G_{km}^{cr} s_{(km)ts} \qquad \forall km \in \mathcal{F} \tag{A.47}$$

$$p_{kts}^{fx} = G_k^{fx} w_{kts} \qquad \forall k \in \mathcal{K} \tag{A.48}$$

$$q_{kts}^{fx} = -B_k^{fx} w_{kts} \qquad \forall k \in \mathcal{K} \tag{A.49}$$

$\forall t \in \mathcal{T}, \qquad \forall s \in \mathcal{S}$

We also add the following constraints to strengthen the QC relaxation as in [13]:

$$(p^{cr}_{(km)ts})^2 + (q^{cr}_{(km)ts})^2 \le l_{(km)ts} w_{kts} \tag{A.50}$$

$$\begin{aligned} l_{(km)ts} = {} & (G^{cr\,2}_{km} + B^{cr\,2}_{km})(w_{kts} + w_{mts} - 2c_{(km)ts}) \\ & + 2(G^{crs}_{km} p^{cr}_{(km)ts} - B^{crs}_{km} q^{cr}_{(km)ts}) - (G^{crs\,2}_{km} + B^{crs\,2}_{km}) w_{kts} \end{aligned} \tag{A.51}$$

$$0 \le l_{(km)ts} \le (\bar{I}_{km})^2 \tag{A.52}$$

$\forall\, km \in \mathcal{K}$, $\forall\, t \in \mathcal{T}$, $\forall\, s \in \mathcal{S}$

where (A.50) is a second-order cone relaxation for the magnitude square of the apparent power flow in circuit *km* where the added variable $l_{(km)ts}$ represents the magnitude squared of the current following in circuit *km*. (A.51) links $l_{(km)ts}$ to the other model variables, and (A.52) bounds it to the current magnitude limits. Notably, the authors in [13] only include the first term in (A.51) (i.e., neglecting the shunt admittance of the circuit). However, the authors provide an extended model that includes the shunt admittance in [88], which is want we use here.

Further, we model the bus voltage limits and circuit current limits as shown below:

$$(\underline{V}_k)^2 \le w_{kts} \le (\bar{V}_k)^2 \tag{A.53}$$

$\forall\, k \in \mathcal{K}$, $\forall\, t \in \mathcal{T}$, $\forall\, s \in \mathcal{S}$

$$(p^{cr}_{(km)ts})^2 + (q^{cr}_{(km)ts})^2 \le (\bar{I}_{km})^2 w_{kts} \tag{A.54}$$

$\forall\, km \in \mathcal{F}$, $\forall\, t \in \mathcal{T}$, $\forall\, s \in \mathcal{S}$

Finally, the QC mathematical model of the μG is given by:

$$\mu G\ QC\ Model \equiv \begin{cases} \text{(4.10)-(4.51), (4.57)-(4.62)} \\ \text{(A.23), (A.24), (A.35)-(A.41), (A.44)-(A.54)} \end{cases}$$

A.3 Tightness and the Dependency on the Objective Function

The presented convex models have shown to provide good approximations in the literature as well as the presented cases in chapter 7 when applied to the legacy OPF problem. The objective function of the legacy OPF problem is to minimize the total generation cost. Notice that the OPF objective function minimizes the system active losses inherently, to minimize the generation cost needed to satisfy the demand. The accuracy of the approximations in the two presented convex models improves when the losses are minimized. To justify this claim, from the active power circuit flow equations of these two models (A.11) and (A.46), we can write the losses for a circuit *km* as follows (*t* and *s* indices are omitted for abbreviation):

$$p_{km}^{cr} + p_{mk}^{cr} = (G_{km}^{cr} + G_{km}^{crs})(w_k + w_m) - 2G_{km}^{cr} c_{km} \tag{A.55}$$

For practical power systems where the conductance G_{km}^{cr} is positive, minimizing the losses maximizes the term c_{km}. In the SOCP model, maximizing c_{km} incentives the relaxed second-order cone constraint in (A.18) to be active satisfying the accurate quadratic equality constraint in (A.17). By that, improving the accuracy of the approximation. Further, in the QC model, maximizing c_{km} moves it to the upper bounds of the McCormick envelopes (A.38). The McCormick envelopes accuracy are known to improve near the bounds [86]. Also, this will in-turn maximize the second term of the McCormick envelopes

in (A.38) (i.e., $\langle \cos(\theta_{km,t,s}) \rangle^C$) as all McCormick bounds for (A.38) are positive. When $\langle \cos(\theta_{km,t,s}) \rangle^C$ is maximized, the approximation in (A.34) gets closer to the actual cosine function (see [13] and [87] for a visualization of the cosine envelopes). Moreover, when the losses are minimized in the QC model, the current magnitude squared variable l_{km} in (A.50) is minimized. Minimizing l_{km} incentivizes the relaxed inequality constraint (A.50) to be active, by that, improving the accuracy of the approximation since (A.50) is a relaxation of $(p^{cr}_{(km)ts})^2 + (q^{cr}_{(km)ts})^2 = l_{(km)ts} w_{kts}$). In the presented objective functions of the proposed μGEMS, the losses are not necessarily minimized. For example, providing regulation-down capacity motivates increasing the losses to increase the downward capacity. Additionally, in the voltage support objective function and when an over-voltage exists in the external grid, the μG is also motivated to increase the losses to reduce the voltage to the target value. In chapter 7, we demonstrated that for these two objective functions, the SOCP and the QC solution methods gave optima with large gaps relative to the global solution. In contrast, in other objective functions when losses are inherently minimized (e.g., cost minimization), the gaps where minimal for the tested cases.

APPENDIX B. THE μG MATHEMATICAL MODEL IN POWER BALANCE FORMULATION

In this appendix, we present the μG mathematical model in power balance formulation. Similar to the current formulation, the μG model under the power balance formulation is quadratic and uses rectangular coordinates. Let the active and reactive bus power balance equations in the μG system be written as follows:

$$p_{kts}^{pq} + p_{kts}^{pcc} + p_{kts}^{fx} + \sum_{\forall m \in A(k)} p_{(km)ts}^{cr} = 0 \tag{B.1}$$

$$q_{kts}^{pq} + q_{kts}^{pcc} + q_{kts}^{fx} + \sum_{\forall m \in A(k)} q_{(km)ts}^{cr} = 0 \tag{B.2}$$

$$\forall k \in \mathcal{K} \quad , \quad \forall t \in \mathcal{T}, \quad \forall s \in \mathcal{S}$$

where p_{kts}^{pq} and q_{kts}^{pq} represent the total active and reactive power injections into the PQ devices, p_{kts}^{pcc} and q_{kts}^{pcc} define the active and reactive power injections to the external grid Thevenin equivalent model, p_{kts}^{fx} and q_{kts}^{fx} are the active and reactive power injections into the fixed shunt device, and $p_{(km)ts}^{cr}, q_{(km)ts}^{cr}$ are the active and reactive power flow through a circuit from bus *k* to bus *m*. The definitions of the active and reactive power injections into PQ devices are identical to those presented in (4.10) and (4.11) in chapter 4, respectively, which sum up the power injections into the net-demand, the DGs, the ESSs, and the TCLs and the DULs of connected homes. Further, the operational equations and constraints of these DERs are also identical to those presented in chapter 4. The differences between the presented μG model in chapter 4 and the power balance model occur in the Thevenin-equivalent injections, the fixed shunt injections, and the circuit injections, which are respectively defined as follows:

$$p_{kts}^{pcc} = G_{ts}^{eg}(e_{kts}^2 + f_{kts}^2) - G_{ts}^{eg}(e_{kts}E_{ts}^{r,eg} + f_{kts}E_{ts}^{i,eg}) + B_{ts}^{eg}(e_{kts}E_{ts}^{i,eg} - f_{kts}E_{ts}^{r,eg}) \quad \text{(B.3)}$$

$$q_{kts}^{pcc} = -B_{ts}^{eg}\ (e_{kts}^2 + f_{kts}^2) + B_{ts}^{eg}(e_{kts}E_{ts}^{r,eg} + f_{kts}E_{ts}^{i,eg}) + G_{ts}^{eg}(e_{kts}E_{ts}^{i,eg} - f_{kts}E_{ts}^{r,eg}) \quad \text{(B.4)}$$

$k \in \{pcc\}, \qquad \forall t \in \mathcal{T}, \qquad \forall s \in \mathcal{S}$

$$p_{kts}^{fx} = G_k^{fx}(e_{kts}^2 + f_{kts}^2) \quad \text{(B.5)}$$

$$q_{kts}^{fx} = -B_k^{fx}\ (e_{kts}^2 + f_{kts}^2) \quad \text{(B.6)}$$

$\forall k \in \mathcal{K} \quad , \qquad \forall t \in \mathcal{T}, \qquad \forall s \in \mathcal{S}$

$$p_{(km)ts}^{cr} = (G_{km}^{cr} + G_{km}^{crs})(e_{kts}^2 + f_{kts}^2) - G_{km}^{cr}(e_{kts}e_{mts} + f_{kts}f_{mts}) + B_{km}^{cr}(e_{kts}f_{mts} - f_{kts}e_{mts}) \quad \text{(B.7)}$$

$$q_{(km)ts}^{cr} = -(B_{km}^{cr} + B_{km}^{crs})\ (e_{kts}^2 + f_{kts}^2) + B_{km}^{cr}(e_{kts}e_{mts} + f_{kts}f_{mts}) + G_{km}^{cr}(e_{kts}f_{mts} - f_{kts}e_{mts}) \quad \text{(B.8)}$$

$\forall km \in \mathcal{F}, \qquad \forall t \in \mathcal{T}, \qquad \forall s \in \mathcal{S}$

Further, the network constraints include the bus voltage limits and the circuit thermal limits as defined in (B.9) and (B.10) respectively.

$$(\underline{V}_k)^2 \le e_{kts}^2 + f_{kts}^2 \le (\overline{V}_k)^2 \quad \text{(B.9)}$$

$\forall k \in \mathcal{K}, \quad \forall t \in \mathcal{T}, \quad \forall s \in \mathcal{S}$

$$(p_{(km)ts}^{cr})^2 + (q_{(km)ts}^{cr})^2 \le (\overline{I}_{km})^2(e_{kts}^2 + f_{kts}^2) \quad \text{(B.10)}$$

$\forall km \in \mathcal{F}, \qquad \forall t \in \mathcal{T}, \qquad \forall s \in \mathcal{S}$

Notably, this constraint in (B.10) is physically equivalent to the current thermal limit constraint used in the current formulation.

The complete μG mathematical model under the power balance formulation is given by:

$$\mu G\ Power\ Balace\ Model \equiv \begin{cases} (4.10)\text{-}(4.51),\ (4.57)\text{-}(4.62) \\ (B.1)\text{-}(B.10) \end{cases}$$

REFERENCES

[1] Peter Asmus, Mackinnon Lawrence, Alex Metz, Pritil Gunjan, Roberto Rodriguez Labastida, Scott Shepard, and Eric Woods, “Integrated DER: orchestrating the grid’s last mile,” *Guide House*, 2020.

[2] D.T. Ton, and M.A. Smith, “The US Department of Energy's microgrid initiative,” *The Electricity Journal*, 2012.

[3] Esther Whieldon, and Garrett Hering, “Natural disasters could spark US microgrid surge,” *S&P Global*, 2019. Available at: https://www.spglobal.com/marketintelligence/en/news-insights/trending/eCxE4GFMDsA7ogojhqRK5A2

[4] P. P. Barker and R. W. De Mello, "Determining the impact of distributed generation on power systems. I. Radial distribution systems," *2000 Power Engineering Society Summer Meeting*, Seattle, WA, 2000.

[5] L. F. Ochoa, A. Padilha-Feltrin and G. P. Harrison, "Evaluating distributed generation impacts with a multiobjective index," in *IEEE Transactions on Power Delivery*, vol. 21, no. 3, pp. 1452-1458, July 2006.

[6] IRENA “Renewable energy capacity statistics 2019,” March 2019. Available at: http://www.irena.org/publications

[7] IRENA “Renewable energy capacity statistics 2020,” March 2020. Available at: http://www.irena.org/publications

[8] Thomas Hoff, and Adam Kankiewicz, “Integration of behind-the-meter pv fleet forecasts into utility grid system operations*,”* No. DOE-CPR-0006329, *Clean Power Research*, *LLC*, Napa, CA, 2016.

[9] North American Electric Reliability Corporation (NERC), “Distributed energy resources: connection modeling and reliability considerations,” February 2017.

[10] AF Kaptue Kamga, S. Voller, and J. F. Verstege, "Congestion management in transmission systems with large scale integration of wind energy," in *2009 CIGRE/IEEE PES Joint Symposium Integration of Wide-Scale Renewable Resources into the Power Delivery System*, IEEE, 2009.

[11] California Independent System Operator, “CAISO settlements and billing: Section 11.10.1.4”, December 2013.

[12] R. A. Jabr, "Radial distribution load flow using conic programming," in *IEEE Transactions on Power Systems*, vol. 21, no. 3, pp. 1458-1459, Aug. 2006.

[13] H. Hijazi, C. Coffrin, and P.V. Hentenryck, "Convex quadratic relaxations for mixed-integer nonlinear programs in power system," in *Mathematical Programming Computation* 9, no. 3, 2017.

[14] Gurobi Optimization, LLC, “Gurobi Reference Manual,” 2020.

[15] D. E. Olivares *et al*., "Trends in Microgrid Control," in *IEEE Transactions on Smart Grid*, vol. 5, no. 4, pp. 1905-1919, July 2014.

[16] Firestone, Ryan, and Chris Marnay, "Energy manager design for microgrids", No. LBNL-54447. *Lawrence Berkeley National Lab.(LBNL)*, Berkeley, CA (United States), 2005.

[17] A. Khodaei, "Microgrid Optimal Scheduling with Multi-Period Islanding Constraints," in *IEEE Transactions on Power Systems*, vol. 29, no. 3, pp. 1383-1392, May 2014.

[18] E. Alvarez, A. C. Lopez, J. Gómez-Aleixandre and N. de Abajo, "On-line minimization of running costs, greenhouse gas emissions and the impact of distributed generation using microgrids on the electrical system," *2009 IEEE PES/IAS Conference on Sustainable Alternative Energy (SAE)*, Valencia, 2009.

[19] Z. Wang and J. Wang, "Self-healing resilient distribution systems based on sectionalization into microgrids," in *IEEE Transactions on Power Systems*, vol. 30, no. 6, pp. 3139-3149, Nov. 2015.

[20] J. Rocabert, A. Luna, F. Blaabjerg and P. Rodríguez, "Control of power converters in AC microgrids," in *IEEE Transactions on Power Electronics*, vol. 27, no. 11, pp. 4734-4749, Nov. 2012.

[21] A. Dimeas and N. Hatziargyriou, "Operation of a multiagent system for microgrid control," *IEEE Transactions on Power Systems*, vol. 20, no. 3, pp. 1447–1455, Aug. 2005.

[22] Z. Wang, K. Yang, and X. Wang, "Privacy-preserving energy scheduling in microgrid systems," *IEEE Transactions on Smart Grid*, vol. 4, no. 4, pp. 1810–1820, Dec. 2013.

[23] E. Crisostomi, M. Liu, M. Raugi, and R. Shorten, "Plug-and-play distributed algorithms for optimized power generation in a microgrid," *IEEE Transactions on Smart Grid*, vol. 5, no. 4, pp. 2145–2154, Jul. 2014.

[24] Rodrigo Palma-Behnke, Carlos Benavides, Fernando Lanas, Bernardo Severino, Lorenzo Reyes, Jacqueline Llanos, and Doris Sáez, "A microgrid energy management system based on the rolling horizon strategy," in *IEEE Transactions on Smart Grid*, vol. 4, no. 2, pp. 996-1006, June 2013.

[25] Tenfen, Daniel, and Erlon Cristian Finardi, "A mixed integer linear programming model for the energy management problem of microgrids," *Electric Power Systems Research* 122, 2015.

[26] L. Igualada, C. Corchero, M. Cruz-Zambrano and F. Heredia, "Optimal energy management for a residential microgrid including a vehicle-to-grid system," in *IEEE Transactions on Smart Grid*, vol. 5, no. 4, pp. 2163-2172, July 2014.

[27] L. K. Panwar, S. R. Konda, A. Verma, B. K. Panigrahi and R. Kumar, "Operation window constrained strategic energy management of microgrid with electric vehicle and distributed resources," in *IET Generation, Transmission & Distribution*, vol. 11, no. 3, pp. 615-626, 16 2 2017.

[28] Sukumar, Shivashankar, Hazlie Mokhlis, Saad Mekhilef, Kanendra Naidu, and Mazaher Karimi. "Mix-mode energy management strategy and battery sizing for economic operation of grid-tied microgrid" *Energy* 118, 2017.

[29] Vergara, Pedro P., Juan Camilo López, Luiz CP da Silva, and Marcos J. Rider, "Security-constrained optimal energy management system for three-phase residential microgrids." *Electric Power Systems Research* 146, 2017.

[30] G. Liu, M. Starke, Xiaohu Zhang and K. Tomsovic, "A MILP-based distribution optimal power flow model for microgrid operation," *2016 IEEE Power and Energy Society General Meeting (PESGM)*, Boston, MA, 2016.

[31] M. AlOwaifeer and A. P. S. Meliopoulos, "Centralized microgrid energy management system based on successive linearization," *2018 North American Power Symposium (NAPS)*, Fargo, ND, 2018.

[32] Bénichou, Michel, Jean-Michel Gauthier, Gerard Hentges, and Gerard Ribiere, "The efficient solution of large-scale linear programming problems—some algorithmic techniques and computational results," *Mathematical Programming* 13, no. 1, 1977.

[33] Bai, Xiaoqing, Hua Wei, Katsuki Fujisawa, and Yong Wang. "Semidefinite programming for optimal power flow problems," *International Journal of Electrical Power & Energy Systems* 30, no. 6-7, 2008.

[34] M. Baradar, M. R. Hesamzadeh and M. Ghandhari, "Second-order cone programming for optimal power flow in VSC-type AC-DC grids," in *IEEE Transactions on Power Systems*, vol. 28, no. 4, pp. 4282-4291, Nov. 2013.

[35] J. S. Giraldo, J. A. Castrillon, J. C. López, M. J. Rider and C. A. Castro, "Microgrids energy management using robust convex programming," in *IEEE Transactions on Smart Grid*, vol. 10, no. 4, pp. 4520-4530, July 2019.

[36] M. F. Zia, E. Elbouchikhi, M. Benbouzid and J. M. Guerrero, "Energy management system for an islanded microgrid with convex relaxation," in *IEEE Transactions on Industry Applications*, vol. 55, no. 6, pp. 7175-7185, Nov.-Dec. 2019.

[37] J. Lavaei and S. H. Low, "Zero duality gap in optimal power flow problem," in *IEEE Transactions on Power Systems*, vol. 27, no. 1, pp. 92-107, Feb. 2012.

[38] C. Coffrin, H. L. Hijazi and P. Van Hentenryck, "The QC relaxation: a theoretical and computational study on optimal power flow," in *IEEE Transactions on Power Systems,* vol. 31, no. 4, pp. 3008-3018, July 2016.

[39] Hijazi, Hassan, Carleton Coffrin, and Pascal Van Hentenryck. "Convex quadratic relaxations for mixed-integer nonlinear programs in power systems," *Mathematical Programming Computation* 9, no. 3, 2017.

[40] Almada, J. B., R. P. S. Leão, R. F. Sampaio, and G. C. Barroso. "A centralized and heuristic approach for energy management of an AC microgrid," *Renewable and Sustainable Energy Reviews* 60, 2016.

[41] H. Kanchev, D. Lu, F. Colas, V. Lazarov and B. Francois, "Energy management and operational planning of a microgrid with a PV-based active generator for smart grid applications," in *IEEE Transactions on Industrial Electronics*, vol. 58, no. 10, pp. 4583-4592, Oct. 2011.

[42] G. E. P. Box, "Evolutionary operation: A method for increasing industrial productivity," *Appl. Statistics,* vol. VI, no. 2, pp. 81–101, 1957.

[43] T. Back, U. Hammel and H. P. Schwefel, "Evolutionary computation: comments on the history and current state," in *IEEE Transactions on Evolutionary Computation*, vol. 1, no. 1, pp. 3-17, Apr 1997.

[44] X. Wu, X. Wang and C. Qu, "A hierarchical framework for generation scheduling of microgrids," in *IEEE Transactions on Power Delivery*, vol. 29, no. 6, pp. 2448-2457, Dec. 2014.

[45] A. Askarzadeh, "A memory-based genetic algorithm for optimization of power generation in a microgrid," in *IEEE Transactions on Sustainable Energy*, vol. 9, no. 3, pp. 1081-1089, July 2018.

[46] M. A. Hannan, M. G. M. Abdolrasol, M. Faisal, P. J. Ker, R. A. Begum and A. Hussain, "Binary particle swarm optimization for scheduling mg integrated virtual power plant toward energy saving," in *IEEE Access*, vol. 7, pp. 107937-107951, 2019.

[47] A. J. Litchy and M. H. Nehrir, "Real-time energy management of an islanded microgrid using multi-objective Particle Swarm Optimization," *2014 IEEE PES General Meeting | Conference & Exposition*, National Harbor, MD, 2014.

[48] C. M. Colson, M. H. Nehrir and S. A. Pourmousavi, "Towards real-time microgrid power management using computational intelligence methods," *IEEE PES General Meeting*, Providence, RI, 2010.

[49] Wang, Tiancai, Xing He, and Ting Deng. "Neural networks for power management optimal strategy in hybrid microgrid," *Neural Computing and Applications* 31, no. 7, 2019.

[50] G. K. Venayagamoorthy, R. K. Sharma, P. K. Gautam and A. Ahmadi, "Dynamic energy management system for a smart microgrid," in *IEEE Transactions on Neural Networks and Learning Systems*, vol. 27, no. 8, pp. 1643-1656, Aug. 2016.

[51] M. E. Gamez Urias, E. N. Sanchez and L. J. Ricalde, "Electrical microgrid optimization via a new recurrent neural network," in *IEEE Systems Journal*, vol. 9, no. 3, pp. 945-953, Sept. 2015.

[52] Ji, Ying, Jianhui Wang, Jiacan Xu, Xiaoke Fang, and Huaguang Zhang. "Real-Time energy management of a microgrid using deep reinforcement learning," *Energies* 12, no. 12, 2019.

[53] Majzoobi, Alireza, and Amin Khodaei. "Application of microgrids in providing ancillary services to the utility grid," *Energy* 123, 2017

[54] Shi, L., Y. Luo, and G. Y. Tu, "Bidding strategy of microgrid with consideration of uncertainty for participating in power market." *International Journal of Electrical Power & Energy Systems* 59, 2014.

[55] D. Chen, Z. Jing and H. Tan, "Optimal bidding strategy for microgrids in energy and spinning reserve markets," *2019 IEEE Power & Energy Society General Meeting (PESGM)*, Atlanta, GA, USA, 2019.

[56] J. Wang, H. Zhong, Q. Xia, Z. Ma, Z. Wang and X. Wu, "Robust bidding strategy for microgrids in joint energy, reserve and regulation markets," *2017 IEEE Power & Energy Society General Meeting*, Chicago, IL, 2017.

[57] J. L. Martínez-Ramos *et al*., "Provision of Ancillary services by a smart microgrid: an OPF approach," *2018 International Conference on Smart Energy Systems and Technologies (SEST)*, Sevilla, 2018.

[58] W. Tang and H. Yang, "Optimal operation and bidding strategy of a virtual power plant integrated with energy storage systems and elasticity demand response," in *IEEE Access*, vol. 7, pp. 79798-79809, 2019.

[59] Peik-Herfeh, Malahat, H. Seifi, and M. K. Sheikh-El-Eslami, "Decision making of a virtual power plant under uncertainties for bidding in a day-ahead market using point estimate method," *International Journal of Electrical Power & Energy Systems* 44, no. 1, 2013

[60] M. Giuntoli and D. Poli, "Optimized thermal and electrical scheduling of a large-scale virtual power plant in the presence of energy storages," in *IEEE Transactions on Smart Grid*, vol. 4, no. 2, pp. 942-955, June 2013.

[61] California ISO Corporation, "Section 8.9: ancillary services, verification, compliance testing, and auditing," Fifth Replacement FERC Electric Tarif, 2019.

[62] U.S. Energy Information Administration., Consumption and Efficiency. Available at: https://www.eia.gov/consumption.

[63] Pengwei Du and Ning Lu, "Appliance commitment for household load scheduling," *PES T&D 2012*, Orlando, FL, 2012.

[64] Stadler, Michael, et.al, "Modelling and evaluation of control schemes for enhancing load shift of electricity demand for cooling devices," *Environmental Modelling & Software* 24, no. 2, 2009.

[65] Y. Zhang, N. Gatsis and G. B. Giannakis, "Robust Energy Management for Microgrids With High-Penetration Renewables," in *IEEE Transactions on Sustainable Energy*, vol. 4, no. 4, pp. 944-953, Oct. 2013.

[66] C. E. Murillo-Sánchez, R. D. Zimmerman, C. L. Anderson and R. J. Thomas, "Secure planning and operations of systems with stochastic sources, energy storage, and active demand," in *IEEE Transactions on Smart Grid*, vol. 4, no. 4, pp. 2220-2229, Dec. 2013.

[67] N. G. Cobos, J. M. Arroyo, N. Alguacil and J. Wang, "Robust energy and reserve scheduling considering bulk energy storage units and wind uncertainty," in *IEEE Transactions on Power Systems*, vol. 33, no. 5, pp. 5206-5216, Sept. 2018.

[68] M. C. Bozchalui, S. A. Hashmi, H. Hassen, C. A. Canizares and K. Bhattacharya, "Optimal operation of residential energy hubs in smart grids," in *IEEE Transactions on Smart Grid*, vol. 3, no. 4, pp. 1755-1766, Dec. 2012.

[69] A. Agnetis, G. de Pascale, P. Detti and A. Vicino, "load scheduling for household energy consumption optimization," in *IEEE Transactions on Smart Grid*, vol. 4, no. 4, pp. 2364-2373, Dec. 2013.

[70] N. Khalid, "Efficient energy management: is variable frequency drives the solution," *Procedia-Social and Behavioral Sciences* 145, 2014.

[71] Z. Yu, L. Jia, M. C. Murphy-Hoye, A. Pratt and L. Tong, "Modeling and stochastic control for home energy management," in *IEEE Transactions on Smart Grid*, vol. 4, no. 4, pp. 2244-2255, Dec. 2013.

[72] M. Zuñiga, K. Agbossou, A. Cardenas and L. Boulon, "Parameter estimation of electric water heater models using extended Kalman filter," *IECON 2017 - 43rd Annual Conference of the IEEE Industrial Electronics Society*, Beijing, 2017.

[73] Anan Zhang, Wenting Tan, Ming Cheng, and Wei Yang. "Thevenin equivalent parameter adaptive robust estimation considering the erroneous measurements of PMU." *Energies* 13, no. 18, 2020

[74] R. E. Griffith, and R. A. Stewart. "A nonlinear programming technique for the optimization of continuous processing systems." *Management science* 7, no. 4, 1961.

[75] R. D. Zimmerman, C. E. Murillo-Sánchez and R. J. Thomas, "MATPOWER: Steady-state operations, planning, and analysis tools for power systems research and education," in *IEEE Transactions on Power Systems*, vol. 26, no. 1, pp. 12-19, Feb. 2011.

[76] F. Bu, Y. Yuan, Z. Wang, K. Dehghanpour, and A. Kimber, "A time-series distribution test system based on real utility data," 2019 North American Power Symposium (NAPS), Wichita, KS, USA, 2019, pp. 1-6.

[77] Open Access Same Time Information System (OASIS) of California electricity markets. Available at: http://oasis.caiso.com.

[78] System Advisor Model Version 2020.2.29 (SAM 2020.2.29). National Renewable Energy Laboratory. Golden, CO.

[79] Zhuang Tian, and Wenchuan Wu, "Recover feasible solutions for SOCP relaxation of optimal power flow problems in mesh networks," *IET Generation, Transmission & Distribution* 13, no. 7, 2019.

[80] Sheldon M. Ross, "Introduction to probability models: section 4.9*,"* Academic press, 2014.

[81] Kai Hou, Hongjie Jia, Xiandong Xu, Zhe Liu and Yilang Jiang, "A continuous time Markov chain based sequential analytical approach for composite power system reliability assessment," *2016 IEEE Power and Energy Society General Meeting (PESGM)*, 2016.

[82] C. Grigg *et al*., "The IEEE Reliability Test System-1996. A report prepared by the Reliability Test System Task Force of the Application of Probability Methods Subcommittee," in *IEEE Transactions on Power Systems*, vol. 14, no. 3, pp. 1010-1020, Aug. 1999.

[83] W. H. Kersting, W. H. Phillips and R. C. Doyle, "Distribution feeder reliability studies," in *IEEE Transactions on Industry Applications*, vol. 35, no. 2, pp. 319-323, March-April, 1999.

[84] B. Kocuk, S. S. Dey, and X. A. Sun, "Strong SOCP relaxations for the optimal power flow problem," in *Operations Research* 64, no. 6, 2016.

[85] Madani, S. Sojoudi and J. Lavaei, "Convex Relaxation for Optimal Power Flow Problem: Mesh Networks," in *IEEE Transactions on Power Systems*, vol. 30, no. 1, pp. 199-211, Jan. 2015.

[86] G. P. McCormick, "Computability of global solutions to factorable nonconvex programs: Part I—Convex underestimating problems," in *Mathematical programming* 10, no. 1, 1976.

[87] D. K. Molzahn, and I.A. Hiskens, "A survey of relaxations and approximations of the power flow equations," in *Foundations and Trends in Electric Energy Systems* 4, no. 1-2, 2019.

[88] Carleton Coffrin, Hassan L. Hijazi, and Pascal Van Hentenryck, "DistFlow extensions for AC transmission systems." *arXiv preprint arXiv:1506.04773*, 2015.

VITA

Maad Alowaifeer was born in Al-Ahsa, Saudi Arabia, in November 1990. He received the B.Sc. and M.Sc. degrees in electrical engineering from the King Fahd University of Petroleum and Minerals (KFUPM), Dhahran, Saudi Arabia, in 2013 and 2015, respectively. He also received the M.Sc. degree in operations research from the Georgia Institute of Technology (GIT), Atlanta, USA, in 2020. He joined GIT to pursue his Ph.D. in Fall 2016. During his Ph.D. studies, Maad worked as a research assistant in the Power Systems Control and Automation Laboratory (PSCAL) from Fall 2018 to Spring Fall 2019. Maad's research interests include home energy management systems, optimization of power system operations planning and control, and reliability assessment of power systems.

Maad was an undergraduate trainee with the Power Division, General Electric Company, New York, USA, from July to December, 2012. In Spring 2014, he joined KFUPM as a graduate assistant teaching undergraduate electrical engineering laboratories and in Fall 2015, he was promoted to be a lecturer and taught for a year before starting his Ph.D.

Maad served as the Vice-Chair of IEEE-KFUPM student branch in 2015. He also served as the Outreach Chair of IEEE PES Chapter at Georgia Tech from Fall 2020 until Summer 2021.